UNIVERSITI TEKNOLOGI MARA

JMechE
Journal of Mechanical Engineering

Regular Issue Jan 2023
Volume No.20(1)
ISSN : 1823 - 5514
e-ISSN : 2550 - 164x
jmeche.uitm.edu.my

JOURNAL OF MECHANICAL ENGINEERING

Journal of Mechanical Engineering (ISSN 1823-5514, e-ISSN 2550-164X) is published by Penerbit UiTM (UiTM Press), Universiti Teknologi MARA, 40450 Shah Alam, Selangor, Malaysia.

JOURNAL OF
MECHANICAL ENGINEERING
An International Journal

Vol 20 (1)	15 January 2023	ISSN 1823-5514	eISSN 2550-164X

Laser Powder Bed Fusion Process Optimization of AlSi10Mg Alloy Using Selective Laser Melting: Dynamic Performance of Fatigue Behaviour, Microstructure, Hardness and Density

Mudda Nirish[*], R.Rajendra, Buschaiah Karolla
Department of Mechanical Engineering,
University College of Engineering (A), Osmania University,
Telangana, INDIA
[*]nirishyadav@gmail.com

ABSTRACT

The quality of a selective laser melting (SLM) component depends on build orientation and layer thickness, which are directly influenced by processing parameters. The present research of layer-by-layer additive simulation before starting the SLM process has several advantages, such as saving time, cost, and material. In this main investigation, the dynamic performance of fatigue strength, density, and hardness of AlSi10Mg alloy was produced by the SLM-AM according to the design of experiments. The L9 orthogonal array of the Taguchi method was created to perform the experimental development process. Finally, the obtained optimal process parameter with the highest values of fatigue strength, density, and hardness was found at a laser power of 225 Watts, a scan speed of 500 mm/s, and a hatching distance of 100 µm. The experimental density result was achieved with a high density value of 99.6% (2.66 g/cm^3) and a defect-free component and hardness of 126±5 HV. The future scope of this study will use optimal process parameters to find out mechanical properties for as built and preheated conditions for aerospace applications.

Keywords: *Selective Laser Melting; Geometric Dimensioning and Tolerance; Fatigue Strength; Microstructure; Density and Hardness*

ISSN 1823-5514, eISSN2550-164X

https://doi.org/10.24191/jmeche.v20i1.21074

Received for review: 2022-03-15
Accepted for publication: 2022-09-19
Published: 2023-01-15

Introduction

Selective laser melting (SLM), also called direct metal laser melting (DMLM), is a layer-by-layer manufacturing technology with fully dense and high-quality metal parts produced by the corresponding 3D computer-aided design (CAD) model [1]. The biggest drawback that limits the applicability of today's technologies is the high cost of AM components compared with conventional manufacturing process [2]. Metal AM provides the advantages of being flexible in terms of free geometric design and wasting less material in the SLM-AM process [3]. The current trend to increase productivity or efficiency is based on the process parameters of optimization technology, multi-laser machine process development, and automation aimed at reducing machine downtime and producing high-density parts [4]. To avoid defects in the SLM process maintain the minimum laser power and scan speed [5]. AM technology has built up within the defense, aerospace, and biomedical industries [6]. In SLM fabricated samples, three types of porosity are present: "lack of fusion", gas and shrinkage porosity, and key holing [7]. A "lack of fusion" is a bonding defect that arises in parts with a low energy density or low laser power [8]-[9]. Aluminum alloys are used common in aerospace application compared to titanium alloys because of AlSi10Mg alloy are easy to melt in SLM printing [10]. This SLM machine normally changes process parameters that can be improved AM part strength and performance [11]. The laser powder bed fusion (LPBF) systems have so many process parameters, mostly used for layer thickness, building direction, laser spot diameter, laser power, scan speed, and hatching distance [12]-[13].

Previous researchers have worked on the microstructure and mechanical properties of parts made of AlSi10Mg: powder properties [14], internal porosity of defective parts [15], hardness, surface roughness, and tensile properties [16]. From the literature survey, it was concluded that the mechanical properties, and particularly the fatigue strength of AlSi10Mg specimens [17], typically depend on internal microstructure, pores, porosity, cracks, and oxide films [18]. The various printing processes have process parameters that affect porosity on SLM-AM parts [19]. The build direction is main role in SLM printing; it can be concluded of AM part density [20]. The various process parameters that affect fatigue, microstructure, density, and hardness of AlSi10Mg alloy were discussed by giving process parameters such as the laser power, scan speed, hatching distance, and layer thickness [21]. The circulation of pores to parts in the AM printing depends on the building orientation. Specimens were displayed with low porosity and expressed with high fatigue performance in horizontal orientation [22]. The optimised parameters are empirically derived to generally produce dense materials, minimise defects, reduce surface roughness [23], increase build rate, and produce parts with acceptable material properties [24]. The process parameters provided by machine manufacturers are typically developed to

provide the best result in the material produced as a compromise of these competing (and interdependent) priorities [25].

In this work, optimization of process parameters with horizontal build orientation was conducted, and a test of bending fatigue test of AlSi10Mg parts manufactured by SLM was also conducted.

- Developed the additive process simulation for AM part using the design of experiment table.
- Using the Artec 3D scanner for geometric dimensioning and tolerance (GD&T) for geometric inaccuracy.
- To determine mechanical properties of fatigue strength, hardness, density and microstructure characterization.
- The output dynamic performance is considered as a prediction of fatigue strength.
- Used the Taguchi method for output statistical evaluation.

Experimental Procedure

Material

The laser power melted AlSi10Mg aluminium alloy printed specimens for fatigue tests were fabricated by the SLM process. Table 1 shows the chemical composition of AlSi10Mg.

Table 1: Chemical composition of AlSi10Mg alloy (www.slm solutions.com)

Al	Si	Fe	Cu	Mn	Mg	Zn	Ti	Ni	Pb	Sn	Other total
Bal.	9 – 11	.55	.05	.45	.20 – .45	.10	.15	.05	.05	.05	.15

Specimen design

The SLM samples were prepared for fatigue strength as per the ASTM standard E2948 and the specimen dimensions were 130 mm in length with an 11diameter, gauged at 40 mm in length with a 7.5 mm diameter, and a radius of 7.5 mm as shown in Figure 1.

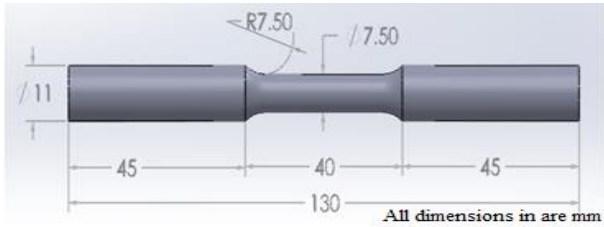

Figure 1: Test specimen size and its dimension considered fatigue testing line diagram

Powder analysis

The power particle size distribution has the main importance in the SLM process because it has the main influence on the part qualification, such as performance. The powder particle size distribution ranged from 20 to 63 µm and was supplied by SLM Solution Group AG, Germany. The powder weighted residual is 0.694%, the specific surface area is 0.154 m^2/g, the surface weighted mean is 38.8 µm and the volume weighted mean is 43.505 µm as shown in Figures 2a and 2b.

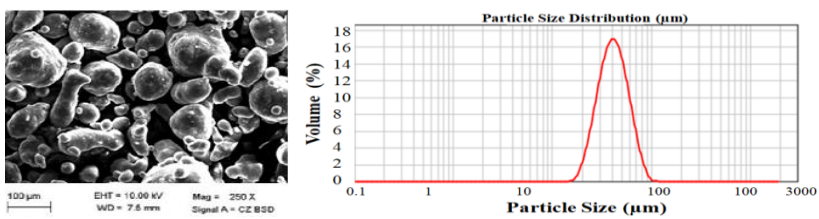

(a) (b)

Figure 2: a) SEM particle analysis, and b) powder particle size distribution

SLM process

This is mostly due to the high cost of the equipment parts being manufactured and operating SLM process parameters in three zones. Lack of fusion (the most common cause for concern; insufficient laser energy density, poor laser parameters, poor hatching strategy, spatter particles), key holing (a common cause for concern and too high laser energy density) and balling (not commonly, usually found only during parameter development and trying to get too fact). The SLM process parameter optimization includes laser power (LP or P), layer thickness (LT or t), beam diameter (D), material feed (mp), hatching distance (HD or h), scan speed (SS or v), building directions (BD or d) (X, Y, and Z axes) and SLM line diagram as shown in Figure 3a.

These are the adjustable parameter layer thickness, laser power, scanning speed, hatch spacing, and recoater speed as shown in Figure 3b.

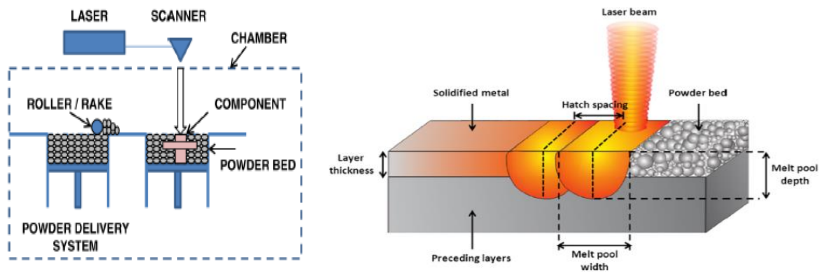

(a) (b)

Figure 3: a) SLM schematic diagram, and b) printing process (www. slm-solutions.com)

All the specimens were fabricated for the optimization of process parameters using the Taguchi L9 orthogonal array (OA) by producing an SLM machine M280 model of the AlSi10Mg alloy. The powder particle distribution used in our experiments ranged from 20 to 63 µm. The SLM build platform dimensions are 280 × 280 × 365 mm and uses a continuous IPG fiber laser. In this study, the process parameters that varied were laser power at three levels: 200, 225, and 250 Watts; scan speed at three levels: 400, 500, and 600 mm/s; and hatch distance at three levels: 60, 80, and 100 m. The remaining process parameters are kept constant as a laser spot diameter of 75 µm, layer thickness of 30 µm, build platform temperature of 150 ºC, and a scanning pattern of 0°. All the specimens were built in a horizontal orientation (i.e., without any support structure) and used only printing support on the SLM base plate (i.e., block support structure). Maintain the atmosphere in the SLM printing process at a maximum oxygen content level of 0.12%. The process parameters were considered as per design of experiment and an L9 (3^3) OA as shown in Tables 2 and 3.

Table 2: Levels and their factors for LPBF of AlSi10Mg alloy

Process Parameters	Level 1	Level 2	Level 3
A: Laser power (LP) in Watts	200	225	250
B: Scan speed (SS) in mm/s	400	500	600
C: Hatching distance (HD) in µm	60	80	100

Table 3: used L9 orthogonal array as per design of experiment

Trials	Laser power (Watts)	Scan speed (mm/sec)	Hatching distance (µm)
Trial (T1)	200	400	60
Trial (T2)	200	500	80
Trial (T3)	200	600	100
Trial (T4)	225	400	80
Trial (T5)	225	500	100
Trial (T6)	225	600	60
Trial (T7)	250	400	100
Trial (T8)	250	500	60
Trial (T9)	250	600	80

The SLM additive designer's inbuilt software was used to generate individual process parameters based on a given design of experiment, and the data was then transferred to an SLM machine for printing process, as shown in Figure 4a. The laser energy density was calculated by Equation (1) and density values as shown in Figure 4b.

$$E = P / s \times h \times t \tag{1}$$

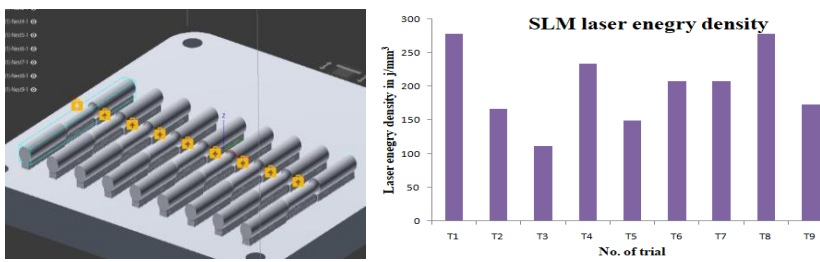

(a) (b)

Figure 4: a) Layout of specimen on SLM 280 build platform and b) Laser energy density value by Taguchi L9 OA

After given .stl file to the SLM printing process based on the process parameters and also calculated the laser energy density according to L9 OA.

Results and Discussion

Previous researchers have worked on the microstructure and mechanical properties of parts made of AlSi10Mg: powder properties, internal porosity of defective parts, hardness, surface roughness, and tensile properties. This research worked on fatigue strength improvement based on the given process parameter optimisation [12], which also increased the life cycles of SLM-AM parts [16].

Simulation of part using experimental design table

The Altair Inspire 3D software used for AM part thermal gradient in SLM printing Process. Temperature is the main important process in the SLM printing process and it is also done thermal analysis simulation (i.e., saving cost, time and material) to optimise the process parameter used for the L9 parameter before SLM print as shown in Figure 5a (displacement) and Figure 5b (temperature ranges). From the simulation results, trial 5 produced better results, with less temperature and less displacement. This parameter is considered to avoid defects and thermal displacement as shown in Figure 6a and temperature range as shown in Figure 6b. If a part was printed at a high temperature, it required a high cooling rate and produced defects with thermal defects (i.e., inaccurate geometry [4]).

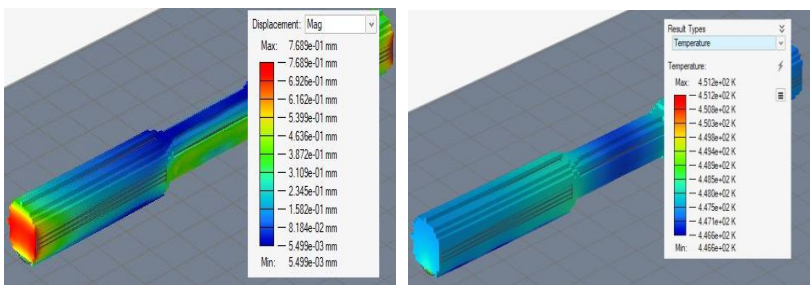

(a) (b)

Figure 5: a) Thermal simulations of displacement, and b) SLM printing temperatures used in printing process

Geometric accuracy of part

As shown in figure 7a, the measured geometric dimensions for part geometry inaccuracy were achieved using an Artec 3D scanner with a high-resolution white laser. The technology used in this research scanned the SLM manufactured parts and observed the geometric shape (such as thermal distortion and deviation, i.e., geometry inaccuracy) [4]. From figure 7b scanned all the specimens after SLM manufactured and also compared the dimensions of the nominal diameter with the SLM printed diameter.

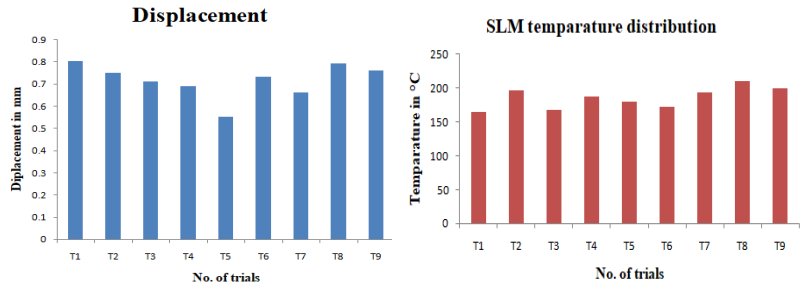

(a) (b)

Figure 6: a) Thermal analysis of displacement, and b) SLM printing process temperature

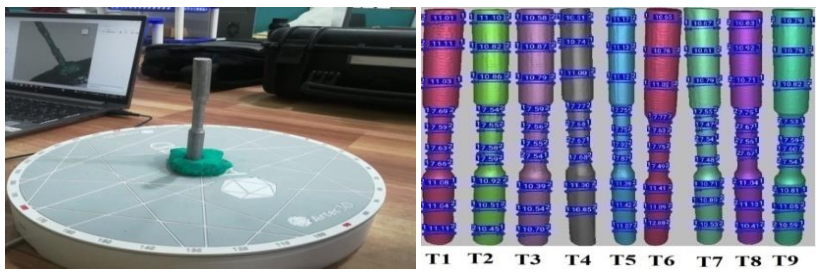

(a) (b)

Figure 7: a) Artec 3D scanning for part geometry and part printed is located, and b) scanned diametrical deviation of top, middle and lower diameter section (T5 part give dimensionally accurate geometry)

The given design diameters of gauge were 7.5 mm in diameter with a 40 mm length at the top and bottom, and 11 mm in diameter with a 45 mm length. The entire specimen diameter (bottom, top, and gauge) was increased due to the high laser with low scan rate as shown in Figures 8a and 8b. Except for Trial5, all of the specimens have geometric inaccuracy due to various process parameter effects.

Dynamic performance of AM part-fatigue testing

Dynamic bending fatigue performance is more important for applied dynamic load on aerospace components. It is well known that the fatigue strength of AlSi10Mg alloys depends on metallurgical defects and porosity effects in oxide layer films. The fatigue performance was conducted in a fully reversed with rotating bending mode. The experiment was conducted as a fatigue test at room temperature on the motor with a driven shaft rotating beam machine. The machine components are: flexible bearing, weight hanger assembly,

bearing spindle (shaft), bearing and its housing assembly, chuck, digital counter, AC electric motor as shown in Figure 9a and after SLM manufactured test specimens for fatigure testing as shown in Figure 9b.

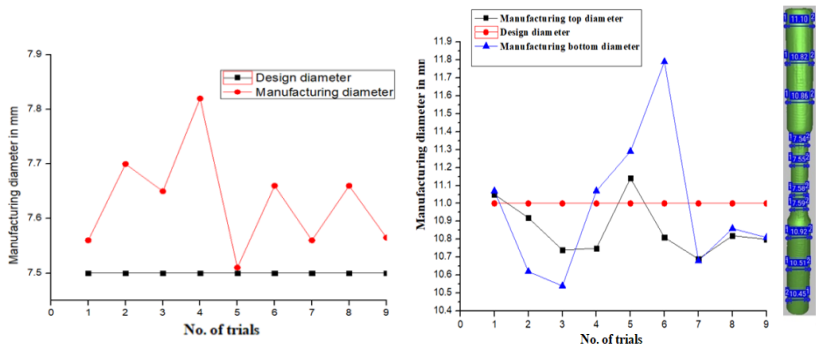

(a) (b)

Figure 8: (a) and, (b) compared the diameters with design diameter

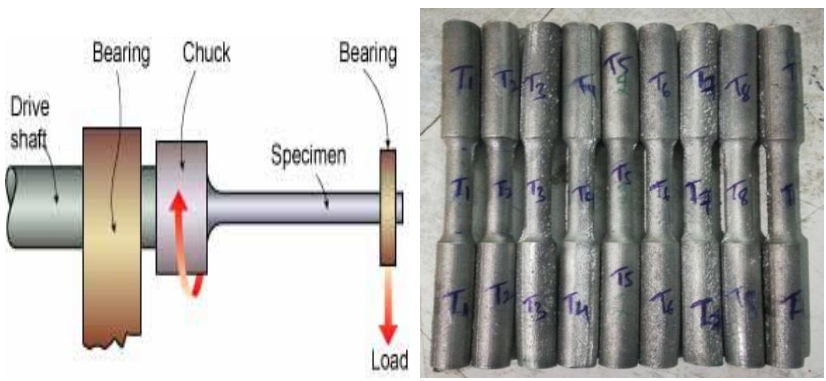

(a) (b)

Figure 9: a) Fatigue testing machine, and b) SLM manufactured parts

From the Figure 9b after SLM manufcatured sample for fatigue tesing as per design of experiments like Trial 1 to Trial 9 and calculated the fatigue life cycles for 3D printed samples. A typical fatigue test piece has three areas: a test section and two grip clamps or ends. The grip hold ends are designed for load transfer from the test machine hold to the test section and can be identical, especially in rotary bending fatigue tests. To eliminate any stress concentrations in the transition from the grip ends to the test region, broad, smoothly blended radii are used. The design and type of test piece used depends on the fatigue tester used and the purpose of the fatigue test.

The test section of the specimen should be sized to take the fatigue load capacity with a reduced cross section to prevent damage to the clamp ends from sample failure. The conducted test for all specimens was obtained as a process parameter at a particular constant load, i.e., a stress amplitude of 10 Kg, or 145.14 MPa [16]. The prediction of fatigue life at applied constant load and calculating the motor rpm at braked of the specimen as shoen in figure 10a, then get the number of cycles ploted as shown in Figure 10b.

- The motor rpm is 2880. 1 minute is equal to 2880 rev (i.e., 1 sec = 2880/60 = 48 rps).
- The number of cycles is equal to the time taken (s) × 48 rps.
- The prediction of the fatigue strength calculation:
  The length of the shaft (L) is 490 mm.
  The diameter of the shaft (d) is 15 mm, and
  For the fatigue test, a load of 10 Kg is applied.
- Weight (W) = 10 × 9.81 = 98.1 N.
- Bending moment, M

$$M = W \times L \tag{2}$$

$= 98.1 \times 490$

$= 48069$ N-mm and

- Bending stress, (σ_b)

$$\sigma b = 32M / \pi d^3 \tag{3}$$

$= 32 \times 48069 / 3.14 \times (15)^3$

$= 145.14$ MPa.

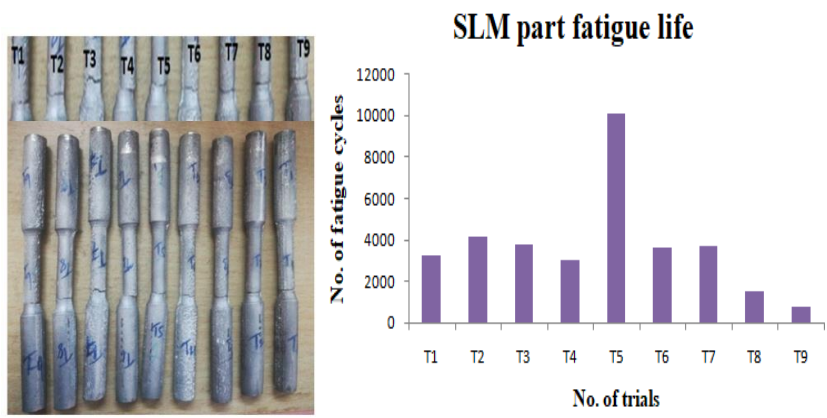

(a) (b)

Figure 10: a) After fatigue tested breaked specimens, and b) results

From Figure 10b, which shows fatigue life cycles for each specimen using constant loads. The fatigue life also depends on the process parameters,

like when using the high and low range parameters, a lot of pores, oxide films, and cracks are formed when using low laser power with scan speed (trai 1, trial 2, and trial 3), and there is also thermal deviation when using high laser power with scan speed (trai 7, trial 8, and trial 9). The trial 5 achieved high fatigue cycles because of geometric accuracy and no metalurgical defects.

Hardness and density

The hardness and density results according to design of experiment L9 OA are shown in Figures 11a and 11b. The hardness and mechanical property values are mainly dependent on the microstructure of pores, cracks, and porosity with thermal deviation. When used, the high laser power and low scan speed due to keyholing of high energy densities Vickers hardness was determined through microhardness testing, with each specimen having an average of three indentations in three different areas. The highest value of hardness achieved was 126±5 HV [6] under a load of 1000 grams with a 10 second duration. The prepared the samples for density testing by the Archimedes standard principle, which is used by xylene water. The theoretical density of AlSi10Mg alloy powder (ρt) is 2.67 g/cm^3 and, after SLM, manufactured parts have the highest density of 2.66 g/cm^3. According to the graph, increasing the laser power from 200 to 250 Watts and the scan speed from 400 to 600 mm/s reduced the density from 99.9% to 95% and the hardness from 126±5 to 96±5 HV compared with literature survey [5], [9]. It shows that the optimum value of hardness and density occurred at trial 5.

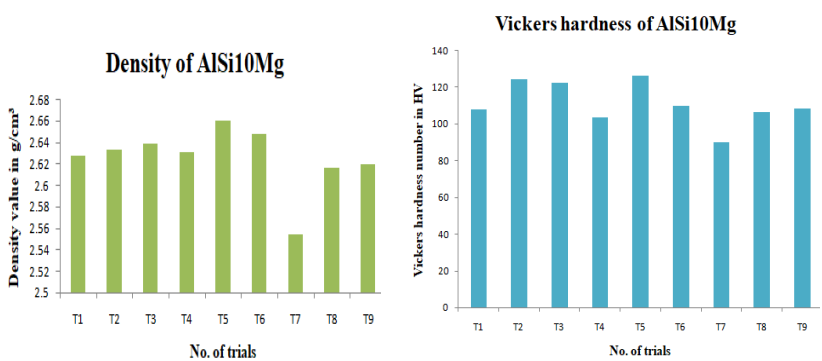

(a) (b)

Figure 11: a) Vickers hardness, and b) density of AlSi10Mg samples

Microstructure evaluation

The scanning electron microscope (SEM) was used for microstructure characterization at the different magnification levels as shown in Figures 12a,

12b, and 12c. As shown in Figures 12d, 12e, and 12f, a lot of pores, oxide films, and cracks are formed when using low laser power with scan speed (trai 1, trial 2, and trial 3), and there is also thermal deviation when using high laser power with scan speed (trai 7, trial 8, and trial 9). In terms of strength and performance, the hatching distance was the most important factor. The pores can be divided into spherical pores and irregular pores. Cracks are observed along with the horizontal direction of the structure. Due to the poor wettability of oxides and metals, long cracks were formed and spread along the surface. Due to the low cooling rate, some of the AlSi10Mg powder particles are formed as a result of oxidation during the SLM process. The decrease in laser power, density, and hardness also decreased. The increase in san speed then hardness increased and density decreased due to porosity.

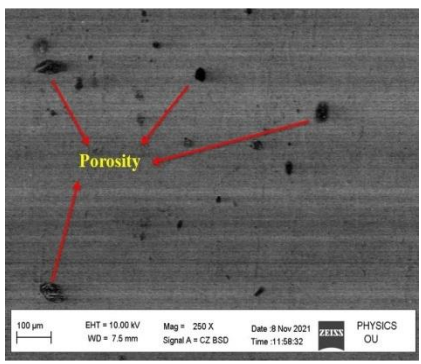

(a)

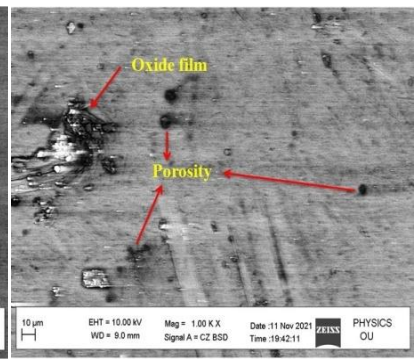

(b)

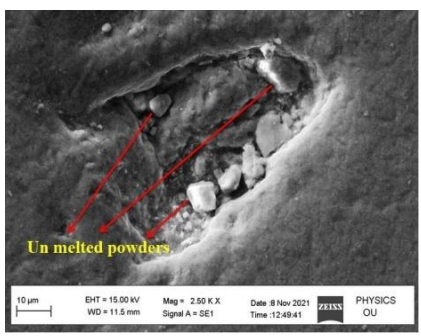

(c)

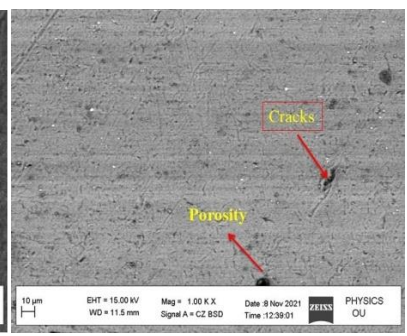

(d)

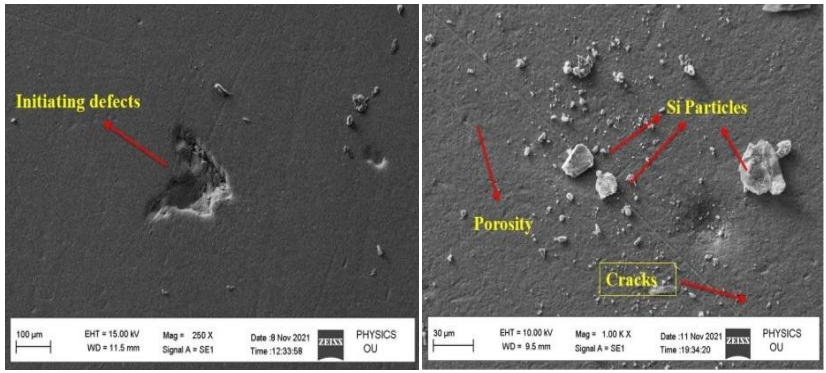

(e) (f)

Figure 12: Defects at different laser power and scan rates; (a) 200 watts with 400 mm/s, (b) 200 watts with 500 mm/s, (c) 200 watts with 4600 mm/s, (d) 250 watts with 400 mm/s, (e) 250 watts with 500 mm/s, and (f) 250 watts with 600 mm/s

From the design of experiment manufactured sample trial 5, all achieved full density and without defects, shown at different magnifications as shown in Figures 13 and 14. The microstructural characterization had the main influence on mechanical properties like strength and hardness.

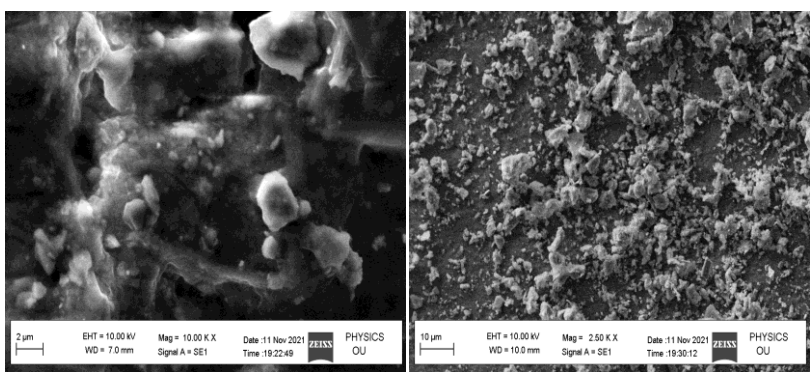

(a) (b)

Figure 13: (a) and, (b) defects free components at 225 watts with 500 mm/s

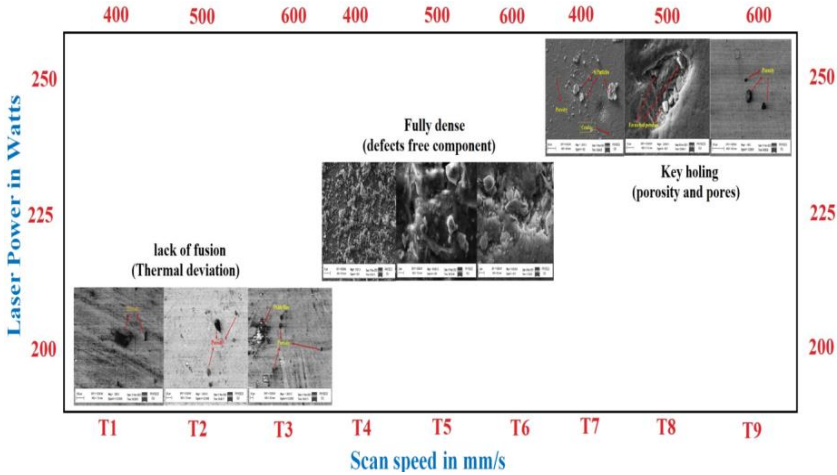

Figure 14: Comparison of laser power with scan speed microstructure evaluation

Taguchi Method

Design of experimental

The Taguchi technique uses experimental results to optimise the process parameters and can be classified into the following steps:

- To design and run the experiment as 3^3 (L9).
- Give the process parameters of levels and factors.
- Next, using the signal-to-noise ratio (S/N) and analysis of variance.
- Examine the experimental design (ANOVA).
- Finally, it receives the optimal process parameters based on the analysis results.

Signal-to-noise (S/N) ratio

In this method, the experimental results for the S/N ratio were considered the higher value (i.e., fatigue strength, density, and hardness). The best way to apply the condition rule to a larger S/N ratio is to use the following Equation (4).

$$S/N = -10 \log \left[\frac{1}{n} \sum_{i=1}^{n} \frac{1}{y_i^2} \right] \quad (4)$$

Where n is the total number of experiments, y_i^2 is the density value for ith experiment, and Taguchi analysis considers the highest number of cycles

(trial 5). From the response table delta statistic, the highest factor rank for laser power is 1, scan speed is rank 2, and hatching distance is rank 3.

Analysis of Variance (ANOVA)

Analysis of variance (ANOVA) is the most frequently used statistical method. In this case, ANOVA was required to determine the contribution of each process parameter to fatigue strength. In ANOVA, the sum of squares (SST), the sum of squares of each factor (SSF), the mean square of each factor (MSF), the degree of freedom (DF), percentage of the contribution (%), P-test, and F-test were calculated by the regression analysis of various process parameters such as laser power, scan speed, and hatching distance. To determine which level of each element provides the best performance and results, levels with values from response table 4 were used. From Figure 15, it is clear that laser power is the most influential factor, followed by scan speed and hatching distance. The slope line was connected at various levels with the process parameters of each variable. A laser power of 225 Watts (A2), a scan speed of 500 mm/s (B2), and a hatching distance of 100 m (C3) were used to achieve the optimal process parameter for fatigue strength.

Table 4: Statistical method used by ANNOVA

Source	DF	Seq SS	Contribution	Adj SS	Adj MS	F-Value	P-Value
Regressi	3	2006853	40.04%	2006853	668951	0.60	0.641
Laser Power in Watts	1	1175440	25.74%	1175440	117544	1.06	0.350
Scan Speed in mm/s	1	228931	15.39%	228931	228931	0.02	0.891
Hatching Distance in µm	1	8085204	12.39%	8085204	808520	0.73	0.432
Error	5	5544076	6.44%	554407	11088		
Total	8	7550930	100.00%				

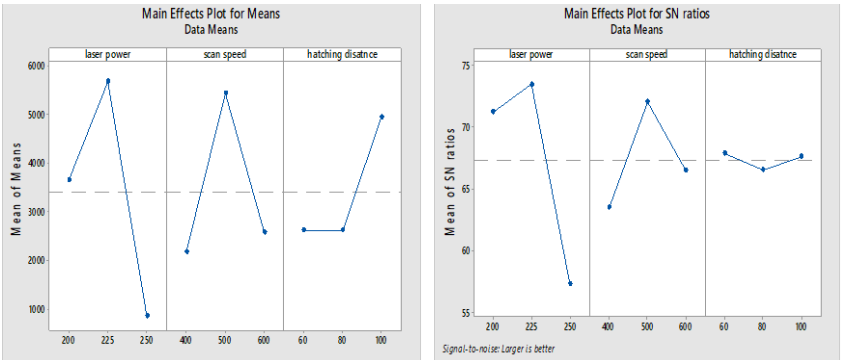

(a) (b)

Figure 15: S/N ratio graph for fatigue strength

Conclusion

This research analysed the defects using various process parameters and found their dynamic performance of highest fatigue strength. In this SLM process, the part build orientation is the most important factor, especially in fatigue performance.

i. It is observed that when using a high laser at the different scan speeds in the SLM process, the additive simulation results are given the AM part displacement (i.e., deviation of geometric defects) due to high laser power [4]. For high density and mechanical strength, it is preferable to consider values such as low laser power with a lower scan speed rate.

ii. A very high SS of 600 mm/s was given a high percentage of porosity, pores, and cracks, i.e., resulting in a drastic reduction in fatigue strength, density, and hardness. The hardness was decreased due to increasing the scan speed rate from 400 to 600 mm/s and the density was decreased due to increasing the laser power from 200 to 250 watts. The porosity depends on the complete scan rate [9].

iii. Finally, achieved a defect-free component without distortion at laser power of 225 Watts, scan speed of 500 mm/s, and hatching distance of 100 µm [12]. The laser energy density at trial (t5) was 150 J/mm^3. The obtained results at t5: fatigue life cycle was 1.08×10^4 (applied stress amplitude of 145.14 MPa) [16], density was 2.66 (99.6%), and hardness was 126±5 HV (applied 1000 grams with a 10 second hold at three different areas).

iv. After using experimental results with a statistical method (ANOVA), it was observed that the most significant parameter was

laser power, which had a contribution of 25.74%, scan speed was 15.39%, and hatching distance was 12.39%.

v. The future scope of this study using optimal process parameters to find out mechanical properties for as-build and preheated conditions for aerospace application.

Contribution of Author

Conceptualization: Mudda Nirish , R.Rajendra; Methodology, Mudda Nirish, R.Rajendra, Buschaiah Karolla.; Software, Mudda Nirish; Formal analysis, Mudda Nirish, Buschaiah Karolla; Investigation, Mudda Nirish, R.Rajendra; Data curation, Mudda Nirish, R.Rajendra; Writing—original draft preparation, Mudda Nirish; Writing—review and editing, Mudda Nirish, R.Rajendra and Buschaiah Karolla; Visualization, Mudda Nirish; Supervision, R.Rajendra.; Funding acquisition, Mudda Nirish. All authors have read and agreed to the published version of the manuscript.

Funding

This research received no external funding.

Conflict of Interests

This research received no Conflict of interests.

Acknowledgement

The authors would like to thank the research facilities centre funded by the Govt. of India's Rashtriya Uchchatar Shiksha Abhiyan (RUSA 2.0) at the University College of Engineering (A), Osmania University, Hyderabad, India.

Nomenclature

W	Wight or Load
l	Length of Shaft
d	Diameter of Shaft
σ_b	Bending Stress
M	Bending Moment
n	Total Number of Experiments
y_i^2	Density Value for i^{th} Experiment
E	Laser Enegry Density
P	Laser Power
v	Scan Speed
h	Hatching Distance
t	Layer Thickness

Abbreviation

FEM	Finite Element Method
S/N	Signal-to-Noise
ANOVA	Analyses Of Variance
AM	Additive Manufacturing
DMLM	Direct Metal Laser Melting
SLM	Selective Laser Melting
LPBF	Laser Powder Bed Fusion
CAD	Computer Aided Design
DoE	Design of Experiments
SST	Sum of Squares
SSF	Sum of Squares of Each Factor
MSF	Mean Square of Each Factor
GD&T	Geometric Dimensioning and Tolerance
SEM	Scanning Electron Microscope

References

[1] Shahrubudin N, Lee TC, Ramlan R, "An overview on 3D printing technology: Technological, materials, and applications," *Procedia Manufacturing*, vol. 35, pp. 1286-96, 2019.

[2] Frazier WE, "Metal additive manufacturing: a review," *Journal of Materials Engineering and performance*, vol. 23, no. 6, pp. 1917-28, 2014.

[3] Nirish M and Rajendra R, "Suitability of metal additive manufacturing processes for part topology optimization–A comparative study," *Materials Today: Proceedings,* vol 27, pp.1601-7, 2020.

[4] Wang P, Lei H, Zhu X, Chen H, Fang D, "Influence of manufacturing geometric defects on the mechanical properties of AlSi10Mg alloy fabricated by selective laser melting," *Journal of Alloys and Compounds*. vol.789, pp. 852-859, 2019.

[5] Mudda Nirish and R.Rajendra, "Optimization of Process Parameter and Additive Simulation for Fatigue Strength Development by Selective Laser Melting of AlSi10Mg Alloy," *International Journal of Mechanical Engineering*, vol. 7, no. 2, pp. 3795-3802, 2022.

[6] Liu Y, Liu C, Liu W, Ma Y, Tang S, Liang C, Cai Q, Zhang C, "Optimization of parameters in laser powder deposition AlSi10Mg alloy using Taguchi method," *Optics & Laser Technology*, vol. 111, pp. 470-80, 2019.

[7] Read N, Wang W, Essa K, Attallah MM, "Selective laser melting of AlSi10Mg alloy: Process optimisation and mechanical properties development," *Materials & Design*, vol. 65, pp. 417-24, 2015.

[8] Mudda Nirish and R.Rajendra, "Heat Treatment Effect on the Mechanical Properties of AlSi10Mg Produced by Selective Laser Melting," *Journal of Mechanical Engineering Research and Development*, vol. 45, no. 2, pp. 19-28, 2022.

[9] Wu H, Li J, Wei Z, Wei P, "Effect of processing parameters on forming defects during selective laser melting of AlSi10Mg powder," *Rapid Prototyping Journal*, vol. 26, no. 5, pp. 871-879, 2020.

[10] Oliveira JP, LaLonde AD, Ma J, "Processing parameters in laser powder bed fusion metal additive manufacturing," *Materials & Design*, vol.193, pp. 108762, 2020.

[11] Bajaj P, Wright J, Todd I, Jägle EA, "Predictive process parameter selection for Selective Laser Melting Manufacturing: Applications to high thermal conductivity alloys," *Additive Manufacturing*, vol. 27, pp. 246-58, 2019.

[12] Mudda Nirish and R.Rajendra, "Additive Layer by Layer Simulation and Taguchi Loss of Function for AlSi10Mg Alloy Samples Manufactured by Selective Laser Melting," International Journal of Mechanical Engineering, vol. 7, no. 5, pp. 765-770, 2022.

[13] Beretta S, Gargourimotlagh M, Foletti S, Du Plessis A, Riccio M, "Fatigue strength assessment of "as built" AlSi10Mg manufactured by SLM with different build orientations," *International Journal of Fatigue*, vol. 139, pp. 105737, 2020.

[14] Mudda Nirish and R.Rajendra, "Effect of Heat Treatment on Wear Characterization of AlSi10Mg Alloy Manufactured by Selective Laser Melting," Journal of Mechanical Engineering Research and Development, vol. 45, no. 2, pp. 10-18, 2022.

[15] Xu ZW, Wang Q, Wang XS, Tan CH, Guo MH, Gao PB, "High cycle fatigue performance of AlSi10mg alloy produced by selective laser melting," *Mechanics of Materials*, vol. 148, pp. 103499, 2020.
[16] Mudda Nirish and R.Rajendra, "Additive Simulation and Process Parameter Optimization for Wear Characterization Development by Selective Laser Melting of AlSi10Mg Alloy," *Journal of Characterization*, vol. 2, no. 2, pp. 103-116, 2022.
[17] Qian G, Jian Z, Qian Y, Pan X, Ma X, Hong Y, "Very-high-cycle fatigue behavior of AlSi10Mg manufactured by selective laser melting: Effect of build orientation and mean stress," *International Journal of Fatigue*, vol. 138, pp. 105696, 2020.
[18] Mudda Nirish and R.Rajendra, "Fatigue Performance Improvement of AlSi10Mg Manufactured by Selective Laser Melting through Heat Treatment," *Journal of Mechanical Engineering Research and Development*, vol. 45, no. 3, pp. 01-13, 2022.
[19] Santos LM, Ferreira JA, Jesus JS, Costa JM, Capela C, "Fatigue behaviour of selective laser melting steel components," *Theoretical and Applied Fracture Mechanics*, vol. 85, pp. 9-15, 2016.
[20] Uzan NE, Ramati S, Shneck R, Frage N, Yeheskel O, "On the effect of shot-peening on fatigue resistance of AlSi10Mg specimens fabricated by additive manufacturing using selective laser melting (AM-SLM)," *Additive Manufacturing*, vol. 21, pp. 458-64, 2018.
[21] Jian ZM, Qian GA, Paolino DS, Tridello A, Berto F, Hong YS, "Crack initiation behavior and fatigue performance up to very-high-cycle regime of AlSi10Mg fabricated by selective laser melting with two powder sizes," *International Journal of Fatigue*, vol.143, pp.106013, 2021.
[22] Mudda Nirish and R.Rajendra, "Optimization Process Parameter on Wear Characterization of Al6061 and AlSi10Mg Alloy Manufactured by Selective Laser Melting," *International Journal of 3D Printing and Additive Manufacturing*, vol. 2, no. 1. pp. 1-10. 2022.
[23] Brandl E, Heckenberger U, Holzinger V, Buchbinder D, "Additive manufactured AlSi10Mg samples using Selective Laser Melting (SLM): Microstructure, high cycle fatigue, and fracture behavior," *Materials & Design*. vol. 34, pp.159-69, 2012.
[24] Zhao J, Easton M, Qian M, Leary M, Brandt M, "Effect of building direction on porosity and fatigue life of selective laser melted AlSi12Mg alloy," *Materials Science and Engineering: A*, vol. 729, pp. 76-85, 2018.
[25] Nirish M, Rajendra R. "Selective laser melting process parameter simulation and topology optimization by aerospace component of AlSi10Mg alloy," *InAIP Conference Proceedings 2022*, vol. 2648, no. 1, pp. 020019, 2022.

Process and Heat Resources for Wire Arc Additive Manufacturing of Aluminium Alloy ER4043: A Review

Nur Izan Syahriah Hussein, Gan Chin Ket, Toibah Abdul Rahim, Mohamad Nizam Ayof, Muhammad Zaimi Zainal Abidin*
Faculty of Manufacturing Engineering,
Universiti Teknikal Malaysia Melaka, Hang Tuah Jaya,
76100 Durian Tunggal, Melaka, MALAYSIA
**chinket_0508@hotmail.com*

Jongkol Srithorn
School of Industrial Engineering, Suranaree University of Technology,
Nakhon Ratchasima, 30000, THAILAND

ABSTRACT

The application of wire arc additive manufacturing (WAAM) in manufacturing has raised interest among researchers. In this paper, the introduction of additive manufacturing and wire arc additive manufacturing, various heat resources for WAAM, aluminium alloys, aluminium alloys ER4043, and performance evaluation of WAAM of ER4043 have been discussed in detail based on bead geometry, microstructure, microhardness, and tensile properties as well as the building path strategies, problems, and future directions. Based on this review, aluminium alloy 4043 (ER4043) is an Al-Si alloy frequently employed as a filler wire because it has superior fluidity and significantly fewer flaws in additively built structures. Next, dwell time and cooling efficiency during the WAAM process significantly affect bead geometry. Besides, a finer microstructure can be obtained with a better cooling rate. However, a coarser microstructure is obtained along with the increased deposition height due to heat accumulation and low solidification rate. Heat input is identified as the main cause of porosity, and CMT with a lower heat input is preferable and outperformed GTAW and GMAW in terms of mechanical properties.

Keywords: *Additive Manufacturing; WAAM; ER4043; Aluminium alloy*

ISSN 1823-5514, eISSN 2550-164X

https://doi.org/10.24191/jmeche.v20i1.21077

Received for review: 2022-04-21
Accepted for publication: 2022-09-12
Published: 2023-01-15

Introduction

Additive manufacturing (AM) is a novel layering technology to produce complicated forms. Compared to traditional (subtractive and formative manufacturing) techniques, AM allows for greater design flexibility, reduced personnel participation, and extensive tool usage [1]-[2]. AM techniques include wire arc additive manufacturing (WAAM), selective laser melting (SLM), and laser additive manufacturing (LAM) [3]. SLM has superior mechanical performance [4] than WAAM because of the high cooling rate and small grain size [5]-[6]. However, SLM's high manufacturing cost and low deposition rate have limited its usage in industries [5]. As a result of the great deposition rate and reduced manufacturing cost, WAAM is gaining popularity worldwide [3].

Aluminium alloys have received a lot of attention to be manufactured by AM method [7]. As a result, WAAM of aluminium alloys has been extensively researched, including a variety of alloy systems such as aluminium-copper (Al-Cu), aluminium-magnesium (Al-Mg), aluminium-silicon (Al-Si), aluminium-copper-magnesium (Al-Cu-Mg), and aluminium-magnesium-silicon (Al-Mg-Si) [8]. However, one of the hurdles to commercializing WAAM for aluminium component production is significant amounts of porosity [9]-[10]. Therefore, various enhancements such as optimizing the process parameter, modification of the WAAM process, and simulation application to anticipate the potential defect of aluminium alloys during the WAAM process have been approached by researchers.

Table 1 summarizes the review of the process and heat resources for WAAM of aluminium alloys. As shown in Table 1, most review publications on WAAM aluminium alloys focus on a specific issue, including the impact of process parameters, different arc modes, challenges, and recommendations for improvement. However, a full analysis of the WAAM of aluminium alloy 4043 and its performance (bead geometries, tensile properties, microhardness, and microstructure) is scarce. As a result, the objective of this study is to assess the performance of WAAM of aluminium alloy 4043 and examine the constraints, future, and outlook.

Table 1: Summary of review related to the process and heat resources for WAAM of aluminium alloy

No	Area of studies	Reference
1	Characteristics of aluminium alloys produced by various WAAM methods.	[9]
2	Introduction of WAAM, advantages, constraints, and mechanical properties of WAAM of aluminium alloy.	[10]
3	Enhancement and challenges of applying WAAM of aluminium alloys.	[11]
4	Common issues related to WAAM of aluminium alloys and performance enhancement.	[12]
5	The influence of process parameters on WAAM-built aluminium alloys.	[13]

Additive Manufacturing (AM)

The expanding manufacturing industry has adopted AM into design and modelling as a rapid prototype tool due to its ability to build complex geometries and produces significantly less material waste and labor [14]. AM has incorporated various manufacturing techniques such as material extrusion, lamination, powder bed fusion, directed energy deposition, and binder jetting to establish a variety of technologies, transforming it from a prototyping method to a finished-product method. AM technology's rapid growth is fueled by research focused on building low-cost machines, increased material variability, and the complexity benefit of catering to a wide range of applications. Previous work has intensively investigated and documented new methodologies, such as WAAM [1].

Wire Arc Additive Manufacturing (WAAM)

WAAM is a novel additive manufacturing technology that feeds wire through layer-by-layer deposition on a predetermined path using an electrical arc as a power supply [15]-[16]. It can deposit material layers for wall construction or clad two materials simultaneously to create a composite [14]. Furthermore, arc rapid prototyping has the advantages of high heat source efficiency and low cost compared to laser 3D printing and electron beam rapid prototyping [16]. Therefore, WAAM is among the most favorable large-part manufacturing techniques in the automotive, aircraft, and marine industries [15], [17]. A welding source, including gas tungsten arc welding (GTAW), plasma welding, and gas metal arc welding (GMAW), is used in WAAM procedures to melt a metallic filler wire for deposition. In addition, the Cold Metal Transfer (CMT) welding method was recently applied as a WAAM

heat source which allows for accurate monitoring of the deposited metal due to accurate regulation of the intensity waveform of the welding source combined with continuous feeding of the metal wire [18].

Various Heat Resources of Wire Arc Additive Manufacturing (WAAM)

Gas Tungsten Arc Welding (GTAW)

GTAW, or tungsten inert gas (TIG) welding, is a kind of arc welding that employs a non-consumable tungsten electrode to generate the weld [19]. To shield the region being welded from contamination, inert gases like argon or helium are employed. Unlike simpler welding processes that create slag, or metal chips prone to crumble off the welds, GTAW is a much "cleaner" technique of welding where welding slag is eliminated.

Gas Metal Arc Welding (GMAW)

GMAW, commonly known as MIG (metal inert gas) welding, is a technology that allows welders to weld non-ferrous materials. With its excellent energy efficiency, deposition rate, material usage, and short production time, GMAW-based additive manufacturing is now frequently used over other AM techniques [20]–[22]. Wang et al. [23], Ding et al. [24], and Cunningham et al. [25] demonstrated that GMAW based AM process had more benefits than laser beam-based, electron beam-based, GTAW-based, and plasma arc welding-based AM processes due to its high deposition rate, reduction of manufacturing cost, and environmental friendliness.

Cold Metal Transfer (CMT)

Controlling the heat input is the key challenge with WAAM. Excessive heat will cause the deposit microstructure to coarsen and flaws to appear, degrading the completed products' surface quality and mechanical performance [26]. The CMT technique, a modification of the GMAW process, delivers a high-quality, spatter-free weld with significantly reduced heat input [8], [27]. There are four arc modes in CMT technology: CMT, CMT advanced (CMT-ADV), CMT advanced pulse (CMT-PADV), and CMT pulse (CMT-P) [16], [28], [29].

Aluminium alloys

Aluminium alloys gained a lot of interest in recent decades for being manufactured by AM, and the WAAM of aluminium has been widely studied [8]. However, the fundamental flaw for aluminium is increased concentrations of porosity which affects the qualifying of both process and components, limiting the commercial application of WAAM [30]-[31].

Porosities are difficult to manage during the WAAM process as aluminium alloys are the most vulnerable to hydrogen due to the large variation in solubility between liquid and solid metal [32]. As a result, even a trace amount of hydrogen may surpass the solid-state solubility limit. Another reason for porosity is that moisture, grease, and other hydrocarbon impurities on the wire are transformed into atomic hydrogen, which is then available for absorption into the molten pool [10], [32], [33]. For example, aluminium alloys 2024 and 7075 are prone to solidification cracking. In addition, volatile materials, such as magnesium, in 5000 series (major alloying element) alloys volatilize during welding, affecting the tensile characteristics of the weld joint [10]. As a result, the 6000 and 7000 series alloys suffer hardening precipitate dissolution, whereas the 2000 alloys endure dissolution and reprecipitation, lowering overall strength [10]. Some pores may also be caused by solidification cavities [34]. These porosities lower the load area and enhance crack propagation during tensile tests, causing local brittle fractures [35]. As a result, high-quality welding wires and certain synergistic operating modes are required to minimize porosity [36].

Aluminium alloy 4043 (ER4043)

With the high fluidity and low sensitivity to hot shortness, 4000 series alloys were widely used as a filler material in welding and brazing [37]. Vimal et al. [38] concluded that the 4000 series outperformed the other series of aluminium alloys in terms of strength and porosity. Among 4000 series aluminium alloys, aluminium alloy 4043 (ER4043) is an Al-Si alloy frequently employed as a filler wire because it has superior fluidity and significantly fewer flaws in additively built structures [4], [6], [29]. Table 2 shows the chemical composition in ER4043 aluminium alloy.

Table 2: Chemical composition of ER4043 aluminium alloy [39]

Element	Si	Fe	Cu	Mn	Mg	Zn	Ti
ER4043	4.5-6.0	0.8	0.3	0.05	0.05	0.1	0.2

Performance evaluation of WAAM of ER4043

Bead height and width

Gupta et al. [40] claimed that the bead geometry influenced the final product's mechanical properties. It could be achieved by meeting the quality requirements, which were highly influenced by various process parameters involved in the process. Therefore, few researchers studied the bead height and width during the WAAM process. For example, Sinha et al. [41] discovered that a greater time interval in a continuous layer build-up,

suggesting better cooling of the previous layer, resulted in a smaller deposit width. However, the deposit width widened with the deposition layer's increase due to the aluminium alloy's high fluidity [41]. Ortega et al. [18] concurred with the findings, pointing out that heat accumulation in earlier deposits resulted in a progressive alteration in the geometry of the deposits. The author also emphasized that an optimal break time during deposition was critical to reducing geometric fluctuations or the width of the deposit increasing with layer addition, especially with greater average power. Path planning is also critical throughout the deposition process. Nie et al. [16] discovered that forming in a single direction might accumulate layers, causing the forming defection that one side of the thin wall was higher than the other due to the collapse and hump.

Process parameters such as wire feed rate (WFR), arc current (AC), travel speed (TS), dwell time (DT), the layer deposited (LD), arc voltage (AV), and shielding gas flow rate (SGFR) also had proved to influence the height and width of the bead. Ortega et al. [18] discovered that the drop weight of ER4043 reduced with travel speed as the energy produced by the electrical arc to melt the wire lowered. However, the author claimed that ER4043's high deposit frequency compensated for the condition and maintained a steady deposit rate throughout the WAAM procedure [18]. Nie et al. [16] concurred with the findings and asserted that when the travel speed surpassed a certain level, the width of the components narrowed, and the surface of the single wall appeared irregular. However, Wang et al. [42] and Panchenko et al. [43] held opposing views, claiming that faster welding rates were favored to optimize production efficiencies and product quality. Hao et al. [44] also found that columnar grains expanded around the fusing line and converted into equiaxed grains towards the top of the build-up wall, decreasing grain size as travel speed increased. Arc length correction (ALC) was also important in bead geometry development [45]. Kannan et al. [46] found that ALC greater than zero resulted in less dilution and higher bead height, whereas ALC less than zero resulted in more dilution and lower bead height. ALC of 10% is recommended by Madhavan et al. [47] for depositing aluminium filler wire with strong interlayer bonding. Besides, increasing the wire-feeding speed, according to Wang et al. [42], reduced weld penetration and resulted in a more convex clad layer. Furthermore, high-quality layered structures depend on metallurgical bonding, the cooling rate, and limiting residual stress [42]. As a result, a high-quality WAAM build-up requires the design of build-up parts, appropriate path planning approaches, and optimal process parameters [48].

Microstructure analysis

The refining function of an aluminium alloy was most noticeable in the refinement of the α-Al phase, such as grain size refinement and secondary dendrite arm spacing reduction [49]. A finer α-Al dendritic structure was

obtained when the time interval increased, which could be explained by the sufficient cooling time for the previously deposited layer [41]. Furthermore, Sinha et al. [41] applied copper tube and molding sand when depositing a wall to accelerate the cooling rate, resulting in a finer microstructure. Ortega et al. [18] emphasized that the first deposited layer recorded the finest microstructure and became coarser when the layer built up. The result obtained was due to the low initial temperature of the substrate, indicating a high cooling rate. The heat accumulation and low solidification rate would result in a coarser microstructure. The same findings were obtained from Pramod et al. [45]. According to the author, the first deposited layer at the base of the cylinder had a fine microstructure, indicating a greater solidification rate, and heat dissipation was increased owing to the existence of the substrate. As more additive layers were applied, the heat dissipation rate towards the substrate reduced, resulting in a coarse microstructure, as illustrated in Figure 1. Kindermann et al. [50] claimed that a high deposition rate, along with increased heat input and solidification time, worsened the porosity in aluminium as more hydrogen was absorbed into the weld pool. Furthermore, Pramod et al. [45] mentioned that majority of the pores observed at the top layers were caused by undissolved hydrogen due to a discrepancy in solubility between the liquid and solid phases. Ortega et al. [18] concurred with the observation. However, Nie et al. [16] asserted that the upper part had a fine dendritic structure, whilst the lower region had a coarse dendrite structure.

Apart from the cooling rate, the arc mode of deposition would also influence the microstructure. CMT-P exhibited improved grain refinement compared to CMT mode [29]. According to Vishnukumar et al. [29], during the short circuit phase of the CMT-P, an instantaneous decrease in heat input led the liquid metal to supercool, resulting in grain refinement and surface nucleation. Furthermore, the high arc pressure caused by the pulsed arc mode could produce adequate oscillations to fracture the dendritic arms, producing more heterogeneous nuclear sites and refining grain size. Grains mainly were Al, and α-Al was generated during the solidification of 4043 deposits. When the Al-Si eutectic ratio was attained, Al-Si eutectic formed at the grain boundaries, forming a thin network that increased crack resistance [51]. The grain size played a significant role, and the grain size of the aluminium alloy was mostly dictated by the number of nucleation, which was greatly influenced by the cooling rate [52]. Grain size could be calculated by multiplying the temperature gradient, G, by the solidification rate, R. Furthermore, the greater the measured value, the finer structure was projected to develop [7]. Wei et al. [53] demonstrated that when the heat input was reduced from the molten pool boundary, the grain size dropped, slowing the grain dislocations and reinforcing the material.

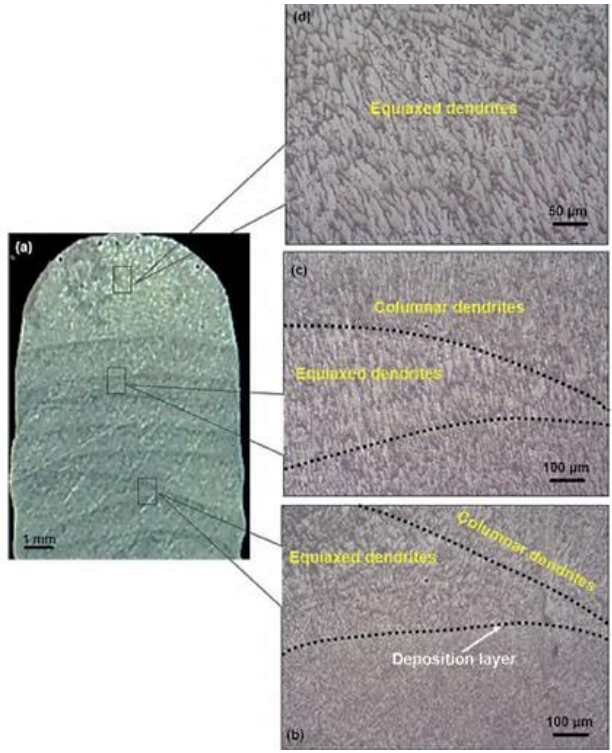

Figure 1: (a) Macrostructure and (b-d) microstructure of WAAM cylinder [45]

Porosity and crack were the majority of defects that altered the mechanical properties of aluminium alloys. First, Ortega et al. [18] noticed small, elongated defects and larger spherical pores on the deposited material. Small and elongated defects are generally caused by hot cracking; however, they were minimal and proved that ER4043 was not sensitive to hot-cracking phenomena. Next, Li et al. [54] agreed with the findings and claimed that WAAM alloy's tendency to form porosity increased with an increase in the Mg content of the filler wire. Besides, Huang et al. [55] emphasized that increasing the WFS weakens the crack rate while increasing the welding speed increases the crack rate. The same conclusion came with Huang et al. [56] as the authors realized that when the WFS exceeded 5.5 m/min, cracks were reduced as the size of the crystal microstructure increased. The mechanical state was stable, which suppressed the occurrence of cracks. However, the large pores were not ignored and needed to be improved by modifying the process. Next, there were normally two types of fracture observed during microstructure studies: quasi-cleavage fracture and the

presence of dimples and voids. The former exhibited a brittle fracture characteristic [16], and the latter indicated a typical ductile fracture [45].

Microhardness analysis

Grain size and element distribution were two parameters that influenced microhardness values. The disordered arrangement of atoms at grain boundaries impeded dislocation migration. The decreasing grain size enhanced the potential of a hindering impact, which was advantageous to plastic deformation resistance. As a result, the microhardness at the grain boundaries was greater than that in the grain body, a phenomenon known as fine-grain strengthening [57]. The finer α-Al dendrites investigated by Sinha et al. [41] had a higher toughness. Pramod et al. [45] made the same observation. The author speculated that it could be related to differences in heating across additional layers, coarse grains, and small pores in the inter-layers resulting in decreased microhardness. Furthermore, the cooling rate was faster in the inter-layer regions, generating equiaxed dendrites, and the fine-grain size encouraged increased microhardness in the middle and bottom zones [58]. Aside from that, no discernible variation in microhardness was noticed with stacking orientation or arc mode. For example, Nie et al. [16] claimed only a minor difference in vertical and parallel hardness in the stacking orientation. The microhardness value fluctuated slightly, showing steady microhardness distribution features in variable polarity gas tungsten arc welding (VP-GTAW) [59].

Tensile properties

The tensile property was essential to be studied as its ability to withstand loads without failure. However, few studies reported that WAAM using ER4043 exhibited superior mechanical over conventional machining. For example, Langelandsvik et al. [60] highlighted that a high cooling rate during solidification in the WAAM process recorded excellent mechanical properties over the casting process. Surprisingly, the authors also noticed relatively low porosity levels when using ER4043 in the WAAM process. The microstructure and porosity of aluminium alloys were the primary determinants of their tensile performance [61]. Porosity lowered mechanical characteristics because it allowed crack propagation [35], particularly in cluster pores, resulting in a smaller loading surface, reduced bearing capacity, and more brittleness [62]. As a result, finer grain and higher density helped improve the characteristics. Pramod et al. [45] also declared that their findings showed that the tensile strength of the WAAM sample was higher than that of the AA4043 generated by the casting process, which Farayibi et al. [63] did.

Furthermore, the improved strength could be related to the shape, size, and distribution of the eutectic composition's predominant silicon particles.

The additive layers' strength was increased because the Si particles were dispersed evenly [64]. Pramod et al. [45] also examined the mechanical qualities of GMAW [65] and GTAW [3] with CMT and discovered that CMT performed the best of all arc welding techniques. It could be related to heat input, as higher heat input would increase porosity.

The orientation or the direction to extract the tensile sample influenced the tensile property of the final product. Two researchers had contradictory opinions on the tensile property, claiming that horizontal extraction was better [16], [48], [54], [60] and vertical extraction was better [27]-[28]. Nie et al. [16] claimed that the inferior tensile property in the vertical direction was due to the thermal accumulation effect. According to Qing et al. [49], more grain boundaries on the horizontal face result in greater elongation. The presence of a grain boundary made it harder for the slip dislocation to penetrate the grain boundary directly, compromising the slip system's continuity and impeding dislocation migration [49]. Besides, Liu et al. [28] asserted that a considerable number of coarsened grains were present in the interface region of the transversely stretched weld beads in thick-walled sections. As mentioned earlier, a finer grain would result in a high microhardness and improve the tensile property. Therefore, the coarsened grain observed in the transverse direction led to poor tensile properties. However, the difference in tensile properties between horizontal and vertical directions was relatively small and might be neglected. For example, there was a difference of 5MPa in tensile strength and 1.5% elongation between horizontal and vertical directions, and Pramod et al. [45] concluded that they were isotropic behaviour. Same conclusion were made by Gu et al. [66] and Campatelli et al. [27].

Table 3 illustrates the different areas of analysis that researchers conducted when using ER4043 during the WAAM process. Based on Table 3, could give a true sight for the reviewers of the findings that had been discovered and a gap for the analysis which could be conducted in further studies.

Challenges and Future Outlook

WAAM has numerous advantages such as reduced material waste and load time, while aluminium alloys with great characteristics such as corrosion resistance, lightweight, and feasibility. As a result, researchers and manufacturers are very interested in the combination of aluminium alloys and WAAM. However, their essential weaknesses are the occurrences of porosity and cracking, which have reduced the mechanical qualities of the final product and limited their employment in industries.

Therefore, the modification of the WAAM process and process parameters are needed, such as an appropriate selection of the deposition

parameter, laser-arc hybrid additive manufacturing, hybrid of feeding wire, high pressure inters pass rolling, and thermal management technique. The WAAM deposited material has shown positive results within these techniques compared to conventional WAAM. However, there are limited studies on the topic. Besides, finite element simulation model build-up has been utilized to anticipate the experiment result and minimize the possibility of the defect occurring. With the aid of simulation, it can reduce the trials and costs during research works.

In short, researchers are advised to study the chemical and physical properties of the feeding wire and the WAAM process. It is also recommended to investigate the hydrogen content of the feeding wires used and monitor the arc stability of subsequent builds to figure out the impact of wire batch on porosity formation. Furthermore, simulation is needed to be considered in research work. It will help the researchers anticipate the progress of the process, heat coverage, and the occurrence of defects during the WAAM process.

Conclusion

Overall, this article reviews the process and heat resources for WAAM of aluminium alloy 4043, including the introduction of AM and WAAM, heat resource for WAAM (GTAW, GMAW, and CMT), property of aluminium alloy, and the performance evaluation of ER4043 aluminium alloys. The conclusion that can be drawn from this review is as follows.

The following conclusion can be drawn from the literature:

i. A greater dwell time during the WAAM indicates a greater cooling rate, resulting in a narrower and higher specimen with finer microstructure.
ii. Unidirectional deposition leads to forming defection that one side of the deposited specimen is higher than the other due to the collapse and hump.
iii. The specimen's microstructure becomes coarser when the layer builds up due to heat accumulation and low solidification rate.
iv. Most of the pores observed at the top layers are caused by undissolved hydrogen due to a discrepancy in solubility between the liquid and solid phases.
v. CMT with lower heat input results in a lower porosity and better mechanical qualities than GTAW and GMAW.
vi. Coarsened grains are presented in the interface region of the transversely stretched weld beads, leading to poor tensile properties.

Table 3: Application of ER4043 during the WAAM process

Filler wire	Substrate	Energy source	Parameter	Area of analysis	Findings	Ref.
ER4043	Al 6061	LAHAM	WFR: 1000 mm/min TS: 250 mm/min AC: 150 A	Microstructure and mechanical analysis after the addition of laser energy	The sample from Laser-arc hybrid additive manufacturing (LAHAM) had a finer microstructure and better mechanical properties as the higher cooling rate and crack deflection in the laser zone.	[3]
ER4043	Al 6061	GMAW	TS: 10 mm/s AC: 164 to 200 A AV: 22.6 to 27 V SGFR: 15 L/min	Size of droplet	A pulsed arc had a higher droplet transfer frequency than a non-pulsed arc, which boosted production efficiency.	[67]
ER4043	Al 7050	CMT	WFR: 5.7 m/min TS: 5.2 mm/s SGFR: 20 L/min DT: 120 s	Ratcheting behavior of specimen on tensile properties	Pre-ratcheted specimens had higher tensile and yield strengths than un-ratcheted specimens.	[68]
ER4043	Al 6082	CMT	WFS: 4 m/min TS: 0.6 m/min Lead angle to vertical: -10˚, 0˚, 10˚, 20˚, 30˚, 40˚	Melt pool behaviour at varied lead angles	The fluctuation of the WAAM globules was more pronounced with a larger lead angle (above 10°), as the wire is fed through the steeper angle over a longer period.	[69]
ER4043	Al 6082	CMT	WFS: 3 to 5 m/min TS: 0.35 m/min SGFR: 4 to 10 L/min	Oxidation effect on aluminium plate during WAAM	A duplex oxide layer formed on the specimen as the shielding gas flow rate was too low led to a threshold of oxygen contamination during the WAAM process.	[70]

ER4043	Al 4043	CMT	WFS: 4 m/min SGFR: 15 L/min	Interlayer temperature analysis	A stable geometric formation could be obtained by controlling the interlayer temperature on the substrate to be lower than 55 ˚C.	[71]
ER4043	Al	CMT	WFS: 1.2, 2 and 3 m/min AC: 16, 30 and 47 A AV: 10.0, 10.7 and 11.1 V	Effect of interpass temperature on deposition	High interpass temperature (200 °C) induced high peak thermal profiles that require more passes to reach a stable deposition.	[72]
ER4043	Al	CMT	WFS: 2.54 m/min TS: 5 mm/s SGFR: 15.34 L/min DT: 5 and 120 s	Microstructure and thermal analysis	Large amounts of Si segregation and increased secondary dendrite arm spacing were observed in a shorter dwell time.	[73]
ER4043	Al 5A06	CMT	WFS: 3.3 and 5.2 m/min TS: 0.353 and 0.867 m/min SGFR: 15 L/min	Process planning strategy analysis	Higher WFR contributed to finer surface quality, higher material utilization, and deposition rate but was restricted by building time or distortion of the component.	[74]

Contributions of Authors

The authors confirm the equal contribution in each part of this work. All authors reviewed and approved the final version of this work.

Funding

This work was supported by the "Large Volume Additive Manufacturing (LVAM) Consortium" [KHAS-KKP/2021/FKP/C00006].

Conflict of Interests

All authors declare that they have no conflicts of interest.

Acknowledgement

The author would like to thank the Centre of Smart System and Innovative Design (CoSSID), Faculty of Manufacturing Engineering, Universiti Teknikal Malaysia Melaka, Malaysia, for the facilities support and the Ministry of Higher Education for the financial support. This research is funded through a grant numbered KHAS-KKP/2021/FKP/C00006.

References

[1] A. Sirisha Bhadrakali, K. L. Narayana, T. Ram Prabhu, and Y. Pratapa Reddy, "Optimization of mechanical properties of ER-4043 specimens fabricated by WAAM process through Grey Relational Analysis," *IOP Conference Series Material Science Engineering*, vol. 1055, no. 1, pp. 012047, 2021.

[2] T. Pereira, J. V. Kennedy, and J. Potgieter, "A comparison of traditional manufacturing vs additive manufacturing, the best method for the job," *Procedia Manufacturing*, vol. 30, pp. 11–18, 2019.

[3] Q. Miao *et al.*, "Comparative study of microstructure evaluation and mechanical properties of 4043 aluminum alloy fabricated by wire-based additive manufacturing," *Materials and Design.*, vol. 186, pp. 108205, 2020.

[4] N. Soro, H. Attar, E. Brodie, M. Veidt, A. Molotnikov, and M. S. Dargusch, "Evaluation of the mechanical compatibility of additively manufactured porous Ti–25Ta alloy for load-bearing implant

applications," *Journal of Mechancical Behavior of Biomedical Materials*, vol. 97, pp. 149–158, 2019.
[5] M. Froend, V. Ventzke, S. Riekehr, N. Kashaev, B. Klusemann, and J. Enz, "Microstructure and microhardness of wire-based laser metal deposited AA5087 using an Ytterbium fibre laser," *Materials Characterization*, vol. 143, pp. 59–67, 2018.
[6] W. Ou, T. Mukherjee, G. L. Knapp, Y. Wei, and T. DebRoy, "Fusion zone geometries, cooling rates and solidification parameters during wire arc additive manufacturing," *International Journal of Heat Mass Transfer*, vol. 127, part. c, pp. 1084–1094, 2018.
[7] C. Su, X. Chen, S. Konovalov, R. Arvind Singh, S. Jayalakshmi, and L. Huang, "Effect of Deposition Strategies on the Microstructure and Tensile Properties of Wire Arc Additive Manufactured Al-5Si Alloys," *Journal of Materials Engineering and Performance*, vol. 30, no. 3, pp. 2136–2146, 2021.
[8] Bolun Dong, Xiaoyu Cai, Sanbao Lin, Xiaolong Li, Chenglei Fan, Chunli Yang, Haoran Sun, "Wire arc additive manufacturing of Al-Zn-Mg-Cu alloy: Microstructures and mechanical properties," *Additive Manufacturing*, vol. 36, pp. 101447, 2020.
[9] Z. Wang and Y. Zhang, "A review of aluminum alloy fabricated by different processes of wire arc additive manufacturing," *Materials Science*, vol. 27, no. 1, pp. 18–26, 2021.
[10] K. S. Derekar, "A review of wire arc additive manufacturing and advances in wire arc additive manufacturing of aluminium," *Materials Science and Technology (United Kingdom)*, vol. 34, no. 8, pp. 895–916, 2018.
[11] M. M. Tawfik, M. M. Nemat-Alla, and M. M. Dewidar, "Enhancing the properties of aluminum alloys fabricated using wire + arc additive manufacturing technique - A review," *Journal of Materials Research and Technology*, vol. 13, pp. 754–768, 2021.
[12] G. Langelandsvik, O. M. Akselsen, T. Furu, and H. J. Roven, "Review of aluminum alloy development for wire arc additive manufacturing," *Materials*, vol. 14, no. 18, pp. 1–26, 2021.
[13] S. Thapliyal, "Challenges associated with the wire arc additive manufacturing (WAAM) of Aluminum alloys," *Materials Research Express*, vol. 6, no. 11, pp. 0–31, 2019.
[14] M. Chaturvedi, E. Scutelnicu, C. C. Rusu, L. R. Mistodie, D. Mihailescu, and S. Arungalai Vendan, "Wire arc additive manufacturing: Review on recent findings and challenges in industrial applications and materials characterization," *Metals*, vol. 11, no. 6, pp. 1-39, 2021.
[15] Z. Qi, B. Cong, B. Qi, H. Sun, G. Zhao, and J. Ding, "Microstructure and mechanical properties of double-wire + arc additively manufactured Al-Cu-Mg alloys," *Journal of Materials Processing Technology*, vol. 255,

pp. 347–353, 2018.
[16] Y. Nie, P. Zhang, X. Wu, G. Li, H. Yan, and Z. Yu, "Rapid prototyping of 4043 Al-alloy parts by cold metal transfer," *Science and Technology of Welding and Joining*, vol. 23, no. 6, pp. 527–535, 2018.
[17] M. Vishnukumar, V. Muthupandi, and S. Jerome, "Effect of post-heat treatment on the mechanical and corrosion behaviour of SS316L fabricated by wire arc additive manufacturing," *Materials Letters*, vol. 307, pp. 131015.
[18] A. G. Ortega *et al.*, "Characterisation of 4043 aluminium alloy deposits obtained by wire and arc additive manufacturing using a Cold Metal Transfer process," *Science and Technology of Welding and Joining*, vol. 24, no. 6, pp. 538–547, 2019.
[19] J. Y. Bai, C. L. Fan, S. Lin, C. L. Yang, and B. L. Dong, "Effects of thermal cycles on microstructure evolution of 2219-Al during GTA-additive manufacturing," *The International Journal Advanced Manufacturing Technology*, vol. 87, no. 9–12, pp. 2615–2623, 2016.
[20] Z. jue Tang *et al.*, "A review on in situ monitoring technology for directed energy deposition of metals," *The International Journal of Advanced Manufacturing Technology*, vol. 108, no. 11–12, pp. 3437–3463, 2020.
[21] A. Majeed, A. Ahmed, J. Lv, T. Peng, and M. Muzamil, "A state-of-the-art review on energy consumption and quality characteristics in metal additive manufacturing processes," *Journal of Brazilian Society of Mechanical Sciences and Engineering*, vol. 42, no. 5, pp. 1-25, 2020.
[22] S. Pattanayak and S. K. Sahoo, "Gas metal arc welding based additive manufacturing—a review," *CIRP Journal of Manufacturing Science and Technology*, vol. 33, pp. 398–442, 2021.
[23] Y. Wang, X. Chen, and S. V. Konovalov, "Additive Manufacturing Based on Welding Arc: A low-Cost Method," *Journal of Surface Investigation: X-ray, Synchrotron and Neutron Techniques*, vol. 11, no. 6, pp. 1317–1328, 2017.
[24] D. Ding, Z. Pan, D. Cuiuri, and H. Li, "Wire-feed additive manufacturing of metal components: technologies, developments and future interests," *The International Journal of Advanced Manufacturing Technology*, vol. 81, no. 1–4, pp. 465–481, 2015.
[25] C. R. Cunningham, J. M. Flynn, A. Shokrani, V. Dhokia, and S. T. Newman, "Invited review article: Strategies and processes for high quality wire arc additive manufacturing," *Additive Manufacturing*, vol. 22, no. June, pp. 672–686, 2018.
[26] B. Zhang, L. Zhang, C. Wang, Z. Wang, and Q. Gao, "Microstructure and properties of Al alloy ER5183 deposited by variable polarity cold metal transfer," *Journal of Materials Processing Technology*, vol. 267, pp. 167–176, 2019.
[27] G. Campatelli, D. Campanella, A. Barcellona, L. Fratini, N. Grossi, and

G. Ingarao, "Microstructural, mechanical and energy demand characterization of alternative WAAM techniques for Al-alloy parts production," *CIRP Journal of Manufacturing Science and Technology*, vol. 31, pp. 492–499, 2020.

[28] Z. qiang Liu, P. lei Zhang, S. wei Li, D. Wu, and Z. shui Yu, "Wire and arc additive manufacturing of 4043 Al alloy using a cold metal transfer method," *International Journal of Minerals, Metallurgy, and Materials*, vol. 27, no. 6, pp. 783–791, 2020.

[29] M. Vishnukumar, R. Pramod, and A. Rajesh Kannan, "Wire arc additive manufacturing for repairing aluminium structures in marine applications," *Materials Letters*, vol. 299, pp. 130112, 2021.

[30] X. S. W. and H. Q. J Bai, H L Ding, J L Gu, "Porosity evolution in additively manufactured aluminium alloy during high temperature exposure," *Journal of Physics: Conference Series*, vol. 755, no. 1, pp. 1-5, 2016.

[31] E. M. Ryan, T. J. Sabin, J. F. Watts, and M. J. Whiting, "The influence of build parameters and wire batch on porosity of wire and arc additive manufactured aluminium alloy 2319," *Journal of Materials Processing Technology*, vol. 262, pp. 577–584, 2018.

[32] R. Fu *et al.*, "Hot-wire arc additive manufacturing of aluminum alloy with reduced porosity and high deposition rate," *Materials and Design*, vol. 199, pp. 109370, 2021.

[33] K. Uehara, K. Katayama, H. Date, and S. Fukada, "Hydrogen gas driven permeation through tungsten deposition layer formed by hydrogen plasma sputtering," *Fusion Eng. Des.*, vol. 98–99, pp. 1341–1344, 2015.

[34] J. Gu, J. Ding, S. W. Williams, H. Gu, P. Ma, and Y. Zhai, "The effect of inter-layer cold working and post-deposition heat treatment on porosity in additively manufactured aluminum alloys," *Journal of Materials Processing Technology*, vol. 230, pp. 26–34, 2015.

[35] T. Ma, J. Ge, Y. Chen, T. Jin, and Y. Lei, "Observation of in-situ tensile wire-arc additively manufactured 205A aluminum part: 3D pore characteristics and microstructural evolution," *Materials Letters*, vol. 237, no. 100, pp. 266–269, 2019.

[36] S. W. Williams, F. Martina, A. C. Addison, J. Ding, G. Pardal, and P. Colegrove, "Wire + Arc additive manufacturing," *Materials Science and Technology*, vol. 32, no. 7, pp. 641–647, 2016.

[37] Z. Gao, "A Micro-milling Study of Al-4043 Workpieces Built Using Wire Arc Additive Manufacturing (WAAM)," Rensselaer Polythenic Institute, 2020.

[38] K. E. K. Vimal, M. N. Srinivas, and S. Rajak, "Wire arc additive manufacturing of aluminium alloys: A review," *Materials Today Proceedings*, no. 41, pp. 1139-1145, 2020.

[39] Y. Zhao, Y. Jia, S. Chen, J. Shi, and F. Li, "Process planning strategy for

wire-arc additive manufacturing: Thermal behavior considerations," *Additive Manufacturing*, vol. 32, pp. 100935, 2020.

[40] R. P. Singh, R. C. Gupta, and S. C. Sarkar, "Analysis of Bead Width and Reinforcement Height During Shielded Metal Arc Welding Under Magnetic Field," *International Journal of Mechanical and Engineering Robotics Research*, vol. 2, no. December, pp. 1-11, 2016.

[41] A. K. Sinha, S. Ranjan, and K. P. Yagati, "Effect on Microstructure and Mechanical Property of 4043 Wire Arc Additively Manufactured Aluminum Alloy with Different Process Parameters," *Next Generation Materials and Processing Technologies. Springer Proceedings in Materials*, vol. 9, no. , pp. 171-184, 2021.

[42] H. Wang, W. Jiang, J. Ouyang, and R. Kovacevic, "Rapid prototyping of 4043 Al-alloy parts by VP-GTAW," *Journal of Materials Processing Technology*, vol. 148, no. 1, pp. 93–102, 2004.

[43] O. Panchenko, D. Kurushkin, I. Mushnikov, A. Khismatullin, and A. Popovich, "A high-performance WAAM process for Al–Mg–Mn using controlled short-circuiting metal transfer at increased wire feed rate and increased travel speed," *Materials and Design*, vol. 195, pp. 109040, 2020.

[44] Z. Hao, S. Ao, Y. Cai, W. Zhang, and Z. Luo, "Formation of SUS304/aluminum alloys using wire and arc additive manufacturing," *Metals.*, vol. 8, no. 8, pp. 1–12, 2018.

[45] R. Pramod, S. M. Kumar, B. Girinath, A. R. Kannan, N. P. Kumar, and N. S. Shanmugam, "Fabrication, characterisation, and finite element analysis of cold metal transfer–based wire and arc additive–manufactured aluminium alloy 4043 cylinder," *Welding in the World*, vol. 64, no. 11, pp. 1905–1919, 2020.

[46] R. A. Kannan, N. S. Shanmugam, and S. Naveenkumar, "Effect of arc length correction on weld bead geometry and mechanical properties of AISI 316L weldments by cold metal transfer (CMT) process," *Materials Today Proceeding*, vol. 18, pp. 3916–3921, 2019.

[47] S. Madhavan, M. Kamaraj, and L. Vijayaraghavan, "Microstructure and mechanical properties of cold metal transfer welded aluminium/dual phase steel," *Science and Technology of Welding and Joining*, vol. 21, no. 3, pp. 194–200, 2016.

[48] C. Zhang, C. Shen, X. Hua, F. Li, Y. Zhang, and Y. Zhu, "Influence of wire-arc additive manufacturing path planning strategy on the residual stress status in one single buildup layer," *The International Journal of Advanced Manufacturing Technology*, vol. 111, no. 3–4, pp. 797–806, 2020.

[49] X. L. and H. W. Qingfeng Yang, Cunjuan Xia, Yaqi Deng, "Microstructure and Mechanical Properties of AlSi7Mg0.6 Aluminum Alloy Fabricated by Wire and Arc Additive Manufacturing Based on Cold Metal Transfer (WAAM-CMT)," *Materials*, vol. 12, no. 16, pp.

564–572, 2019.
[50] R. M. Kindermann, M. J. Roy, J. A. Francis, and P. Prangnell, "Oil & Gas Wire + Arc Additive Manufacturing Technique Development," *2nd Conference Expo - NACE International*, 2018.
[51] H. L. Wei, J. W. Elmer, and T. DebRoy, "Three-dimensional modeling of grain structure evolution during welding of an aluminum alloy," *Acta Materialia*, vol. 126, pp. 413–425, 2017.
[52] S. Mereddy, M. J. Bermingham, D. H. StJohn, and M. S. Dargusch, "Grain refinement of wire arc additively manufactured titanium by the addition of silicon," *Journal of Alloys and Compounds*, vol. 695, pp. 2097–2103, 2017.
[53] H. L. Wei, J. W. Elmer, and T. Debroy, "Origin of grain orientation during solidification of an aluminum alloy," *Acta Materialia*, vol. 115, pp. 123–131, 2016.
[54] C. Li *et al.*, "Effects of magnesium on the microstructure and properties of Al–Si alloy deposited by wire and arc-based additive manufacturing," *Materials Technology*, vol. 36, no. 13, pp. 793–798, 2021.
[55] L. Huang *et al.*, "Modeling and Optimization of Solidification Cracking of 4043 Aluminum Alloys Produced by Cold Metal Transfer Welding," *Journal of Materials Engineering and Performance*, vol. 31, no. 6, pp. 4746–4760, 2022.
[56] L. Huang, X. Chen, S. Konovalov, A. N. Siddiquee, G. Lu, and X. Pan, "The effect of wire feeding speed on solidification cracking of cmt welding for al-si alloys," *Metals*, vol. 11, no. 2, pp. 1–13, 2021.
[57] T. Inoue, Z. Horita, H. Somekawa, and K. Ogawa, "Effect of initial grain sizes on hardness variation and strain distribution of pure aluminum severely deformed by compression tests," *Acta Materialia*, vol. 56, no. 20, pp. 6291–6303, 2008..
[58] C. Su, X. Chen, C. Gao, and Y. Wang, "Effect of heat input on microstructure and mechanical properties of Al-Mg alloys fabricated by WAAM," *Applied Surface Science*, vol. 486, pp. 431–440, 2019.
[59] Z. Qi, B. Qi, B. Cong, and R. Zhang, "Microstructure and mechanical properties of wire + arc additively manufactured Al-Mg-Si aluminum alloy," *Materials Letters*, vol. 233, pp. 348–350, 2018.
[60] G. Langelandsvik, A. Horgar, T. Furu, H. J. Roven, and O. M. Akselsen, "Comparative study of eutectic Al-Si alloys manufactured by WAAM and casting," *The International Journal of Advanced Manufacturing Technology*, vol. 110, no. 3–4, pp. 935–947, 2020.
[61] C. Zhang, M. Gao, and X. Zeng, "Workpiece vibration augmented wire arc additive manufacturing of high strength aluminum alloy," *Journal of Materials Processing Technology*, vol. 271, pp. 85–92, 2019.
[62] J. Y. Bai, C. L. Yang, S. B. Lin, B. L. Dong, and C. L. Fan, "Mechanical properties of 2219-Al components produced by additive manufacturing

with TIG," *The International Journal of Advanced Manufacturing Technology*, vol. 86, no. 1–4, pp. 479–485, 2016.
[63] P. K. Farayibi, B. O. Akinnuli, and S. Ogu, "Mechanical Properties of Aluminum – 4043 / Nickel- coated Silicon Carbide Composites Produced via Stir Casting," *International Journal of Engineering Technologies*, vol. 4, no. 1, 2018.
[64] S. A. Jawade, R. S. Joshi, and S. B. Desai, "Comparative study of mechanical properties of additively manufactured aluminum alloy," *Materials Today Proceedings*, vol. 46, no. 19, pp. 9270–9274, 2019.
[65] A. S. Haselhuhn, M. W. Buhr, B. Wijnen, P. G. Sanders, and J. M. Pearce, "Structure-property relationships of common aluminum weld alloys utilized as feedstock for GMAW-based 3-D metal printing," *Materials Science and Engineering: A*, vol. 673, pp. 511–523, 2016.
[66] J. Gu *et al.*, "The strengthening effect of inter-layer cold working and post-deposition heat treatment on the additively manufactured Al-6.3Cu alloy," *Materials Science and Engineering: A*, vol. 651, pp. 18–26, 2016.
[67] Y. Luo, J. Li, J. Xu, L. Zhu, J. Han, and C. Zhang, "Influence of pulsed arc on the metal droplet deposited by projected transfer mode in wire-arc additive manufacturing," *Journal of Materials Processing Technology*, vol. 259, pp. 353–360, 2018.
[68] Y. Wang, S. Yang, C. Xie, H. Liu, and Q. Zhang, "Microstructure and Ratcheting Behavior of Additive Manufactured 4043 Aluminum Alloy," *Journal of Materials Engineering and Performance*, vol. 27, no. 9, pp. 4582–4592, 2018.
[69] T. Hauser, A. Da Silva, R. T. Reisch, J. Volpp, T. Kamps, and A. F. H. Kaplan, "Fluctuation effects in Wire Arc Additive Manufacturing of aluminium analysed by high-speed imaging," *Journal of Manufacturing Processes*, vol. 56, no. A, pp. 1088–1098, 2020.
[70] Tobias Hauser, Raven T. Reisch, Philipp P. Breese, Yogesh Nalam, Kaivalya S. Joshi, Katharina Bela, Tobias Kamps, Joerg Volpp, Alexander F.H. Kaplan, "Oxidation in wire arc additive manufacturing of aluminium alloys", *Additive Manufacturing*, vol. 41, pp.1-11, 2021.
[71] Z. Yu, Z. Pan, D. Ding, Z. Rong, H. Li, and B. Wu, "Strut formation control and processing time optimization for wire arc additive manufacturing of lattice structures," *Journal of Manufacturing Processes*, vol. 79, pp. 962–974, 2022.
[72] B. Wu, Z. Pan, Y. Ziping, S. van Duin, H. Li, and E. Pierson, "Robotic skeleton arc additive manufacturing of aluminium alloy," *The International Journal of Advanced Manufacturing Technology*, vol. 114, no. 9–10, pp. 2945–2959, 2021.
[73] Z. Gao, J. F. Nowak, J. Corbin, L. Delgado, and J. Samuel, "Sensitivity of Micromilling Responses to Grain Variations in Wire Arc Additively Manufactured Aluminum Alloy 4043," *Journal of Micro and Nano-Manufacturing*, vol. 8, no. 4, pp. 1–9, 2020.

[74] Y. Zhao, F. Li, S. Chen, and Z. Lu, “Unit block–based process planning strategy of WAAM for complex shell–shaped component,” *The International Journal of Advanced Manufacturing Technology*, vol. 104, no. 9–12, pp. 3915–3927, 2019.

Design and Dynamic Stiffness Evaluation of Magnetorheological Elastomer Bushing using FEMM and Dynamic Testing Machine

Mohamad Ihsan Abdul Hamid, Saiful Amri Mazlan, Nur Azmah Nordin
Engineering Materials & Structures (eMast) Ikhoza,
Malaysia-Japan International Institute of Technology (MJIIT),
Universiti Teknologi Malaysia, 54100 Kuala Lumpur, MALAYSIA

Abdul Yasser Abd Fatah[*]
Department of Engineering and Technology,
Razak Faculty of Technology and Informatics,
Universiti Teknologi Malaysia,
Jalan Sultan Yahya Petra, 54100 Kuala Lumpur, MALAYSIA
[*]*yasser.kl@utm.my*

Ubaidillah, Fitrian Imaduddin
Mechanical Engineering Department, Faculty of Engineering,
Universitas Sebelas Maret,
Jl. Ir. Sutami 36A, Kentingan, Surakarta 57126, Central Java, INDONESIA

Fitrian Imaduddin
Department of Mechanical Engineering, Islamic University of Madinah,
Medina 42351, SAUDI ARABIA

Izwan Ismail
Faculty of Manufacturing and Mechatronics Engineering Technology,
Universiti Malaysia Pahang, 26600 Pekan, Pahang, MALAYSIA

ABSTRACT

This research presents a simulation study on electromagnetic behaviour of magnetic flux density distribution in a magnetorheological elastomer (MRE) bushing. The design concept of MRE bushing is based on the design of the bushing used in the conventional car, only the natural rubber is being replaced by the MRE compound. Furthermore, the electromagnetic simulations were

ISSN 1823-5514, eISSN 2550-164X
Received for review: 2022-03-02
Accepted for publication: 2022-08-19
Published: 2023-01-15

https://doi.org/10.24191/jmeche.v20i1.21077

conducted by using Finite Element Method Magnetics (FEMM) software where the main aim is for more magnetic flux density in the MRE, which indicates better performances for MRE bushing in this study. The best configuration of the MRE bushing for this study is using single coil, magnetic material for all parts except for coil bobbin, and the thickness of ring plate of 4 mm, which yield the highest magnetic flux density of 0.205 T. By using this configuration, the dynamic stiffness of this MRE bushing is ranging from 2259.13 N/mm to 2671.06 N/mm with the applied currents of 0.5 A to 2.5 A and frequencies from 1 Hz to 15 Hz. All in all, the optimized configurations improve the performance of MRE bushing remarkably.

Keywords: *Magnetorheological Elastomer (MRE); MRE Bushing; Electromagnetic; FEMM; Dynamic Stiffness*

Introduction

Magnetorheological elastomer (MRE) is a branch of smart materials that is rapidly evolving and actively studied by other researchers [1]-[4]. In particular, MRE provides an active response by the presence of magnetic field to change the rheological properties of the MRE continuously, rapidly, and reversibly. MRE is made up of matrix, magnetic particles and also additives [5]-[10]. Due to the ability of the MRE that can be changed rheologically, the stiffness and damping of MRE can be controlled by the magnetic field using an electromagnetic circuit [11].

Many researchers have incorporated MRE into diverse applications, such as isolator, engine mount, and prosthetics device [12]-[16]. Since then, these devices managed to achieve controllable stiffness and thus, acted as a vibration absorber based on their applications. Apart from that, MRE compound also being used in the development of the MRE bushing, where there are a few studies regarding that matter [17]-[20]. With the help of MRE, the MRE bushing managed to control and reduce the vibration, thus, decreasing the external loadings and transmitting the vibrations between parts.

Conventional rubber bushing had a passive behaviour that mainly used natural rubber (NR) as its compound. Consequently, conventional bushing had fixed stiffness characteristics, which can only cater to a certain rigid range of stiffness [21]. Therefore, Kumbhar et al. [17] had developed an MRE bushing and compared it with the conventional bushing for transmissibility in terms of isolation between that two devices. Furthermore, Elie et al. [19] and Ginder et al. [20] had designed another type of MRE bushing and measured the stiffness while varying the applied current. These studies showed the reaction of MRE bushing to the applied current where the higher the applied current, the higher force and stiffness obtained. Meanwhile, Blom et al. [22] conducted an engineering stiffness formula that predicts the frequency and amplitude

dependent stiffness of MRE bushing. From these calculations, it predicted and clearly displayed the possibility of controlling the stiffness of MRE bushing over a large frequency range. In addition, Kim et al. [23] did a simulation for MRE bushing based on their design for magnetic field analysis.

However, further studies are vital for the design of MRE bushing. In fact, other elements for the development of MRE bushings such as the design and simulation configurations, are not adequately investigated. Thus, in this study, an asymmetrical model of an MRE bushing was designed and simulated using Finite Element Method Magnetics (FEMM) software. From the FEMM simulation, the magnetic flux was flown through the MRE, hence, the magnetic flux density within the MRE can be determined. The performance of MRE bushing is depending on the amount of magnetic flux density flown into the MRE bushing, which translated into adjustable dynamic stiffness. Therefore, the configuration of the coil, the material selections, and geometrical dimensions in designing the MRE bushing was determined and considered to enhance the performance of the MRE bushing respectively. The best configuration based on simulation analysis is achieved and that design proceeds for the experimental testing of dynamic stiffness.

Design of MRE Bushing using FEMM

The design of MRE bushing in this study is based on the design of the bushing used in the conventional car. The main difference between the conventional bushing and the MRE bushing is the compound used, where the NR is used for conventional bushing, while the MRE bushing will be using natural rubber-based MRE (NR-MRE). The structural design of this MRE bushing is influenced by prior works which suitable for industrial and research scales [17], [19]-[20], [24]-[25]. Mainly, the structural design of the MRE bushing has been enhanced so that the ultimate aims have been achieved. In addition, an electromagnetic circuit is also added into the device for generating the magnetic field by manipulating the input current.

The next steps for designing the MRE bushing are the material selection and geometrical dimension of parts. For this design the important criteria are the overall size of the MRE bushing, the thickness of parts, the selection of the materials, and the design of coil. Notwithstanding, these design criteria can affect the outcome performance of MRE bushing. Therefore, this MRE bushing has been designed to utilize the controllable stiffness ability of MRE.

In this design, the MRE bushing is comprised of five main parts. The first part corresponds to the top and bottom ring plates. Next is the MRE, where the stiffness of the bushing can be adjusted, and vibration absorption happened. Then, the inner and outer pipes, where they sandwiched the MRE compound in the device. The fourth part is referred to as the electromagnetic coil that wound around the coil bobbin, which is made of aluminium, a non-magnetic

material. Lastly is the housing, where it covers all the aforementioned parts. Figure 1 shows the axisymmetric conceptual design of the MRE bushing used for this study. Meanwhile, Table 1 shows the structure parameter of the MRE bushing.

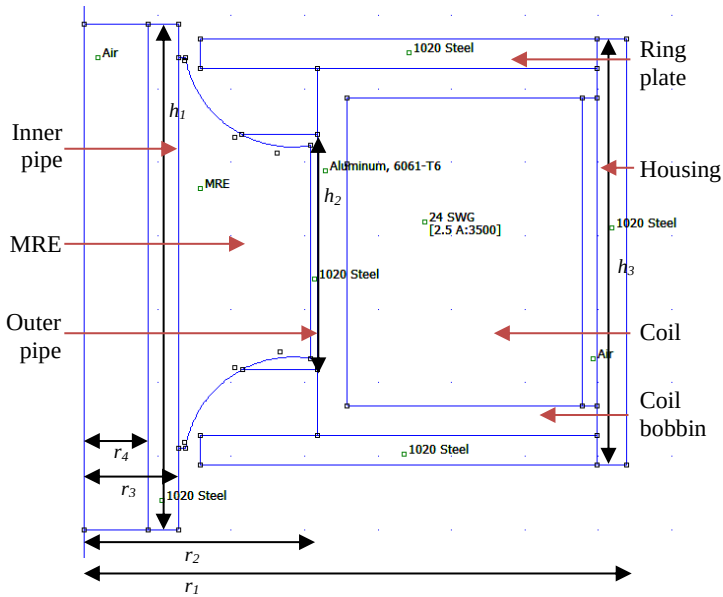

Figure 1: Axisymmetric conceptual design of the MRE bushing

Table 1: Structure parameter of the MRE bushing

Item	Parameter	Value (mm)
r_1	Radius of the structure	50
r_2	Radius of the bushing	25
r_3	Inner radius of the MRE	7.5
r_4	Inner radius of the inner pipe	5
h_1	Height of the inner pipe	69
h_2	Height of the outer pipe	32
h_3	Height of the cylindrical housing	50

For the coil, the wire is calculated to be 3500 turns based on the size allocated for the coil and the wire type of SWG 24. From the work of Fatah et al. [26], number of turns of coil configuration are based on the diameter of the wire and the dimension of the coil bobbin. The electromagnetic coil is wound around a cylindrical coil bobbin and placed internally within the housing in order to generate magnetic field inside the MRE bushing. By placing it

internally, the magnetic field strength can be distributed directly into the MRE effective area of the bushing. The effective area is referring to the MRE compound as it produces the stiffness of the device since it has the viscoelastic behaviour. The investigation on the effective area can be seen in other prior works of MRE devices as well [13], [16], [27]-[28].

Besides the coil, each part is also important to guide the magnetic flux density across the MRE bushing. The arrangement of parts in the design also plays an important role as well. By placing the combination of metal as a magnetic material and aluminium as a non-magnetic material, the flux can be guided to allow or avoid areas in the MRE bushing. Other than that, the material selection is also important in doing the same task of guiding the magnetic flux. Besides the use of metal and aluminium, the NR-MRE is another material used in the MRE bushing. It is used for adjusting the dynamic stiffness of the device based on the presence of magnetic flux density. Thus, the attributes of NR-MRE are being input into FEMM based on B-H curve data obtained from the vibrating sample magnetometer (VSM) test [13]. The list of all the parts used is shown in Table 2.

Table 2: List of parts and material for MRE bushing

Part Name	Type of Material	Material	Type
Ring plate	Magnetic	Low carbon steel	AISI 1020
Elastomer	Magnetic	MRE	NR-MRE
Inner pipe	Magnetic	Low carbon steel	AISI 1020
Outer pipe	Magnetic	Low carbon steel	AISI 1020
Coil bobbin	Non-magnetic	Aluminum	6061-T6
Electromagnetic Coil	Non-magnetic	Copper wire	SWG 24
Housing	Magnetic	Low carbon steel	AISI 1020

For MRE bushing, one of the most significant factors to consider is electromagnetic performance. It is referring to the investigation on the electromagnetic circuit design. In this research, simulation of the electromagnetic circuit design was done using FEMM. It is used to simulate and analyze the electromagnetic circuit design for the MRE bushing. In addition, FEMM is practical for analysing magnetic behaviour and magnetic field strength inside the effective region of the MRE bushing. Thus, an axisymmetric two-dimensional (2D) cross-section of the MRE bushing is drawn in the FEMM. After that, the type of materials is being assigned for each part of MRE bushing.

Moreover, the coefficients in a boundary condition for an asymptotic boundary condition can be represented by Equation (1) as follows:

$$\frac{1}{\mu_r \mu_o} \frac{\partial A}{\partial n} + c_o A + c_1 = 0 \tag{1}$$

where A is the magnetic vector potential, μ_r is the relative magnetic permeability of the region adjacent to the boundary, μ_o is the permeability of free space, and n represents the direction normal to the boundary. Coefficients of c_0 and c_1 can be represented by Equation (2) and Equation (3) as follows:

$$c_o = \frac{1}{\mu_r \mu_o R} \tag{2}$$

$$c_1 = 0 \tag{3}$$

where R is the outer radius of a sphere problem domain.

After the designing stage, applying the boundary conditions, and inputting all of the material properties, the 2D MRE bushing model is then being analysed in the FEMM. 2.5 A current is being applied to generate the magnetic field across the effective area of MRE bushing. 2.5 A is the maximum applied current in this study for simulation and experimental. The data from this simulation is then collected and analysed to investigate the performances of the bushing during the presence of magnetic field, therefore the distribution of the magnetic flux in the MRE bushing can be observed. The distribution of magnetic flux of the MRE bushing in the FEMM is shown in Figure 2. FEMM helps to adjust different configurations applied to the MRE bushing such as the electromagnetic coil configuration, the materials configuration of parts, and the geometrical configuration of parts.

For the coil configuration, there are three configurations considered for the design of coil in the electromagnetic circuit: single, double and triple coils. As mentioned by Fatah et al. [26], the configuration of coil can be divided into two, which are single and multiple coils. The differences between single and multiple coils used in MRE bushing are significant, as it involves different ways to arrange the magnetic flux path in the bushing. Besides, for the materials selections, they are selected from the use of either magnetic (AISI 1020), or non-magnetic materials (Al 6061-T6), or a combination of both. Lastly, the geometrical configuration is based on the effects of the thickness of ring plates with configuration from 1 mm to 4 mm with the increment of 1 mm. All in all, this configuration analysis of MRE bushing lead to the optimized performance remarkably.

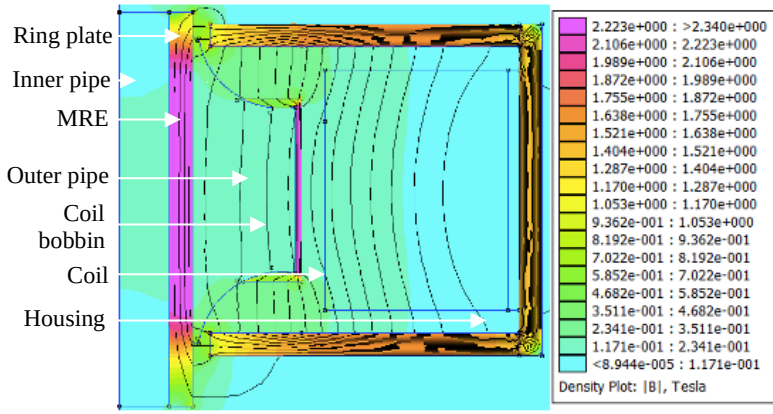

Figure 2: Simulated of magnetic flux density in MRE bushing

Experimental Setup

The dynamic compression test was performed to observe the dynamic stiffness from various frequencies by using a servopulser test machine (Shimadzu) equipped with a 20-kN load cell. The test machine for this experimental setup is shown in Figures 3. By using this machine, the MRE bushing can experimentally tested using frequency sweep method to observe the stiffness characteristic of MRE bushing, from increasing frequencies under different applied current. In addition, this experiment is a non-destructive test conducted to determine the MRE bushing behavior towards the dynamic performance in terms of stiffness characteristic on varied applied frequencies.

The test is performed under the compression behavior with the presence of magnetic field by supplying input currents from 0.5 to 2.5 A with an interval of 0.5 A, and the amplitude was fixed at 1.0 mm. When the current is applied, the frequency sweep begins from 1 Hz (low frequency) to 15 Hz (high frequency). Then, the same procedure was applied to the same sample but with different current input.

Before the experiment is done, a jig is mounted to an exciter and a load cell accordingly to hold the MRE bushing. This jig is made of aluminum so that it will not be affected by the magnetic field to prevent the magnetic field distortion. A shaft is inserted into the inner pipe of MRE bushing to join the bottom brackets that are mounted to the testing machine. The 20-kN load cell is installed on top of the jig to measure the load applied to the MRE bushing. The wire coil from MRE bushing is connected to the voltage regulator to provide the input current. The voltage regulator was supplied with 5760 watt (240 V x 24 A) to generate magnetic field to the MRE bushing throughout the

experiment. Table 3 shows a summary of the variable arrangement of the experimental test.

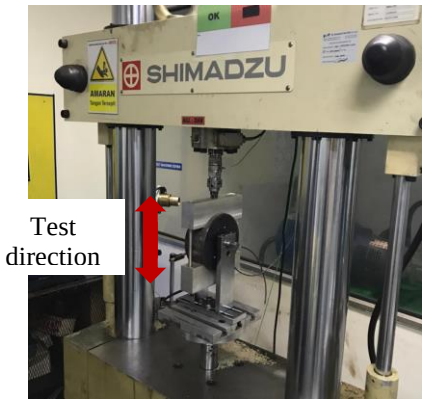

Figure 3: Experimental setup that show the testing machine for assessing the stiffness of the MRE bushing

Table 3: Summary of the variable arrangement of experimental test

Frequency sweep (Hz)	Excitation Amplitude (mm)	Input Current (A)
1 - 15	± 1.0	0.5 – 2.5

Results and Discussions

The results and discussion shown are from the FEMM simulation and experiment done to get the optimum performance of the bushing from the parameters tested. These include coil configurations, materials configuration of parts, geometrical configuration, and the dynamic stiffness from the experimental testing. For the simulation, the results are based on the average value of magnetic flux density at the effective area in the MRE bushing (Figure 4). For the current input, it is set at a constant of 2.5 A for simulation, however it is set ranging from 0.5 A to 2.5 A for experimental testing.

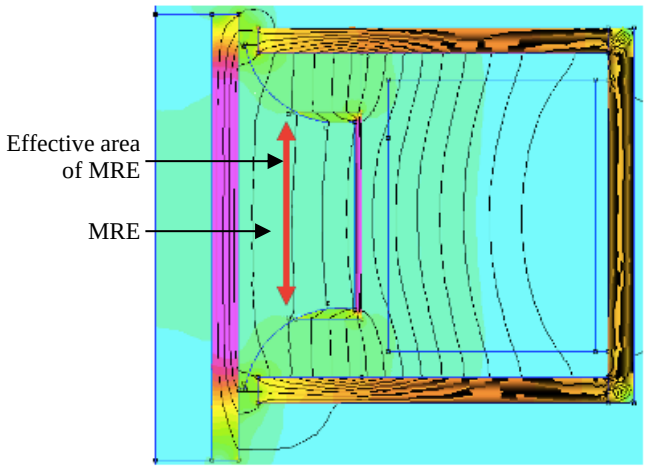

Figure 4: The effective area of MRE bushing

MRE bushing performance based on coil configurations

The coil configurations can lead to the maximum magnetic flux density in the MRE bushing. As previously mentioned, there are three configurations considered for the design of coil in the electromagnetic circuit: single, double and triple coils (Figure 5). The average values of magnetic flux density were taken at the same position in the bushing, which is the effective area in the MRE.

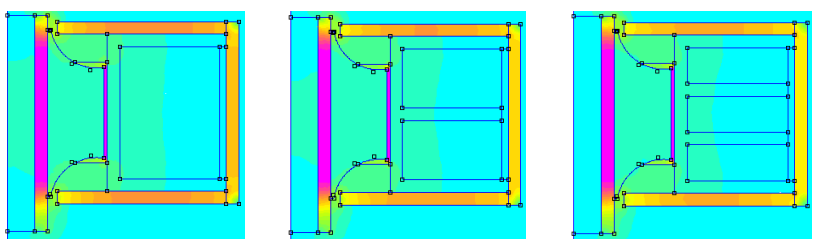

Figure 5: Design and arrangement of coil configurations for MRE bushing; (a) single coil (b) double coils, and (c) triple coils

For the single coil, the MRE bushing is designed with 3500 turns. Meanwhile, the double coil consisted of 1500 turns on each coil and triple coil has 900 turns on each coil. Based on the simulation analysis, the bushing with a single coil produces the highest value of the magnetic flux density at 0.21 T,

followed by double coil (0.17 T), and triple coil at 0.15 T. Figure 6 shows the magnetic flux density for these three configurations.

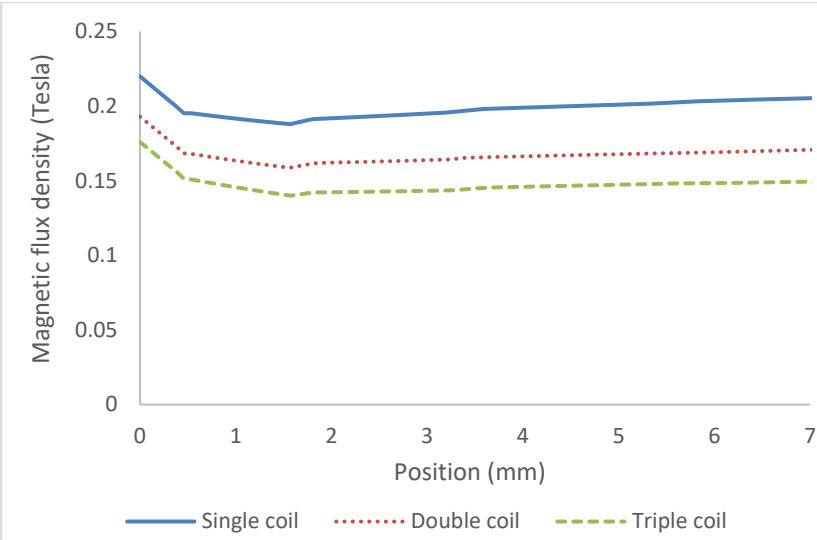

Figure 6: Magnetic flux density for different configurations of coil

From the graph, the single coil produced the highest magnetic field strength in the MRE effective area, and the double and triple coil yield lower magnetic flux density because the flux encircled the coil bobbin with uneven magnetic field strength and had the highest magnetic flux leakage compared to the single coil. In addition, the total number of coils turns needed to be divided by two or three coils, and thus, it was affecting the amount of magnetic flux flowing through the center of the bushing. Thus, the single is selected for the design of MRE bushing.

Material configurations of parts

The material configurations are based on the influence of the material on the distribution of the magnetic flux in the effective area of the MRE bushing. For this analysis, the parts of MRE bushing consisted of the use of magnetic (AISI 1020) or non-magnetic materials (Al 6061-T6), or both. Then, the selection of materials is done to obtain the highest magnetic flux density at the effective area of the MRE bushing respectively. Thus, the parts for MRE bushing such as inner and outer pipes, housing, and ring plates have been simulated by alternately changed between magnetic and non-magnetic materials except for coil bobbin which remains as non-magnetic material (Al 6061-T6). Based on the FEMM simulation done, each of the parts is made from the magnetic

material that has high magnetic permeability and magnetic saturation. Table 4 shows different combinations of material selections for the parts of MRE bushing.

Table 4: The material selections of MRE bushing parts

Design	Inner Pipe	Outer Pipe	MRE	Coil bobbin	Coil	Ring Plate	Housing
A	Magnetic	Magnetic	Magnetic	Non-magnetic	Non-magnetic	Magnetic	Magnetic
B	Non-magnetic	Magnetic	Magnetic	Non-magnetic	Non-magnetic	Non-magnetic	Non-magnetic
C	Magnetic	Non-magnetic	Magnetic	Non-magnetic	Non-magnetic	Magnetic	Non-magnetic
D	Non-magnetic	Non-magnetic	Magnetic	Non-magnetic	Non-magnetic	Non-magnetic	Magnetic
E	Non-magnetic	Non-Magnetic	Magnetic	Non-magnetic	Non-magnetic	Non-magnetic	Non-magnetic
F	Magnetic	Magnetic	Magnetic	Non-magnetic	Non-magnetic	Non-magnetic	Non-magnetic
G	Magnetic	Non-Magnetic	Magnetic	Non-magnetic	Non-magnetic	Non-magnetic	Non-magnetic

Figure 7 shows the magnetic flux density at the effective area of MRE bushing for the different configurations of MRE bushing materials. The order of the design from the highest to the lowest value of average magnetic flux density are as follows: A (0.205 T), C (0.177 T), D (0.14 T), E (0.136 T), B (0.087 T), G (0.085 T), and F (0.048 T). Based on this order, design A which has the highest value of magnetic flux density is chosen for the design of MRE bushing. The combinations of magnetic and non-magnetic material for design A are optimum for this MRE bushing, where the inner and outer pipe, ring plate, and housing are from a magnetic material, while the coil bobbin is from non-magnetic material. This is because, the use of magnetic materials for inner and outer pipe, ring plate, and housing shows higher flux density in the effective region than any other combination. Consequently, higher magnetic flux can enhance the performance of MRE bushing respectively.

Geometrical configuration of part of MRE bushing

The geometrical configuration is based on the effects of the thickness of ring plates to the distribution of the magnetic flux in the effective area of the MRE bushing, where they guide the magnetic flux through the MRE and prevent it leaked from the MRE bushing. For this reason, the thickness of ring plates is configured from 1 mm to 4 mm with the increment of 1 mm as shown in Figure 8. In this finding, the order of the configuration from highest to lowest value of average magnetic flux density are as follows: 4 mm (0.205 T), 3 mm (0.185

T), 2 mm (0.145 T), and 1 mm (0.093 T). Based on this order, the thickness of 4 mm yields the highest value of magnetic flux density among the other three. Therefore, it can be concluded that, the thicker the plates, the better the distribution of flux density due to the larger surface area. Thus, the 4 mm is selected for the design of MRE bushing.

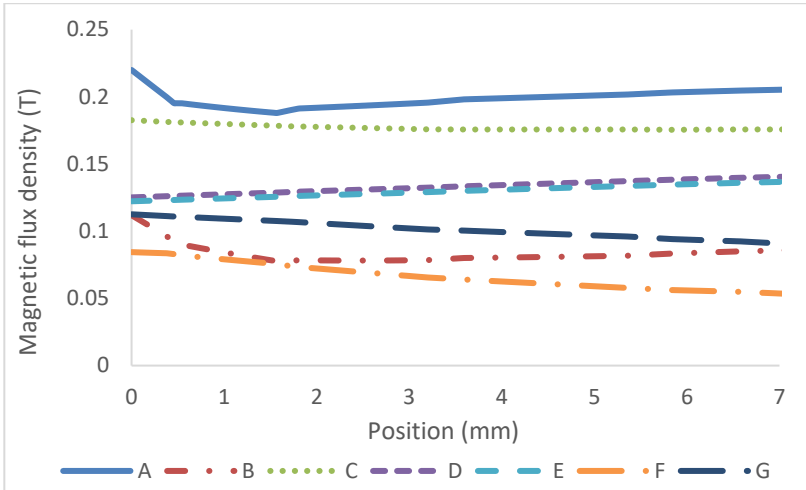

Figure 7: Magnetic flux density for different configurations of materials

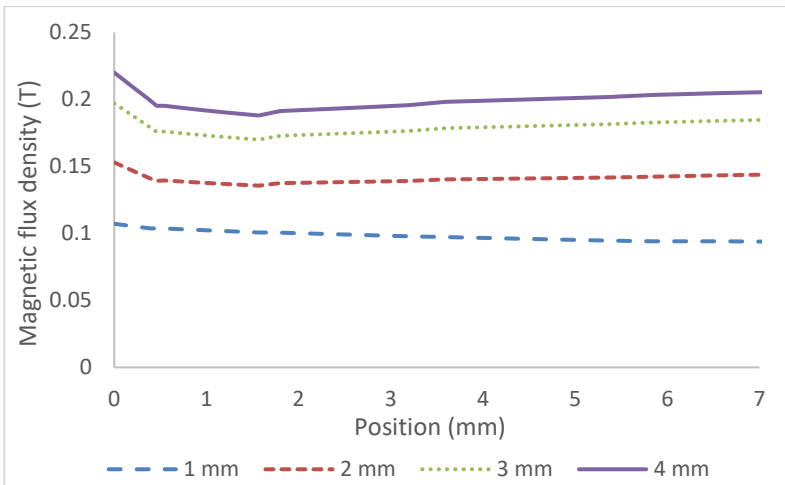

Figure 8: Magnetic flux density for difference thickness

Dynamic stiffness

After the frequency sweep experiment on the MRE bushing, the result of dynamic stiffness is obtained as shown in Figure 9. As can be seen from the graph, the stiffness is increased by increasing the frequency from 1 to 15 Hz and the input current from 0.5 to 2.5 A. Table 5 shows the result of dynamic stiffness at different current input and frequencies.

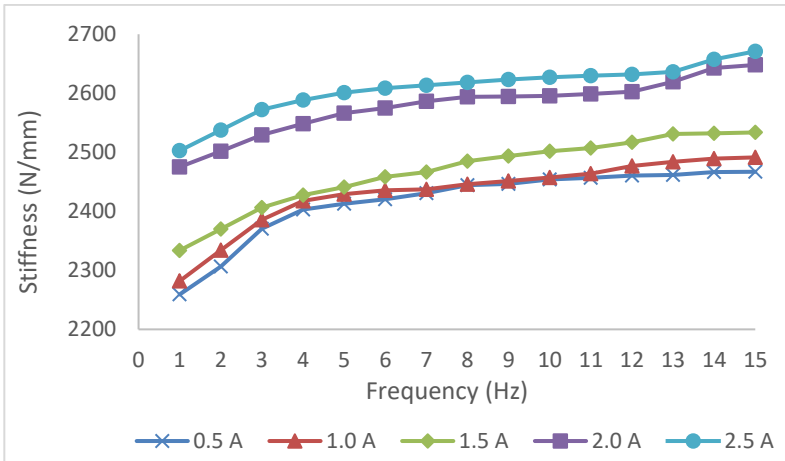

Figure 9: Stiffness of MRE bushing with varies applied current

Table 5: Result of dynamic stiffness at different current input and frequencies

Current	Frequency	
	1 Hz	15 Hz
0.5 A	2259.13 N/mm	2466.98 N/mm
1.0 A	2281.87 N/mm	2491.38 N/mm
1.5 A	2333.75 N/mm	2533.62 N/mm
2.0 A	2475.15 N/mm	2648.01 N/mm
2.5 A	2502.74 N/mm	2671.06 N/mm

Accordingly, the stiffness has been steadily increased when the applied current is from 0.5 to 2.5 A. The percentage increment for the stiffness from minimum applied current (0.5 A) to maximum applied current (2.5 A) for low frequency (1 Hz) and high frequency (15 Hz) are 10.78% and 7.52% respectively. Due to the stiffness of MRE being dependent on the magnetic field, the applied current plays the main role to change the stiffness. As the magnetic field strength increases, the stiffness of MRE can be significantly increased [29]. The results revealed that the MRE bushing is stiffer when more input currents and frequencies are applied. This is because when more input

current is applied, the magnetic field strength is increasing in the bushing which causes the bushing to become stiffer. On the other hand, as the frequencies increased, the stiffness of the bushing increased as well as is related to a high amount of vibration applied to the bushing. It is a regular occurrence in viscoelastic materials that frequency intensities will lead to increased intricacy in the matrix since the deformation of molecule chains has failed to keep up with the shear force, hence causing the stiffness to increase with increasing frequency intensities [30]. Thus, the bushing tends to act stiffer for vibration absorption. This is beneficial for the suspension system as stiff suspension bushing yields excellent handling, while softer suspension bushing improved ride comfort significantly [17].

Apart from that, dramatic changes in the stiffness behavior can be seen between the applied current of 1.5 A and 2.0 A for all excitation frequencies. The applied current in this study can be classified into two categories which are as low current range (0.5-1.5 A) and the high current range (2.0-2.5 A). When the high current is applied, it leads to a high magnetic flux density in the MRE bushing which attributed to the MRE compound rigidity and increasing the stiffness abilities. Here, the carbonyl iron particles (CIPs) are well-embedded and randomly distributed in the matrix. CIPs are a soft magnetic material which has an obvious active response to the presence of the magnetic field. The application of high current triggered the magnetic particles to react rigorously towards the compound. This phenomenon is related to the magnetic saturation and coercivity force [31]. As the magnetic field intensity keep increasing, it reduced the displacement between the particles as a result of strong interaction that had linked the particles in the matrix. The reduced distance between the magnetic particles leads to a stronger bonding interaction of magnetic particles in the MRE bushing. The magnetic field will continuously trigger the magnetic particles until achieving saturation point. Therefore, that is the reason for the significant changes in stiffness between low and high applied currents. The stiffness, in this case, strongly depended on the strength of the magnetic field.

Therefore, this MRE bushing is able to achieve variable stiffness behavior. All in all, it can be observed that the stiffness of MRE bushing is increasing according to the intensity of the magnetic field.

Conclusions

In this paper, an MRE bushing is simulated to study the effects of various configurations such as coil, materials, and geometrical dimensions of the part used in the bushing. The conceptual design of MRE bushing undergoes the analysis of magnetic flux density by FEMM simulation, where the magnetic flux density across the MRE effective area has been maximised based on different configurations applied. It can be noted that the use of a single coil,

the use of magnetic material for all parts except the coil bobbin, and the higher thickness of the ring plates can help to maximise the magnetic field strength in the bushing. The best configuration based on simulation analysis is achieved and that design proceeds for the experimental testing of dynamic stiffness. Based on the experimental test, the variable stiffness behavior of MRE bushing can be determined, where the higher magnetic field strength provides higher stiffness significantly. It is found that the changes in current and frequencies caused changes in the dynamic stiffness of the bushing. Thus, it has proven the concept of MRE as a smart material, which should be explored more and intensely reinvestigated in the future. In a nutshell, MRE bushing is potential as a vibration control in automotive applications especially in suspension systems due to its behaviour which is adjustable, tuneable, and controllable stiffness.

Contributions of Authors

M.I.A.H.: writing—original draft preparation, methodology, investigation, validation; A.Y.A.F., N.A.N. and S.A.M.: supervision, conceptualization, writing—reviewing and editing, funding acquisition; U.U., F.I. and I.I.: writing—review and editing. All authors have read and agreed to the published version of the manuscript.

Funding

This research work is supported and funded by Universiti Teknologi Malaysia (UTM) under UTM Prototype Research Grant (UTMPR) (Vot no. 00L46). The authors also thank Japan International Cooperation Agency Fund (JICA Fund) (Vot no. 4B696).

Conflict of Interests

The authors declare no conflict of interest. The authors also declare that they have no known competing financial interests or personal relationships that could have appeared to influence the work reported in this paper.

Acknowledgement

Million thanks to the Engineering Materials and Structures group member (eMast iKohza), Universiti Teknologi Malaysia that always provide morale support and constructive discussion throughout the research work.

References

[1] M.A. Faizal Johari, S.A. Mazlan, Ubaidillah, et al, "An Overview of Durability Evaluations of Elastomer-Based Magnetorheological Materials," *IEEE Access, vol.* 8, pp. 134536–134552, 2020.

[2] S.A.B.A. Aziz, S.A. Mazlan, N.A. Nordin, et al., "Material characterization of magnetorheological elastomers with corroded carbonyl iron particles: Morphological images and field-dependent viscoelastic properties," *International Journal of Molecular Sciences*; vol. 20, pp. 1-20, 2019.

[3] G. Zhang, Zhang J, Guo X, et al., "Effects of graphene oxide on microstructure and mechanical properties of isotropic polydimethylsiloxane-based magnetorheological elastomers," *Rheologica Acta*, vol. 61, pp. 215–228, 2022.

[4] S. Eraslan, I.M. Gitman, H. Askes, et al., "Determination of representative volume element size for a magnetorheological elastomer," *Computational Materials Science*; vol. 203, pp. 11070, 2022.

[5] Yunus NA, Mazlan SA, Ubaidillah, et al., "Rheological properties of isotropic magnetorheological elastomers featuring an epoxidized natural rubber," *Smart Materials and Structures*, vol. 25, pp. 1–11, 2016.

[6] Shabdin MK, Zainudin AA, Mazlan SA, et al., "Tunable low range Gr induced magnetorheological elastomer with magnetically conductive feedback" *Smart Materials and Structures*, vol. 29, no. 5, 2020.

[7] Zainudin AA, Yunus NA, Mazlan SA, et al., "Rheological and resistance properties of magnetorheological elastomer with cobalt for sensor application",. *Applied Sci*ences, vol. 10, no. 5, pp. 1638, 2020.

[8] Burhannuddin NL, Nordin NA, Mazlan SA, et al., "Physicochemical characterization and rheological properties of magnetic elastomers containing different shapes of corroded carbonyl iron particles," *Scientific Reports*, vol. 11, pp 1–17, 2021.

[9] Khairi MHA, Fatah AYA, Mazlan SA, et al., "Enhancement of particle alignment using silicone oil plasticizer and its effects on the field-dependent properties of magnetorheological elastomers," *International Journal of Molecular Sciences*, vol. 20, no. 17, 2019.

[10] Gong XL, Zhang XZ, Zhang PQ, "Fabrication and characterization of isotropic magnetorheological elastomers," *Polymer Testing, vol. 24, no. 5, pp. 669-676,* 2005.

[11] Liu T, Xu Y., "Magnetorheological Elastomers: Materials and Applications," Smart and Functional Soft Materials, 2019.
[12] Ubaidillah, Sutrisno J, Purwanto A, et al., "Recent progress on magnetorheological solids: Materials, fabrication, testing, and applications," *Advanced Engineering Materials,* vol. 17, no. 5, pp. 563-597, 2015.
[13] Wahab NAA, Mazlan SA, Ubaidillah, et al., "Fabrication and investigation on field-dependent properties of natural rubber based magneto-rheological elastomer isolator," *Smart Materials and Structures,* vol. 5, no. 11, pp. 1-11, 2016.
[14] Kang SS, Choi K, Nam J Do, et al. Magnetorheological elastomers: Fabrication, characteristics, and applications. *Materials* 2020; 13: 1–24.
[15] Jang DI, Yun GE, Park JE, et al., "Designing an attachable and power-efficient all-in-one module of a tunable vibration absorber based on magnetorheological elastomer" *Smart Materials and Structures*, vol. 27, 2018.
[16] Ubaidillah, Hadi S, Harjana, et al., "Design and fabrication of magnetorheological elastomer vibration isolator," *Journal of Mechanical Engineering*, vol. 5, no. 6, pp. 192-210, 2018.
[17] Kumbhar SR, Maji S, Kumar B., "Development and Testing of MRE Bushing for Road Vehicle Suspension System," *International Journal of Recent Advances in Mechanical Engineering*, vol. 2, no. 3, 2013.
[18] Abdelfatah MM. *Magnetorheological bushing steering system*. US, 2018.
[19] Elie LD, Ginder JM, Stewart WM, et al. *Variable Stiffness Bushing using Magnetorheological Elastomer*. European, 2002.
[20] Ginder JM, Nichols ME, Elie LD, et al., "Controllable-Stiffness Components based on Magnetorheological Elastomers," *Smart Structures and Materials 2000: Smart Structures and Integrated Systems*. *SPIE*, vol. 3985, pp. 418, 2000.
[21] Ikeda K, Sakuragi A, of Japan B. *Rubber Bushing*. United State, 1993.
[22] Blom P, Kari L., "The frequency, amplitude and magnetic field dependent torsional stiffness of a magneto-sensitive rubber bushing," *International Journal of Mechanical Sciences*, vol. 60, no. 1, pp. 54-58, 2012.
[23] Kim SH, Park YJ, Cha AR, et al., "A feasibility work on the applications of MRE to automotive components," *IOP Conference Series: Materials Science and Engineering*, vol. 333, 2018.
[24] Lee HS, Shin JK, Msolli S, et al., "Prediction of the dynamic equivalent stiffness for a rubber bushing using the finite element method and empirical modeling," *International Journal of Mechanics and Materials in De*sign, vol. 15, no. 1, pp. 77–91, 2019.
[25] Ginder JM, Nichols ME, Elie LD, et al., "Magnetorheological Elastomers: Properties and Applications," *Smart Structures and Materials 1999. Smart Materials Technologies*, vol. 3675, pp. 131–138. 1999.

[26] Fatah AYA, Mazlan SA, Koga T, et al., “A review of design and modeling of magnetorheological valve,” *International Journal of Modern Physics B*, vol. 29, no. 4, 2015.

[27] Wahab NAA, Mazlan SA, Hairuddin K, et al., “Simulation study of electromagnetic circuit design in laminated magnetorheological elastomer isolator,” *IOP Conference Series Materials Science and Engineering*; vol. 100, no. 1, 2015.

[28] N.A. Wahab, S.A. Mazlan, F. Imaduddin, et al., "Development Of Magnetic Circuit Design In Multi Sandwich Magneto Rheological Elastomer (MRE) Isolator,” Journal of Physics Conference Series, vol. 1908, no. 1, pp. 2497-2508, 2016.

[29] A. Fuchs, Q. Zhang, J. Elkins, et al., "Development and characterization of magnetorheological elastomers," *Journal of Applied Polymer Science*, vol. 105, no. 5, pp. 2497–2508, 2007.

[30] Y.C. Fan, X.L. Gong, W.Q. Jiang, et al., "Effect of maleic anhydride on the damping property of magnetorheological elastomers," *Smart Materials and Structures*, vol. 19, no. 5, pp. 055015, 2010.

[31] N. Hapipi, S.A.A. Aziz, S.A. Mazlan, et al., "The field-dependent rheological properties of plate-like carbonyl iron particle-based magnetorheological elastomers," *Results in Physics*, vol. 12, pp. 2146–2154, 2019.

The Effects of Beeswax Additions on the Structural, Thermal, Mechanical and Mass Loss Properties of Soy Wax Blends

Sharifah Imihezri Syed Shaharuddin[*]*, Mohd Ashhar Mansor*
Mastura Abdul Rashid, Norhashimah Shaffiar, Zuraida Ahmad
Department of Manufacturing and Materials Engineering,
Kulliyyah of Engineering, International Islamic University Malaysia,
53100, Kuala Lumpur, MALAYSIA
[*]*shaimihezri@iium.edu.my*

ABSTRACT

The typical batik wax compositions used in Malaysia consist of various blends of beeswax, dammar, rosin, paraffin, and microcrystalline wax. This study aims to characterize soy wax/beeswax blends' structural, thermal, strength, and mass loss properties as potential alternative batik wax compositions. The Fourier transform infrared spectroscopy (FTIR) results showed that the additions of beeswax (wt%) into soy wax resulted in possible chemical interaction for the esters (C=O stretching and C-H bending vibrations), hydrocarbons (CH_2 scissor formation), and cholestral esters (C=O stretching vibrations). The thermal profile obtained via differential scanning calorimetry (DSC) and thermogravimetric analysis (TGA) respectively revealed an increase in peak melting temperature and reduced thermal stability of the blends with further increments of beeswax. In addition, beeswax enhances the compression strength by 150% but did not have any significant impact on the modulus of the blends. Evaluation of the mass loss test suggested that beeswax in the range of 40 wt% to 60 wt% can be considered as alternative batik resist material due to its moderate leaching tendency. Future works shall be conducted to evaluate the performance of these wax compositions against other batik wax criteria and the feasibility of printing these waxes using an in-house designed batik printer.

Keywords: *Batik Wax; Batik Printer; Thermal; Compression Strength; Leaching*

ISSN 1823-5514, eISSN 2550-164X

https://doi.org/10.24191/jmeche.v20i1.21079

Received for review: 2022-03-14
Accepted for publication: 2022-09-20
Published: 2023-01-15

Introduction

The creation of batik textiles involves using various kinds of resist materials to block the diffusion of dye on the fabric and create beautiful batik motifs. In Southeast Asia, batik artisans in Indonesia use wax-based resist materials from beeswax that are blended with shorea javanica (*damar mata kucing*), pine gum (*gondorukem*), wax waste, gum rosin, coconut oil, animal fat, lancing wax, and paraffin [1]-[2]. The ratio of the batik resist materials varies as their batik industry spans across its vast archipelago. The batik artisans located near the coastal areas use different wax blends compared to the batik produced in the cold plateau regions [3]. The batik artisans in Malaysia use wax ingredients that are made up of a blend of beeswax, dammar, rosin, vegetable oil, paraffin, and microcrystalline wax. These waxes are melt-blended at various ratios depending on the desired aesthetic effect. Kudiya et al. [3]-[4] summarised the attributes of a good batik wax as being resistant against alkali and chemicals, durable against hot and cold dye solutions, does not break/crack easily, able to create sharp wax lines, does not create additional staining effects on the fabric, easy to set, non-sticky, not easy to be removed and recyclable.

Wax is a greasy solid that melts readily at low melting points in the range of 40 °C to 75 °C [5] with varying degrees of glossiness, slipperiness, and plasticity [6]. Waxes are categorized as lipids as they are non-polar and only dissolved in organic solvents. The main constituents of wax are hydrocarbons, medium chain length of monoesters-diesters-triesters of fatty acids, long-chain, and free long-chain alcohols, aldehydes, sterols, ketones and ß-diketones, triterpenols, and triterpenic acids [7]-[8]. The use of naturally sourced waxes such as paraffin has raised environmental concerns as they are non-sustainable and non-biodegradable [9]. Hence there is a high demand for "green" waxes. Natural plant-based waxes have risen in popularity due to their abundant supply and low price [10]. Recently, soy oil-based wax has been given attention as a sustainable replacement for paraffin wax [11].

Soy oil is composed of several fatty acids as follows: palmitic acid (10%), stearic acid (4%), oleic acid (18%), linoleic acid (55%), and linolenic acid (13%) [12]. The hydrogenation process at high temperature with nickel catalyst converts the unsaturated fatty acids in the oil into a saturated form. This procedure chemically stabilizes and raises the melting temperature of soy oil resulting in a more solid form of partial or fully hydrogenated soy oil, also known as soy wax [10]. Fully hydrogenated soy wax mainly consists of triglycerides with a high proportion of stearic acid [13]. The use of vegetable oil-based waxes is considered a viable alternative to paraffin as they readily biodegrade compared to paraffin [14]. Despite being hydrophobic, soy wax has a high water uptake [15]. Therefore, the dye colorant may diffuse across the wax lines and leave a staining effect on the batik design. At room temperature, pristine soy wax has a greasy surface texture and is brittle [10]-[11]. Thus, in this study, increments of beeswax are added to improve soy wax properties.

Purified beeswax is processed via various methods such as steam extraction, hot water extraction, and centrifugation [16]. Beeswax consists of multi-component material of at least 284 different compounds [17] and its prominent compound families comprised of 72% fatty acid esters, 13% free acids, and 13% hydrocarbons [18]. Beeswax is a natural water repellant material and has one of the highest water vapor permeability properties attributed to its fatty acids, alcohols, and esters content [19].

A substantial amount of studies have been focused on beeswax [20]. The aromatic hydrocarbon structure of beeswax is said to be responsible for the hydrophobic spreading of beeswax on fabric [21]. The formation of long molecular chains and complex molecules suppresses the formation of stable lamellar structure which contributes to the good pliability nature of beeswax [14]. Kusumawati et al. [1] reported that the presence of a high non-polar functional group in beeswax composition is responsible for its high alkaline resistance. Hu and Yu's [22] study revealed that beeswax's natural structure of hydrocarbon lipid acts as a lubricant that imparts flexibility and viscoelastic properties. Besides Bowen’s study [23] on the use of soy wax/beeswax for batik purposes, to our knowledge, information about the thermal, structural, mechanical, and mass loss properties of beeswax and soy wax blends has been lacking.

Methodology

Material preparation

The ratios of beeswax (Global Sdn. Bhd., Malaysia) and soy wax (Jargeous Sdn. Bhd., Malaysia) were weighed according to the wt% ratios shown in Table 1. In this study, beeswax was melted first at 70 °C due to its high melt temperature followed by soy wax. Once the soy wax/beeswax blends had completely dissolved, the prepared batik wax blends were then left to solidify for 48 hours before being re-melted for ensuing tests.

Table 1: Sample codes for the soy wax/beeswax blends

Sample code	Beeswax (wt%)	Soy wax (wt%)
Neat beeswax	100	-
Soy20bees80	80	20
Soy40bees60	60	40
Soy60bees40	40	60
Soy80bees20	20	80
Neat soy wax	-	100

Fourier Transform Infrared Spectroscopy (FTIR)

Identification of the functional group of soy wax/beeswax blends was obtained by using Tensor 27 FTIR Spectrometer (Bruker, USA). The spectra were collected within 4000-6000 cm^{-1} regions with a resolution of 4 cm^{-1} and 16 scans.

Thermal characterizations

The thermograms of beeswax and soy/beeswax blends were obtained using a Sapphire Differential Scanning Calorimetry (Perkin Elmer Instrument, USA). About 5 mg of the sample was sealed in an aluminum pan and heated from 30 ℃ to 200 ℃ at a rate of 10 ℃/min and a constant flow rate of 50 ml/min nitrogen gas. Two readings were taken for each sample.

The thermogravimetric analysis (TGA) of the soy wax/beeswax samples was performed using a Simultaneous Thermal Analyzer (STA7300) (Hitachi High Technologies, USA). The thermal profile of the samples was determined using approximately 15 mg to 20 mg under an air atmosphere at a heating rate of 10 ℃/min, from 40 ℃ to 450 ℃. The initial degradation temperature (T_i) and the temperature for the final degradation (T_f) were obtained based on extrapolated onset data.

Compression test

The soy wax/beeswax compositions were remelted and cast into a coated cylindrical acrylonitrile butadiene styrene (ABS) mold with a 30 mm diameter. Upon solidification, the cylindrical soy wax/beeswax samples were removed from the mold and cut into 40 mm lengths as per the compression test for beeswax by Morgan et. al [17]. Five samples (n = 5) for each composition were prepared for compression test using Shimadzu Universal Tensile Machine (AGS-5K NXD). The test was performed at a crosshead speed of 1 mm/min and a load cell of 5 kN at an ambient temperature of 27 °C.

Mass loss test

A 3 cm x 3 cm inner square was sketched on each 8 cm x 8 cm square cotton fabric. The wax blends were re-melted, and a glass syringe was used to apply a consistent wax volume of 1 ml onto the 3 cm x 3 cm inner square. Six samples were prepared for each composition. The mass of the wax-covered cotton fabric was weighed to obtain its initial mass (M_i). Each waxed fabric sample was then immersed in 1000 ml of 100 °C water for 5 and 15 minutes. The sample fabric was then removed and dried for 24 hours. The final mass (M_f) was measured for each sample. The mass loss (%) was calculated according to Equation (1).

$$\text{Mass loss } \% = \frac{M_i - M_f}{M_i} \times 100\% \quad (1)$$

Results and Discussions

Fourier Transform Infrared Spectroscopy (FTIR)

Figure 1 shows the absorption of infrared light at different wavelengths of the studied soy wax/beeswax blends. The FTIR spectra of soy wax showed the typical peaks at 718 cm^{-1} and 1176 cm^{-1} and were assigned as C-C group vibrating and C = O stretching respectively. Two distinct peaks were also detected at 1741 cm^{-1} and 2917 cm^{-1} which arose from C = O stretching and CH_2 asymmetric stretching respectively. The FTIR peaks for soy wax in this study are consistent with the available data reported in the literature [22], [24]-[25].

Distinctive compounds or ′fingerprints′ for beeswax occur in the spectral region of 1800 cm^{-1} and 800 cm^{-1}. These high absorption bands correspond to the monoesters and carboxyl group of free fatty acids [26]-[27]. FTIR peaks at absorbance intensities of 1172 cm^{-1}, 1463 cm^{-1}, and 1736 cm^{-1} were also noted and are consistent with published values [5], [27]. It can also be confirmed that the wax used in this study is indeed beeswax rather than other hydrocarbon compounds due to the strong peak intensity at 1736 cm^{-1} which indicates the formation of an ester bond between fatty acid and cholesterol's hydroxyl group [28]. The sharp peak at 2849 cm^{-1} corresponds to aliphatic hydrocarbon chains for CH_2 symmetric stretching vibrations and the peak at 2918 cm^{-1} is due to CH_2 asymmetric stretching vibrations.

Table 2 tabulates the wavenumber and assigned functional groups for the FTIR absorption. It was observed that further increments of beeswax into soy wax resulted in an apparent peak position shift of the beeswax's ′fingerprints′ compound towards higher wavenumber suggesting chemical interaction for the esters (C = O stretching and C-H bending vibrations), hydrocarbons (CH_2 scissor formation), and cholestral esters (C = O stretching vibrations).

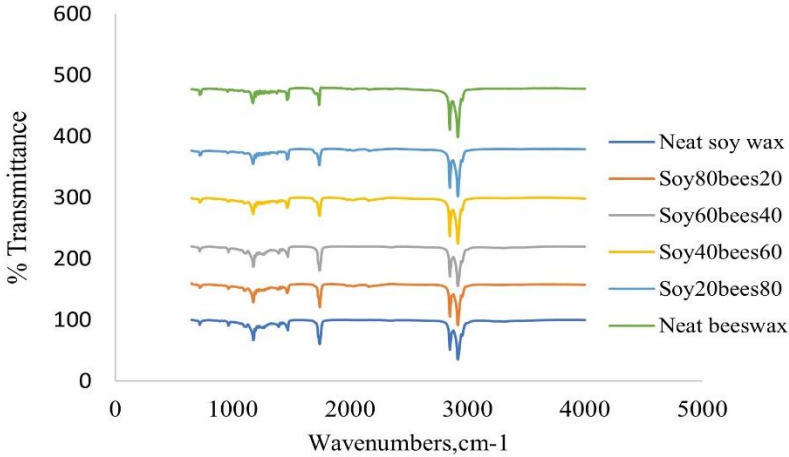

Figure 1: FTIR spectra of soy wax/beeswax blends

Table 2: Assigned wavenumber and vibrating group for the soy wax/beeswax blends used in this study

Sample code wavenumber						Vibrating group
Neat soy wax	Soy 80 bees 20	Soy **6**0 bees **4**0	Soy **4**0 bees **6**0	Soy **2**0 bees **8**0	Neat beeswax	
718	720	720	720	720	720	CH_2 rocking mode (hydrocarbons - alkenes)
1176	1175	1175	1175	1174	1172	C=O stretching and C-H bending vibrations (ester)
1470	1465	1463	1463	1463	1463	CH_2 scissor formation (hydrocarbons -alkanes)
1741	1742	1741	1739	1738	1736	C=O stretching vibrations (cholesterol esters)
2850	2850	2849	2849	2850	2849	CH_2 symmetric stretching vibrations (aliphatic hydrocarbons)
2917	2918	2918	2918	2918	2918	CH_2 asymmetric stretching vibrations (aliphatic hydrocarbons - alkanes)

Thermal properties

Figure 2 shows the DSC thermograms of the soy wax/beeswax blends used in this study. The glass transition temperature for neat soy wax and neat beeswax was hardly discernable from the DSC curve suggesting that these waxes consist of heavily crosslinked molecular chains that eventually disrupt the ease of cooperative segmental mobility. Soy wax's thermogram showed a single smooth melting peak at 57 °C, which is possibly due to the heat absorbed by esters and partial acyl glyceride with long and saturated acyl chains [10]. It is also concluded from the thermogram that the soy wax used in this study is in the fully hydrogenated form since the melting peak occurred in the range of 53 °C-63 °C [11]. In comparison to soy wax, beeswax exhibited higher melting temperatures as it is composed of mixed esters with high molecular weights and complicated structures [21]. Beeswax's melting peak in the range between 40 °C to 60 °C is associated with the heat absorbed by free acids and hydrocarbons, whilst a second larger and well-defined peak detected at 72 °C is due to the heat absorbed by the dominant fatty acid and wax ester component [18], [31]. Beeswax also exhibited a broader melting peak region compared to soy wax. Therefore it is anticipated that melted beeswax can spread easily and penetrates better through the cotton fabric before becoming completely solidified [26]. Further additions of beeswax (wt%) into soy wax increased the melting temperature of the blends.

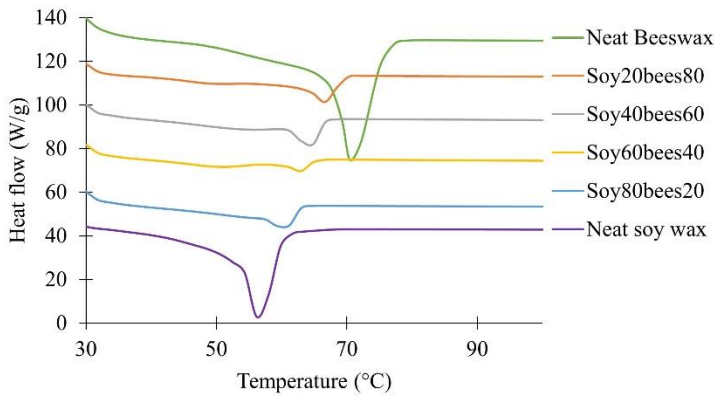

Figure 2: DSC thermogram of the soy wax/beeswax blends

Figure 3 shows the weight-loss (%) trends of the soy wax/beeswax blends as a function of temperature. Each composition exhibited an initial plateau region of constant mass followed by a single-stage decomposition. Neat soy wax is the most thermally stable material compared to other waxes in this study as its thermal degradation region occurred between 376 ℃ and 450 ℃. Neat beeswax experienced thermal degradation starting at 304 ℃. As it reached

400 °C, neat beeswax experienced 70% weight loss due to the degradation of most of its polar and non-polar bonds in its hydrocarbon and esters [32]-[33]. Beyond 430 °C further decomposition took place for the beeswax's long-chain molecules [26] resulting in more than 90% weight loss Further addition of beeswax (wt%) into soy wax resulted in a reduction in thermal stability of the soy wax/beeswax blends from 376 ℃ to 328 ℃. It was also noted that all studied waxes underwent complete pyrolysis with almost no remaining residues beyond 480 °C.

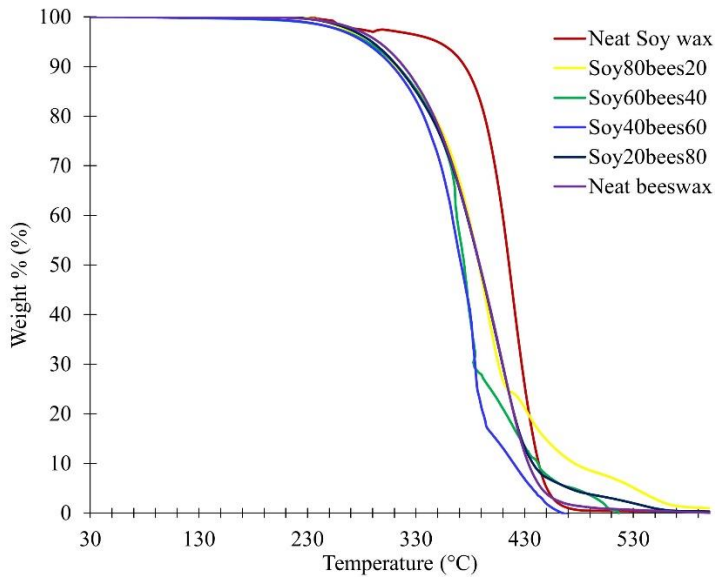

Figure 3: Thermogravimetric analysis of soy wax/beeswax blends

Mechanical properties

The stress-strain profile and the average ultimate strength and modulus for the soy wax/beeswax blends are shown in Figure 4 and Figure 5, respectively. The compressive stress-strain profile shows that the waxes behaved in a ductile manner as their stress values gradually decreased beyond their well-defined yield point of ultimate strength. In comparison to soy wax, the compression test results indicated that neat beeswax had higher ultimate strength attributed to the presence of fatty acid components in its chemical structure [32]. The ultimate strength of neat beeswax at 0.8 MPa is slightly lower than the value reported by Morgan et al. [17]. Their study reported a strength value of 1.0 MPa since their test was conducted at a lower temperature of 24 °C. Increments of beeswax additions up to 80 wt% into soy wax resulted in a significant increase in compression strength of the blends by approximately 150%.

However, the additions of beeswax did not impart any improvements on the modulus of the blends due to beeswax's inherently pliable nature [14]. Images of the samples under compression are shown in Figure 6. It was observed that neat soy wax responded to the compression load with a higher number of cracks compared to beeswax, which reflects the brittle and lack of cohesiveness of soy wax.

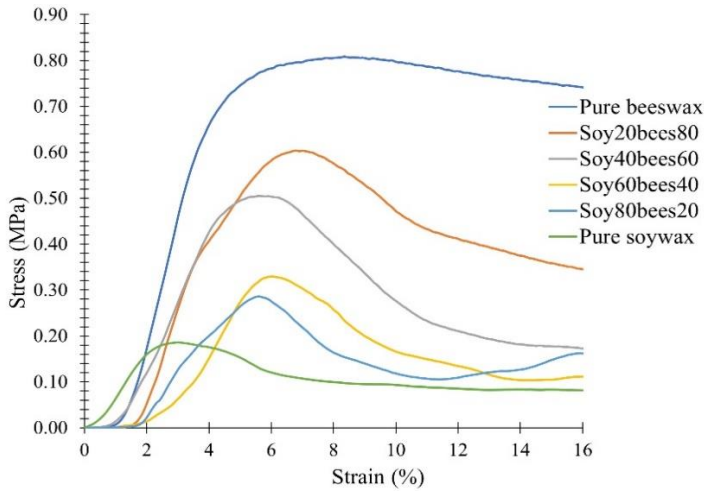

Figure 4: Stress-strain curves of soy wax/beeswax blends via compression test

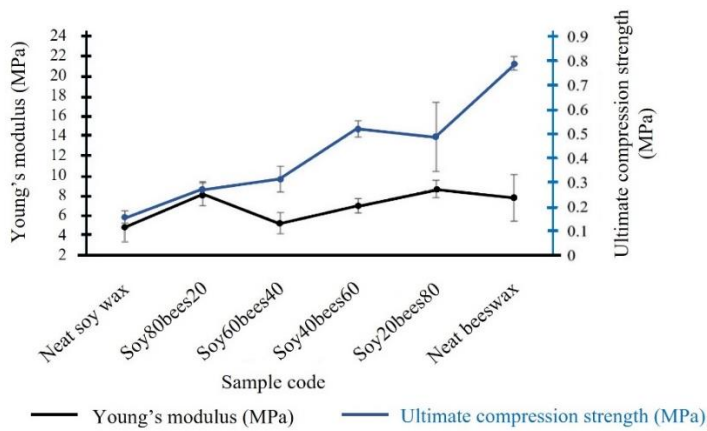

Figure 5: The ultimate compression strength and Young's modulus of soy wax/beeswax blends via compression test

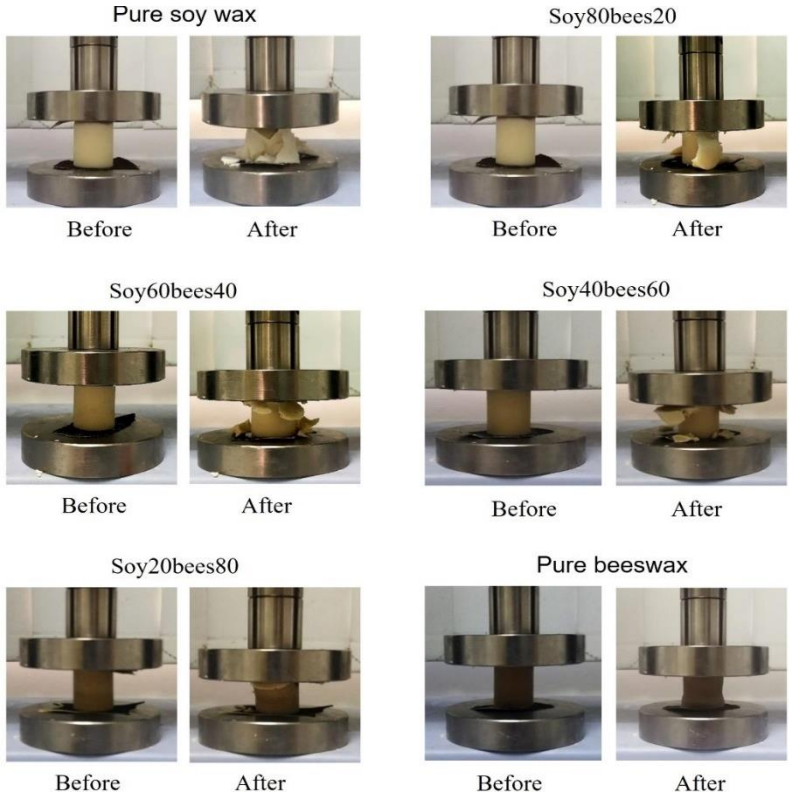

Figure 6: The soy wax/beeswax specimens under compression load

Mass loss properties

Figure 7 shows the blends' mass loss (%) upon immersion in 100 °C water for 5 minutes and 15 minutes. Beeswax and soy wax are superhydrophobic materials [13], [33]-[34]. However, at high immersion temperatures, these materials' superhydrophobic properties denature which enables the leaching of the waxes into the water. It was observed that soy wax recorded the highest mass loss of 33% and 39% for the immersion period of 5 minutes and 15 minutes respectively. DSC thermogram showed that soy wax has a low melt temperature which may have made it easier for the soy wax to disintegrate and leach into the immersion water. Bowen's [23] study also observed that soy wax used for batik applications can be easily dissolved in water and can be removed using the hot iron technique. In comparison, beeswax showed the lowest mass loss at 5% and 12% for the immersion period of 5 minutes and 15 minutes respectively.

It was evident from the mass loss (%) trends that the initial addition of 20 wt% of beeswax for Soy80bees20 composition resulted in a marked reduction of mass loss (%) of the wax blend for both immersion periods. Further beeswax additions (wt %) led to a decreasing mass loss (%) trend. The result suggests that beeswax provides a better barrier against water contact with the surface of the wax blends which led to a reduced leachability into the immersion water. However, it was also noted that further additions of beeswax at 60 wt% and 80 wt% did not show an appreciable mass loss difference for the 15 minutes immersion period compared to the 5 minutes immersion period. The leaching of material into the immersion medium behaves in a nonlinear manner [35]. During the 5 minutes immersion period, the amount of mass loss (%) is attributed to the initial leaching of the waxes due to surface contact with water. As the immersion period was increased to 15 minutes, the leaching of the soy wax/beeswax blends eventually slowed down and reached a limiting value possibly as a consequence of intraparticle water diffusion into the bulk of the solid waxes that are attached to the cotton fabric.

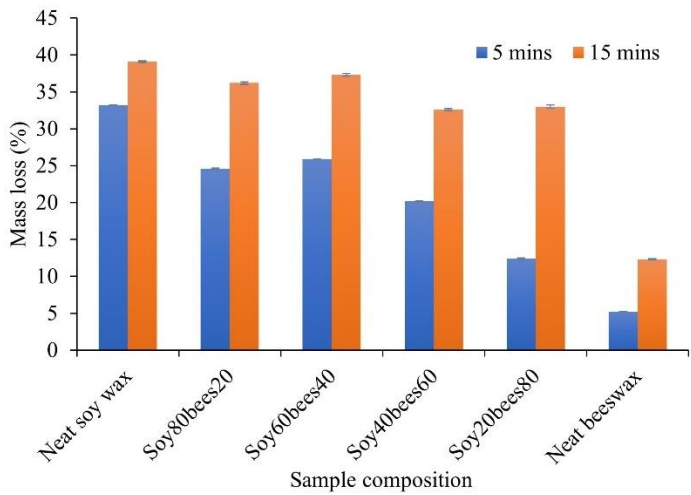

Figure 7: Mass loss (%) for soy wax/beeswax blends at 100 °C water after 5 minutes and 15 minutes

In batik production, the leaching tendency of the waxes is an important parameter that affects its overall process. Batik waxes with a low leaching performance increase the time and energy consumption during the wax removal phase. On the other hand, wax compositions with a high leaching tendency facilitate the wax removal phase but may not be robust enough to be used in multiple dyeing processes which limits the creative batik process. Wax compositions with beeswax in the range of 40 wt% to 60 wt% provided

moderate leaching performance, therefore can be considered as alternative batik wax resist materials. Further studies are currently being conducted to investigate whether these compositions can impart other batik wax qualities such as the ability to impart 'crackle', a batik trademark effect [36], and continuous wax lines via a recently developed batik printer.

Conclusions

Worldwide enforcement for 'greener' products has instigated this study on the characterization of alternative sustainable and biodegradable resist material consisting of soy wax/beeswax blends. The effect of blending beeswax into soy wax was noted with a chemical interaction for the FTIR 'fingerprint' region for beeswax. The T_g for soy wax and beeswax was hardly discernable from the DSC curve suggesting that these waxes consist of heavily crosslinked structures that eventually disrupt the ease of segmental mobility. The study also showed a decreasing trend in thermal stability as measured from the initial temperature (T_i) of the TGA profile with subsequent beeswax additions. The results obtained suggest that the incorporation of beeswax is effective in improving the strength as well as leaching properties of the soy wax blends which shows the promising application as batik resist material.

Contribution of Authors

The authors confirm the equal contribution in each part of this work. All authors reviewed and approved the final version of this work.

Funding

This work was supported by the Fundamental Research Grant Scheme [FRGS/1/2018/TK03/UIAM/02/3, Investigation on the Effectiveness of Various 'Green' Batik Wax Blends Extruded via Fused Deposition Modeling (FDM), 2018]

Conflict of Interests

All authors declare that they have no conflicts of interest

Acknowledgement

The authors would like to express their deepest gratitude for the technical supports provided by the lab assistants and the information provided by batik entrepreneurs, Maryam Samirah Shamsuddin and Mohd. Hafidz Drahman.

References

[1] N. Kusumawati, A. Kistyanto, and S. Muslim, "The effect of blending composition against latched power and the resistance of batik wax against cracking and alkaline chemicals," *International Journal Advanced Science Engineering and Information Technology*, vol. 7, no. 4, pp. 1141–1147, 2017.

[2] A. Malik, F. I. Rahmillah, B. D. Atmaja, and B. F. Ihsan, "The effect of microwax composition on the staining quality of Klowong batik wax," *MATEC Web of Conference*, vol. 154, pp. 10–13, 2018.

[3] K. Kudiya, B. Sumintono, S. Sabana, and A. Sachari, Batik artisans' judgment of batik wax quality and its criteria: An application of the Many-Facets Rasch model, Pacific Rim Objective Measurement Symposium (PROMS) 2016 Conference Proceedings, pp. 27–37, 2018.

[4] K. Kudiya, S. Sabana, and A. Sachari, "The waxing optimization in finding the best melting point of wax for staining cirebon batik," *Art and Design Studies*, vol. 20, pp. 10–19, 2014.

[5] M. Baglioni, G. Poggi, G. Ciolli, E. Fratini, R. Giorgi, and Piero Baglioni, "A Triton X-100-based microemulsion for the removal of hydrophobic materials from works of art : SAXS characterization and application," *Materials (Basel).*, vol. 11, no. 7, pp. 1144, 2018.

[6] Y. Lan, Waxes, Encyclopedia of Food Chemistry, 1st edition, Amsterdam: Elsevier, pp. 312-316, 2019.

[7] J. Planeta, P. Novotn´a, V. Pac´akov´a, K. Stulik, M. Mikesov´a, and J. Vejrosta, "Application of supercritical fluid chromatography to the analysis of waxes in objects of art," *Journal of High-Resolution Chromatography*, vol. 23, no. 5, pp. 393–396, 2000.

[8] J. S. Mills and R. White, The organic chemistry of museum objects, 2nd edition, Butterworth, Oxford, 1994.

[9] T. Fei, J. A. Walker, K. L. Vickerman, L. M. Stanley, D. Jarboe, and T. Wang, "Synthesis and characterization of soybean oil-based waxes and their application as paraffin substitute for corrugated coating," *Journal of Industrial and Engineering Chemistry*, vol. 58, pp. 113–122, 2018.

[10] L. Yao, J. Lio, T. Wang, and D. H. Jarboe, "Synthesis and characterization of acetylated and stearylyzed soy wax," *Journal of the American Oil Chemists' Society*, vol. 90, no. 7, pp. 1063–1071, 2013.

[11] K. Rezaei, T. Wang, and L. A. Johnson, "Hydrogenated vegetable oils as candle wax," *Journal of the American Oil Chemists' Society*, vol. 79, no. 12, pp. 1241–1247, 2002.
[12] T. E. Clemente and E. B. Cahoon, "Soybean oil: Genetic approaches for modification of functionality and total content," *Plant Physiology*, vol. 151, no. 3, pp. 1030–1040, 2009.
[13] T. Shen, S. Fan, Y. Li, G. Xu, and W. Fan, "Preparation of edible non-wettable coating with soybean wax for repelling liquid foods with little residue," *Materials (Basel).*, vol. 13, no. 15, pp. 1–11, 2020.
[14] L. Yao and T. Wang, "Textural and physical properties of biorenewable 'waxes' containing partial acylglycerides," *Journal of the American Oil Chemists' Society*, vol. 89, no. 1, pp. 155–166, 2012.
[15] S. M. Won *et al.*, "Natural wax for transient electronics," *Advanced Functional Materials*, vol. 28, no. 32, pp. 1–10, 2018.
[16] R. W. Coppock, Bee products as nutraceuticals to nutraceuticals for bees, Nutraceuticals, 2nd edition, Cambridge: Academic Press, pp. 813–833, 2021.
[17] J. Morgan, S. Townley, G. Kemble, and R. Smith, "Measurement of physical and mechanical properties of beeswax," *Materials Science and Technology*, vol. 18, no. 4, pp. 463–467, 2002.
[18] Z. Ruguo, Z. Hua, Z. Hong, Y. Feng, L. Kun, and Z. Wenwen, "Thermal analysis of four insect waxes based on differential scanning calorimetry (DSC)," *Procedia Engineering*, vol. 18, pp. 101–106, 2011.
[19] R. Németh, M. Bak, and D. Tsalagkas, "Effect of soil contact on the modulus of elasticity of beeswax-impregnated effect of soil contact on the modulus of elasticity of beeswax-impregnated wood," *Bioresources*, vol. 10, no. 1, pp. 1574–1586, 2015.
[20] Y. Gaillard, A. Mija, A. Burr, E. Darque-Ceretti, E. Felder, and N. Sbirrazzuoli, "Green material composites from renewable resources: Polymorphic transitions and phase diagram of beeswax/rosin resin," *Thermochimica Acta*, vol. 521, no. 1–2, pp. 90–97, 2011.
[21] M. Masae, P. Pitsuwan, L. Sikong, P. Kongsong, K. Kooptarnond, and P. Phoempoon, "Thermo- physical characterization of paraffin and beeswax on cotton fabric," *Thammasat International Journal of Science and Technology*, vol. 19, no. 4, pp. 69–77, 2014.
[22] W. Hu and X. Yu, "Thermal and mechanical properties of bio-based PCMs encapsulated with nanofibrous structure," *Renewable Energy*, vol. 62, pp. 454–458, 2014.
[23] D. B. Bowen, Soy Wax : An Alternative Resist, Kuala Lumpur International Batik Convention, no. 1, pp. 1–12, 2005.
[24] L. Hocevar, V. R. B. Soares, F. S. Oliveira, M. G. A. Korn, and L. S. G. Teixeira, "Application of multivariate analysis in mid-infrared spectroscopy as a tool for the evaluation of waste frying oil blends,"

Journal of the American Oil Chemists' Society, vol. 89, no. 5, pp. 781–786, 2012.

[25] J. Yoo, S. J. Chang, S. Wi, and S. Kim, "Spent coffee grounds as supporting materials to produce bio-composite PCM with natural waxes," *Chemosphere*, vol. 235, no. 9, pp. 626–635, 2019.

[26] A. Bucio, R. Moreno-tovar, L. Bucio, J. Espinosa-dávila, and F. Anguebes-franceschi, "Characterization of beeswax, candelilla wax and paraffin wax for coating cheeses," *Coatings*, vol. 11, no. 3, pp. 1–18, 2021.

[27] L. Svečnjak, M. Vinceković, G. Baranović, and S. Prđun, "An approach for routine analytical detection of beeswax adulteration using FTIR-ATR spectroscopy," *Journal of Apicultural Science*, vol. 59, no. 2, 2015.

[28] V. Vyshniak, O. Dimitriev, S. Litvynchuk, and V. Dombrovskiy, "Identification of beeswax and its falsification by the method of infrared spectroscopy," *Ukraine Food J*ournal, vol. 7, no. 3, pp. 421–433, 2018.

[29] R. Buchwald, M. D. Breed, and A. R. Greenberg, "The thermal properties of beeswaxes: Unexpected findings," *Journal of Experimental Biology*, vol. 211, no. 1, pp. 121–127, 2008.

[30] A. Dinker, M. Agarwal, and G. Das Agarwal, "Experimental performance analysis of beeswax/expanded graphite composite for thermal energy storage in a shell and tube unit," *International Journal of Green Energy*, vol. 15, no. 11, pp. 585–595, 2018.

[31] A. R. Chowdhury, G. Sabat, N. Gouda, and A. K. Panda, "Production of hydrocarbon rich fuel from abandoned beehive by pyrolysis," *Environmental Progress and Sustainable Energy*, vol. 40, no. 12, 2021.

[32] R. Buchwald, M. D. Breed, L. Bjostad, B. E. Hibbard, and A. R. Greenberg, "The role of fatty acids in the mechanical properties of beeswax," *Apidologie*, vol. 40, no. 5, pp. 585–594, 2009.

[33] Z. Diyana, R. Jumaidin, M. Selamat, and M. Suan, "Thermoplastic starch/beeswax blend: Characterization on thermal mechanical and moisture absorption properties," *International Journal of Biology Macromolecules*, vol. 190, pp. 224–232, 2021.

[34] W. Zhang, H. Xiao, and L. Qian, "Enhanced water vapour barrier and grease resistance of paper bilayer-coated with chitosan and beeswax," *Carbohydrate Polymers*, vol. 101, no. 1, pp. 401–406, 2014.

[35] Y. Wei and R. L. Brainard, Advanced Processes for 193-nm Immersion Lithography, Advanced Processes for 193-nm Immersion Lithography, The International Society for Optical Engineering, pp. 53–73, 2009.

[36] S. I. S. Shaharuddin *et al.*, "A review on the Malaysian and Indonesian batik production, challenges, and innovations in the 21st Century," *SAGE Open*, vol. 11, no. 3, pp. 1–19, 2021.

Investigative Studies on Performance Behavior on an IDI diesel engine with a Geometrically Modified Swirl Chamber using Biodiesel Blends

Manjunath S.
Shri Madhwa Vadiraja Institute of Technology and Management, Bantakal-574115, INDIA

*Ramakrishna N Hegde**
Srinivas Institute of Technology, Mangaluru-574143, INDIA
**rkhegderk@gmail.com*

ABSTRACT

In this experimental study, combustion, performance and emission characteristics of conventional swirl chamber (CSC) and geometrically modified swirl chamber (GMSC) of IDI diesel engines were studied. A GMSC was designed and fabricated in a separated engine head, for performance testing and comparison purpose. Biodiesel from chia seed oil was extracted by transesterification process and blended with diesel based on volumetric ratios of 5% to 25%, in steps of 10% increase. The performance and emission characteristics of biodiesel blends were compared with petroleum diesel using the CSC and GMSC. The result shows BTE of biodiesel blend BC05, BC15 and BC25 using the GMSC are 3.18%, 0.21% and 1.19% lesser compared to CSC 75% load. In-cylinder pressure of blends BC05, BC15 and BC25 are 66.3 bar, 59.04 bar and 54.34 bar with GMSC. BSFC of BC05, BC15 and BC25 with GMSC are 2.56%, 9.38% and 11.95% higher compared to diesel due to the low CV of biodiesel. NOx emissions for diesel, BC05, BC15 and BC25 are 9.47%, 18.41%, 6.98% and 1.67% respectively less at 75% load with GMSC compared to CSC. From the performance and emission characteristics blend B15 may be recommended as a promising substitute for petroleum diesel.

Keywords: *Swirl chamber; Biodiesel; Emission; Exergy*

ISSN 1823-5514, eISSN 2550-164X

https://doi.org/10.24191/jmeche.v20i1.21080

Received for review: 2022-04-21
Accepted for publication: 2022-10-31
Published: 2023-01-15

Nomenclature	
B05	Diesel 95% + Chia seed oil methyl ester 5%
B15	Diesel 85% + Chia seed oil methyl ester 15%
B25	Diesel 75% + Chia seed oil methyl ester 25%
BSFC	Brake-specific fuel consumption
CO	Carbon monoxide
CSC	Conventional swirl chamber
CV	Calorific value
DI	Direct injection
GMSC	Geometrically modified swirl chamber
IDI	Indirect injection
KV	Kinematic viscosity
NOx	Nitrogen oxides
P-Θ	In-cylinder pressure versus crank angle
PD	Petroleum diesel
SFC	Specific fuel consumption

Introduction

Over the past century, the Population of the entire world has increased 4.68 times and energy demand has increased exponentially pushing the world towards an energy crisis. Diesel engines are crucial prime movers used for transportation, power generation, agriculture and industries. Fast depleting petroleum products have made scientists and engineers look for alternate sources which can replace conventional fuels. Biofuels are promising unconventional energy sources near future that are capable of replacing fossil fuels. The first and second-generation biofuels were extracted from non-edible plant seeds and animal fats. Methyl esters from algae are being extracted in the third-generation biodiesel [1]-[3].

Transesterification is a process of extracting esters from oils by reacting with alcohols in presence of a catalyst. This extraction process is quite an expensive one due to the cost involved in machinery investment, raw material, chemicals and labour. A different method for the transesterification process and blending of two different biodiesel has been tried by a few researchers to reduce the overall cost [4]-[5]. The new trend of blending the two different biofuels has been tried by a few researchers. Biodiesel extracted from rice bran was blended with n-butanol and diesel on a volume basis (10+10+80% and 20+20+60%). Biodiesel blends were tested in the DI engine without any modification. CO and smoke emissions were found to be low, but, NOx emissions were reported to be high compared to diesel [6]. Another investigation was carried out wherein n-butanol was blended with Karanja methyl ester in the proportion of 5-20% with an increment of 5%. Diethyl ether was added in small portions to bring down hydrocarbon

emissions. A blend of 15% n-butanol showed low emissions and better performance [7].

Alcohols have low cetane numbers and also low lubricating properties which may cause trouble in nozzles and fuel lines. To study the effect, butanol was blended with diesel at 5%, 10% and 20% on a volume basis. NOx emissions were slightly higher and no change in HC emissions was observed [8]. To increase the cetane number, Di-tertiary-butyl peroxide was added. The blend of n-butanol (10% and 20%) was tested and compared with diesel. BSFC was marginally higher and BTE was almost the same. CO was less because of higher oxygen content, but at the same time, NOx emissions were higher [9]. Researchers have concerns about the greenhouse effect of IC engine emissions and petroleum fuel depletion. In this regard, fatty acid methyl esters were used as fuel for the IDI diesel engine in volume proportion (5% and 20%). NOx formation was found to be 15% higher than diesel [10]. In an experiment, fatty acid methyl ester transesterified from cottonseed oil was used as fuel (with a 20-50% of mass ratio) in a CI engine. The investigation outcome showed good performance with biodiesel (50% blend) and also, NOx emissions were less [11].

NOx emissions are always high with biodiesel due to high oxygen content and at the same time, IDI engines have a low NOx emission advantage over DI engines. Such combination for the experiment was carried out by using mahua methyl ester blend in IDI engine with methanol as additive. Experimental results showed a reduction in NOx by 27%, HC by 57% and CO by 20% with a methanol additive of 3% [12]. Extracting biofuels from edible oil is restricted by regulating bodies. This has led to a new approach to extracting biodiesel from waste cooking oil. In this regard, an experiment has been conducted on extracting biodiesel from waste palm oil and coconut oil which was blended with diesel (5% blend). Results showed a 0.7% and 1.2% reduction in brake power with coconut oil and palm oil, respectively [13]. Novel fuel, methyl ester extracted from waste chocolate oil was used as biofuel in an IDI engine. Properties of the chocolate oil methyl ester were found similar to that of diesel and modification was required [14].

In recent years, a lot of investigation has been conducted on the farming, harvesting and extraction of biodiesel from algae. Biofuel extraction from Dunaliella tertiolecta microalgae was done for the first time. Biodiesel blends of 10% and 20% were prepared and tested in a vertical, air-cooled DI engine. Reductions in the exhaust emissions were noticed for the B20 blend (18.28% in HC, 6.97% in NOx and 23.54% in CO) and a 3.46% increase in BSFC [15]. The search for new fuel which can replace petroleum diesel has got intensified in the last few years. A novel fuel extracted from direct sugar is used as biofuel in the IDI engine. Hydrocarbon molecules produced from sugar and yeast were processed which resulted in a high Cetane number. A blend of 50% biofuel with diesel was tested and encouraging results were

noticed [16]. From the above literature survey, it is clear that the quest for new fuel is still in progress. The experimentation to improve the mixing of hot compressed air with atomised fuel and enhance combustion efficiency is still going on. In this regard, in the present experimental study, methyl ester derived from the chia seed oil is blended with diesel and used as fuel in the IDI engine. Combustion, performance and exhaust emission characters of the original swirl chamber and geometrically modified swirl chamber of the IDI engine were studied.

Transesterification and Fuel Properties

Figure 1 shows the chia seed and chia seed oil which is golden yellow. Biodiesel extraction from the waste chia seed oil was extracted from the transesterification process.

Figure 1: Chia seed and Chia seed oil

The properties of chia seed oil methyl ester are shown in Table 1. The flash point of biodiesel was tested using the Pensky Martin flash point apparatus and kinematic viscosity (KV) was measured using a viscometer instrument with a Cannon-Fensky tube (tube no 100, direct type). The test bath temperature was kept at 40 °C for 30 minutes. The kinematic viscosity was calculated as follows.

$$KV = No\ of\ Seconds * Standard\ factor\ of\ bulb\ viscosity \quad (1)$$

where, KV of Chia seed oil methyl ester = 137 * 0.0238 = 3.26 cst

Figures 2a and 2b show the equipment for the transesterification process and biodiesel separated from impurities. During the transesterification process, a molar ratio of 1:9 for oil to methanol with

sodium hydroxide as catalyst (2% w/v) was used. Reaction time was 60 minutes with a reaction temperature of 70 °C. To remove the impurities, the products of the reaction were transferred to a separating funnel and allowed to settle for 3 hours. After impurities settle at the bottom and were drained off as shown in Figure 2b. The test samples BC05, BC15 and BC25 were prepared by blending Chia seed methyl ester with diesel having volumetric ratios of 5%, 15%, and 25% respectively.

(a) (b)

Figure 2: Biodiesel extraction process; (a) transesterification, and (b) chia seed oil methyl ester

Table 1: Comparison of fuel properties

Properties	Diesel	Chia seed oil methyl ester	Standards
Flashpoint (°C)	56	165	ASTM D93
Kinematic viscosity (cst) at 40 °C	3.05	3.26	ASTM D445
Specific gravity	0.82	0.865	ASTM D4052

Experimental Setup and Procedure

This comparative study was carried out in a naturally aspirated, single-cylinder, water-cooled, 4-S IDI engine. Fuel was injected at a pressure of 140 bar and injection timing is 18^{o} before TDC. Specification of the engine is given in Table 2 and the experimental test rig is shown in Figure 3. This compression ignition engine is coupled to a rope brake dynamometer.

Table 2: Specification of experimental test rig

Engine	IDI diesel engine
Model	12A, Topland Engines Pvt. Ltd
Type	4S, water-cooled
Combustion	Swirl chamber
Cylinders	Single
Bore x stroke (cm)	11.43 x 13.97
Swept volume (cc)	1433
Compression ratio	18:1
Power output	5.9 kW
SFC (g/kW-hr)	268

A spare engine head was procured and redesigned to install a geometrically modified swirl chamber. The diesel engine could be loaded by tightening the rope of the brake drum, and the test runs were made at 25%, 50%, 75% and 100% load (corresponding loads 9.2 kg_f, 18.4 kg_f, 27.6 kg_f and 36.8 kg_f) on the rope brake drum respectively. In-cylinder pressure was measured by using a Generic analogue pressure sensor (100 bar) and an average of 100 cycles was accounted for. All the experiments were repeated 3 times.

At first, the test engine was started at zero load condition with diesel fuel and continued running till a steady state is reached. This standard condition was maintained with all the blends throughout the experiment. Based on the CV of fuel, diesel and three biodiesel blends (B05, B15 and B25) were tested with CSC and GMSC. The readings were taken for diesel and blends at four different loads (25%, 50%, 75% and 100%).

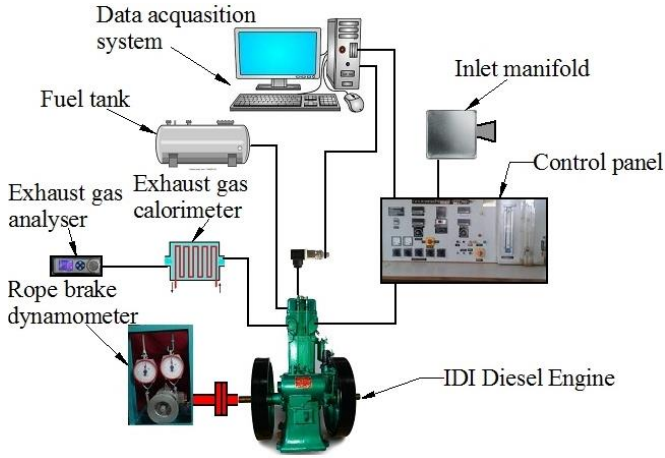

(a)

(b)

Figure 3: Schematic diagram of the experimental test rig; (a) block diagram of the experimental test rig, and (b) photographic view of the test engine

Original and geometrically modified swirl chamber

In a small high-speed diesel engine, proper mixing of the hot compressed air and fuel does not take place and the piston cup does not produce enough swirl for mixing. To overcome this problem, a separate chamber with a

spherical shape that produces turbulence and adequate mixing of fuel and air takes place during fuel injection [24].

Figure 4a shows the isometric and orthographic view of the CSC and the volume of the CSC is 74 cc. The main chamber is connected to the auxiliary chamber through nozzle. The lower injection pressure of 140 bar is sufficient to inject fuel into the swirl chamber at the closing of the compression stroke. Figure 4b shows the orthographic and 3D-modelled view of the GMSC. For the fabrication of the GMSC, the bean shape opening was cut opened by CNC vertical milling machine. A pair of crescent shape cast iron metal sections were joined by welding inside the swirl chamber. This redesigned chamber produces a twin swirl which amplifies the mixing of fuel and hot air, which consequently improves the efficiency of the combustion. In an IDI diesel engine, about 75% of compressed air is compelled to the swirl chamber in course of the compression stroke. The design of the swirl chamber is such that compressed air creates high turbulence with an opposed dual vortex pattern, which amplifies the stir of hot air and fuel. Figures 5a and 5b show the pictorial view of the CSC and GMSC with the plug opened.

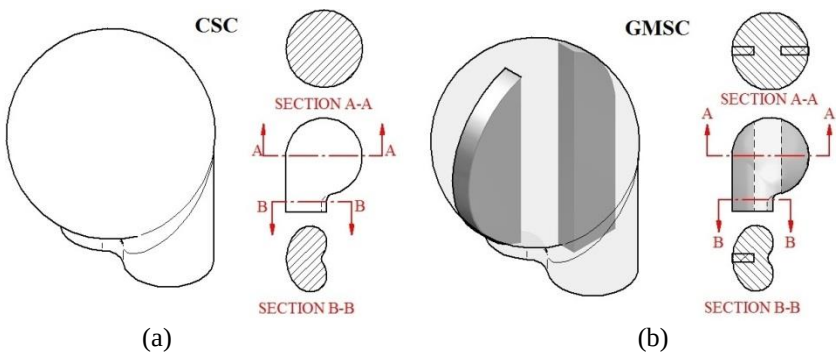

(a) (b)

Figure 4: (a) Sectional view, and (b) isometric view of the CSC and GMSC

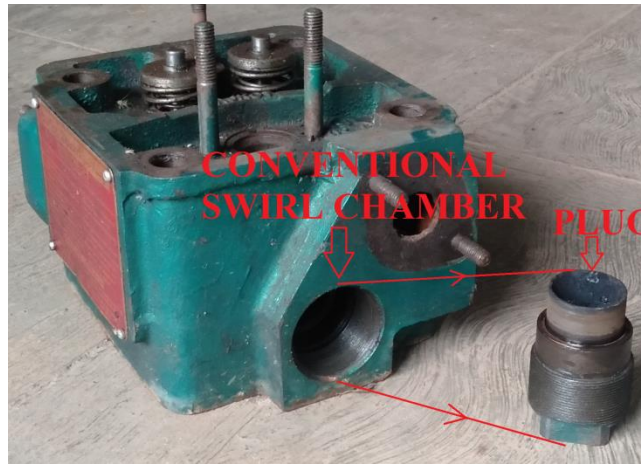

(a)

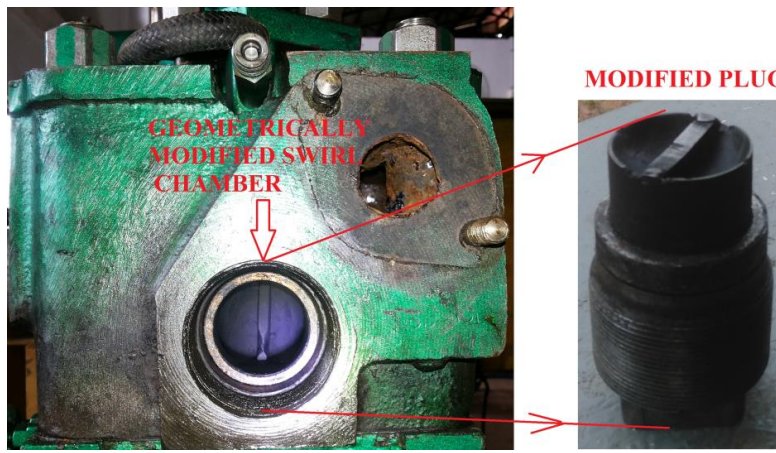

(b)

Figure 5: Pictorial view of the CSC & GMSC; (a) front view with modified plug, and (b) front view with modified plug

Uncertainty calculation

The validity of the experimental readings is obtained by the uncertainty analysis and in this experiment, the method developed by Kline and McClintock is followed to arrive at uncertainties in measured values [23]. ViniTech EFM-2000 emission gas analyzer was used to measure NO_x, CO_2 and CO.

Results and Discussion

Injection pressure and CR recommended by the manufacturer are 140 bar and 18:1 respectively for the test rig. In the first trial of experiments, operation parameters were set as per the manufacturer's recommendations. Figure 6 represents the In-cylinder pressure versus crank angle of the engine for various fuels at 75% load. In-cylinder pressure 67.54 bar and 69.11 bar were developed by diesel with CSC and GMSC respectively. It can be observed that the delay period for all fuels with GMSC is greater. This can be attributed to the hemispherical shape of the GMSC similar to the Pelton wheel bucket. Separation in the hemispherical shape divides the charge and swirl which leads to an increase in the delay period. It can be noted that with the biodiesel blends, the delay period has decreased with both CSC and GMSC due to more oxygen content in biodiesel. Similar trends were reported with blends of fatty acid methyl ester [10]. Biofuel blend B25 has developed in-cylinder pressure of 49.44 bar and 54.34 bar with CSC and GMSC respectively and it can also be noticed that ignition delay is lowest for B25. Figure 7° depicts the variations of the BFSC against load. BSFC is known as the fraction of fuel combusted in the engine cylinder to the brake power attained. At 75% load, BSFC of diesel, blends BC05, BC15 and BC25 with CSC are 0.245 kg/kW-hr, 0.241 kg/kW-hr, 0.255 kg/kW-hr and 0.261kg/kW-hr. It can be noticed that with the percentage increase in blend BSFC is rising due to low CV compared to diesel. BSFC of same fuels with GMSC are 1.6%, 2.9%, 3.5% and 2.2% higher compared to CSC. The engine was made to run from no-load to full-load with diesel fuel with CSC and GMSC. Values of BSFC are 0.2456kg/kW-hr and 0.2418kg/kW-hr for GMSC and CSC respectively which is the least value compared to a biodiesel blend. Comparing CSC with GMSC, it can be spotted that BSFC is high for GMSC with all the fuels. Partition wall in the design of GMSC is acting as an extended surface leading to more heat loss which in turn has led to a rise in BSFC value. With biodiesel samples, a shoot-up in the values of BFSC is due to low CV and high kinematic viscosity [18], [25].

Figure 7b shows the variation of the BTE versus the load. The fraction of brake power to the fuel combusted in the engine is known as BTE. The values of BTE for biodiesel blend BC05, BC15, BC25 and diesel at 75% load are 34.29%, 32.45%, 31.32% and 33.68%, respectively with CSC. With GMSC for same fuel, values are 33.23%, 32.38%, 31.7% and 34.21% respectively for the same condition. The design of the GMSC has enhanced turbulence leading to improved combustion, but due to soaring heat loss in the engine head, the BTE values of CSC are higher compared to GMSC. It can also be observed that the performance of all fuels at 75% load is maximum compared to lower part loads. This can be attributed to better mixing of air-fuel and higher efficiency. This is in a row with the outcome

obtained for various biodiesel blends i.e., BTE increases when tested for blends of biodiesel derived from trout oil and palm oil [17], [21].

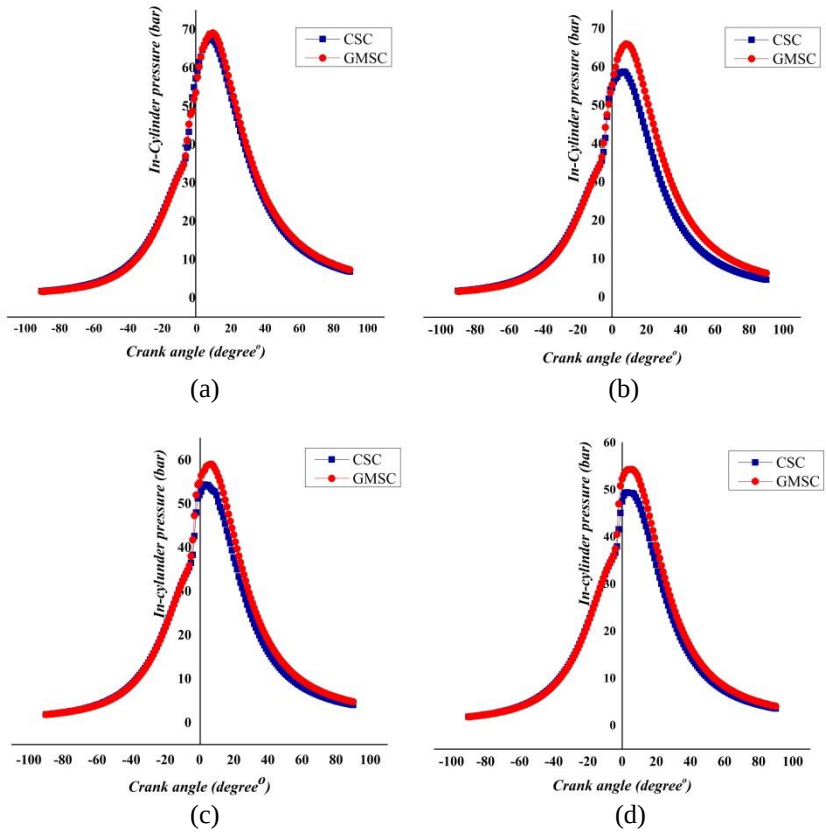

Figure 6: In-cylinder Pressure Vs Crank angle diagram for CSC and GMSC with biofuel blends at 75% load; (a) petroleum diesel, (b) biofuel blend B05, (c) biofuel blend B15, and (d) biofuel blend B25

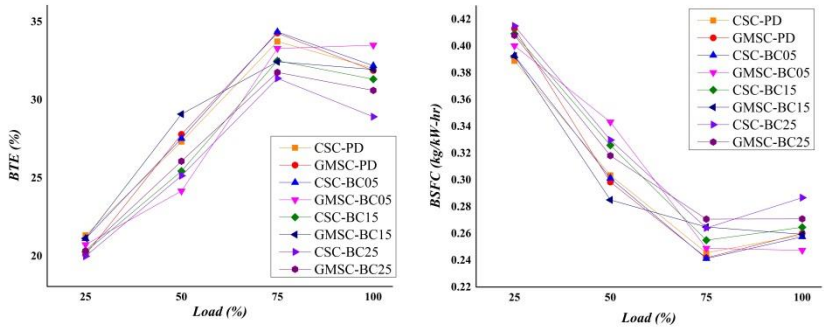

Figure 7: Performance of CSC and GMSC for biodiesel blends; (a) BTE Vs load, and (b) BSFC Vs load

It is a proven hypothesis from many investigations that, NOx formation is enhanced at elevated temperatures from a chemical reaction involving oxygen and nitrogen in the air. The high energy required for the chain reaction is supplied by the high temperature and NOx formation is triggered by the excess air. The NOx emission of CSC with biodiesel blends BC05, BC15 and BC25 and diesel fuel are 31.59 mg/Nm^3, 31.09 mg/Nm^3, 31.51 mg/Nm^3 and 36.98 mg/Nm^3 respectively. The NOx values of GMSC are 13.5%, 6.5%, 1.6% and 8.65% sequentially for same fuels. The difference in NOx emissions between diesel and biodiesel blends is excessive due to higher oxygen content. Ignition delay is highly influenced by cetane number, higher cetane number leads to less ignition delay and less time for air-fuel mixing. This results in less NOx emission due to weaker mixture formation and after burning [17], [22]. It can be noticed that CO emission is lesser for the same blend in Figure 8b and CO_2 emission is higher for the BC25 blend with GMSC in Figure 8c. Air-fuel ratio decreases as the load increases which in turn accelerates the CO emissions. This trend can be observed with diesel fuel. Oxygen content in the biodiesel blends is high which decreases the formation of CO. The combustion of diesel fuel results in the formation of CO molecules, but it will react with oxygen molecules abundantly available in biodiesel to form CO_2 [11], [13].

Figure 8a shows the variation of the NOx emission against the load and it can be noticed that, of all the blends, low NOx emission is observed for B05 with GMSC.

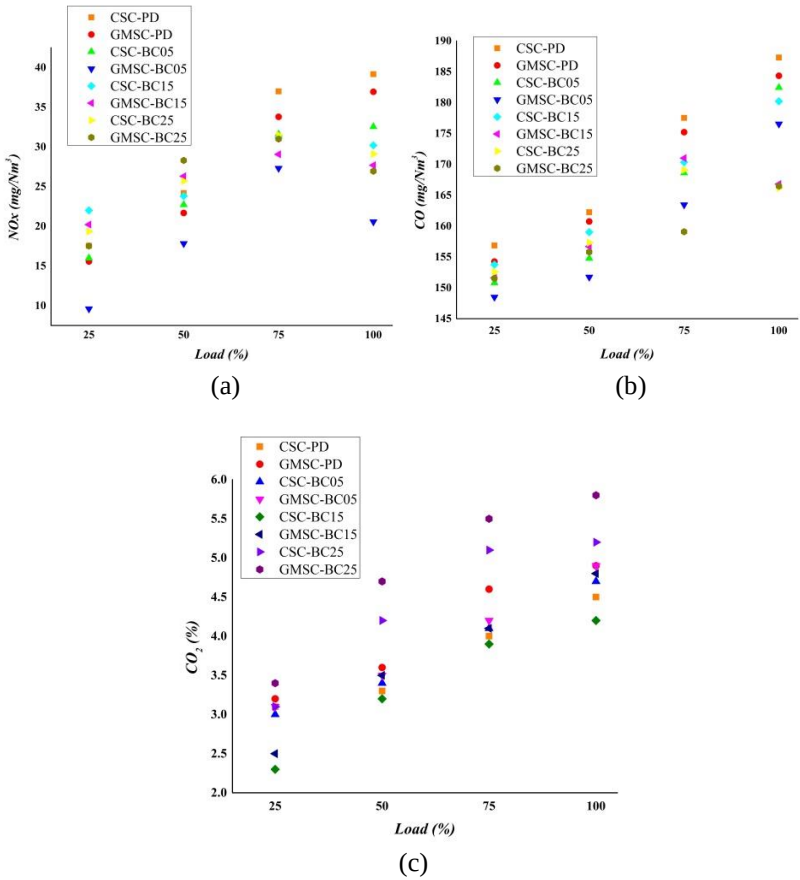

Figure 8: Emission characteristics of CSC and GMSC for biodiesel blends; (a) NOx emission Vs load, (b) CO emission Vs load, and (c) CO_2 emission Vs load

Exergy analysis

Exergy (also called availability) is the highest useful work that can be obtained from the system at a given state in a specified environment. Energy is examined on a quantity basis by utilizing the first law of thermodynamics. But the quality of energy is evaluated by the second law of thermodynamics. In an engine heat energy released by the combustion of the fuel gets converted to shaft work, and some percentage is lost to cooling water and exhaust gases. The fraction of energy that cannot be converted to useful work (losses like radiation) is called unavailability and is also accounted for in exergy analysis [18], [25].

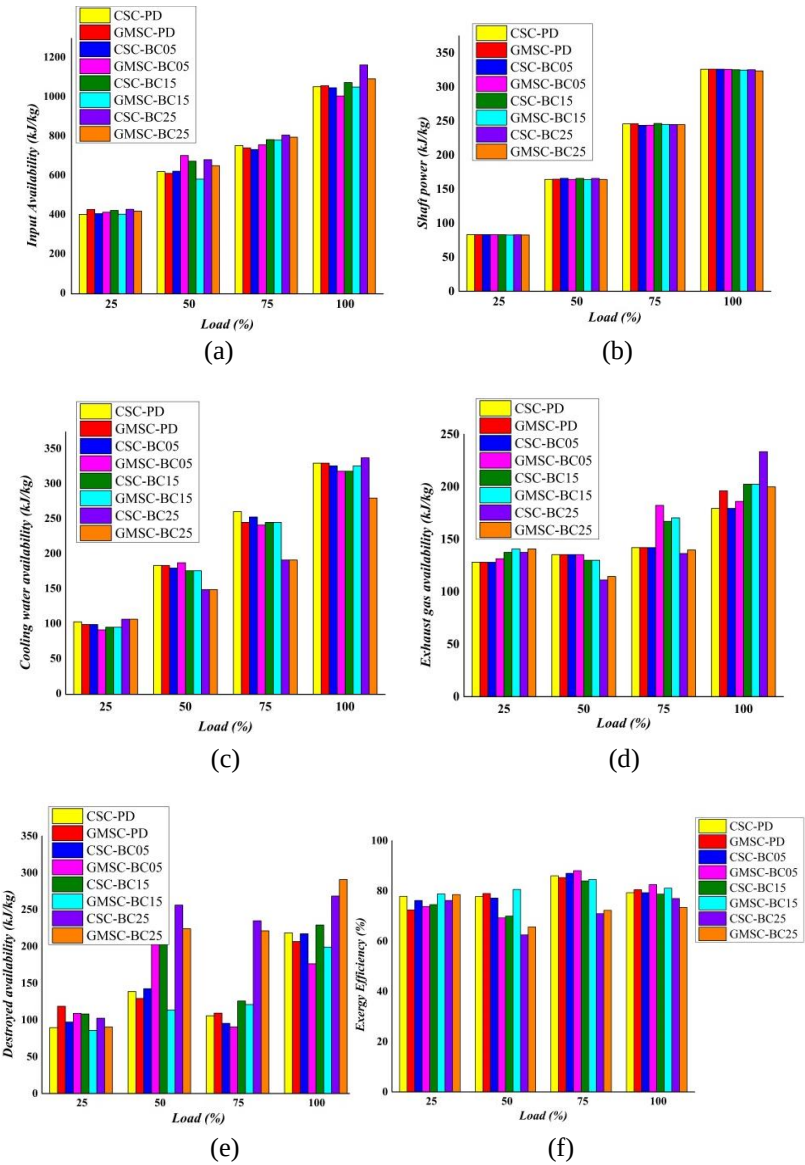

Figure 9: Exergy analysis of CSC and GMSC performance; (a) input availability Vs load, (b) shaft power Vs load, (c) cooling water availability Vs load, (d) exhaust gas availability Vs load, (e) destroyed availability Vs load, and (f) exergy efficiency Vs load

Input availability

Figures 9a shows the variation of input availability against load, a well-known fact that as the load increases, input availability also increases. To achieve the rated power, an increase in fuel consumption can be noticed. All the test fuels display an increasing tendency as the load increases. Input availability for B05, B15, B25 & diesel fuel are 1049.09 kJ/min, 1075.61 kJ/min, 1165.10 kJ/min and 1054.091 kJ/min with CSC and 1007.07 kJ/min, 1052.58 kJ/min, 1094.77 kJ/min and 1059.13 kJ/min with GMSC, respectively. A similar trend was noticed with methyl ester derived from pumpkin seed oil [18].

Shaft power availability

Part of the energy (converted useful work) available is called shaft power. Figures 9b demonstrate the contrast of shaft power availability versus load. For all the biodiesel blends, shaft power availability at lower loads is almost the same and increases with an increase in load. Diesel, B05, B15 and BC25 blends have 326.03 kJ/min, 326.06 kJ/min, 325.37 kJ/min and 325.29 kJ/min for CSC and 326.06 kJ/min, 325.84 kJ/min, 324.74 kJ/min and 323.53 kJ/min for GMSC at 100% load. Availability of shaft power increases when the maximum percentage of input power gets converted to useful mechanical work which is possible with better mixing of the air-fuel mixture, high combustion temperature and reduced delay period. Similar shaft power availability was noticed with rubber seed oil methyl ester [19].

Cooling water availability

Figure 9c shows the variation of cooling water availability versus load. It can be observed that there is an increase in circulation of cooling water with an increase in load due to the high temperature of combustion and the mass of the fuel burnt is also high. Fuel blend BC25 depicts the higher value of cooling water availability 339.21 kJ/min for CSC at full load. The engine utilizes more fuel to attain rated power for which more circulation of cooling water is required. The identical propensity of cooling water availability was spotted with Aegle marmelos oil [20].

Exhaust gas availability

Figure 9d depicts the variation of exhaust gas availability versus load. One can observe that exhaust gas availability is shooting up with the increase in load. Exhaust gas availability of 233.34 kJ/min for biofuel blend B25 with CSC can be noticed when the engine is running at 100% load. With GMSC, values of exhaust gas availability are less for all the biodiesel blends at lower loads. The combustion of part of fuel takes place in the region of controlled combustion and after the burning region [18].

Destroyed availability

Figure 9(e) shows the contrast of destroyed availability against load. At 100% load, the value of destroyed availability is 290.91 kJ/min for biodiesel blend B25 with GMSC which is highest compared to all other blends. At 75% load, there is a significant reduction in destroyed availability for blends B05 and B15 with both CSC and GMSC. It can be attributed to the maximum work output of the engine at 75% load and also values of shaft availability are high at the same load [20].

Exergy efficiency

Figure 9f depicts the contrast of exergy efficiency versus load. It can be observed that exergy efficiency is maximum at 75% load for all the blends. Exergy efficiency is 88.06% for blend B05 with GMSC which is the maximum value. At 100% load, diesel, B05, B15 and B25 have exergy efficiency of 79.28%, 79.29%, 78.7% and 76.96%, respectively with CSC and 80.49%, 82.48%, 81.09% and 73.42%, respectively with GMSC. It can be evaluated that exergy efficiency with GMSC is higher compared to CSC which can be attributed to higher turbulence, and better mixing of air-fuel leading to higher combustion efficiency. There is a deterioration of the exergy value with a decrease in load for all blends. At 25% load, the value of exergy efficiency is less for all the fuels with both CSC and GMSC due to the truant of shaft power. A similar improvement in exergy efficiency was noticed with the methyl ester of rubber seed oil [19].

Conclusion

In the current assessment, the performance and emission characteristics of GMSC were compared with the CSC (recommended by the manufacturer). Also, exergy analysis of both swirl chambers with biodiesel blends and diesel as fuel is presented. From the experimental study, it can be concluded that;

i. Comparing GMSC with CSC, the shape of GMSC is similar to the hemispherical shape and the projected surface which divides the swirl chamber of GMSC is acting as an extended surface increasing the heat loss.
ii. BSFC is 3.14% higher and BTE 2.34% lesser for biodiesel blend B05 at 75% load, due to an increase of heat loss GMSC compared to CSC.
iii. NOx and CO emissions are 6.98% and 4.22% less for blend B15 with GMSC when compared to CSC.
iv. Biodiesel blend B15 can be considered an efficient one based on the performance and emission characteristics.

Contributions of Authors

The authors confirm the equal contribution in each part of this work. All authors reviewed and approved the final version of this work.

Funding

This work received no specific grant from any funding agency.

Conflict of Interests

All authors declare that they have no conflicts of interest.

Acknowledgment

The authors would like to thank staff members of the Department of Mechanical Engineering for their wholehearted support and assistance during the conduction of the experiment.

References

[1] Sahoo, P.K. and Das, L.M., "Process optimization for biodiesel production from Jatropha, Karanja and Polanga oils," *Fuel*, vol. 88, no. 9, pp.1588-1594, 2009.

[2] Borah, M.J., Das, A., Das, V., Bhuyan, N. and Deka, D,. "Transesterification of waste cooking oil for biodiesel production catalyzed by Zn substituted waste eggshell derived CaO nanocatalyst," *Fuel*, vol. 242, pp.345-354, 2019.

[3] Nautiyal, P., Subramanian, K.A. and Dastidar, M.G., "Production and characterization of biodiesel from algae," *Fuel Processing Technology*, vol. 120, pp.79-88, 2014.

[4] Hanifa, M.A., Mushtaqa, A., Zubairb, M. and Rashidc, U., Production and Characterization of Biodiesel from Tamarind Seed Oil.

[5] Hegde, R.N. and Bantwal, J., "Characterization of Cotton Seed and Simarouba Oil Blend and Exploration of its Suitability as an Alternate Fuel for CI Engine" *Asian Journal of Engineering and Technology*, vol. *3*, no. 4, 2015.

[6] Goga, Geetesh, Bhupendra Singh Chauhan, Sunil Kumar Mahla, and Haeng Muk Cho. "Performance and emission characteristics of a diesel

engine fueled with rice bran biodiesel and n-butanol," *Energy Reports*, vol. 5, pp. 78-83, 2019.

[7] Killol, Abhijeet, Niklesh Reddy, Santosh Paruvada, and S. Murugan, "Experimental studies of a diesel engine run on biodiesel n-butanol blends," *Renewable Energy*, vol. 135, pp. 687-700, 2019.

[8] Yilmaz, Nadir, Francisco M. Vigil, Kyle Benalil, Stephen M. Davis, and Antonio Calva, "Effect of biodiesel–butanol fuel blends on emissions and performance characteristics of a diesel engine," *Fuel*, vol. 135, pp. 46-50, 2014.

[9] Zhang, Tankai, Karin Munch, and Ingemar Denbratt, "An experimental study on the use of butanol or octanol blends in a heavy-duty diesel engine," *SAE International Journal of Fuels and Lubricants*, vol. 8, no. 3, pp. 610-621, 2015.

[10] Ku, Y. Y., & Lu, J. H., "Variations in heat release rates and NO_x formation of indirect injection (IDI) diesel engine fueled with fatty acid methyl esters (FAME)," *Biofuels*, vol. *7*, no. 3, pp. 207-217, 2016.

[11] Soloiu, Valentin, Spencer Harp, Channing Watson, Martin Muinos, Sherwin Davoud, Gustavo Molina, Brian Koehler, Julia Heimberger, Marcis Jansons, and Christopher Butts, "Performance of an IDI engine fueled with fatty acid methyl esters formulated from cotton seeds oils," *SAE International Journal of Fuels and Lubricants*, vol. 8, no. 2, pp. 277-289, 2015.

[12] Rao, K. Prasada, and BV Appa Rao, "Performance and emission characteristics of an indirect diesel injection engine fueled with Mahua methyl ester and methanol as an additive," Biofuels 5, no. 4, pp. 369-378, 2014.

[13] Kalam, M. A., H. H. Masjuki, M. H. Jayed, and A. M. Liaquat, "Emission and performance characteristics of an indirect ignition diesel engine fuelled with waste cooking oil," *Energy*, vol. 36, no. 1, pp. 397-402, 2011.

[14] Haik, Yousef, Mohamed YE Selim, and Tahir Abdulrehman, "Combustion of algae oil methyl ester in an indirect injection diesel engine," *Energy* 36, no. 3, pp. 1827-1835, 2011.

[15] Tizvir, A., M. H. Shojaeefard, A. Zahedi, and G. R. Molaeimanesh, "Performance and emission characteristics of biodiesel fuel from Dunaliella tertiolecta microalgae," *Renewable Energy*, vol. 182, pp. 552-561, 2022.

[16] Hamilton, Len, Dianne Luning-Prak, Jim Cowart, Andrew McDaniel, Sherry Williams, and Richard Leung, "Direct Sugar to Hydrocarbon (DSH) fuel performance evaluation in multiple diesel engines," *SAE International Journal of Fuels and Lubricants*, vol. 7, no. 1, pp. 270-282, 2014

[17] Buyukkaya, Ekrem, Serdar Benli, Salih Karaaslan, and Metin Guru, "Effects of trout-oil methyl ester on a diesel engine performance and

emission characteristics," *Energy conversion and management*, vol. 69, pp. 41-48, 2013.

[18] Karthickeyan, V., "Effect of combustion chamber bowl geometry modification on engine performance, combustion and emission characteristics of biodiesel fuelled diesel engine with its energy and exergy analysis," Energy, vol. 176, pp. 830-852, 2019.

[19] Murugapoopathi, S., and D. Vasudevan, "Energy and exergy analysis on variable compression ratio multi-fuel engine," Journal of Thermal Analysis and Calorimetry, vol.136, no. 1, pp. 255-266, 2019.

[20] Krishnamoorthi, M., and R. Malayalamurthi, "Experimental investigation on performance, emission behaviour and exergy analysis of a variable compression ratio engine fueled with diesel-aegle marmelos oil-diethyl ether blends," Energy, vol. 128, pp. 312-328, 2017.

[21] Aditya Kolakoti, "Experimental Investigation of Palm Biodiesel on Diesel Engine Combustion Performance, cylinder head vibrations and NOx Emissions," *Journal of Mechanical Engineering*, vol. 19, no. 1, pp 273-290, 2022.

[22] Bikkavolu Joga Rao, "Effect of injection pressure on the performance and emission characteristics of Niger-Diesel-Ethanol Blends in CI engine," *Journal of Mechanical Engineering*, vol. 18, no. 3, pp 77-95, 2021.

[23] HG How, HH Masjuki, MA Kalam, and YH Teoh, "An investigation of the engine performance, emissions, and combustion characteristics of coconut biodiesel in a high-pressure common-rail diesel engine," *Energy*, vol. 69, pp 749–759, 2014.

[24] Heywood, John B. Internal Combustion Engine Fundamentals. McGraw-Hill Education, 2018.

[25] Manjunath, S., and Ramakrishna N. Hegde, "Performance, Emission, and Exergy analysis of an IDI Dual Swirl combustor Diesel engine with Blended Waste Chia seed oil as a Biofuel," *International Journal of Ambient Energy*, vol. 43, no. 1, pp. 1-35, 2022.

Shielding Cosmic Ray Muon using Copper and Aluminium Sheets Composited with Polyethylene Sheets for a Better Protection

Tayser Sumer Gaaz[1,2], Malik N. Hawas[1]*
[1]Technical College Al-Musaib, Al-Furat Al-Awsat Technical University, Babil 51009, IRAQ
[2]Faculty of Engineering and Built Environment, Universiti Kebangsaan Malaysia, Bangi 43600, MALAYSIA
**taysersumer@atu.edu.iq*

ABSTRACT

Muons are usually among the most common secondary cosmic ray particles on Earth's surface. Muon research has confirmed their occurrence in a variety of locales. It has been claimed that cosmic radiation in general, and muons in particular, have disastrous consequences on biological things and electrical components on Earth and in space. According to medical sources, cosmic rays have been linked to many ailments affecting people and other creatures. Because of these issues, cosmic ray shielding has become a crucial component of this and comparative studies. Muons emitted by cosmic rays were detected using a muon telescope made of coaxial Geiger-Muller (GM) tubes. This experiment was carried out within the muon lab of Universiti Kebangsaan Malaysia (UKM) in Malaysia to examine how the cosmic ray muon count fluctuates with the shielding of metals (Copper (Cu) and Aluminium (Al)) and polyethylene. The measured muon count for each metal sample was statistically analysed. Using both metals as shielding in this experiment revealed that adding additional Cu and Al sheets reduced the muon count. Generally, the numbers drop as the thickness increases. The results suggest that Cu outperforms Al in shielding efficacy (19% vs 16%). Because Cu has a more significant density than Al, the correlation coefficient R^2 for Cu = 0.9372 is greater than R^2 for Al = 0.6593, indicating that the trend for Cu is better than the trend for Al in this experiment. To study the shielding capabilities of the two composites, Al/PE and Cu/PE, ten sheets of Polyethylene (PE) were gradually put individually between the Al and Cu

ISSN 1823-5514, eISSN 2550-164X

https://doi.org/10.24191/jmeche.v20i1.21081

Received for review: 2022-08-19
Accepted for publication: 2022-11-09
Published: 2023-01-15

sheets. The results showed that PE sheets slightly increased cosmic ray shielding.

Keywords: *Muon, Cosmic ray, Copper, Aluminium, Polyethylene*

Introduction

The scope of the risks associated with the health, safety, and performance of crews exposed to ionizing radiation during space flight have been identified previously [1]. A lepton is a fundamental constituent and primary particle of the matter [2]. Electron, proton, and neutron are the essential components of atom. The preferable recognized of all leptons is the electron that governs nearly all chemistry that tied to the chemical characteristics [3]. The primary generation is the electronic (e^-) leptons. The e-lepton first compromises the (e^-) and electron neutrinos (ν_e). Moreover, the muonic leptons compromise muons (μ^-) and muon neutrinos (ν_μ). The third lepton is the tauonic leptons which compromises taus (τ^-) and tau neutrinos (ν_τ). For all leptons flavour, there is a corresponding kind of anti-particle, recognized as anti-lepton, that is different from the lepton in its characteristics; however, it has equal magnitude but opposite sign. According to certain theories, neutrinos may be their own anti-particle, but it was theorized in the mid-19th century [4]-[8] and was find out in 1897 by Thomson [9]. The second lepton to be shown was the muon, found out through Stone [10], but it was erroneously categorized as a meson at the time [10]. After investigations, it was understood that the muon did not have the expected characteristics of a meson but rather behaved like an electron, only with a higher mass. It was until 1947, leptons were considered as a part of the family of charged particles. The first neutrino, the electron neutrino, was suggested by Jung [11] to demonstrate certain properties of beta decay as shown by the Cowan-Reines neutrino experiment that was carried out by Reines et al. [12]. The muon neutrino was discovered by Danby et al. [13] in 1962 while the tau discovery was between 1974 and 1977 by Perl [14]. The tau neutrino remained elusive until July 2000, when the donut collaboration from Ericson announced its discovery [15]-[16]. Leptons are a significant part of the Standard Model. Instead of electrons, exotic atoms with muons and taus could be synthesized along with lepton–antilepton particles such as positronium. The Geiger-Muller (GM) tube was used as a radiation counter in 1908 at Manchester University by Hans Geiger and Ernest Marsden and later improved by Walther Muller [17]. This study aims at detecting cosmic ray muons event at ground level at UKM using a muon telescope of coaxial GM tubes; to observe the count rate of muons at ground level through the shielding layer of Copper (Cu) and Aluminium (Al); and to determine the

attenuation coefficient when there is the exponential decay rate of muon due to the increases of shielding thickness.

The shielding process is not limited to a metal sheet such as Cu or Al; it can also be done using sheets of polymers of different thicknesses. In this report, the focus on the particular importance of polyethylene (PE) as reference material for laboratory tests of shielding materials was also carried out. PE, the most widely produced plastic in the world, is a thermoplastic polymer with a variable crystalline structure and a vast range of applications. It is one of with tens of millions of tons produced worldwide each year. PE can be found either with High-Density Polyethylene (HDPE) or Low-Density Polyethylene (LDPE), where HDPE has more applications than LDPE Laurenzi et al. [18]. The chemical structure of PE is shown in Figure 1. The two hydrogen atoms are highly effective and one carbon atom per molecule (CH_2) [19]. PE is readily available, non-toxic, and chemically stable under typical conditions, making it a convenient reference material for shielding tests at heavy-ion accelerators.

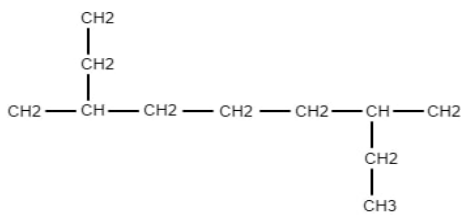

Figure 1: The structure of PE [19]

The current study discusses one of the most important topics concerning the health hazards caused by cosmic radiation. Previous studies have focused on using inorganic materials such as aluminum and copper as muon-stopping materials. The authors have separately added polyethylene with aluminum or copper as organic material in the current study. The results showed an increase in the performance of composite aluminum/polyethylene and copper/polyethylene in cosmic stopping materials. The study adds an essential piece of knowledge that plays a vital role in avoiding the consequences of cosmic radiation.

Theoretical Approach

The cosmic-ray muon's source known as a cosmic-ray proton is resulted at the surface of the earth caused by the cosmic-ray muon's source which is originated from deep-space supernova remnants [20]. As the protons arrive at the atmospheric earth, they produce hadronic showers caused by the highly

energetic cosmic-ray proton interacting with atmospheric nuclei forming secondary particles, including hadrons and mesons. The delta resonance of this interaction is responsible for most of the pion production in the atmosphere. A high energy cosmic-ray proton interacts with a nucleon in the atmosphere producing a delta baryon, Δ, and residual nucleus, N, as shown in Equation (1) [21]:

$$p+N=\Delta+N \tag{1}$$

As a result of delta resonance, the group of $\Delta^-, \Delta^0, \Delta^+,$ and Δ^{++} is produced where $\Delta^- \rightarrow n + \pi^-$ and $\Delta^{++} \rightarrow p + \pi^+$, with $\pi^- \rightarrow \mu^- + \bar{\nu_\mu}$, $\pi^+ \rightarrow \mu^+ + \nu_\mu$, and $\pi^0 \rightarrow \gamma + \gamma$.

At altitude of nearly 15 km, the cosmic-ray muons originate and pass through the atmosphere losing about 2 GeV due to ionization [22]. The cosmic rays reach the earth's surface with the energy of ~3-4 GeV and slow down due to interaction and decaying. Upon decay of the cosmic-ray muon, an electron (or positron) and two neutrinos are emitted as described in Equation (2) [18]:

$$\mu^- \rightarrow e^- + \bar{\nu_e} + \nu_\mu, \text{ and} \quad \mu^+ \rightarrow e^+ + \bar{\nu_\mu} + \nu_e \tag{2}$$

Reyna model

Reyna, [23] has proposed a model ($\Phi_R(p,\theta)$) to extend the vertical sea-level model that estimated the differential flux to all zenith angles (θ) of Bugaev's original model ($\Phi_B(pcos\theta)$). Reyna verified the new model using experimental data analysis of sea-level muons. The Reyna model has shown that there was no significant difference between multiplying the flux by $\cos^3(\theta)$ or $p * \cos(\theta)$. Based on this finding, Reyna model proposed using momentum ($p * \cos(\theta)$) instead of the coefficient $\cos^3(\theta)$, where $0 \leq \theta \leq 90$ and p lies between 1 GeV and 2000/cosθ, as shown in Equation (3) [20]:

$$\Phi_R(p,\theta) = \cos^3(\theta)\, \Phi_B(p\cos\theta) \tag{3}$$

The momentum distribution of $\Phi_R(p,\theta)$ represents the muon distribution at the surface of earth.

Mechanism of Muon energy

The essential foundation of cosmic-ray muon energy loss mechanisms depends on the ionization and radiative processes where the binding energy is considered to identify the energy loss. Critical energy is the amount of energy loss between ionization and radiative processes. For cosmic-ray muons, the average energy of the cosmic-ray muon spectrum is ~3-4 GeV. For muons,

energy could demonstrate total energy loss in a material. The range of achieving total energy loss of muon stopping criteria may occur within the order of meters for a cosmic-ray muon with an average energy of 4 GeV. This penetrative power of muons enabled the actual uses of cosmic-ray muons to measure pyramids and mine shafts.

The roles of materials in cosmic radiation

Muons are low-energy particles, yet they may be a source of radioactive background due to capture processes in certain materials. The employment of inorganic materials, such as copper and aluminium, and organic materials, such as polyethylene, as stopping materials is crucial for protecting those who operate close to a cosmic ray environment. The use of plastic track detectors to quantify the ratio between the vertical and horizontal components of the flux of deficient energy terrestrial muons at ground level [24].

The uncontrolled interaction of biological and nonbiological substances is one of the broad issues of space radiation. As a result, the safety of biological beings has become a significant concern and developing shields according to the ALARA principle is needed. Therefore, the availability of the data to space stations might make cosmic radiation safe for the community of aerospace engineers. From a materialistic perspective, shielding is a procedure that requires several materials with distinct properties. Such materials are mostly unavailable now; nevertheless, researchers are experimenting with polymer and inorganic material composites to attain this objective. The rationale for utilising composite materials is to minimise, to some extent, secondary neutron generation in order to reduce radiation produced by neutrons [25].

In another research, the effects of cosmic radiation were analysed in detail, exposing the difficulties engineers face when coping with this radiation during space travel [26]. In addition to this peril, humans on earth face a similar, albeit less severe, issue brought about by cosmic radiation. Microsatellites and other unscrewed spacecraft may be vulnerable to the effects of cosmic radiation on their electronics and varied materials. This conclusion opens the door to the requirement of employing spaceship-covering materials or materials used to manufacture electronic equipment such as transistors and processors. In this way, the fibre may be appropriate for reaching this objective [26].

A variety of organisations have conducted research into long-term effects on astronauts. Proton exposure alters the function of neurons and microglia, resulting in cognitive impairment [27]. Other studies have suggested that the central nervous system may be damaged [28] and that muscular movement may be disturbed [28]. In response to galactic cosmic irradiation, Almeida-Porada et al. [29] found DNA damage and alterations in human hematopoietic stem cells [29]. Since it is more challenging to repair

complex DNA damage caused by HZE irradiation, it is likely to cause substantial issues [30]. Other health concerns include carcinogenesis, which has been studied extensively in animal studies, with results revealing that HZE particles cause more aggressive cancers. In contrast, long-term exposure to gamma or X rays has shown much lower risks of carcinogenesis than acute exposure [31].

Data analysis

The cosmic ray muon data analysis is performed using Excel or MATLAB. Data analysis can be divided into two stages: separation thickness analysis and angle observation analysis. Excel was used to analyse the preliminary data for the different separation counts of cosmic ray muon and the different thicknesses of Cu sheets, Al sheets, and PE. Descriptive statistics were used to analyse muon data. The descriptive statistical parameters are used to consolidate a large amount of information which contains minimum, maximum, median, mode, average, range, standard deviation, coefficient of variation, skewness, and kurtosis.

Descriptive statistics

In this research the descriptive statistical parameters of average, minimum, maximum, median, standard deviation, mode, range, coefficient of variation, skewness and kurtosis were used to analyse the data according to a set of numbers $x_1, x_2, x_3, \dots, x_{20}, x_n$, where n is the total number of the samples. The estimation of the values of the descriptive statistical parameters are performed by measuring the maximum value (x_{max}), then, the minimum value (x_{min}), followed by the range value (R_x) using $R_x = x_{max} - x_{min}$, then, the median value (x_{mid}), followed by the mode value, and the average value ($\bar{x}$) according to the following equation $\bar{x} = \frac{\sum_{i=1}^{n} x_i}{n}$, and the standard deviation (S_x), and the coefficient of variation (C_v), and finally the standard error (S_e).

Other measurements of the descriptive statistics include the skewness value, which measures the symmetry of the data distribution (positive, negative, or zero) and the kurtosis value, which measures whether the data are peaked or flat relative to a normal distribution. Data sets with high kurtosis tend to have a distinct peak near the mean. The kurtosis for a standard normal distribution is three.

The linear regression equation

When muon passes through a sheet as a charged particle, the number of the particles is reduced by the sheet layers due to absorption of these particles. The change of muon counts with the shielding thickness results in calculating the correlation coefficient and the absorption (attenuation) coefficient (μ) of the Cu, Al, or PE sheets. Linear regression used to determine the relationship

between two variables such as x and y using linear equation: $y = mx + c$, where c is the intercept on the y-axis, and m is the slope. To explain the trend line using the basic linear regression equation and the value of R^2 as explained by [32]. The two error types (small and large) of prediction for a point are a value minus the predicted value (the value on the line). Then we can calculate m, c, and their standard error of Δm, and Δc. The value of R^2 (between 0 and 1.0) is the correlation coefficient (or coefficient of determination) measures the strength of the relationship between the variables or statistically shows closeness between the data are to the fitted regression line.

Materials and Method

Materials

The equipment used in this research consists of the RM60 radiation monitor, coincidence box (C-box), LCD-60 display module, and muon telescope. Concerning the addition complimentary materials, three sheet materials of Cu and Al of impurity 99.9% for each, and sheets of polyethylene. All sheets were available locally in the lab.

Radiation monitor (RM-60)

The radiation monitor used in this experiment is RM-60 manufacture by Aware Electronics (www.aw-el.com). It is a highly sensitive and easy to use Geiger counter that can continuously record natural background radiation, and low levels radiation from building materials. The RM-60 can detect all types of radiation emitted by radioactive elements such as alpha, gamma, or X-ray radiation. It is also used to detect the cosmic ray muons. Figure 2 shows the radiation monitor RM-60.

(a) (b)

Figure 2: the appearance of RM-60 radiation monitoring system; (a) outside, and (b) inside where a LND712 Geiger-Muller (GM) tube

The window of the GM tube Figure 3 has an areal density that varies from 1.5 to 2.0 mg/cm^2, effective diameter D of 9.14 mm and effective area of 65.61 mm^2. The wall of the radiation monitor has a thickness of 0.381 mm, and effective length L of 38.1 mm. The distances of the GM tubes from the radiation monitor box upper and lower edges are 0.9 cm and 0.5 cm. The power supply of the RM60 radiation monitor is a 9 V battery. Figure 3 shows the LND712 GM tube produced by LND Inc (www.lndinc.com).

Figure 3: The LND 712 GM tube used in the RM-60 radiation monitor

Coincidence Box (CB)

CB is used to detect simultaneous events in GM tubes. The box's output sends an impulse to an external counter, when two (or optionally three) of the inputs receive an impulse simultaneously (i.e. within 1 microsecond). CB detects the radiation cascade whether it is caused by Co-60 or the cosmic ray. CB connects to two or three single GM tubes. The output impulses are registered by a GM counter 513600, counter 200250 or via a Pasco digital adapter PS-2159.

The coincidence box (CB-box) manufactured by Aware Electronic (www.aw-el.com) is used to give out a signal when the two radiation monitors register simultaneous radiation events as shown in Figure 4. It is connected to the two RM-60 radiation monitors by RJ-45 telephone cables (Figure 4a). The schematic diagram of the coincidence box where RM1 and RM2 are the two RM-60s radiation monitors producing the two radiation events of RE1 and RE2, the RE1 and RE2 is the radiation output connected to coincidence box CB and the coincident event produced a muon event ME connected to LCD-60 display module as shown in Figure 4b.

LCD-60 display module

The LCD-60 (powered by a 9-V battery) display module produced by Aware Electronics (www.aw-el.com) is used to display the output signal of the coincidence box to indicate a cosmic ray muon event. The LCD-60 used to display the count of cosmic ray muon events within a time period. It has two-digit readouts, one show counts per minute or counts per second and the other displays total counts. It is often useful to have the ability to separate the

readout from the sensor unit with the snap in telephone wire. Figures 5a and 5b show the LCD-60 display module.

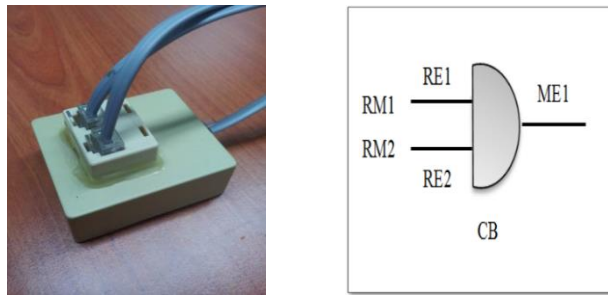

(a) (b)

Figure 4: (a) Coincidence box, and (b) schematic diagram of the coincidence box

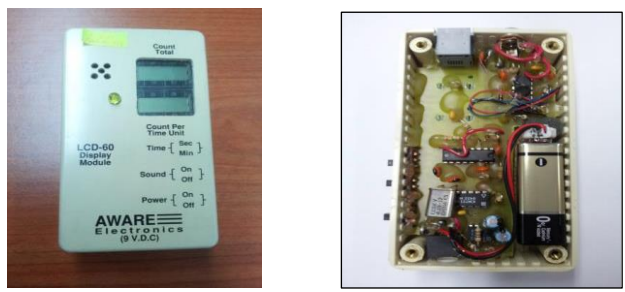

(a) (b)

Figure 5: The LCD-60 display module from; (a) outside, and (b) inside

Housing box

A housing box was fabricated to hold the MT telescope and metal sheets, as shown in Figure 6. The housing box is made of Perspex plastic with dimension 30 x 60 x 30 cm. The MT telescope is placed inside the housing box and the metal sheets are placed at the top of the housing box. The housing box is strong enough to carry the weight of the metal sheets.

Copper, aluminium, and polyethylene sheets

Sheets of the metals of Cu, Al and PE sheets are used as the absorber or shielding material in this study as shown in Figures 7a, 7b, and 7c. There are 14 copper sheets of dimension 20 x 20 x 0.12 cm and 6 sheets of dimension 20 x 20 x 0.2 cm. For Al, 20 sheets of dimension 20 x 20 x 0.12 cm. In

addition, there are 20 PE sheets with dimensions of 20 x 20 x 0.1 cm. Table 1 summarizes the physical properties of the three used sheets.

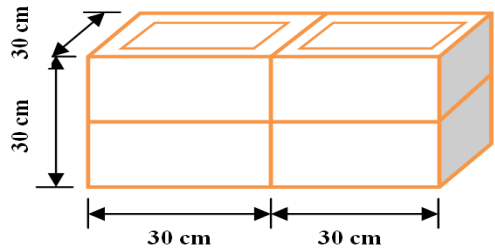

Figure 6: Dimensions of the housing box

Table 1: The physical properties of the Cu, Al, and PE sheets

Property	Cu	Al	PE
Density (g/cm^3)	8.9	2.71	0.91
Melting Temperature (℃)	1083	660	110
Thermal Conductivity (W/mK)	390	226	0.4
Thermal Expansion (1/℃)*10^{-6}	17	24	100-126
Specific Heat Capacity (kg.℃)	385	946	1550
Dimensions (cm)	20 x 20 x 0.12	20 x 20 x 0.20	20 x 20 x 0.10

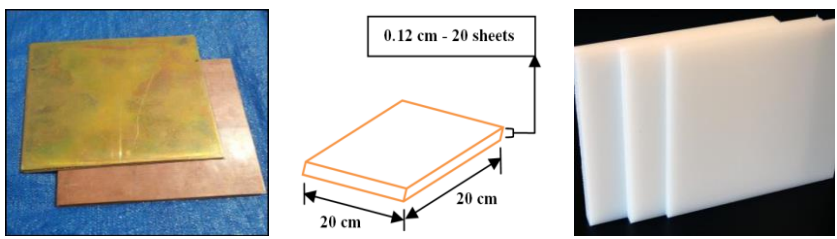

(a) (b) (c)

Figure 7: The sheets used (a) Cu sheet, (b) Al sheet, and (c) PE sheet

Muon telescope

Cosmic ray muon telescope (MT) is used to detect muon events or coincidence. The coincidence means that the radiation events occur simultaneously in both RM60s determined by a coincidence box (CB-box). Two of the RM60 radiation monitor units are stacked on top of each other making a cosmic ray MT, which can be connected to an LCD-60 display module. The measurements are performed with a smaller solid angle $\Delta\Omega$. The smallest angle is better defined, suggesting that the smaller $\Omega(\theta)$ is better for the arrival direction of the cosmic ray muon. Figure 8 shows a schematic

diagram of the cosmic ray muon telescope comprising of two RM-60 that were stacked together (coaxially) with no separation between the two GM tubes.

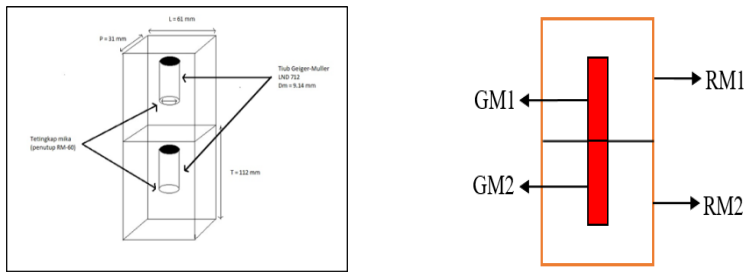

(a) (b)

Figure 8: The schematic diagram of a cosmic ray muon telescope; (a) front view, and (b) side view

Measurement Method

The experiment set up

This study was designed to detect the effect of Cu sheet, Al sheet, and PE sheets on shielding cosmic ray muon event rate at ground level using an MT which consists of two RM-60 radiation monitors. The monitor contains two coaxially GM tubes with no separation. The muon telescopes were pointed coaxially, i.e., at the zenith angle of θ = 0º. The two RM-60 radiation monitors connected to a coincidence box (CB) to determine the radiation events that occur simultaneously in both RM-60s. CB is connected to the LCD-60 display module where the counts recorded appear on it. The MT is placed inside a housing box and the metal sheets are placed at the top of the housing box. Figure 9a shows the diagram of the experimental set up while Figure 9b shows the schematic diagram of the experiment set up. The setup consists of RM1, RM2, RM60, two GM tubes (GM1 and GM2). The experimental setting produces two radiation events of RE1 and RE2, where both are connecting to the radiation output to coincidence box CB where the coincidence event produced a muon event.

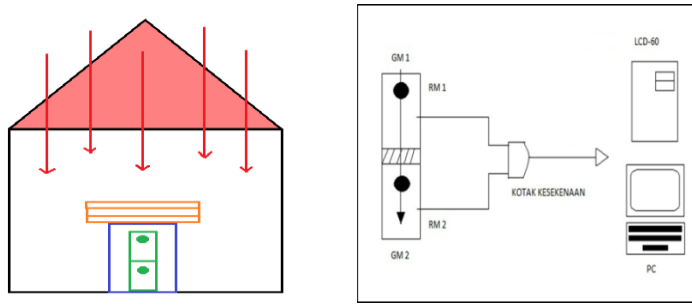

(a) (b)

Figure 9: (a) Geometric diagram of the experiment set up, and (b) schematic diagram of the experiment set up

The experiment procedure

The experiment is divided into two similar parts in terms of methodology and location. However, the two parts are different in the material used. Previous studies on ground level muon at UKM were performed either inside the physics building which contains walls, ceilings, and roof shielding [33] or in the open area on the third floor of the physics building [34]. This experiment was performed to measure the cosmic ray muon inside and the third floor of the physics building. The first part is called the external experiment that was designed to detect the effect of various sheets of aluminium on cosmic ray muon at ground level (inside). The second part is the internal experiment that was designed to detect the effect of sheets of Cu and PE on cosmic ray muon at ground level inside the muon lab (room no. 3113). Figure 10 shows the muon telescope MT experiment set up inside the building.

Figure 10: Two sets of MT experiment set up (2 metals simultaneous Cu and Al) inside the building)

Measurement of density of Cu and Al sheets

There are 11 sheets of Al of dimension 20 x 20 x 0.12 cm and 11 sheets of Cu of dimension 20 x 20 x 0.2 cm and 10 sheets of PE of dimension 20 x 20 x 0.10 cm. The measurement of density of Cu and Al sheets is to verify the impurity of the Cu and Al sheets to compare it with the standard values of the pure Cu and Al sheets. Table 2 shows the mathematical values of the density ρ (mass/volume) (kg/m^3) of Cu and Al sheets. Figure 11 shows the density (ρ) (mass/volume) (kg/m^3) of Cu and Al sheets as a function of the number of layers.

Table 2: The experimental values of mass, volume and density of Cu and Al sheets

No. layers	Mass (m) (kg)		Volume (V) (m^3)	
	Cu	Al	Cu	Al
2	1.00	0.42	0.000104	0.00016
4	1.93	0.83	0.000208	0.00032
6	2.92	1.29	0.000312	0.00048
8	3.90	1.70	0.000416	0.00064
10	4.82	2.10	0.00052	0.0008

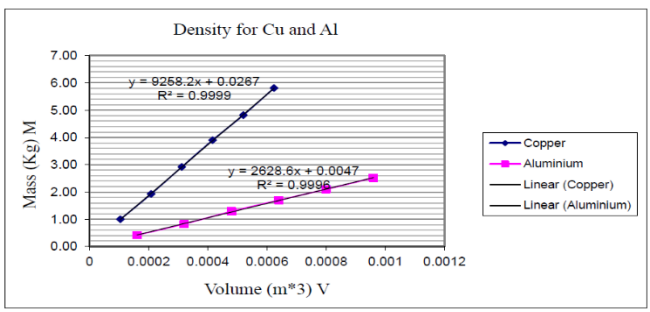

Figure 11: The mass of metal versus the volume of metal

From the graph, the density of Cu and Al sheets are 9258 ± 26 kg m^{-3} and of 2628 ± 4 kg m^{-3}, respectively. The results are very close to the reported results of Cu ≈ 9.3 g/m^3 and Al ≈ 2.6 g/m^3. The standard values for the density of pure Cu and Al sheets are ρ for (Cu = 8.96 g/m^3) and ρ for (Al = 2.70 g/m^3).

Measurement of Muon events

The muon counts through metal sheets were studied with different sheets of Al and Cu sheets separately. A single sheet was tested first (0 layers), and then the number was increased by another sheet to form the first layer. The

process continued until reaching 11 sheets which represent ten layers. The exact process was repeated to the Al sheets. The second part of the experiment was performed by adding 10 PE sheets gradually until using all PE sheets. Two experiments were performed: one for Al and another for Cu sheets.

An internal experiment to observe the muon event rate on metal layers has been conducted and measured from August to November 2021 on all sheets of Cu and Al of dimension 20 × 20 cm with 11 samplings set for each metal with a sampling period overnight (≥ 24 hours) per count inside the building at muon lab. This experiment was done inside the muon lab overnight to determine the muon event at ground level for a longer time and with more shielding (the more shielding is the concrete of the muon lab ceiling and walls). All experiments were done in the exact location and within the same period of two months. The muon telescope was pointed at the vertical direction, where $\theta = 0°$ under defining the size of the detector (RM-60s) as the solid angle of the telescope.

Result and Discussion

Muon telescope performance test unit

Ten observations of muon were performed using two muon telescopes simultaneously by placing a coaxially 2-radiation monitor with no spacer. Performance testing was conducted to test the observed ability of both muon telescopes. This test is essential because both units are used simultaneously on different material thicknesses. Table 3 explains the two-set observations of the muon telescope.

Table 3: The performance of the two sets of observations of the test muon telescope

Observations	Set A	Set B	Observations	Set A	Set B
1	35	35	6	52	56
2	152	145	7	56	58
3	35	64	8	43	57
4	53	45	9	53	47
5	50	44	10	57	59

Set A and B to consist of radiation monitoring equipment, the coincident, and the display module. Table 4 shows the observed data with a sampling period of 24 hours without shielding material placed above the muon telescope. Paired t-test was performed to test both the muon telescopes. Based on Table 3, the value obtained was 0.60, which is greater than the alpha value set to 0.10. In conclusion, there is no difference in the

mediator between the two muon telescopes used. Therefore, the two muon telescopes have the same performance.

Table 4: Two-sample t-test of paired for min

	Set A	Set B
The mean	2.066	2.152
Variance	0.082	0.098
Observation	10	10
Pearson correlation	-0.414	-0.405
Hypothesis distinction the mean	0	0
Degree of Freedom	9	9
t Stat	-0.537	-0.502
p $(t \leq 1)$ one end of	0.302	0.297
t critical one end of	1.833	1.785
p $(t \leq 1)$ two-end	0.604	0.589
Critical two-tailed t	2.262	2.198

Al and Al/PE sheets

The observations of muon events with 11 Al sheets of dimension 20 x 20 x 0.12 cm from August to November 2019 are reported in Table 5 where I is the number of samplings, NL is the number of layers, N is the muon count and the time is the sampling time. The same experiments were repeated with sandwiching 10 PE sheets to make with Al sheet 10 layers. The sampling time is the time of exposing the layers to cosmic rays and N is the number of GM tube ionization events.

The rate of counts () in the table above are shown graphically in Figures 12a and 12b for Al sheets and Al/PE sheets, respectively. From Equation (4) and Equation (5), the shield caused was 17% and 19% for the Al sheets and Al/PE sheets, and the coefficient of determination (R^2) at 0.6593 and 0.8717, respectively. The values of the coefficients are accepted. The effect of Al ($\rho = 2.71$ g/cm^3 on the muon shielding is described by Equation (4) which states that the muon radiation decreases at rate of about 22% due to inserting 11 sheets whose total thickness is 1.32 cm. The shielding result is lower than the recent study which was found at about 33% [35]. The variance can be attributed to the method used in detecting the cosmic ray and to timing, location, and the instrument used.

$$R = -0.1685 * x + 2.422 \text{ and } R^2 = 0.6593 \quad (4)$$

and;

$$R = -0.1926 * x + 2.2853 \text{ and } R^2 = 0.8717 \quad (5)$$

The calculated by N/h are shown in (a).

Table 5: Muon sampling for 10 layers of Al and Al/PE sheets

Al					
I	NL	x(cm)	Sampling Time (s)	N	N/h
1	0	0.12	79200	54	2.45
2	1	0.24	86400	56	2.33
3	2	0.36	79200	53	2.41
4	3	0.48	90000	55	2.20
5	4	0.60	86400	57	2.38
6	5	0.72	86400	55	2.29
7	6	0.84	88200	55	2.24
8	7	0.96	72000	44	2.20
9	8	1.08	81900	53	2.33
10	9	1.20	86400	53	2.21
11	10	1.32	86400	49	2.04
Al/PE					
I	NL	X (cm)	Sampling Time (s)	N	N/h
1	0	0.22	81600	54	2.29
2	1	0.44	83700	56	2.11
3	2	0.66	79500	53	2.17
4	3	0.88	82500	55	2.09
5	4	1.10	88500	57	2.16
6	5	1.32	91300	55	2.01
7	6	1.54	88400	55	2.04
8	7	1.76	87600	45	1.89
9	8	1.98	92600	52	1.87
10	9	2.20	93400	53	1.85
11	10	2.32	95700	49	1.77

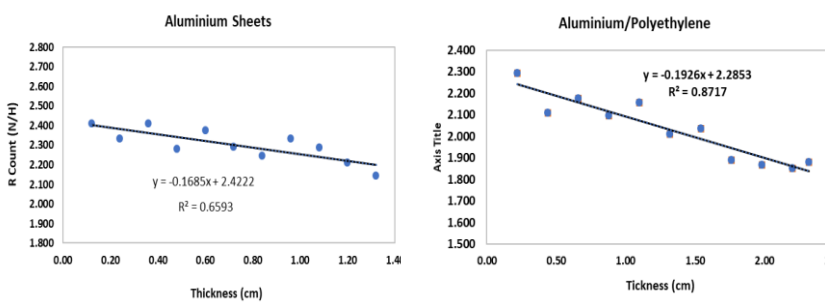

(a) (b)

Figure 12: The effect of; (a) Al sheet, and (b) Al/PE on shield of muon

Cu and Cu/PE Sheets

The observations of muon events with 11 Cu sheets of dimension 20 x 20 x 0.20 cm from August to November 2021 are reported in Table 6 where I is the number of samplings, NL is the number of layers, N is the muon count and the time is the sampling time. The same experiments were repeated with sandwiching ten PE sheets to make with Al sheet ten layers. The sampling time is the time of exposing the layers to cosmic rays and *N* is the number of GM tube ionization events.

The rate of counts (R) in the table above are shown graphically in Figure 13a and 13b for Cu sheets and for Cu/PE sheets, respectively. From Equation (6) and Equation (7), the shield caused was 20% and 21% for the Cu sheets and Cu/PE sheets, respectively. In addition, Equation (6) and Equation (7) show that the coefficient of determination (R^2) is 0.9372 and 0.9382, respectively. The values of the coefficients are very high. The effect of Cu ($\rho = 8.96$ g/cm^3 on the muon shielding is described by Equation (6) which states that the muon radiation decreases at rate of about 20% due to inserting 11 sheets whose total thickness is 2.20 cm. The shielding behaviour of Cu is similar to the conclusion of the work of DeWitt and Benton [25]; however, there was no figure is available.

$$R = -0.2003 * x + 2.6827 \quad \text{and } R^2 = 0.9372 \tag{6}$$

and;

$$R = -0.2099 * x + 2.6813 \quad and\, R^2 = 0.9382 \tag{7}$$

It can be noticed from Table 1 that the value of the correlation coefficient for copper is greater than that for Al ($R^2 = 0.9372 > R^2 = 0.6693$) due the fact that Cu is much denser than Al. This result agrees with the statistical approach performed by Altameemi and Gopir [36]. However, the most controversial result was that the shielding trends in the experiment performed by Altameemi and Gopir [36] has shown that the shielding increased for both Cu and Al which violates the logical trend of the shielding. For this reason, the conclusion that was adopted by Altameemi and Gopir [36] which states that "the Cu and Al are not suitable as shielding materials for cosmic ray muons" was seemingly based on the wrong assumption and wrong calculation.

Table 6: Muon sampling for 10 layers of Cu and Cu/PE sheets

Cu					
I	NL	X(cm)	Sampling time (s)	N	N/h
1	0	0.20	75800	55	2.61
2	1	0.40	81300	60	2.66
3	2	0.60	82300	58	2.54
4	3	0.80	85400	61	2.57
5	4	1.00	86400	59	2.46
6	5	1.20	85400	58	2.44
7	6	1.40	82700	55	2.39
8	7	1.60	76500	49	2.31
9	8	1.80	82400	53	2.32
10	9	2.00	87400	56	2.31
11	10	2.20	87500	55	2.26
Cu/PE					
I	NL	X(cm)	Sampling Time (s)	N	N/h
1	0	0.30	73400	54	2.65
2	1	0.60	73500	53	2.60
3	2	0.90	75200	53	2.54
4	3	1.20	77400	51	2.37
5	4	1.50	83800	54	2.32
6	5	1.80	87600	54	2.22
7	6	2.10	84200	53	2.27
8	7	2.40	83500	49	2.11
9	8	2.70	84200	51	2.18
10	9	3.00	82700	48	2.09
11	10	3.20	85600	48	2.02

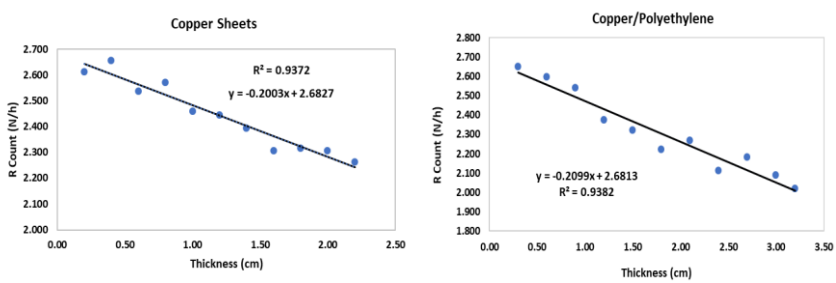

(a) (b)

Figure 13: The effect of; (a) Cu sheet, and (b) Cu/PE on shield of muon

The influence of PE

PE is a good shielding material because it has high hydrogen content, and hydrogen atoms are good at absorbing and dispersing radiation. PE is widely used for radiation shielding in space and therefore it is an excellent benchmark material to be used in comparative investigations [37]. In this work, 10 sheets of PE (thickness of 1 mm and density 0.9 g/cm^3) were inserted between either Al or Cu sheets and the original experiments were repeated. The results can be traced in Table 4 (Al/PE) and in Table 5 (Cu/PE). Figure 12b and Figure 13b show the effect of inserting up to 10 PE sheets between the Al and Cu sheet, respectively. The results depicted in Equation (4) (Al/PE) and Equation (6) (Cu/PE) have shown that the PE has increased the shielding effect in the Al case from 16% to 19% with $R^2 = 0.8717$ and from 20% to 21% with $R^2 = 0.9382$ in case of Cu. Despite the fact that PE has hydrogen, the results have not shown the expected increase in shielding effect. However, Naito et al. [35] have noticed that the energy of cosmic rays was not enough to make the ionization need to be detected by GM tube [35].

Conclusion

Due to the relativistic effect, muons are one of the most abundant secondary cosmic ray particles detected at ground level. Numerous investigations on muons have been conducted in various locations using diverse equipment. It has been stated that cosmic radiation, in general, and muons, in particular, have devastating effects on living organisms. Those who work closely on cosmic radiation and fly to investigate space are influential. In addition, it has been observed that cosmic rays directly harm electronic components. According to reports in the medical field, cosmic rays have been implicated in several diseases affecting humans and other organisms. Due to these factors, protection against cosmic rays has become an essential component of this and similar research. This study is one of the studies that detected muon occurrences at ground level in tropical regions. Muons from cosmic rays were captured using a muon telescope comprised of coaxial GM tubes. This experiment was conducted to observe how the cosmic ray muon count varies with metals (Cu and Al) shielding and PE. Cu and Al sheets constituted the metal's shielding. The sample was conducted from August to November 2021; the muon count was measured throughout the night, with variations in thickness causing changes in the muon count. Statistical analysis was conducted on the measured muon count for each metal sample. Using both metals as shielding in this experiment, it was discovered that the muon count changed due to adding more Cu and Al sheets. Generally, the counts decrease with the increase of thickness of either metal. The results have shown that Cu is better than Al in shielding effectiveness (19% compared to 16%). The

correlation coefficient R^2 for Cu = 0.9372 is bigger than R^2 for Al = 0.6593, meaning the trend for Cu is better than the trend for Al for this experiment because Cu is higher density than Al. In addition to investigating the Al and Cu sheets, ten sheets of PE sheets were gradually inserted separately between the Al and Cu sheets to investigate the shielding ability of the two composites Al/PE and Cu/PE. The results have shown a slight increase in the shielding of cosmic rays caused by PE sheets.

Contributions of Authors

Tayser Sumer Gaaz conducted all of the experiments and wrote the manuscript as part of his project. Malik N. Hawas was the principal investigator. The published version of the manuscript has been read and approved by all authors.

Funding

This research received no external funding.

Conflict of Interests

The authors declare no conflict of interest.

Acknowledgement

This work was supported by the Universiti Kebangsaan Malaysia, Malaysia and Al-Furat Al-Awsat technical university, Iraq.

List of abbreviations

e^-	Electron
e^+	Positron
v_e	Electron neutrino
$\overline{v_e}$	Antielectron neutrino
μ^-	Negative Muon
μ^+	Positive Muon
v_μ	Muon neutrino
$\overline{v_u}$	Antimuon neutrino

π^O	Neutral pion
$\pi\pm$	Charged pion
γ	Gamma ray
x	Thickness of the floor
X	Effective thickness
N(X)	Muon counts at effective thickness X
N_o	Muon counts when the effective thickness X=0 at vertical direction (θ=0°)
α	Linear absorption coefficient of the shielding material

References

[1] S. D. Mhatre, J. Iyer, S. Puukila, A. M. Paul, C. G. Tahimic, L. Rubinstein, *et al.*, "Neuro-consequences of the spaceflight environment," *Neuroscience & Biobehavioral Reviews,* vol. 132, pp. 908-935, 2021.

[2] D. Griffiths, *Introduction to elementary particles*: John Wiley & Sons, 2020.

[3] M. Ivanova, "The aesthetics of scientific experiments," *Philosophy Compass,* vol. 16, no. 3, pp. e12730, 2021.

[4] W. V. Farrar, "Richard Laming and the coal-gas industry, with his views on the structure of matter," *Annals of Science,* vol. 25, no. 3, pp. 243-253, 1969.

[5] T. Arabatzis, Representing electrons: A biographical approach to theoretical entities, University of Chicago Press, 2006.

[6] J. Z. Buchwald and A. Warwick, "Histories of the Electron: The Birth of Microphysics. Dibner Institute Studies in the History of Science and Technology," ed: MIT Press, Cambrideg, Mass, 2001.

[7] A. Bagdonas and A. Kojevnikov, "Funny origins of the Big Bang Theory," *Historical Studies in the Natural Sciences,* vol. 51, no. 1, pp. 87-137, 2021.

[8] C. Weicheng, "On an axiomatic foundation for a theory of everything," *Philosophy,* vol. 11, no. 4, pp. 241-267, 2021.

[9] J. J. Thomson, "XL. Cathode rays," *The London, Edinburgh, and Dublin Philosophical Magazine and Journal of Science,* vol. 44, no. 269, pp. 293-316, 1897.

[10] S. H. Neddermeyer and C. D. Anderson, "Note on the nature of cosmic-ray particles," *Physical Review,* vol. 51, pp. 884, 1937.

[11] C. G. Jung and W. Pauli, *Atom and Archetype: The Pauli/Jung Letters, 1932-1958*: Princeton University Press, 2014.

[12] F. Reines, C. Cowan Jr, F. Harrison, A. McGuire, and H. Kruse, "Detection of the free antineutrino," *Physical Review,* vol. 117, no. 1, pp. 159, 1960.

[13] G. Danby, J. Gaillard, K. Goulianos, L. Lederman, N. Mistry, M. Schwartz, *et al.*, "Observation of high-energy neutrino reactions and the existence of two kinds of neutrinos," *Physical Review Letters*, vol. 9, no. 1. pp. 36, 1962.
[14] M. L. Perl, "The discovery of the tau and its major properties, 1970--1985," Stanford Linear Accelerator Center1990.
[15] T. Ericson and P. Landshoff, *Neutrino physics* vol. 14: Cambridge University Press, 2000.
[16] K. Kodama, N. Ushida, C. Andreopoulos, N. Saoulidou, G. Tzanakos, P. Yager, *et al.*, "Observation of tau neutrino interactions," *Physics Letters B*, vol. 504, no. 3, pp. 218-224, 2001.
[17] G. Hudoba, "Visualize Particle Radiation in Physics Education," vol. 1, no. 1, 2010.
[18] S. Guetersloh, C. Zeitlin, L. Heilbronn, J. Miller, T. Komiyama, A. Fukumura, *et al.*, "Polyethylene as a radiation shielding standard in simulated cosmic-ray environments," *Nuclear Instruments and Methods in Physics Research Section B: Beam Interactions with Materials and Atoms*, vol. 252, no. 2, pp. 319-332, 2006.
[19] Y. Zhang, A. A. Tamijani, M. E. Taylor, B. Zhi, C. L. Haynes, S. E. Mason, *et al.*, "Molecular surface functionalization of carbon materials via radical-induced grafting of terminal alkenes," *Journal of the American Chemical Society*, vol. 141, pp. 8277-8288, 2019.
[20] T. Sato, "Analytical model for estimating terrestrial cosmic ray fluxes nearly anytime and anywhere in the world: Extension of PARMA/EXPACS," *PLoS one*, vol. 10, no. 12, pp. e0144679, 2015.
[21] D. Biehl, "Nuclear Cascades and Neutrino Production in the Sources of Ultra-High Energy Cosmic Ray Nuclei," 2019.
[22] L. Oláh and D. Varga, "Investigation of soft component in cosmic ray detection," *Astroparticle Physics*, vol. 93, pp. 17-27, 2017.
[23] D. Reyna, "A simple parameterization of the cosmic-ray muon momentum spectra at the surface as a function of zenith angle," *arXiv High Energy Physics-Phenomenology*, 2006.
[24] A. Chiriacescu and I. Lazanu, "Measurement of low energy component of the flux of cosmic rays using nuclear track detectors," *arXiv Physics-Instrumentation and Detectors*, 2017.
[25] J. DeWitt and E. Benton, "Shielding effectiveness: A weighted figure of merit for space radiation shielding," *Applied Radiation and Isotopes*, vol. 161, pp. 109141, 2020.
[26] T. Blachowicz and A. Ehrmann, "Shielding of Cosmic Radiation by Fibrous Materials," *Fibers*, vol. 9, no. 10, pp. 60, 2021.
[27] K. Krukowski, X. Feng, M. S. Paladini, A. Chou, K. Sacramento, K. Grue, *et al.*, "Temporary microglia-depletion after cosmic radiation modifies phagocytic activity and prevents cognitive deficits," *Scientific reports*, vol. 8, no. 1, pp. 1-13, 2018.

[28] M. M. Acharya, J. E. Baulch, P. M. Klein, D. B. Al Anoud, L. A. Apodaca, E. A. Kramár, "New concerns for neurocognitive function during deep space exposures to chronic, low dose-rate, neutron radiation," *Eneuro,* vol. 6, no. 4, 2019.

[29] G. Almeida-Porada, C. Rodman, B. Kuhlman, E. Brudvik, J. Moon, S. George, "Exposure of the bone marrow microenvironment to simulated solar and galactic cosmic radiation induces biological bystander effects on human hematopoiesis," *Stem Cells and Development,* vol. 27, no. 18, pp. 1237-1256, 2018.

[30] E. Sage and N. Shikazono, "Radiation-induced clustered DNA lesions: Repair and mutagenesis," *Free Radical Biology and Medicine,* vol. 107, pp. 125-135, 2017.

[31] T. Imaoka, M. Nishimura, K. Daino, A. Hosoki, M. Takabatake, Y. Nishimura, "Prominent dose-rate effect and its age dependence of rat mammary carcinogenesis induced by continuous gamma-ray exposure," *Radiation Research,* vol. 191, no. 3, pp. 245-254, 2019.

[32] R. T. Warne, "Beyond multiple regression: using commonality analysis to better understand R 2 results," *Gifted Child Quarterly,* vol. 55, no. 4, pp. 313-318, 2011.

[33] H. M.A.A., "Effect of sheilding building on muon eventsat ground level," *Thesis,* 2012.

[34] S. F.S.T., "Effect of Copper and Aluminum sheldings on cosmic ray muon event rate at ground level," *Thesis,* 2012.

[35] M. Naito, S. Kodaira, R. Ogawara, K. Tobita, Y. Someya, T. Kusumoto, "Investigation of shielding material properties for effective space radiation protection," *Life sciences in space research,* vol. 26, pp. 69-76, 2020.

[36] R. N. Altameemi and G. Gopir, "Effect of copper and aluminium on the event rate of cosmic ray muons at ground level in Bangi, Malaysia," in *AIP Conference Proceedings*, 2016, pp. 040005.

[37] L. Narici, M. Casolino, L. Di Fino, M. Larosa, P. Picozza, A. Rizzo, "Performances of Kevlar and Polyethylene as radiation shielding on-board the International Space Station in high latitude radiation environment," *Scientific reports,* vol. 7, no. 1, pp. 1-11, 2017.

Low-cost Polyurethane Coating as Dielectric Component in Digital Microfluidics

E. N. Abdul Latip[1, 2], L. Coudron[1], M. C. Tracey[1]*
[1]School of Physics, Engineering & Computer Science,
University of Hertfordshire,
College Lane, Hatfield, AL10 9AB, UK
[2]School of Mechanical Engineering, College of Engineering,
Universiti Teknologi MARA, 40450 Shah Alam, MALAYSIA
**elinadia@uitm.edu.my*

ABSTRACT

Digital microfluidics (DMF) as a platform for precise handling of liquid droplets is a powerful tool but the affordability of the device has been one of the hindrances to its wide implementation. This paper reports the development of DMF devices using low-cost materials and simple deposition techniques specifically for the device dielectric component. Three commercial polyurethane coatings were investigated for their feasibility as the dielectric layer. The electrowetting behaviour of these materials was investigated by evaluating the change in contact angle with applied voltage of a water droplet sitting on the dielectric samples prepared using easy deposition methods such as spraying and spin coating. Devices were then fabricated using these materials to evaluate their capability to actuate droplets. Five types of polyurethane dielectric sample exhibited contact angle reversibility with hysteresis ranging between 4° to 25° after 250 V_{DC} application. Droplet transportation back and forth across 8 electrodes at 180 V_{RMS} has been demonstrated in a device made of one of the polyurethane coatings using a spraying technique. This result implies the potential of using polyurethane for future development of low-cost and disposable DMF devices.

Keywords: *Digital Microfluidics; Polyurethane; Electrowetting-On-Dielectric*

ISSN 1823-5514, eISSN 2550-164X

https://doi.org/10.24191/jmeche.v20i1.21082

Received for review: 2022-06-30
Accepted for publication: 2022-12-20
Published: 2023-01-15

Introduction

Digital microfluidics (DMF) manipulates multiple individual droplets to move, mix, merge, and split on a surface using electrowetting-on-dielectric (EWOD) mechanism to perform specific functions such as sample preparation, DNA amplification and immunoassays [1]–[3] in a lab-on-a-chip platform. The volume of droplet required in a DMF device is in the microliter range, resulting in reduced consumption of sample and reagents and fast results. EWOD controls droplets by electrostatic energy, allowing for fully-automated devices with simple design to be realised [4]-[5]. Another advantage of an EWOD-based DMF device is its open architecture where no physical features such as micro-channels, pumps or valves are necessary, making it a versatile tool that can be reconfigured to perform more than one function [6]. An EWOD device typically consists of a base plate composed of a substrate patterned with control electrodes. These electrodes are buried underneath a layer of dielectric material which generates electric fields when a voltage is applied across the dielectric layer [1]–[7].

The dielectric layer sustains the capacitance or the electrostatic energy that drives the droplet actuation by preventing electron transfer from the electrodes to the droplet. The change in contact angle of a water droplet sitting on an electrode coated with a dielectric layer when a voltage is applied is regulated by the following Young-Lippmann equation:

$$cos\,\theta_v = cos\,\theta + \frac{1}{2\,\gamma_{lg}} cV^2 \quad (1)$$

where θ_v is CA at applied voltage, θ is initial CA, γ_{lg} is liquid-gas surface tension, and V is the applied voltage. The capacitance per unit area, c is equivalent to $\frac{\varepsilon_o \varepsilon_r}{d}$ where ε_o is the vacuum permittivity, ε_r is the dielectric constant, and d is the dielectric thickness.

Ideally, the dielectric material should have a high dielectric constant which will result in a higher electrostatic energy to actuate droplets more efficiently. To ensure a reliable electrowetting performance, it is also desirable for the dielectric material to have a high CA reversibility, i.e. low hysteresis after an electrowetting cycle, indicating no charges are trapped in the layer after removal of voltage [8]-[9].

While there are numerous reports of DMF devices in the academic literature, they have not been widely demonstrated as real-world point-of-care diagnostic platforms due to the high fabrication cost [5], [10]-[11]. For the device dielectric component, commonly used materials such as Parylene-C and Teflon™ AF are expensive while others, for example, silicon dioxide and aluminium oxide, require clean-room facilities and elaborate processes [8], [10]-[11]. Dielectric materials with superior dielectric constant such as

aluminium oxide (9.5) [12] and tantalum pentoxide (20-25) [13]-[14] possess the same challenge of requiring deposition techniques that are expensive and time consuming.

There were studies experimented with low-cost products such as Saran™ wrap [15] and parafilm [16] applied using simple deposition methods but the robustness and reliability of these materials have not been well-investigated and proven yet. Some studies attempt to overcome this by using low-cost material such as SU-8 [17]-[18] and PDMS [19]-[20]. These materials however pose another challenge which is the formation of pinholes in the layer [11]. Other unconventional materials for EWOD dielectric component that have been demonstrated are: ion gel [11], PMMA/fluoropolymer bilayer [21] and cyanoethyl pullulan [22]. All these alternative materials employed easy deposition techniques such as spin coating and roll coating. Meanwhile, Yamamoto et al. [23] replaced the solid dielectric layer by infusing the electrodes with silicone oil which acted as liquid dielectric.

This paper aims to explore the potential of readily available consumer products as the alternative to conventional dielectric materials. One of the products that can be utilised is polyurethane (PU) coating, typically used as a protection layer on various types of surfaces. Three types of PU coatings were investigated for their feasibility as dielectric component. The contact angle (CA) evolution of a deionised (DI) water droplet sitting on the dielectric surface as a function of applied voltage was measured. If the CA of the water droplet was found to be reversible after voltage application, further investigation was conducted by employing the material in the EWOD plate fabrication to evaluate whether droplet transportation could be established.

Materials and Methods

Dielectric sample preparation

The samples for CA measurement, structure shown in Figure 1, consist of a silicon wafer substrate (p-type, <100>, 1-10 Ω·cm, Pi-Kem Ltd), a dielectric layer, and a hydrophobic coating (Cytop®, Asahi Glass Co., Ltd.). Three types of products were investigated: Blackfriar Polyurethane Varnish (BF), Rust-Oleum® Polyurethane Finish (RO-PU), and Rust-Oleum® Crystal Clear (RO-CC). The materials are supplied in liquid form inside aerosol cans except for BF which is a varnish in a metal container. The deposition methods used for each material are summarised in Table 1.

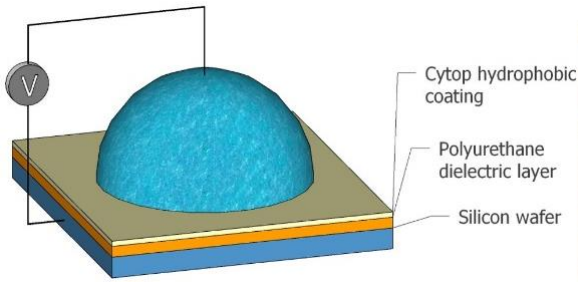

Figure 1: The dielectric sample's structure

Table 1: Deposition methods for dielectric materials

Dielectric material	Deposition method	Number of layers	Curing time and temperature
Blackfriar PU Varnish (BF)	Squeegee	1 and 2	24 hours, ambient temperature
Rust-Oleum® PU Finish (RO-PU)	Spraying	1 and 2	24 hours, ambient temperature
	Spin coating	1	1 hour, 100 °C
Rust-Oleum® Crystal Clear (RO-CC)	Spraying	1 and 2	24 hours, ambient temperature
	Spin coating	1	1 hour, 100 °C

For the two-layer samples, a second layer was applied after 2 hours of drying for the BF samples and after two minutes for the spray-coated samples (both RO-PU and RO-CC). Spin coating (LabSpin6, SUSS MicroTec) of the materials was performed at 1500 rpm for 30 s. The hydrophobic layer was spin-coated on top of the dielectric and cured for 30 minutes at 140 °C. The dielectric thickness was evaluated using a surface profilometer (AlphaStep® D-500, KLA Tencor).

Contact angle measurements

The CA measurements were performed using Theta Lite tensiometer (Biolin Scientific). A positive voltage was applied via a platinum wire to a DI water droplet (20 µl) sitting on the sample (set-up in Figure 2). The voltage was varied between 0 V and 250 V using a DC power supply (Digimess) and the CA value was identified at three levels: the initial 0 V, the maximum voltage at 250 V, and again at 0 V after voltage application. The voltage was increased to 250 V in approximately 20 seconds and left at the maximum level for about 10 seconds before returning to 0 V. The same steps were repeated with a lower maximum voltage, 150 V.

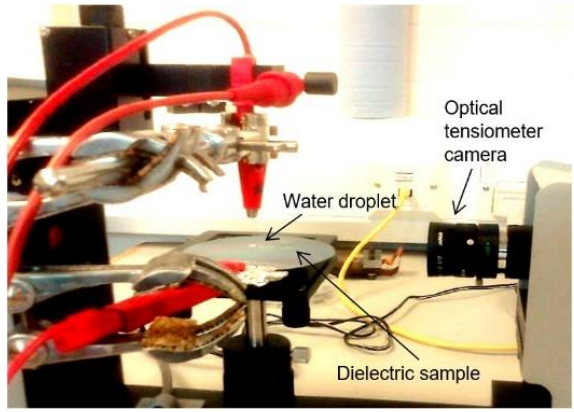

Figure 2: The CA measurement set-up

EWOD plates fabrication and droplet transportation

For each dielectric surface that demonstrated CA reversibility, two actuation plates were prepared using an identical deposition method as described previously. The EWOD plates design (Figure 3a and 3b) consisted of three rows of 16 square electrodes, 1.7 mm in nominal size with 200 µm nominal inter-electrode spacing. The parallel-plate configuration (Figure 3c) was employed with ITO-coated glass slide (Diamond Coatings) as the cover plate. The electrodes were made of PEDOT:PSS ink (Sigma Aldrich) patterned on a hydrophilic polyethylene terephthalate (PET) substrate using inkjet printing technique (Fujifilm Dimatix DMP-2850). The set-up and drive electronics for droplet actuation were similar to the one previously reported in [24]-[25].

Results and Discussion

Contact angle measurements

Figure 4 and Table 2 show the contact angle response of DI water droplet on different types of dielectric samples with applied voltage. Five types of surfaces have shown CA reversibility after 250 V voltage application, with thickness ranging from 9 to 71 µm. The spray-coated RO-PU and RO-CC samples exhibited reversibility on both one-layer and two-layer samples. The two-layer BF and one-layer spray-coated RO-CC demonstrated good reversibility with low hysteresis, 4° and 6° respectively with a wide range of CA modulation, both more than 40°. These results are comparable to 3.2 µm thickness Parylene-C employing the same Cytop® hydrophobic surface [13]. As predicted, the thicker the insulating layer, the narrower the CA modulation for any types of samples. Both of the two-layer spray-coated RO-PU and RO-

CC exhibited small CA change when 150 V was applied, requiring a higher voltage to induce larger CA change.

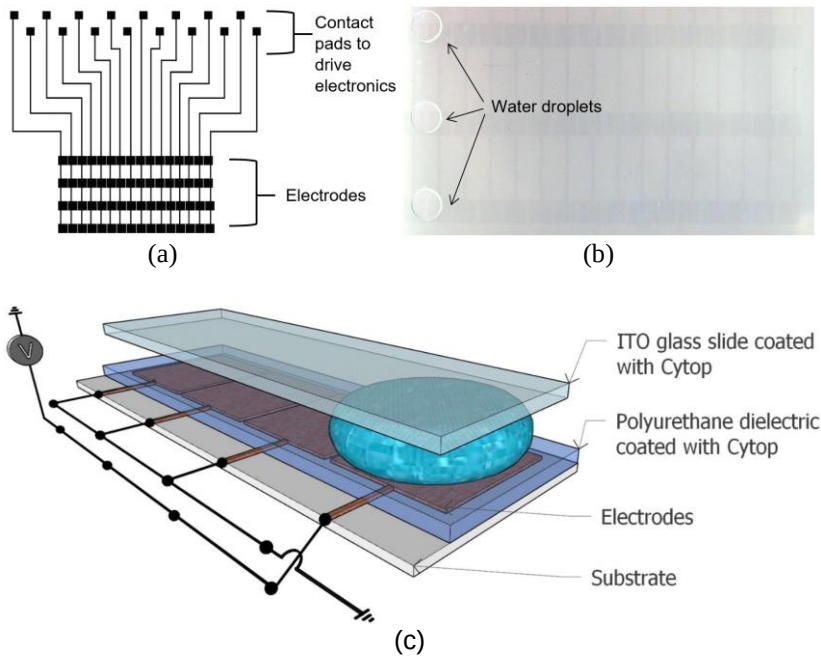

Figure 3: a) The design of the inkjet-printed EWOD plate, b) water droplets in the inkjet-printed device, and c) the parallel-plate configuration

As discussed previously, the Young-Lippmann equation governs the contact angle evolution with applied voltage and is given by equation 1 where the capacitance per unit area, c is equivalent to $\frac{\varepsilon_o \varepsilon_r}{d}$. The electrowetting number, $\frac{\varepsilon_o \varepsilon_r}{2\,\gamma_{lg} d}\,V^2$ at 150 V was calculated for all the reversible surfaces. This dimensionless number measures the electrostatic energy strength compared to the surface tension. Based on the calculated values, two-layer RO-PU is the least efficient at 150 V with the lowest electrowetting number (0.08) followed by two-layer RO-CC (0.09). The two-layer BF surface has the highest number (0.49), while one-layer RO-PU and one-layer RO-CC numbers are 0.39 and 0.38 respectively.

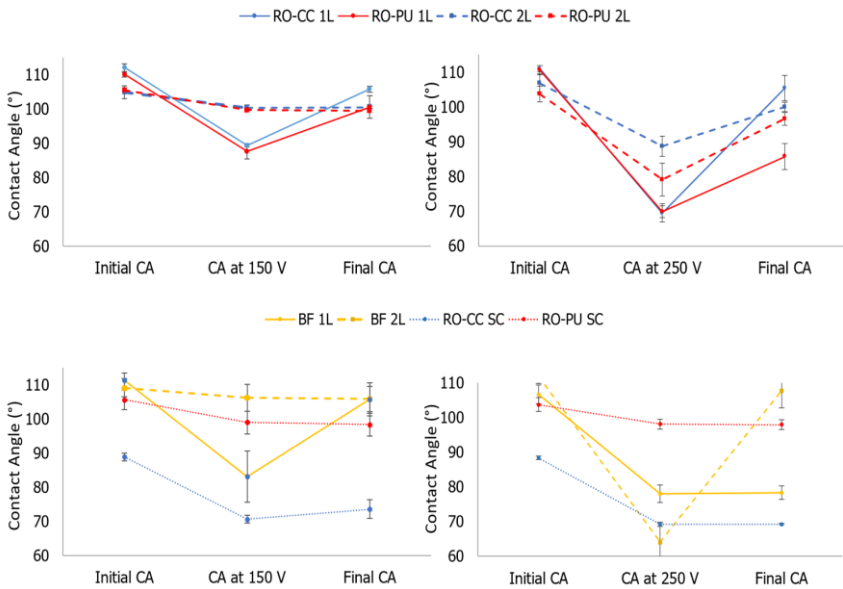

Figure 4: The CA response of the RO-CC (blue), RO-PU (red), and BF (yellow) materials. The solid lines denote the one-layer while the dashed lines denote the two-layer samples. The dotted lines represent the spin-coated samples

The one-layer BF and both spin-coated RO-CC and RO-PU were irreversible; it is suspected that formation of pinholes during dielectric deposition caused the failure. Bubbles generation can be observed (Figure 5) in the droplet due to electrolysis during the electrowetting cycle. In Figure 5a, bubbles began to form when voltage was increased, and more were generated in Figure 5b at higher voltage. Notice that the droplet CA has decreased in Figure 5b compared to in Figure 5a and it remained at the same value after removal of voltage application, demonstrating its irreversibility. All of the irreversible surfaces have thicknesses below 5 µm, indicating that more than one layer is required to produce a higher thickness to prevent pinholes formation and dielectric breakdown. However, it should be noted that if the thickness is too high it will affect the droplet actuation performance by increasing the operating voltage requirement [26]-[27].

Table 2: Electrowetting hysteresis, thickness, and electrowetting number of the dielectric samples

Dielectric material	No. of layer & deposition method	Hysteresis (°)	Electrowetting number at 150 V	Average thickness (µm)
Blackfriar PU Varnish (BF)	1-layer squeegee	Irreversible	-	0.5 ± 0.2
	2-layer squeegee	4 ± 5	0.49	9 ± 1
Rust-Oleum® PU Finish (RO-PU)	1-layer spray-coated	6 ± 4	0.38	26 ± 4
	2-layer spray-coated	7 ± 2	0.09	56 ± 7
	1-layer spin-coated	Irreversible	-	4.6 ± 0.3
Rust-Oleum® Crystal Clear (RO-CC)	1-layer spray-coated	25 ± 3	0.39	40 ± 10
	2-layer spray-coated	7.1 ± 0.8	0.08	71 ± 3
	1-layer spin-coated	Irreversible	-	1.83 ± 0.03

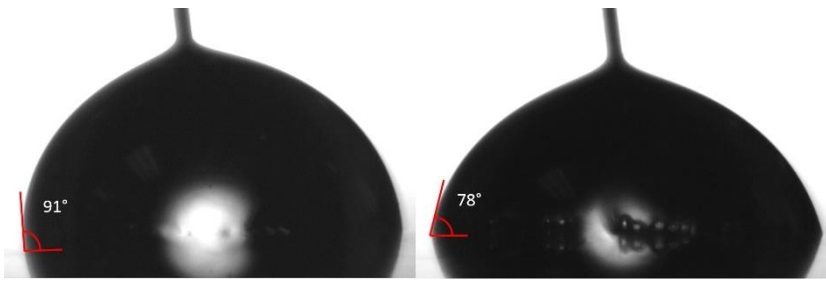

(a) (b)

Figure 5: Progressive bubbles development due to electrolysis in 20 µl water droplet sitting on one-layer BF sample; (a) bubbles formation at lower voltage, and (b) at higher voltage

The CA measurement for the one-layer RO-PU surface, which has the best actuation performance (discussed in the next section), during five successive cycles is presented in Figure 6. The CA at 0 V decreased after the completion of each cycle and reduced to 77° after the fifth cycle. The CA modulation also decreased as the repetition progressed with only about 7°

change induced during the 5th cycle. The CA at 250 V for each cycle were fairly constant, ranging between 68° to 71°.

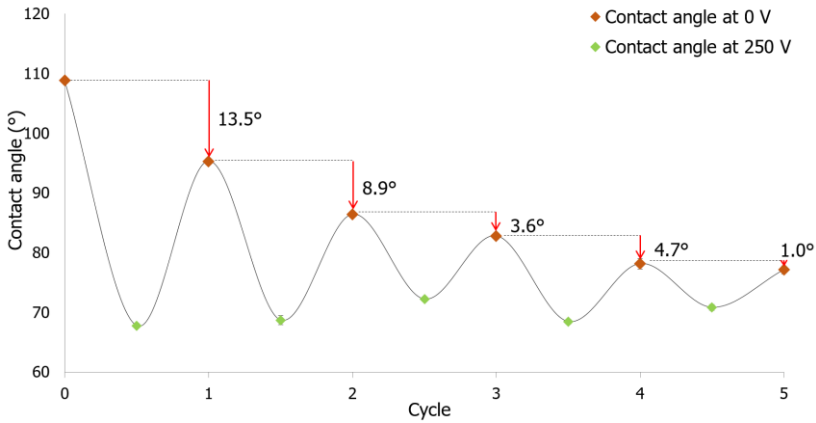

Figure 6: CA evolution of one-layer spray-coated RO-PU during repeated electrowetting cycle

Droplet transportation

The three types of dielectric surfaces that have shown reversibility and good electrowetting efficiency were selected for EWOD plate's fabrication: one-layer spray-coated RO-CC, one-layer spray-coated RO-PU, and two-layer BF. Two EWOD plates were fabricated for each type. The maximum voltage for the droplet actuation is limited to 225 V_{RMS}. Both RO-CC and RO-PU were able to instigate droplet movement to the next electrode at 150 V_{RMS}. As summarized in Table 3, the RO-PU plate 2 has the best performance with reliable droplet actuation across eight electrodes in one of the three electrode arrays at 180 V_{RMS}; both of the RO-PU plates were capable of droplet transportation. One of the RO-CC plates transported droplet across four electrodes at 180 V_{RMS}; the other plate was not functional. Both BF plates were unable to demonstrate any droplet movement. It is believed that the non-functioning BF plates including the non-functioning regions in RO-PU and RO-CC plates could be due to non-uniformity of the dielectric thickness where some areas are thicker than the others, thus requiring a higher voltage of more than 225 V_{RMS} to actuate the droplet. By actuating droplet at 165 V_{RMS} – 180 V_{RMS}, the RO-PU and RO-CC plates have performed comparably well to previously reported devices. Low-cost device which employed Saran™ wrap as dielectric layer operated at 400 - 500 V_{RMS} [15] while another [16] using parafilm required 300 V_{RMS} operating voltage.

Table 3: Droplet transportation performance of EWOD plates with difference types of dielectric layer

Dielectric material	Voltage to instigate droplet movement to the next electrode	Lowest voltage requirement to actuate across three or more electrodes
BF (2-layer)	-	Both plates not functional
RO-CC (1-layer spray-coated)	150 V_{RMS}	Plate 1: not functional Plate 2: 4 electrodes at 180 V_{RMS}
RO-PU (1-layer spray-coated)	150 V_{RMS}	Plate 1: 3 electrodes at 165 V_{RMS} Plate 2: 8 electrodes at 180 V_{RMS}

Conclusions

Polyurethane coatings were investigated for their feasibility as low-cost dielectric in DMF devices by evaluating the electrowetting reversibility of these materials. It has been found that the reversibility of the three selected dielectric PU materials is highly dependent on the thickness of the layer which in turn depends on the method used to deposit the materials. An adequate thickness of the dielectric layer is required to avoid pinholes which cause electrolysis of the droplet when voltage is applied.

The dielectric samples that demonstrated good CA reversibility after voltage application were investigated further to prove their ability to transport droplets across electrodes in an EWOD device. All three materials have shown potential to be used as dielectric component in EWOD, albeit further improvement is needed in terms of the deposition technique. The RO-PU product produced the most promising results by transporting droplet dependably at 180 V_{RMS}. The findings suggest that the key to the successful integration of commercial materials into DMF technology is a deposition method that can produce a layer without pinholes and with uniform thickness reliably across the substrate. Equipment such as an automated spray gun system can help to reduce human error as the amount of substance can be applied consistently whereas manual techniques rely heavily on the operator's skills to produce good surfaces. Spin coating is another deposition method that can be used for these materials but multiple layers are required to overcome the aforementioned failure.

This study proposes commercial PU materials as an approach to address the challenge of high cost in DMF device fabrication. Apart from being low cost, these materials also required simple deposition methods. The evaluated

PU products have shown high potential as the alternative to conventional materials by exhibiting CA reversibility and capability to transport droplets. Hopefully, the findings will contribute towards the realisation of an affordable and robust future DMF device for diagnostic and bio-detection applications.

Contributions of Authors

The authors confirm the equal contribution in each part of this work. All authors reviewed and approved the final version of this work.

Funding

The authors gratefully acknowledge Dato' Azmil Khalid for the funding for this project through PhD Student Scholarship in Engineering.

Conflict of Interests

All authors declare that they have no conflicts of interest

References

[1] Y. Zhang and Y. Liu, "Advances in integrated digital microfluidic platforms for point-of-care diagnosis: a review," *Sensors & Diagnostics*, vol. 1, pp. 648-672, 2022.

[2] B. J. Coelho *et al.*, "Digital Microfluidics for Amplification Monitoring of Cancer Biomarkers," *Materials Proceedings*, vol. 8, no. 1, pp. 103, 2022.

[3] A. B. Alias, H.-Y. Huang, and D.-J. Yao, "A review on microfluidics: An aid to assisted reproductive technology," *Molecules*, vol. 26, no. 14, pp. 4354, 2021.

[4] J. Li, "Current commercialization status of electrowetting-on-dielectric (EWOD) digital microfluidics," *Lab on a Chip*, vol. 20, no. 10, pp. 1705–1712, 2020.

[5] K. Leirs *et al.*, "Bridging the Gap between Digital Assays and Point-of-Care Testing: Automated, Low Cost, and Ultrasensitive Detection of Thyroid Stimulating Hormone," *Analytical Chemistry*, vol. 94, no. 25, pp. 8919-8927, 2022.

[6] L. Malic, D. Brassard, T. Veres, and M. Tabrizian, "Integration and detection of biochemical assays in digital microfluidic LOC devices," *Lab on a Chip*, vol. 10, no. 4, pp. 418–431, 2010.
[7] M. G. Pollack, R. B. Fair, and A. D. Shenderov, "Electrowetting-based actuation of liquid droplets for microfluidic applications," *Applied Physics Letter*, vol. 77, no. 11, pp. 1725–1726, 2000.
[8] H. Liu, S. Dharmatilleke, D. K. Maurya, and A. A. O. Tay, "Dielectric materials for electrowetting-on-dielectric actuation," *Microsystem Technologies*, vol. 16, no. 3, pp. 449, 2010.
[9] F. Mugele and J. Heikenfeld, Electrowetting: Fundamental Principles and Practical Applications, John Wiley & Sons, 2018.
[10] V. Soum *et al.*, "Affordable fabrication of conductive electrodes and dielectric films for a paper-based digital microfluidic chip," *Micromachines*, vol. 10, no. 2, pp. 109, 2019.
[11] V. Narasimhan and S.-Y. Park, "An ion gel as a low-cost, spin-coatable, high-capacitance dielectric for electrowetting-on-dielectric (EWOD)," *Langmuir*, vol. 31, no. 30, pp. 8512–8518, 2015.
[12] J. Chang, D. Y. Choi, S. Han, and J. J. Pak, "Driving characteristics of the electrowetting-on-dielectric device using atomic-layer-deposited aluminum oxide as the dielectric," *Microfluids and Nanofluidics*, vol. 8, no. 2, pp. 269–273, 2010.
[13] Y. Li *et al.*, "Anodic Ta 2 O 5 for CMOS compatible low voltage electrowetting-on-dielectric device fabrication," *Solid-State Electronics*, vol. 52, no. 9, pp. 1382–1387, 2008.
[14] Y.-Y. Lin, R. D. Evans, E. Welch, B.-N. Hsu, A. C. Madison, and R. B. Fair, "Low voltage electrowetting-on-dielectric platform using multi-layer insulators," *Sensors and Actuators B: Chemical*, vol. 150, no. 1, pp. 465–470, 2010.
[15] M. Abdelgawad and A. R. Wheeler, "Low-cost, rapid-prototyping of digital microfluidics devices," *Microfluidics and Nanofluidics*, vol. 4, no. 4, pp. 349, 2008.
[16] M. Yafia, S. Shukla, and H. Najjaran, "Fabrication of digital microfluidic devices on flexible paper-based and rigid substrates via screen printing," *Journal of Micromechanics and Microengineering*, vol. 25, no. 5, pp. 57001, 2015.
[17] M. Jönsson-Niedziółka *et al.*, "EWOD driven cleaning of bioparticles on hydrophobic and superhydrophobic surfaces," *Lab on a Chip*, vol. 11, no. 3, pp. 490–496, 2011.
[18] S.-K. Fan, H. Yang, and W. Hsu, "Droplet-on-a-wristband: Chip-to-chip digital microfluidic interfaces between replaceable and flexible electrowetting modules," *Lab on aChip*, vol. 11, no. 2, pp. 343–347, 2011.
[19] M. Abdelgawad, S. L. S. Freire, H. Yang, and A. R. Wheeler, "All-terrain droplet actuation," *Lab on a Chip*, vol. 8, no. 5, pp. 672–677, 2008.

[20] C. Karuwan *et al.*, "Electrochemical detection on electrowetting-on-dielectric digital microfluidic chip," *Talanta*, vol. 84, no. 5, pp. 1384–1389, 2011.

[21] P. G. Yedewar, S. M. Wadhai, Y. B. Sawane, and A. G. Banpurkar, "Polymethyl methacrylate (PMMA)/fluoropolymer bilayer: a promising dielectric for electrowetting applications," *Journal of Materials Science*, vol. 57, no. 19, pp. 9018–9027, 2022.

[22] C. Dixon, A. H. C. Ng, R. Fobel, M. B. Miltenburg, and A. R. Wheeler, "An inkjet printed, roll-coated digital microfluidic device for inexpensive, miniaturized diagnostic assays," *Lab on a Chip*, vol. 16, no. 23, pp. 4560–4568, 2016.

[23] K. Yamamoto, S. Takagi, Y. Ichikawa, and M. Motosuke, "Electrowetting-on-liquid-dielectric (EWOLD) enables droplet manipulation with a few volts," *arXiv Prepr. arXiv2201.09496*, 2022.

[24] E. N. A. Latip *et al.*, "Protein droplet actuation on superhydrophobic surfaces: A new approach toward anti-biofouling electrowetting systems," *RSC Advances*, vol. 7, no. 78, pp. 49633-49648, 2017.

[25] E. N. A. Latip, "Development of a digital microfluidic toolkit: alternative fabrication technologies for chemical and biological assay platforms." University of Hertfordshire, 2020.

[26] F. Saeki, J. Baum, H. Moon, J.-Y. Yoon, C. J. Kim, and R. L. Garrell, "Electrowetting on dielectrics (EWOD): reducing voltage requirements for microfluidics," *Polymer Materials Science and Engineering*, vol. 85, pp. 12–13, 2001.

[27] H. Moon, S. K. Cho, R. L. Garrell, and C.-J. "CJ" Kim, "Low voltage electrowetting-on-dielectric," *Journal of Applied Physics*, vol. 92, no. 7, pp. 4080–4087, 2002.

Seismic Performance Assessment of Murum Dam Under Various Seismic Event

Rozaina Ismail[*]*, Nurul Damia Sukati, Nurul Nabilah Moktar,*
Ainnur Zulsyamilatil Huda Abd Halim, Dayang Nur Erliyani Fitri Erwan,
Azmi Ibrahim, Norliyati Mohd Amin
School of Civil Engineering, College of Engineering,
Universiti Teknologi MARA, 40450, Shah Alam Selangor, MALAYSIA
[*]*dr.rozaina.ismail@gmail.com*

Azlan Adnan
Faculty of Civil Engineering, Universiti Teknologi Malaysia,
81310 Johor Bahru, Johor, MALAYSIA

Ade Faisal
Program Studi Teknik Sipil, Universitas Muhammadiyah Sumatera Utara,
Medan 20238, INDONESIA

ABSTRACT

Dams are considered as vital assets for countries; therefore, the dam must be built to withstand natural disasters. However, the performance of the dam structure comes to attention since the Ranau earthquake occurrence in 2015 is the strongest earthquake recorded in Malaysia. The behavior of the dam became deteriorated across the year due to earthquake motion which caused damage to the dam. This study aims to assess the performance of Murum dam using Incremental Dynamic Analysis (IDA) which subjected was subjected to a set of 6 ground motion records scaled to increasing intensity levels by using ABAQUS. A different scale Peak Ground Acceleration (PGA) of 0.05 g, 0.10 g, 0.15 g, 0.20 g, and 0.30 g were applied in this study. Based on the results, the cracking area increases when the acceleration increases due to the high tensile stress. The maximum displacement value was located at the crest part of the dam. The findings revealed that the concentration of stresses in the dam body, especially heel and neck. The maximum normal stress was found at the heel zone of the dam. The trend of maximum shear stress shows a fluctuated value when the scale PGA increased. This showed that the performance level of the dam based on seismic loadings depend on ground motion pattern.

ISSN 1823-5514, eISSN 2550-164X
Received for review: 2022-07-23
Accepted for publication: 2022-12-20
Published: 2023-01-15

https://doi.org/10.24191/jmeche.v20i1.21083

Keywords: *Behavior of dam; Cracking; Displacement; Earthquake; Incremental Dynamic Analysis*

Introduction

Dam systems are high value infrastructure projects with significant importance. Building a dam in earthquake prone countries is increasingly demanding the safety of their structures. Inadequate seismic behavior of dams can lead to serious impacts on local communities. Dams constructed are considered vital assets for countries, and they must be built to withstand natural disasters, as dam failure would result in both human and financial losses [1]. However, the performance of the dam structure has deteriorated with the year due to earthquake occurrence which caused damages like a longitudinal or latitudinal crack of the dam due to land movement, floodway due to inundation of land, and more. In addition, the tremendous cost of dam construction and the severity of the implications caused by dam instability make dam protection, retention, and permanent evaluation a key issue since greater dam safety usually comes at a cost, it is vital to assure dam stability through design, implementation, and utilization procedures [2]. On top of that, the concern of less than one percent of the buildings in Malaysia are seismic resistant which can easily cause them damage when earthquake occurs [3]. Impact of earthquakes is one of the major concerns of scientists and engineers for a long time. Many studies have been made to mitigate the seismic responses of structures due to seismic loads [4-19].

Murum Hydro Power is placed at the top of Rajang River Basin on the Murum River, whereby Danum and Plieran Rivers, two of Murum's primary tributaries are combined to produce the Murum River. It has a power of 944 Megawatts and has produced 5952 Gigawatt-hours every year [20]. Murum Hydropower is made up of an RCC gravity dam with a tiered spillway, a water intake, a powerhouse, and an ecological power plant, which its ecological power plant is one of the company's distinguishing attributes. its goal is to maintain the downstream habitat by allowing for a regulated and continuous release of water while producing energy for Tegulang's resettlement. Next, the Murum dam is a massive concrete gravity in Belaga, Sarawak, Malaysia on the Murum River. The dam has a height of 141 meters, a length of 473 meters along the crest portion, a width of 75 meters transverse to the riverbed, and a depth of 135 meters [21]. The Murum dam is classified as a low seismic zone resulting in the dam facing any damaged occurrence caused by seismic gravity. Based on the previous researcher, the dam's static response recorded stresses at the dam body that were within acceptable limits. The result suggests that in the downstream segment, medium-level shaking (0.1 g) occurs, resulting in the

maximum capacity of Murum dam has been determined to be up to 0.1 g, which is adequate for Sarawak's minimal seismicity.

The shape of a concrete gravity dam is triangular in section, with the top crest frequently enlarged to allow a walkway over the dam. Concrete mass helps in resisting the water pressure of the dam, and the dam is made of vertical concrete blocks that are not reinforced and have joints between them [22]. Therefore, the structure must be built on a solid foundation to support the load. Upstream slope sliding at the auxiliary dam is one of the slope stability failure scenarios which occur due to earthquake shaking. Alternatively, a fast drawdown collapse of the auxiliary dam's upstream slope might have been precipitated by the quick emptying of the tiny reservoir through the main dam's break. The apparent lack of severe damage to this embankment's downstream slope, as well as the multiple slips in natural land surrounding the reservoir rim, corroborate the latter option [23]. High tensile strains form at the dam's base, on its downstream face, and close to its change in slope. Because the dam's rock contact and the rock underneath are projected to have lower tensile strengths than concrete, the magnitudes of stresses are larger near the base dam [24].

Methodology

Description of dam

Murum dam, which is located in Sarawak, is selected for this study. The concrete gravity of the Murum dam has a dimension of 141 meters in height, 75 meters in width, and 18.68 meters at the crest of the dam as shown in Figure 1. The material properties of the Murum dam must be considered such as density, elasticity, Poisson's ratio, and other properties as shown in Table 1.

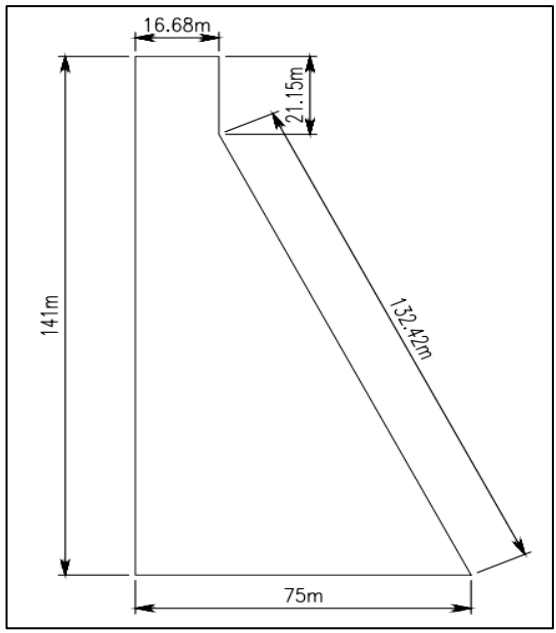

Figure 1: Cross sectional area of Murum dam in metre

Table 1: Properties of Murum dam

No	Parameter	Concrete
1	Density (kg/m^3)	2643
2	Elastic Modulus (GPa)	31.2
3	Poisson's Ratio	0.18
4	Compressive Strength (MPa)	24.10
5	Dilation angle	36.31

Model and analysis

In this study, six sets of earthquake motion were selected in various locations, which are Chichi, Chuetsu-Oki, Iwate, Northridge, Ranau, and Trinidad as shown in Table 2. The records were obtained from Pacific Earthquake Engineering Research Centre (PEER) data repository for various earthquake data. The data is then transferred into the SeismoSignal, which is Earthquake software for signal processing of strong-motion data to get the acceleration data in the horizontal and vertical directions and to obtain the maximum PGA as shown in Figure 2. Then, a scale PGA of 0.05 g, 0.10 g, 0.15 g, 0.20 g, and

0.30 g was selected. The Rayleigh stiffness proportional damping value is selected by using:

$$\beta = \zeta 1 / \omega 1 = 2(0.03)/18.61 = 0.00323\ s \quad (1)$$

Table 2: Detail of earthquake data

Earthquake	Date	PGA (g)	Period (s)
Chichi (Taiwan)	1999	0.36	49.94
Chuetsu-oki (Japan)	2007	0.17	11.98
Iwate (Japan)	2016	0.12	23.98
Northridge (USA)	1994	0.56	39.98
Ranau (Malaysia)	2015	0.15	70.76
Trinidad (America)	2015	0.19	21.40

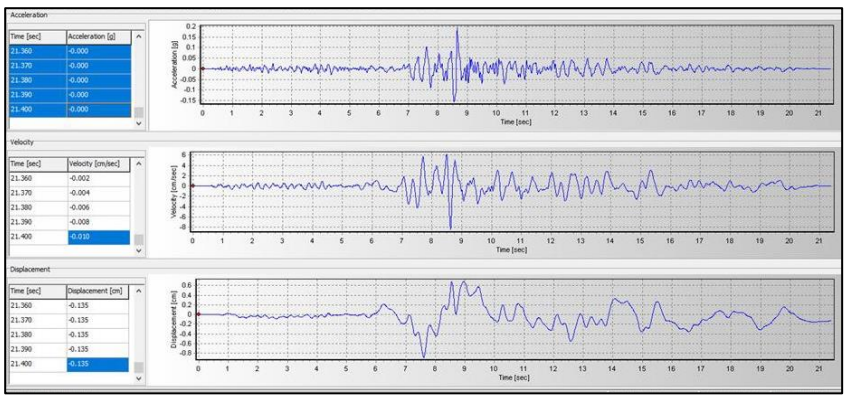

Figure 2: Ground motion in the horizontal and vertical direction of Trinidad earthquake

The initial design is started with the part module. A coordinate is used as it is easier to set up the initial point to draw the model and ease the meshing process to show valuable cues of each axis to the observer. Figure 3 shows a dam modeling, whereby a 2D planar is chosen in the modeling space of a solid shape with an approximate size of 300. The X-axis and Y-axis are used to set up the initial coordinate of (0,0) and continue until the dam is fully designed with a given dimension. In addition, the property module is selected to create the material by choosing the material behavior such as damping, density, elasticity, concrete tension damage, and concrete damage plasticity. The value of material properties collected such as Young's Modulus, density, Poisson's

ratio, and other properties are input under the property module. There are two steps used in this modeling, which are static and dynamic. These steps are used to select a range of incrementation of hydrostatic pressure toward the dam structure according to the incrementation of time. Step one, which is static or general is used with an incrementation of 100. Then, step two which is dynamic and implicit is used with the period of x seconds, whereas x depends on the period for each seismic loading selected in this study and the maximum number of increments is 100, 000. Next, two loads are used which are gravity and hydrostatic pressure. The first load, which is the gravity load, is selected as it indicates a self-weight load for step one. Then, the density load value of -9.81 kg/m^3 is input at y-axes with uniform distribution. Then, the second load which is the hydrostatic load is assigned with a magnitude formula $P= \rho gh$. Next, the first boundary condition is created, and displacement or rotation is selected for step one. Then, the requirement points or region are selected and the displacement values for both the x-axis and y-axis are considered 0 to indicate fixed support. The second boundary condition is created based on step two, and acceleration or angular acceleration is selected for step two. Then, the surface region is selected and the acceleration value at the x-axis is considered 9.81 kg/m^3. Amplitude is set as tabular, and the step time is selected to set the amplitude data according to the PEER ground motion database. Then, the step in the second boundary condition is repeated for the third boundary condition is created at the y-axis. Then, the data of seismic loading is applied to the amplitude data. Furthermore, a meshing module is created, whereby the independent mesh is used. A job module is created to submit and run the model.

Result and Discussion

The Murum dam has formed a major crack pattern when applied Ranau and Northridge's seismic loading at a scale Peak Ground Acceleration (PGA) of 0.3 g as shown in Figure 4. Meanwhile, the minor crack patterns of the Murum have been obtained when applied to the Iwate's seismic loading at a scale PGA of 0.3 g. A significant fracture appeared at the heel of the dam at the upstream surface as a general pattern indirectly as the cracking started at the dam from the neck of the dam on the downstream surface [25].

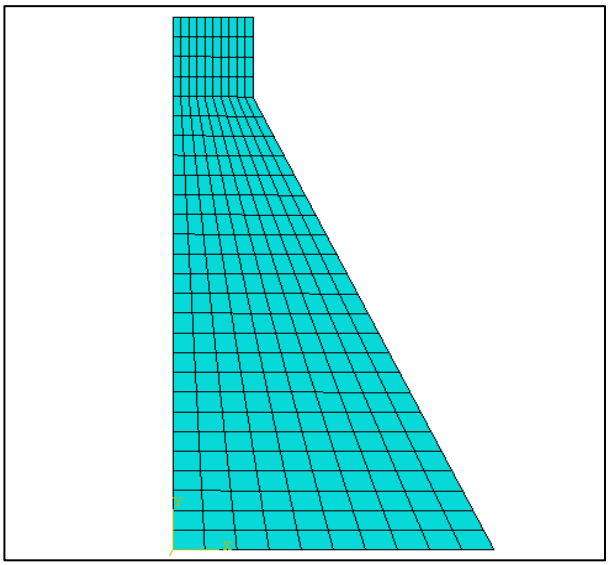

Figure 3: 2D of Murum dam using ABAQUS

When the PGA of the motion grew, fractures began to form at the dam's neck on the upstream surface, spread forward from both faces, and eventually united. the cracking area increases when the acceleration increases. The statement is because the strong earthquake shaking produced high acceleration, resulting in a high impact on the dam, particularly crack shapes. In addition, crack patterns started to occur on the dam at the lower PGA scale since the material of the dam was not able to cater to the seismic loading. Logically, the height of the dam might be influenced by its durability and stability of the dam. The higher the dam, the higher the tendency of cracks formation.

The maximum normal stress value for each seismic loading shows a fluctuated value when the PGA scale is increased as shown in Table 3. For example, the fluctuated value of maximum stress was found at Trinidad's seismic loading between scale PGA 0.15 g, 0.20 g, 0.30 g with the value are 98.50 kN/m^2, 5.31 kN/m^2, and 293.90 kN/m^2 respectively. The fluctuated values obtained by using ABAQUS are because each part of the dam structure such as the upstream, crest, downstream, heel, and toe of the dam experienced different pressure act on them. Figure 5 illustrates the maximum normal stress for Trinidad's seismic loading at a scale PGA of 0.30 g. The maximum tensile and compressive stresses are 293.90 kN/m^2 and 2375 kN/m^2 respectively. The maximum normal stress was formed around the heel zone of the dam due to the maximum pressure being located at the highest depth of the dam.

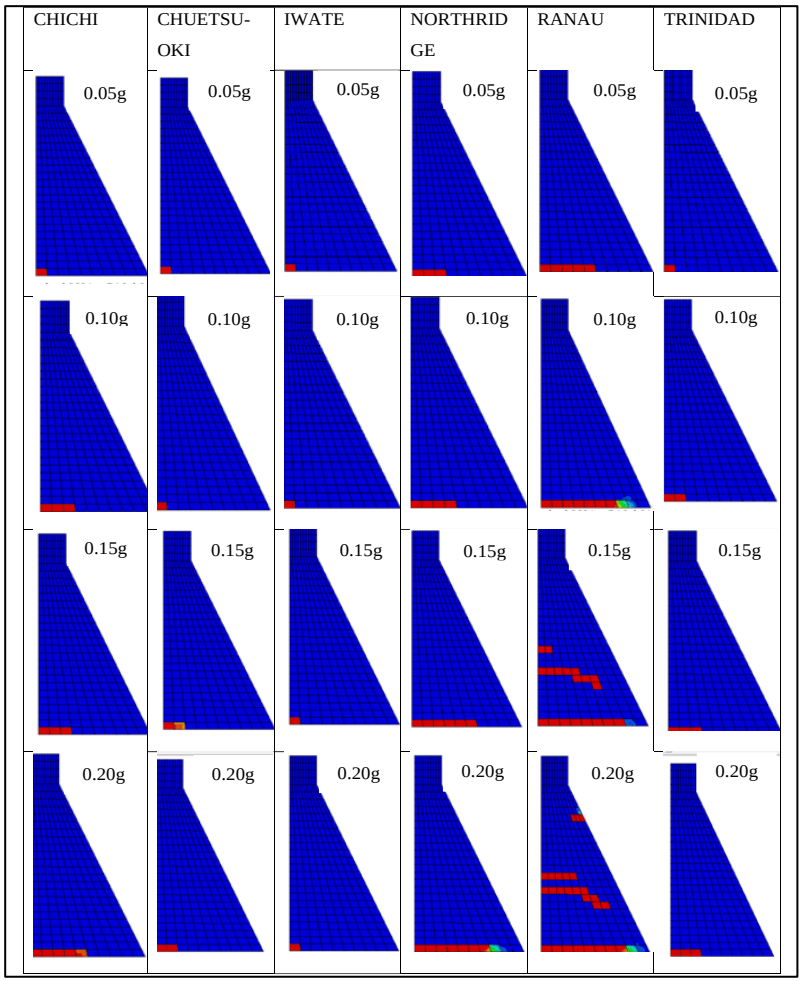

Figure 4: Crack patterns of Murum dam

Table 3: Maximum normal stress of Murum dam

Scale (g)	Chichi (kN/m^2)	Chuetsu-oki (kN/m^2)	Iwate (kN/m^2)	Northridge (kN/m^2)	Ranau (kN/m^2)	Trinidad (kN/m^2)
0.05	2.27	2.23	2.16	87.41	314.40	2.66
0.10	93.16	2.12	2.55	214.70	318.50	1.77
0.15	155.40	1.49	2.71	308.40	217.20	98.50
0.20	298.30	1.99	2.79	340.70	313.60	5.31
0.30	310.80	34.50	1.98	342.20	441.10	293.90

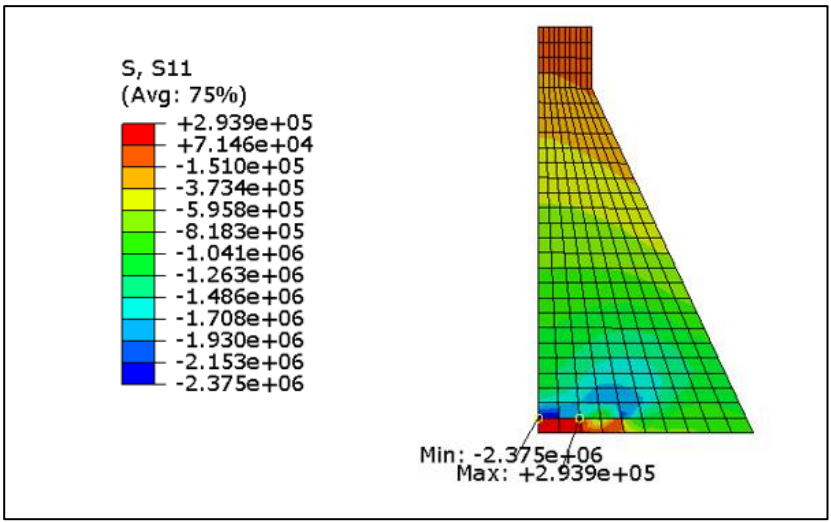

Figure 5: Contour maps of maximum normal stress under Trinidad's seismic loading

The formation of maximum shear stress for Trinidad's seismic loading can be found around the toe of the dam at a scale PGA of 0.30 g as shown in Figure 6. There are fluctuated maximum shear stress values as the scale PGA increased as shown in Table 4. For example, there are fluctuated maximum shear stress was found at Chuetsu-Oki's seismic loading between scale PGA 0.10 g, 0.15 g, and 0.20 g with the value of 1646.00 kN/m^2, 1640.00 kN/m^2, and 1717.00 kN/m^2 respectively. The fluctuated values obtained by using ABAQUS are because each part of the dam structure such as the upstream, crest, downstream, heel, and toe of the dam experienced different pressure act on them. The key static forces to be considered in a shear force situation are the self-weight of the dam, the hydrostatic pressure upstream, and the uplift pressure at the dam [26]. The maximum normal stress occurs on the major primary plane [27].

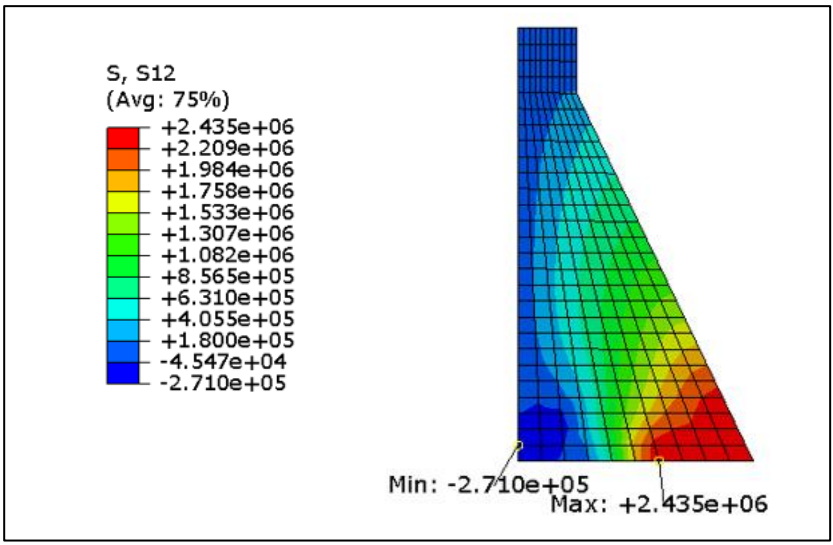

Figure 6: Contour maps of maximum shear stress under Trinidad's seismic loading

Table 4: Maximum shear stress of Murum dam

Scale (g)	Chichi (kN/m^2)	Chuetsu-oki (kN/m^2)	Iwate (kN/m^2)	Northridge (kN/m^2)	Ranau (kN/m^2)	Trinidad (kN/m^2)
0.05	1653.00	1650.00	1643.00	1803.00	2334.00	1669.00
0.10	1810.00	1646.00	1668.00	2222.00	4048.00	1648.00
0.15	1948.00	1640.00	1677.00	2976.00	5036.00	1745.00
0.20	2285.00	1717.00	1686.00	3744.00	6298.00	2023.00
0.30	2865.00	1886.00	1730.00	4872.00	7770.00	2435.00

The maximum displacement for each seismic loading was located at A which indicates as crest part of the dam. The scale PGA of 0.30 g with a maximum displacement value of 0.435 meters was found under Ranau's seismic loading. The trend in Figure 7 shows that the maximum displacement is increased as the scale PGA increases. For instance, the maximum displacement for Iwate's seismic loading is increased from 0.05 g to 0.30 g with its value of 0.063 g to 0.238, respectively. This is because the strong impact of seismic loading results in a higher value of crest displacement owing to the strength degradation of the material of the dam. Earthquake motion gives an impact on the dam in terms of displacement at the crest dam due to the joint opening and leads to cracks occurrence.

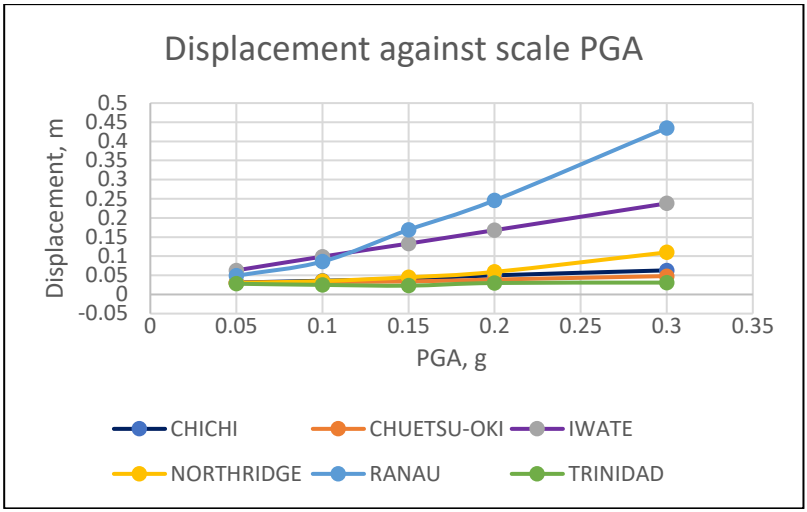

Figure 7: The relationship between maximum displacement and PGA

Conclusion

The study of seismic analysis by using the IDA method study of Murum dam provides insights into the performance or behavior of the dam under various sets of seismic loads with Rayleigh stiffness proportional damping of 3%. The 2D model of Murum dam by using ABAQUS displays the crack patterns of the structure due to seismic loads. The major crack pattern of the dam occurs under Ranau's seismic loads. In addition, the maximum normal stress and maximum shear stress distribution were identified. The formation of maximum normal stress occurs around the heel zone of the dam due to the maximum pressure produced at the highest depth of the dam. The trend for both maximum normal stress and shear stress presents a fluctuation value obtained by using ABAQUS since each part of the dam experience different pressure act on them. Next, the maximum displacement of the Murum dam occurs at the crest of the dam. The maximum displacement increases as the scale PGA increases due to the seismic motion, resulting in the joint opening.

Future studies will be highly interesting to conduct seismic analysis of the dam through the IDA method. Furthermore, utilization of a 3D finite-element method is necessary with a finer size of meshing to obtain the data accuracy. In addition, Rayleigh stiffness proportional damping value must be considered as it provides a reasonable estimate of dynamic response like

seismic motion. The material properties of the dam must be correctly input in the ABAQUS to ensure the reliability of the data.

Contributions of Authors

The authors confirm the equal contribution in each part of this work. All authors reviewed and approved the final version of this work.

Funding

This work received no specific grant from any funding agency.

Conflict of Interests

All authors declare that they have no conflicts of interest

Acknowledgment

The authors would like to acknowledge the facilities provided by Universiti Teknologi MARA (UiTM), Research Nexus UiTM (ReNeU), Institute of Quality and Knowledge Advancement (InQKA) and support from School of Civil Engineering, College of Engineering, Universiti Teknologi MARA (UiTM). The author is grateful for the constructive comments and guidance of the Editor and anonymous reviewers.

References

[1] Mahmoodi, K., Noorzad, A., Mahboubi, A., & Alembagheri, M, "Seismic performance assessment of a cemented material dam using incremental dynamic analysis," *Structures*, 29, 1187–1198, 2021.
[2] Ghanizadeh, E., & Ghanizadeh, M, "Evaluation of Stability and Performance of Dam Foundations at Static State," *European Journal of Sustainable Development*, 6(2), 2017.
[3] Sooria. S. Z., Sawada S., and Goto. H, "Proposal for Seismic Resistant Design in Malaysia: Assessment of Possible Ground Motions in Peninsular Malaysia," Annuals of Disaster Prevention Research Institute, Kyoto University, no. 5, 2012.

[4] Ismail. R, Ibrahim. A, Adnan, "Determination of Shear Wave Velocity Profile by Using Multi-Channel Analysis of Surface Wave (MASW)," *Journal of Architecture and Civil Engineering*, vol. 7, no. 2, pp. 1-6, 2022.
[5] Ismail, R., Hussin, N.S.A., Ibrahim, A, Rusop. M., Adnan, A, "The Performance of Roller Compacted Concrete (RCC) Dam Under Seismic Load," *Journal of Architecture and Civil Engineering*, vol. 6, no. 6, pp. 13-23, 2021.
[6] Ismail. R., Shamsudin. N., Arshad. M.F., Ibrahim. A., Rusop. M., Adnan. A, "2-Dimensional Finite Element Analysis of Reinforced Concrete Buildings Subjected to Seismic Load," *Journal of Architecture and Civil Engineering*, vol. 6, no. 6, pp. 1-6, 2021.
[7] Ismail, R. Rajhan, N. H., Hamid, H. A., & Ibrahim, A, "Experimental data for effect of carbon black loading on tensile, hardness and rebound of magnetic iron filled natural rubber composites," *Data in Brief*, vol. 25, pp. 1-10, 2019.
[8] R Ismail, A Ibrahim, M Rusop, A Adnan, "Dynamic mechanical properties of natural rubber vulcanizates with different carbon nanotubes-loaded," *AIP Conference Proceedings*, vol. 2151, no. 1, 2019.
[9] R Ismail, A. Ibrahim, M Rusop, A Adnan, "Magnetic properties of carbon nanotubes-natural rubber composites." *AIP Conference Proceedings*, vol. 2151, no. 1, 2019.
[10] R. Ismail, A. Ibrahim, H. Hamid, M. Rusop, A. Adnan, "Experimental study on mechanical properties of elastomer containing carbon nanotubes," *Journal of Engineering Science and Technology*, vol. 13, no. 3, pp. 565 – 664, 2018.
[11] R. Ismail, A. Ibrahim and A. Adnan, "Damage Assessment of Medium-Rise Reinforced Concrete Buildings in Peninsular Malaysia Subjected to Ranau Earthquake," *International Journal of Civil Engineering and Technology*, vol. 9, no. 7, pp. 881–888, 2018.
[12] A Faisal, TA Majid, F Ahmad, F Tongkul, SM Sari, "Influence of large dam on seismic hazard in low seismic region of Ulu Padas Area, Northern Borneo." *Natural hazards*, vol. 59, no. 1, pp. 237-269, 2011.
[13] MZAM Zahid, TA Majid, A Faisal, "The Effect of Behaviour Factor on The Seismic Performance of Low-Rise and High-Rise RC Buildings." *Journal of Engineering Science and Technology*, vol. 12, no.1, pp. 31-41, 2017.
[14] Ismail, R.; and Ismail, M.I., "Dynamic Analysis of Concrete Faced Rockfill Dam Using Finite Element Method," *Journal of Engineering and Applied Sciences*, vol. 12, no. 7, pp. 1772-1776, 2017.
[15] Ismail, R.; and Abdul Karim, M.R., "Concrete Bridge Pier Performance Under Earthquake Loading." *Journal of Engineering and Applied Sciences*, vol. 12, no. 9, pp. 2254-2258, 2017.

[16] Ismail R.; Ibrahim, A.; and Razali, N., "Vulnerability study of public buildings subjected to earthquake event." *MATEC Web of Conferences*, vol. 103, pp. 9, 2017.
[17] Ismail, R.; Kamsani, M.H.; and Mohd Nadzri, N.I., "Seismic Analysis of Concrete Dam by Using Finite Element Method." *MATEC Web of Conferences*, vol. 103, pp. 9, 2017.
[18] Ismail, R., and Zamahidi, N. F., An evaluation of High-Rise Concrete Building Performance Under Low Intensity Earthquake Effects, InCIEC 2014, pp. 79-86, 2015.
[19] Rozaina Ismail, A'in Fatin Najihah Akmat, Ade Faisal, Azmi Ibrahim, Azlan Adnan, Izzul Syazwan Ishak, "Behaviour of earth fill dam under earthquake load using Finite Element Method: A case study of Semenyih dam," *Journal of Sustainable Civil Engineering and Technology*, vol.1, no. 2, pp. 63-77, 2022.
[20] Hussain, M. (2017). Harnessing hydropower for SCORE: A success story of Murum hydroelectric plant Realtime flood forecasting and early warning system for hydro plants View project Assessing climate change impact on hydropower generation in Sarawak View project Harnessing hydropower for SCORE: A success story of the Murum hydroelectric plant. https://www.researchgate.net/publication/320344272
[21] Roslan, L., Ahmadi, R., Lau, K. K. F., Trinh, L. T., & Rosyadi, M., "Risk-assessment of hydropower plant susceptible to seismic hazard by 3D spectrum analysis," *IOP Conference Series: Materials Science and Engineering*, vol. 910, no. 1, 2020.
[22] Jabbar Mizhir Alfatlawi, T., Jawad Kadhim, M., & Noori Hussein, M. (2021). "Relation between cracks behavior and curvature in cracked concrete arch dam under earthquake," *Materials Today: Proceedings*, 2021.
[23] Kayen, R, "Preliminary Observations of the Fujinuma Dam Failure Following the Tohoku Offshore Earthquake," Japan Related papers, 2011.
[24] Ghanaat, Y., & Chudgar, A. K, "Seismic Design and Evaluation of Concrete Dams," An Engineering Manual, 2012.
[25] Nik Azizan, N. Z., Majid, T. A., Nazri, F. M., Maity, D., & Abdullah, J, "Incremental Dynamic Analysis of Koyna Dam under Repeated Ground Motions," *IOP Conference Series: Materials Science and Engineering*, vol.318, no. 1, 2018.
[26] Monteiro Azevedo, N., Bretas, E. M., & Lemos, J. V, "Shear sliding of gravity dams for maximum design earthquake analysis," *15th World Conference on Earthquake Engineering (15WCEE)*, vol. 1995, pp. 1–10, 2012.
[27] Sharma, S, "Principal stresses and shear stress," Nov 20, 2020. [Online]. Available: https://civilengineering.blog/2020/11/20/principal-stresses-and-shear-stress/

Development of an Analysis Method for Radial Forging Parameters Based on Hardness Criterion

Saeed Darki[*], *Evgeniy Yurevich Raskatov*
New Material and Technology Institute
Ural Federal University
[*]*saeed.darki@yahoo.com*

ABSTRACT

Considering the complexity of the radial forging process, the study of dynamic and thermodynamic parameters is of great importance. With the severe deformation of a workpiece in a plastic state, the effects of all parameters affecting the final geometry of the forging pipe need to be optimized. Thus, the mathematical model of the process is based on visco-plastic material, taking into account thermomechanical coupling and the surface properties during forging, including the hardness of the workpiece and friction. The results present the effects of a die angle on residual stress, total wear, and contact force, leading to ideal operating conditions and the ideal design of machine parts. In order to ensure the accuracy of the calculations and predictions made through software, a hardness test was performed experimentally, which showed the hardness curve of the microstructure and the strain of the workpiece. This indicates the consistency and accuracy of the results obtained from both methods. In order to improve the process and the tube employed, using an optimized die is recommended.

Keywords: *Finite Element Method; Radial Forging Tube; Residual Stress; Hardness Microstructure; Neutral Plate Coordinate*

Introduction

One tube-forming technique is the Radial Forging Process (RFP), during which the product is surrounded by four dies. This is designed to create round products such as tubes, shafts, stepped shafts, axes, gun bars, and rifle barrels. Reducing the diameter of specimens is the main purpose of radial forging [1]. Accordingly, four dies with special feed rates and rotational angles surround

ISSN 1823-5514, eISSN 2550-164X
Received for review: 2022-06-14
Accepted for publication: 2022-11-16
Published: 2023-01-15

https://doi.org/10.24191/jmeche.v20i1.21084

the specimen. When feeding stops, these dies reduce the diameter and deform the specimen via frequent strokes. Based on these deformations, variations in specimen dimensions in both the radial and axial directions occur. In other words, geometry changes occur in both directions: in the radial direction, which changes the radius, and in the longitudinal direction, which changes the length of the hollow shaft [2].

Farahani et al. [3] found the optimum design profile of the die. Based on this study, they applied two methods of analysis (FEM and the slab method) and compared the results of these two methods for conical and curved specimens. In this comparison between analytical and numerical methods, the results showed only a 6% difference. They also claimed that by increasing the angle and plug angle up to 20°, the normalization of the die presser by plug pressure decreases. In order to estimate the total load except for FEM, the upper bound method can calculate the total force within RFP. Therefore, Groche and Hebdzyński [4]-[5] expressed the relationship between strain and hardening, one of the essential phenomena during cold processes that can directly affect the total load. Studies performed with a sensor element with two separate mandrels have shown that neglecting hardening zone materials with a high hardness coefficient leads to a deviation in the residual stress up to 30%. Designing a radial forging machine and its components, Herrmann et al. [6] and Kocich [7] devised a machine that included four levers and one eccentric sleeve: a ball-and-socket joint supported the levers. Within the new design, they studied the effect of die angle and feed rate, claiming that the forging force decreased. A die surface was designed in order to improve the reduction zone. It was shown that by increasing the amplitude factor, the axial forging force decreases: the designed tools also do not require lubricating material. In addition, Lahoti [8] investigated a multiplier bar within an Al/Cu/Al structure. They analyzed the total force and microstructure behavior through simulation and experiments. According to the results, the total force depends on the length of the multiplier bar, while the maximum force is located at the midpoint in the axial direction. The length of the specimen can affect friction between the various layers. Through an experimental study, Lim et al. [9] presented the microstructure, hardness, and diameters of a bar after the swaging process. Accordingly, they showed that the density of the material increased by decreasing grain size: the hardness and diameter reduction have a direct relationship.

To analyze RS (Residual Stress), strain, and the effect of friction coefficient, Liu et al. [10]-[11] investigated RFP through 2D FEM simulation. Most variations in RS occurred in the axial direction when increasing the feed rate, while the hoop stress criteria are very sensitive to variations in the reduction rate. The final strain is reduced by enhancing the friction value. Due to the nature of RFP, the optimal value of each parameter should be adjusted according to the material and other parameters, but the changing trend is almost constant. Accordingly, the drawing force is decreased by increasing the

die angle; after an increase of almost 6°-8°, the drawing force will increase through the drawing bar [12]. The maximum reduction on the bar and strain hardening are directly proportional. While most scientists have studied this using a 2D mathematical model, this cannot cover all variations during the process.

In this regard, Moumi et al. [13] studied the material flow of the swaging process via FEM. A neutral plate was subjected to a variety of friction and feed velocities. This simulation, based on a 2D cloud, describes various process parameters. By increasing the velocity of feeding, the rate of the neutral plate's location change decreases. One of the essential boundary conditions in order to simulate RFP is the assumed flow material within the process. Therefore, Pantalé and Gueye [14] investigated the Ludwik and Johnson-Cook laws of the behavior of the 2D materials. The elasto-viscoplastic equation is unable to describe the strain rate in cold forging, while the Johnson-Cook law can describe material behavior during cold forging in terms of the strain rate. They show that maximum thickness occurs with a 17% reduction in specimen diameter when operating without a mandrel.

Investigating the microstructure of a forged tube can present the relevant criteria during the process, such as die geometry. The analysis of micro hardness can be used as a validation method. Thus, Sanjari et al. [15]-[17] claimed through a microstructural investigation that by increasing the friction coefficient, the homogeneity of deformation will increase. Moreover, they showed that increasing the friction factor can increase the effective strain: the variations of strain range will increase. The die angle makes the most significant contribution to optimizing the parameters.

Sonmez and Demir [18] measured effective strain values at several points along with a specimen. Therefore, the hardness was calculated via the hardness function and measured values. While FEM produces fewer errors than the upper bound method (based on validation by experimental outcomes), Yang et al. [19] analyzed radial forging with rectangular die and specimens through the upper bound method and FEM. They showed that by increasing the die angle, the axial flow of the material decreases. Due to the wide range of RFP applications, Zhang et al. [20] utilized RFP to join tubular parts. They showed that the length of overlapping could increase the connecting strength; however, if the necking for aluminum increases by more than 45%, the aluminum will fail.

Although FEM and parameter impact have been considered in previous investigations, they have neglected the interaction of parameters with each other or the implementation of the most accurate model and method. Therefore, it is necessary to examine this complex process through variations in the essential parameters that influence the process and to take a comprehensive view of the effects of these changes on the specimen. Therefore, a 3D visco-elastoplastic model was chosen, as it predicts and characterizes this process and all factors affecting it with high accuracy. In

addition, the results were validated through the two parameters of total load and micro hardness. The experimental and simulation results agree, indicating the accuracy of the simulation and prediction process. The equipment for the experiment was located in the metallurgical and rotary machines and organizations of machine-building production in the enterprise Ural NITI (Ekaterinburg).

The parameters and methodology of RFP

RFP is one of the basic tools for metal deformation. This machine includes four dies, which surround the specimen and make consecutive strokes in order to increase material strength. There are many types of radial machines with different functions, such as hot or cold forging, hydraulic or mechanical stroking, and rotary swaging. The radial forging equipment used in the simulation is shown in Figure 1. The mandrel is fixed to the specimens and then four dies deform the product with consecutive strokes.

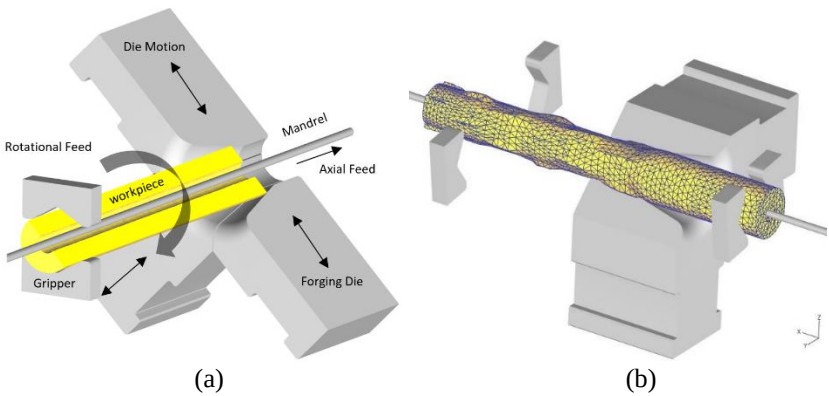

Figure 1: (a) Components and direction of elements in RFP, and (b) the 3D section of simulation with the mesh grid of the workpiece during the simulation process

Quality and dimension precision depend heavily on the process parameters. These parameters directly affect the longevity of the die and forging machine by helping to calculate the residual stress and principal stress on the other components. As such, investigating die geometry through 3D finite element simulation, which can present all interactions between the equipment during operation, is essential. Moreover, regardless of the geometric characteristics of the workpiece, other end-product features, such as residual stress and microstructure, can be affected by the design criteria of the radial forging machine. The geometrical parameters of the die are presented in Figure 2.

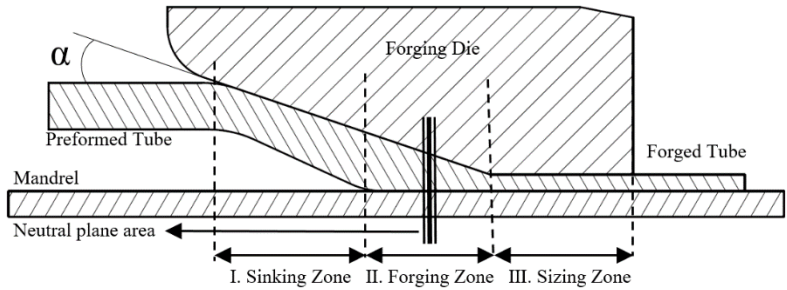

Figure 2. Die angle and three typical zones in the radial forging process

In this figure, the three sections of the die are shown. These have three roles: sinking, forging, and sizing. The die angle has direct effects on sinking and forging. It can also change the coordinates of the neutral plane according to the material flow. The section of the die has a direct relationship with the feed rate and homogeneity deformation of the specimen's surface. The important factors in RFP, such as total force, die angle, type of friction, and value of the coefficient friction, can have a principal role in microstructure hardness, material flow, residual stress, and the amount of increased strength of the specimen. Therefore, these factors are discussed below via a comparison between different types of friction and the value of parameters.

Two types of friction are considered: Coulomb (sliding) and constant shear (sticking). The coulomb law describes the contact forces between two objects under elastic deformation. However, these objects can be elastic-plastic: one is elastic and the other is rigid during elastic deformation. Moreover, the simulation of sheet forming is recommended. Frictional stress is calculated to describe the contact of two plastic or porous objects by the flow stress of the object. The frictional force in the Coulomb's law model is defined via:

$$f_s = \mu P \tag{1}$$

where f_s is frictional stress, P is the interface pressure between two bodies, and μ is the friction factor. Constant shear friction includes highly precise measurement and modeling of bulk-forming simulations. The frictional force in the constant shear law is defined as follows:

$$\tau = m\sigma_y/\sqrt{3} \tag{2}$$

where m is the frictional coefficient and σ_y is the normal yield stress of the material. This states that friction is a function of the yield stress of the deforming body.

The steel DIN-16CrMo4 is considered to create mathematical modeling and simulation. The material parameters are as follows (Table 1).

Table 1: Mechanical properties of the used material

Density (kg/m3)	7870
Young's modulus (GPa)	212
Poisson's ratio	0.3
Specific heat (J/kg/· C)	750
Conductivity (W/m/· C)	15
Melting temperature (C)	1450-1510
Inelastic heat fraction	0.9
Thermal expansion coefficient (1/· C)	11×10^{-5}
Yield Strength (Mpa)	275

Regarding the primary boundary condition for the workpiece, a temperature of 900 °C was used to begin the forging process. This is the primary temperature recommended by previous studies, a necessary experimental condition in order to keep the mechanical properties of the material, and the best temperature for the forging process. In addition, the mathematical model of flow stress is driven by the Johnson-Cook equation:

$$\bar{\sigma} = (A + B\bar{\varepsilon}^{n})\left(1 + C\ln(\frac{\dot{\bar{\varepsilon}}}{\dot{\bar{\varepsilon}}_0})\right)\left(\frac{\dot{\bar{\varepsilon}}}{\dot{\bar{\varepsilon}}_0}\right)^{\alpha}(D - ET^{*m}) \quad (3)$$

where $T^{*} = \left(\frac{T - T_{room}}{T_{melt} - T_{room}}\right)$ and $(\bar{\sigma})$ is the material flow stress. Effective plastic strain rate $(\dot{\bar{\varepsilon}})$ and (T_{melt}) are at melting temperature. $A, B, C, D, E, n, \alpha, \dot{\bar{\varepsilon}}_0$ are model coefficients of the material, and T , m are the thermal softening of the material. A flow stress chart is presented in Figure 3.

As mentioned, parameters such as residual stress can have a direct impact on the strength of the specimen and its longevity. Residual stress is a function of multiple factors such as temperature, die angle, total force, and friction: thus, the effect of these factors is presented and analyzed separately. Thus, material flow velocity, one of the factors used for calculating the microstructure of the material and the amount of hardness, is examined in the following sections. Moreover, the effect of die angle on the neutral plane coordinates via material velocity and the location of the neutral plane relative to the die zone are presented. In terms of friction, the effects of different values of coefficient friction on temperature, residual stress, and specimen quality are shown. The most accurate and most suitable types of friction have been determined by comparing the simulation results for two types of friction and their effect on forging force. It is worth mentioning that the type of friction has been determined using the simulation results closest to the actual results. In

this investigation, the simulation has been validated by comparing experimental hardness values and simulated hardness values. Specimen hardness itself is a function of different parameters, however; it is expressed here using temperature and effective strain. For this purpose, a hardness test was designed to measure hardness at several points along the specimen. Finally, as simulation verification, the experimental and measured graphs were compared. Other outcomes of the simulation could be cited, such as residual stress and the analysis of other influences on specimen quality.

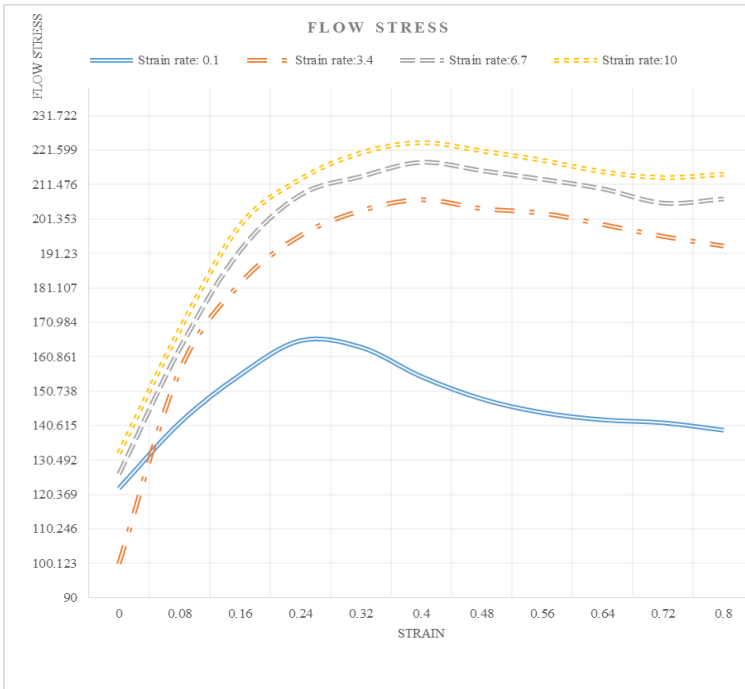

Figure 3. Flow stress-strain curve of the DIN-16CrMo4 steel at 900 ˚C

In general, due to the complex nature of the process, which is a function of overlapping multiple factors, there is no explicit concept of optimization for the whole process. When expressing an optimal value for die angle, total force, or feed rate, other parameters may be neglected. Thus, it seems that the best way to study this process is a comprehensive analysis of the effects of the parameters on each other. Due to the wide potential application of this process, it is worthwhile attempting to increase the quality of the specimen and meet working conditions.

Numerical analysis and experimental method

There are several methods for analyzing the forging process, such as the upper bounds methods, the slab method, and others investigated and implemented by previous authors: however, the most accurate results were obtained by FEM using 3D Deform software. This method provides a comprehensive view of all the phenomena and conditions during forging.

By applying appropriate boundary conditions and simulation parameters, simulation accuracy can be significantly increased. Therefore, conditions such as friction in all process components (the back spring pressure of manipulators and the mandrel and their impacts on material flow) are considered. Using specimen temperature, the heat transfers of the mandrel and the specimen have been calculated: this can have a direct effect on specimen hardness. Therefore, the visco-plastic model has been used for a more accurate examination of the material flow rate. The Von Mises yield criterion has been implemented in order to determine the flow rules. Darki et al. [1] have presented the relation between the essential matrices of FEM.

Although other models such as the rigid plastic or elastoplastic ones have been used in most previous studies, these do not have the necessary precision to determine neutral plate coordinates. In other words, it can be stated: (i) the viscoelastic properties have been considered for workpieces; (ii) there is heat transfer during the forging process; and (iii) the other components of the forging machine have been assumed to be rigid materials, including the dies and mandrel. The final stress after each stroke on the product is defined as residual stress within the final product.

In order to investigate the effects of the die angle, six different specimens are considered: these are described in the following Table 2. Other geometrical dimensions of the components are listed in Table 2. It should be noted that all measurements in the simulation after each stroke have been taken into account to show that stroke effect remains the same over the length of the tube. The length of the specimen is 200 mm. The simulation dynamic parameters, such as rate of stroking (stroke per min), rotating feeds, axial feed (mm), number of strokes, number of passes, and rotations per pass, are respectively; 400, 36°, 20, 12, 2, and 10°.

Table 2: Dimensions of the components of radial forging machine

Outer diameter – Reduction rate	30mm – 20%
Inner diameter – Reduction rate	10mm – 60 %
Outer diameter for mandrel	4mm
Length of die	70mm
Length of die land	25mm
Die angle	5°, 10°, 12.5°, 15°, 20°, 90°

To validate the simulation, the hardness criterion is measurable. For this purpose, two auxiliary criteria, effective strain and temperature, have been used. These two criteria have an impact on the hardness of the specimen as illustrated in Figure 4. For this reason, a tube with the geometry of the simulated specimen is used. A hardness tester measured the length, radius, and thickness of the sample. The following is a view of the measured sample.

Figure 4: The specimen of the tube for the hardness test

The experiment used standard temperature conditions and a portable hardness tester to measure the hardness in different sections at random points. According to the dimensions of the tube, the impact device type D was considered for measuring the hardness of the tube in different sections through the variations of effective strain. For this purpose, about 50 points were marked and measured. It should be noted that the die angle for this test was 5°. After measuring the radius variations and calculating the effective strain on the sample, the hardness-strain curve was obtained. The effective strain equation is given below [2].

$$\overline{\varepsilon} = \frac{\sqrt{2}}{3}\sqrt{(\varepsilon_1 - \varepsilon_2)^2 + (\varepsilon_2 - \varepsilon_3)^2 + (\varepsilon_3 - \varepsilon_1)^2} \tag{4}$$

where $\varepsilon_{1,2,3}$ are the principal strains and $\overline{\varepsilon}$ is the effective strain. By measuring the different strains on the specimen through simulation and placing them into the hardness function, the hardness value of the specimen is shown. To apply the temperature effects to other types of die and to show the distribution of hardness in all sections of the specimen, the hardness-temperature curve was defined by the hardness values obtained for different strains and temperature values. The hardness distribution is thus rendered visible by the temperature and strain effects. After comparing the experimental and simulation results and verifying the accuracy of the simulation, the same method of simulation was used to analyze the other parameters. The following equation expresses the hardness function, where (Hv) is hardness and ($\bar{\varepsilon}$) is effective strain.

$$Hv = -60.7\bar{\varepsilon}^2 + 119.1\bar{\varepsilon} + 115.1 \quad (5)$$

In terms of the comparison between the error percentage of the simulation and experimental results, the current simulation procedure can be used for developing and expanding the investigation of parameters such as coefficient friction and die geometry. This simulation has been verified by comparing it with experimental results for cold RFP, which is presented in Table 3 [1].

Table 3: Specimen geometry and contact force via the experimental and simulation results of process [1]

Sample type	Outer radius of perform (mm)	Inner radius of preform (mm)	Out radius of product (mm)	Inner radius of product (mm)	Die force (KN)
Experiment	18	14.6	13.70	9.30	385.00
FEM	18	14.5	13.66	9.45	366.480

Based on the methodology section and Table 3, the dimensions of the experimental and mathematical models for a cold forging sample are illustrated. According to the obtained results, a good correspondence is established between the practical and FE model results in terms of contact force. In Figure 5, it is shown that a radial forging machine can produce experimental contact force. The difference in the obtained results is less than 5%, which might be due to a thermal effect. In this figure, two different parts of the radial forging machine are shown. Figure 5a shows the position of the workpiece relative to the die and hammer and the location of the workpiece and the feeding device. Figure 5b shows a side view of the machine to present the shape of the die, die angle, and zones of the die.

In order to measure the contact force between the die and the workpiece, two different methods have been considered based on experimental testing and FEM. During the experimental testing, in the case of contact force, the radial forging machine has the ability to calculate the contact force: the diameter is measured by the operator manually. Likewise, for FEM, commercial software can calculate the contact force at each step: the deformation and reduction of the diameter can be measured by the simulation. The stress and wear distribution on the die and workpiece can be calculated.

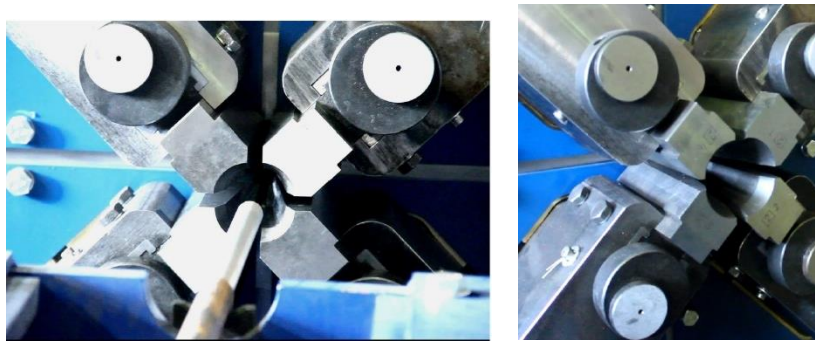

(a) (b)

Figure 5: Radial forging machine with a feeding system during the practical test

Results and Discussion

Since the contact force is one of the principal criteria of RFP in order to analyze the process, the examination of contact force vs radius reduction leads to an estimate of the quality of the created tube and the dimensions of the radial machine. Therefore, Figure 6 displays the contact force in the experimental results [9] and the FEM results vs the reduction to the outer radius of tube. This has been obtained to estimate applied force vs reduction radius for the used material. According to this comparison, the current simulation results have less error than other methods and previous investigations [16].

The importance of force calculation is twofold. First, force is the most fundamental parameter in the forging process: on its basis, the validation of the simulation and calculations can be confirmed. Second, the changes in the force parameter in relation to the reduction of the workpiece's diameter and the prediction of the required force for the design of the forging process can be shown. Therefore, the die contact force is shown based on the changes to the diameter of the workpiece: this can be used to verify the simulation. The force change function, based on the reduction of the tube diameter, needs to be obtained for other designs in order to give a criterion for predicting the total force of the process.

Die angle impacts

In Figure 7, the effective strain distribution along the specimen at different angles is displayed. The most uniform deformation belongs to the 15° angle. The 5° and 90° angles have the highest strain oscillations, indicating surface non-uniformity.

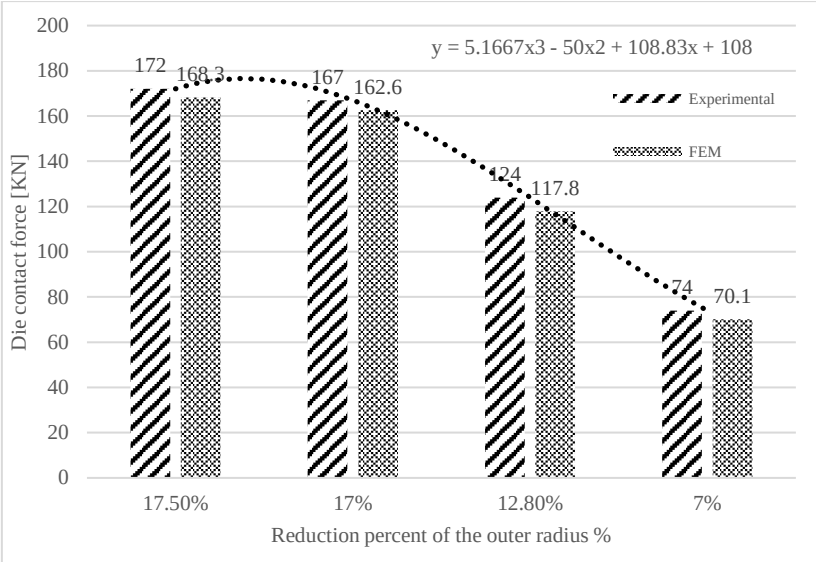

Figure 6: The reduction radius rate vs applied force with an estimate by a 3-degree polynomial function

Sanjari et al. [16] claimed that at an angle of 5°, the neutral plate is in the forging section. According to the obtained results, as the angle increases, the position of the neutral plate moves from the size section to the forging section. Similarly, as the angle decreases, the distance of the neutral plate from the edge of the pipe increases. On the other hand, as the die angle increases, the angle of the distribution of velocity zones in the material increases (β), which in turn can affect the shape of the granular material, thereby establishing a criterion for describing the microstructure. Figure 8 illustrates this phenomenon, the variation of the angles of the material flow layers, and the position of the neutral plate.

Just as angle changes have different effects on the specimen, these changes can also occur in the forging machine. Residual stress is an important parameter in die analysis. For this purpose, the maximum stroke amplitude for different angles in the first pass was considered and the residual stress in the same motion range calculated.

These variations are displayed in Figure 9. According to the results, the lowest value is produced by an angle of 12.5°. After this angle, the residual stress on the die increases significantly. There are no drastic changes for angles lower than 12.5°.

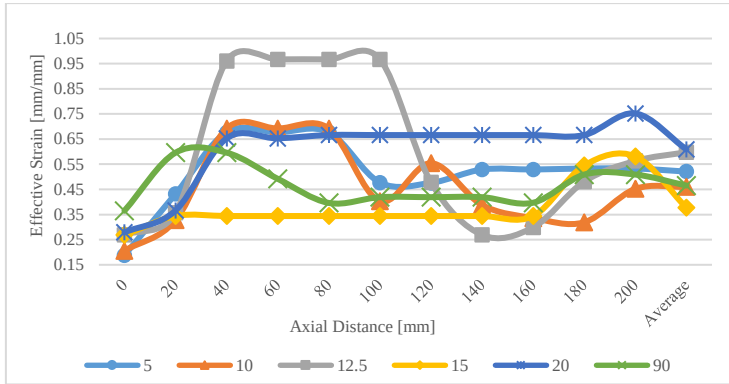

Figure 7: Distribution of effective strain along the specimen at different die angles

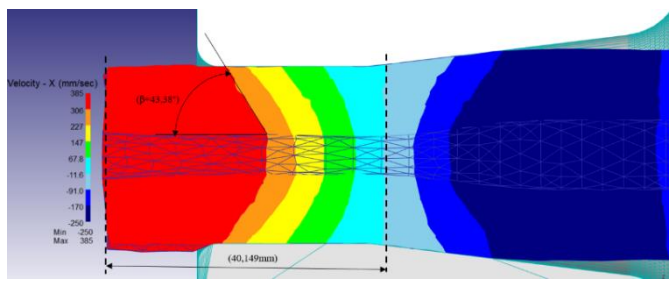

(a)

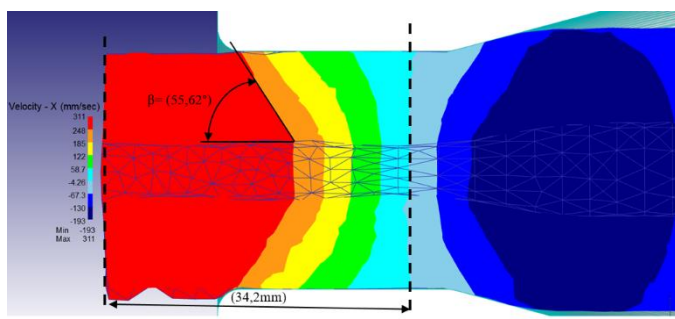

(b)

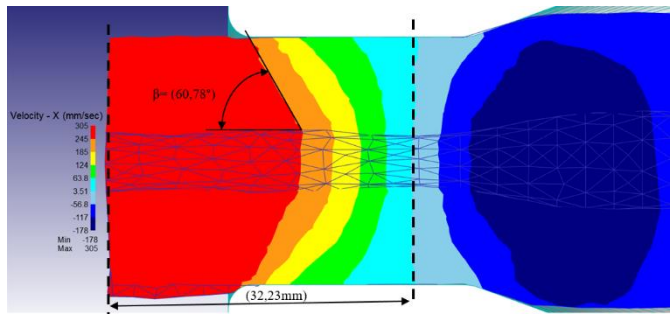

(c)

Figure 8: (a) 5 die angles, (b) 15 die angles, and (c) 20 die angles vs the distribution of velocity and the distance between the end of the specimen, the neutral plane, and the angle of velocity

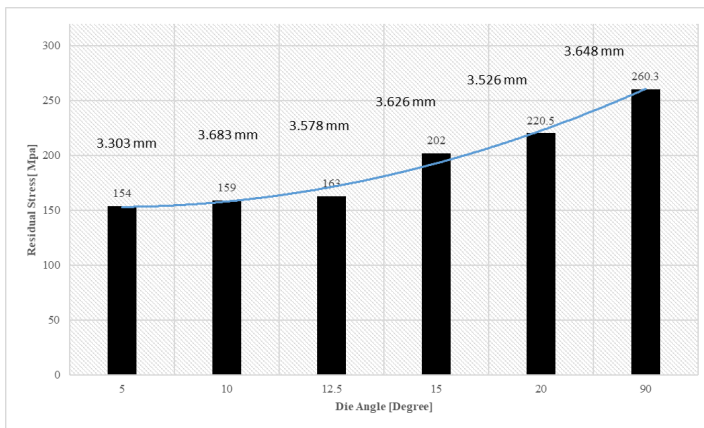

Figure 9: Die distribution of residual stress at maximum strokes at different die angles

Hardness

Tube hardness analysis here consists of two parts: analysis of the experimental results and analysis of the simulation results. In the experimental section, after calculating the effective strain value and measuring the hardness of the specimen with a hardness tester, the curves of the effective strain and hardness were obtained. Figure 10 expresses the strain-hardness curve obtained via 4 approximated polynomials. Similarly, Figure 11 shows that the measured values by a hardness tester were between 0.2-0.3 mm/mm effective strain. Finally, the investigation and analyses have been validated by comparing the hardness-strain curve obtained through the simulation and the experiment.

Given the strong agreement between the simulation and experimental results, it can be claimed that other simulation results are reliable for analyzing radial forging in industrial conditions.

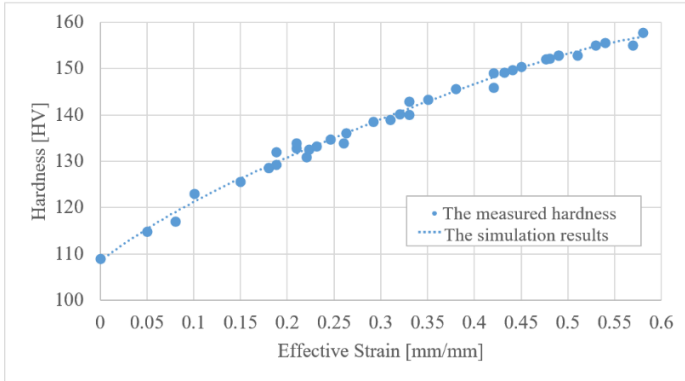

Figure 10: Comparison of the hardness-strain experimental curve (measurement) and simulation values by an approximate fourth-order polynomial

Figure 12 shows the hardness distribution on the specimen's surface along the longitudinal line. According to the results, the lowest value for hardness distribution on the surface is produced by an angle of 15°. On the other hand, this angle leads to the highest hardness uniformity. The uniformity of the hardness distribution can be a criterion of microstructure quality and the uniformity of granularity in the surface layers.

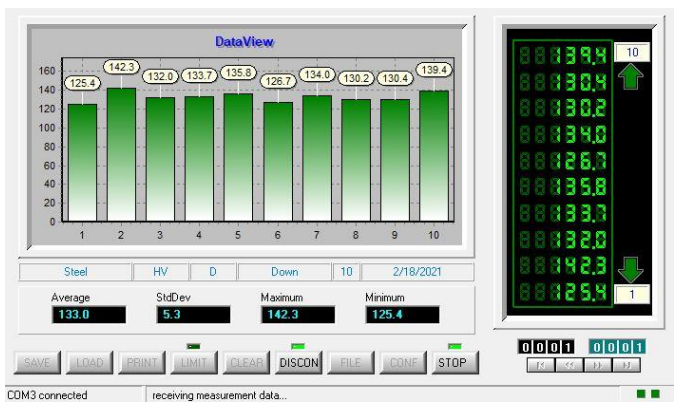

Figure 11: The display of measured values by a tester on a computer

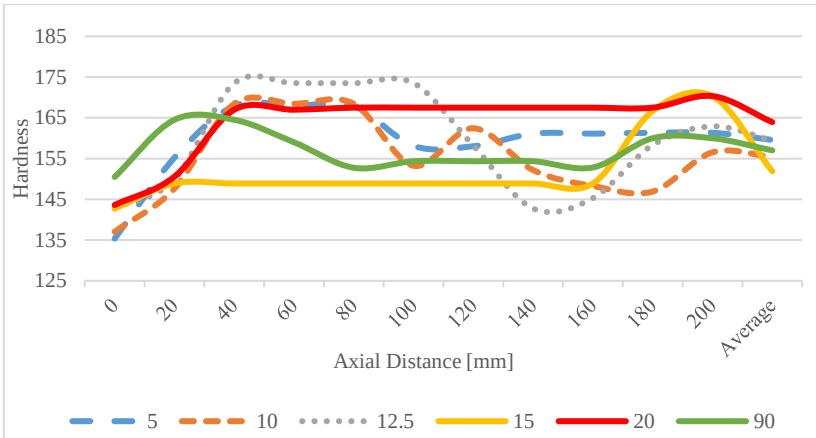

Figure 12: Distribution of hardness along the specimen at different die angles

According to the calculations and simulation, the relationship between the die angle and the effective strain is shown along the length of the tube. Moreover, the lowest effective strain rate is produced by an angle of 15 degrees, which is shown in Figure 7. The relationship between the effective strain and the hardness of the tube is illustrated in Figure 10. The hardness of the workpiece increases as the effective strain increases by an approximate fourth-order polynomial. For this reason, it can be concluded that an angle of 15 degrees produces the lowest strain rate and thus has the lowest level of hardness.

Conclusion

In this research, a three-dimensional model of a radial forge was simulated and subjected to numerical analysis based on FEM. The simulation and experimental results were compared to each other. The strong agreement of the obtained results indicates the accuracy of the simulation for analysing and predicting the characteristics of specimens based on the required conditions. In this research, an attempt has been made to analyse all the parameters affecting this process in order to provide the specimen with the required characteristics.

To investigate the current forging process further, other parameters can be analysed after improving the quality of the workpiece, such as the die stress and the wearing of the die. In addition, the improvement of different shapes of die by taking into account the wear rate and stress of the die can be recommended. Therefore, the results can be summarized as follows:

i. As the die angle increases, the angle of the velocity layers (β) in the material increases. This can reduce the distance between the neutral plate and the end of the specimen, transferring it to the sizing area. As a result, the radial force increases.
ii. Increasing the die angle increases residual stress in the die. Thus, for angles above 12.5°, residual stress in the die increases considerably, which indicates a decrease in the longevity of the die and an increase in die fatigue.
iii. The highest hardness is obtained at an angle of 20°, which creates uniform hardness along the entire length of the specimen. The amount of hardness changes greatly at other angles.

Contributions of Authors

The authors confirm the equal contribution in each part of this work. All authors reviewed and approved the final version of this work.

Funding

This work received no specific grant from any funding agency.

Conflict of Interests

All authors declare that they have no conflicts of interest.

References

[1] S. Darki and E. Y. Raskatov, "Analysis of the hot radial forging process according to the finite element method," *The International Journal of Advanced Manufacturing Technology*, vol. 110, no. 3–4, pp. 1061–1070, 2020.
[2] V. Deform and P. C. Documentation, "DEFORM V11.0 (PC) Documentation," vol. 1. Instruction and tutorial of 3D Deform software.
[3] N. D. Farahani, A. Parvizi, A. Barooni, and S. A. Naeini, "Optimum curved die profile for tube drawing process with fixed conical plug," *The International Journal of Advanced Manufacturing Technology*, vol. 97, no. 1–4, pp. 1–11, 2018.
[4] P. Groche and M. Krech, "Efficient production of sensory machine elements by a two-stage rotary swaging process—Relevant phenomena

and numerical modelling," *Journal of Materials Processing Technology*, vol. 242, pp. 205–217, 2017.
[5] R. Hebdzyński, S. Kajzer, and R. Kozik, "Forging on the four-lever arms swaging machines," *Journal of Materials Processing Technology*, vol. 64, no. 1–3, pp. 199–206, 1997.
[6] M. Herrmann, C. Schenck, and B. Kuhfuss, "Dry Rotary Swaging with Structured Tools," *Procedia CIRP*, vol. 40, pp. 653–658, 2016.
[7] R. Kocich, L. Kunčická, C. F. Davis, T. C. Lowe, I. Szurman, and A. Macháčková, "Deformation behavior of multilayered Al-Cu clad composite during cold-swaging," *Materials and Design*, vol. 90, pp. 379–388, 2016.
[8] G. D. Lahoti and T. Altan, "Analysis of the radial forging process for manufacturing rods and tubes," *American Social Mechanical Engineers*, vol. 98, no. 1, pp. 265–271, 1975.
[9] S. J. Lim, H. J. Choi, and C. H. Lee, "Forming characteristics of tubular product through the rotary swaging process," *Journal of Materials Processing Technology*, vol. 209, no. 1, pp. 283–288, 2009.
[10] L. Liu and L. Fan, "Study of residual stresses in the barrel processed by the radial forging," *2009 2nd International Conference on Information Computing Science ICIC 2009*, vol. 4, pp. 131–134, 2009.
[11] Y. Liu, M. Herrmann, C. Schenck, and B. Kuhfuss, "Plastic Deformation Components in Mandrel Free Infeed Rotary Swaging of Tubes," *Procedia Manufacturing*, vol. 27, pp. 33–38, 2019.
[12] M. M. Mahdavi and H. Haghighat, "On the Optimum Die Angle in Rod Drawing Process Considering Strain- hardening Effect of Material," *Iranian Journal of Mechanical Engineering*, vol. 20, no. 1, pp. 113-128, 2019.
[13] E. Moumi, S. Ishkina, B. Kuhfuss, T. Hochrainer, A. Struss, and M. Hunkel, "2D-simulation of material flow during infeed rotary swaging using finite element method," *Procedia Engineering*, vol. 81, pp. 2342–2347, 2014.
[14] O. Pantalé and B. Gueye, "Influence of the constitutive flow law in FEM simulation of the radial forging process," *Journal of Engineering*, vol. 2013, pp. 1-8, 2013.
[15] M. Sanjari, A. Karimi Taheri, and A. Ghaei, "Prediction of neutral plane and effects of the process parameters in radial forging using an upper bound solution," *Journal of Materials Processing Technology*, vol. 186, no. 1–3, pp. 147–153, 2007.
[16] M. Sanjari, P. Saidi, A. Karimi Taheri, and M. Hossein-Zadeh, "Determination of strain field and heterogeneity in radial forging of tube using finite element method and microhardness test," *Materials and Design*, vol. 38, pp. 147–153, 2012.
[17] M. Sanjari, A. K. Taheri, and M. R. Movahedi, "An optimization method for radial forging process using ANN and Taguchi method," *The*

International Journal of Advanced Manufacturing Technology, vol. 40, no. 7–8, pp. 776–784, 2009.

[18] F. O. Sonmez and A. Demir, "Analytical relations between hardness and strain for cold formed parts," *Journal of Materials Processing Technology*, vol. 186, no. 1–3, pp. 163–173, 2007.

[19] X. Yang, X. Dong, and Y. Wu, "An upper bound solution of forging load in cold radial forging process of rectangular cross-section billet," *The International Journal Advanced Manufacturing Technology*, vol. 92, no. 5–8, pp. 2765–2776, 2017.

[20] Q. Zhang, Y. Zhang, M. Cao, N. Ben, X. Ma, and H. Ma, "Joining process for copper and aluminum tubes by rotary swaging method," *The International Journal of Advanced Manufacturing Technology*, vol. 89, no. 1–4, pp. 163–173, 2017.

Study of Viscoelastic Behavior and Mechanical Characteristics of Graphene-Filled ABS Composites

Basanta Kumar Behera
Department of Polymer Engineering,
B. S. Abdur Rahman Crescent Institute of Science and Technology,
Chennai-48, INDIA

Thirumurugan M[*]
Department of Mechanical Engineering,
B. S. Abdur Rahman Crescent Institute of Science and Technology,
Chennai-48, INDIA
[*]*thirumurugan@crescent.education*

ABSTRACT

Acrylonitrile-Butadiene-Styrene (ABS) thermoplastic composites were reinforced with graphene fillers for three different weight ratios of 0.3%, 0.6%, and 0.9%. The compounding was prepared using a twin-screw extruder, and the specimens were made using an injection molding machine. The thermal gravimetric analysis (TGA)study revealed that the thermal stability of ABS composites was improved (~7%) by adding graphene fillers in pure ABS.The tensile and flexural strength of the ABS/grapheme composites was maximumwith the addition of 0.6 wt% graphene fillers. But the impact strength was reduced (~42%) for the addition of graphene fillers of more than 0.6 wt%. The stiffness of pure ABS was enhanced by more than ~27% with the addition of graphene fillers. It was found from a Dynamic Mechanical Analysis(DMA) study that the storage modulus and Tan Delta values of the composites were improved compared to pure ABS. The storage modulus was increased by more than ~70% over a wide range of temperatures. The addition of graphene fillers in the ABS matrix improved the glass transition temperature (increased from 110 ˚C to 118 ˚C). Scanning Electron Microscope (SEM) images confirmed the homogeneous mixing of the ABS matrix and the graphene fillers, and better dispersion was noticed with 0.6 wt% of graphene fillers.

Keywords: *ABS; Graphene; Viscoelastic; Thermal; Mechanical Properties*

ISSN 1823-5514, eISSN2550-164X

https://doi.org/10.24191/jmeche.v20i1.21086

Received for review: 2022-03-13
Accepted for publication: 2022-11-03
Published: 2023-01-15

Introduction

For the last few decades, metallic components have been replaced by lightweight plastic and composite materials in the automobile and manufacturing industries. Acrylonitrile Butadiene Styrene (ABS) is one of the very commonly used engineering plastic materials in automobile industries because of its lightweight and ease of processing characteristics. The glass transition temperature of ABS material is 105 ℃, and it is used for various applications within a temperature range of – 20 ℃ to 80 ℃ because of its low melting temperature. Extensive research is available to enhance polymer matrix's mechanical, thermal, and viscoelastic characteristics by adding fillers. The purpose of adding fillers in thermoplastic polymers is to reduce cost and improve the physical, mechanical, and thermal characteristics. Shrinkage and warpage are the problems encountered while producing injection-molded plastic parts. These issues can be addressed by adding a certain amount of fillers to the plastic materials. Mechanical and tribological properties characterized the incorporation of ZnO as filler in a pure ABS polymer matrix. It was reported that the tensile and flexural strengths increasedup to 10 wt% of the filler content before declining. Still, the stiffness of the composites gradually increased with the increment in the wt % of the ZnO in the ABS matrix of the injection-molded composites [1].

Thermoplastic composites were also prepared with Polytetrafluoroethylene (PTFE) and nano zirconia as filler in the ABS matrix via compression molding. It is reported that the thermal stability, storage modulus, tensile strength, and flexural strength are improved. However, the damping properties are reduced due to the addition of nano zirconia [2]. Investigation results revealed that the inclusion of graphite in ABS material lowers the mechanical properties. In contrast, the tribological properties are improved as the wt% of graphite (Gr) increases, and it was concluded that 7.5 wt % of filler shows the best coefficient of friction and weight loss [3]. The ABS's thermal, mechanical, and electrical properties were enhanced by adding carbon nanotubes (CNT). The stiffening effects of ABS are improved for the (1, 2, 4, 6, and 8 wt%) of CNT addition, and the 6 wt% of CNT shows good electrical conductivity compared to pure ABS [4]. Incorporating nano alumina in ABS increases thermal stability but reduces the stiffness of pure ABS. The alumina nanocomposites and carbon nanotubes with ABS improve hardness, Young'smodulus, tensile strength, and flexural modulus [5]-[6]. The rheological, thermal, and mechanical properties were studied, and it reported that 20wt% of Gr in ABS decreases melt flow index (MFI) and ABS+20wt% of Gr composites exhibited the highest heat capacity (0.84 J/g) [7]-[8].

Graphene consists of many carbon atoms, which are arranged in hexagonal positions. Graphene and graphene oxide has better mechanical (hardness, elasticity) and thermal properties (thermal conductivity), and the

scientific community has used this material to improve the properties of other plastic materials**.** The strength of graphene is many times more than steel, and it finds applications in electronics, solar panels, and automotive electric vehicles. Graphene is incorporated into various polymers to enhance the properties of the polymer, and the results showed that it affects the mechanical and thermal characteristics of the matrix. It was also reported that graphene oxide could be used as a compatibilizer in ABS composites to improve the thermal and mechanical properties and enhance the adhesion between the matrix and filler. The tensile strength, flexural strength, and flexural modulus increased by 30, 15, and 90%, respectively [9]. Researchers used graphene as filler in thermoplastic materials like Polyamide (PA), High-density Poly Ethylene (HDPE), Poly Propylene (PP), and Polyethylene (PE) to improve the toughness, mechanical, thermal, and thermal conductivity [10]–[16].

It was reported that adding only 0.6wt% graphenes enhances the mechanical properties [17]. The optical properties of Poly-Methyl—Met-Acrylylate and Polyvinyl alcohol (PMMA-PVA)/graphene oxide composites improve the optical properties (absorption – 400%, absorption coefficient – 337%, reflective index – 51%), and these types of composites find applications in radiation shield and optoelectronic applications**.** The incorporation of graphene and graphite in polyester material reported improved viscoelastic and thermal properties. They characterized the properties using Dynamic Mechanical Analysis (DMA), Thermo gravimetric Analysis (TGA), and Scanning Electronic Microscope (SEM)and made the analytical inference of storage modulus and damping factor by Einstien and Neilson method, respectively [18]. It was noticed that the dispersion of graphene oxide made efficient chain grafting and improved the bonding between the matrix and filler [19]-[20].

The dynamic mechanical analysis (DMA) technique characterizes the viscoelastic properties of injection-molded plastic composites. It is one of the most commonly employed techniques to measure storage modulus, loss modulus, and the Tan Delta of thermoplastic composite materials. The plastic parts used for automobile applications are subjected to vibration with various frequencies and temperature changes.

In the dynamic mechanical analysis method, the storage modulus gives information concerning time and temperature. The stiffness of any material is directly proportional to the storage modulus, and the loss modulus demonstrates how the plastic material dissipates energy for the heat generated by molecular movement. When the temperature increases in any material, the molecules move faster, and the internal frictional resistance also increases. As a result, the heat is converted from one form to another. The damping factor Tan Delta is the ratio between the storage and loss modulus. The peak value of Tan Delta in dynamic mechanical analysis indicates the glass transition temperature of plastic composite. Tan Delta value indicates

the compatibility and interfacial adhesion between two phases of composite [23]-[27]. The heights of Tan Delta peaks are also an indication of bonding quality.

Research has been done to investigate the mechanical, thermo-mechanical, thermal, and dynamic mechanical characteristics of neat ABS by adding ZnO, nano zirconia, alumina, copper, and carbon nanotubes. Still, tothe author's knowledge, no such work has been reported on ABS/graphene composites prepared by injection molding [1], [3], [5]. This research aims to investigate the viscoelastic, thermal, and mechanical properties ofcomposites prepared by adding 0.3, 0.6, and 0.9 wt% of graphene via the injection molding process and compare the results with the neat ABS polymer. The SEM images revealed the uniform dispersion of graphene powder in the pure ABS. DMA, TGA, and Universal Testing Machine (UTM) instruments investigated the dynamic mechanical, thermal, and mechanical characteristics. The results showed that the presence of graphene filler improved pure ABS's storage modulus, mechanical properties, and thermal stability.

Methodology

Materials

Acrylonitrile Butadiene Styrene (ABS) of 1.06 g/cm^3 and melt flow index (MFI) of 28 gm/10 minutes were procured from Formulated Polymers, Chennai, in the granular form. The graphene powder of particle size 60 microns was purchased from Chem – O – Chem, a Chemical supplier in Chennai, India. Figure 1 shows macroscopic images of the procured raw materials ABS and Graphene.

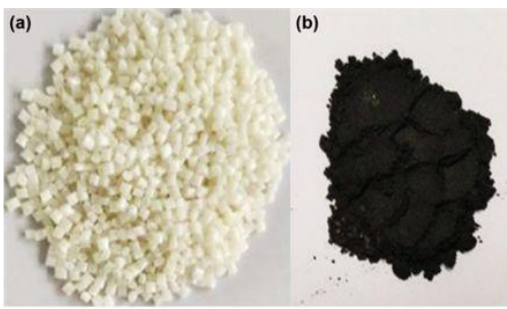

Figure 1: (a) Pure ABS, and (b) graphene

Compounding and sample preparation

The moisture of granular ABS material was removed by keeping it in an oven for 6 hours at a temperature of 80 ˚Cand then mixed manually with graphene powder of wt% 0.3, 0.6, and 0.9. The amount of ABS material was 2 kg for each composition, and the paraffin oil used was 10 mL to mix the ABS and graphene. A counter-rotating twin-screw extruder was used for the uniform dispersion of the graphene filler in the ABS matrix. Before compounding, both materials were kept for 4 hours at a temperature of 80 ˚C in an oven. The temperature ranges of the three zones in the twin-screw extruder barrel were maintained in the range of 220-260 ℃ and the screw speed was maintained at 80rpm. Water cooling was given at the exit of the extruder to remove the heat caused due to the extrusion process. Then it was passed through a pelletizer, and uniform sizes of granules were obtained.

The samples were prepared by injection molding technique in a 300 x 300 mm two-plate mold. The injection pressure for injecting the material was set at a pressure of 85 bar, a holding pressure of 50 bar, and back pressure was 15 bar. The overall cycle time per cycle was 68 seconds.

Characterizations

Thermo Gravimetric Analysis (TGA)

This method is commonly used to assess the thermal stability of polymeric materials. The loss of mass of the samples was measured using TGA Q50 V20.13 Build 39 instrument, and the temperature was increased from 30 ℃ to 800 ℃ with a heating ramp of 10 ℃/min.

Dynamic Mechanical Analysis (DMA)

The DMA tests were conducted on DMA (DMS 6100, SII Nano Technology, Japan) instrument (Polymer Nano Technology Center, BSACIST). The samples of dimensions 45 x 10 x 2 mm were heated at a rate of 3 ℃/min. The composites' storage modulus, loss modulus, and Tan Deltawere tested at1 Hz. The results were compared with the neat ABS.

Analysis of mechanical properties

The dog bone shape specimenwas obtained from injection molding dimensions 160 x 10 and 3 mm. The tensile test was conducted per international ASTM D638 using the universal testing machine of load cell capacity 5 kN at a crosshead speed of 50 mm/min. Test results were recorded, and the average value was calculated. The flexural strength of the composites was measured as per ASTM standard D790, and the specimen size was 100 x 10 x 3 mm.

Hardness is another important property of any material, and it was measured for the samples prepared using a digital-type hardness tester. The average values of a minimum of 5 samples were taken.

Scanning Electron Microscopy (SEM)

The morphological analysis of the composites was conducted using a scanning electron microscope (SEM Carl Zeiss, USA, Bruker,German). The dispersion of filler in the matrix and the voids created during the compounding of the matrix and filler were analyzed using SEM images with different magnifications.

Result and Discussion

Thermogravimetric Analysis (TGA)

Thermogravimetric analysis (TGA) is a material characterization technique used to investigate the thermal stability of polymeric materials. In TGA, the mass loss with the temperature increase at a constant rate is measured. Particularly the plastic products, injection molded, and the polymers used for adhesives and food industries are analyzed the thermal stability as plastic materials lose their properties as the temperature changes [2], [6], [26].

Derivative thermogravimetry (DTG) is a derivative curve. It is possible to find the temperature at which the thermal degradation starts, the maximum degradation rate, the temperature at the end of thermal degradation, and the number of steps involved in the thermal degradation of the composite materials. The addition of graphene particles in the neat ABS matrix restricts the movement of the polymer chain, and as a result, the thermal property of ABS material improves.

The TGA graphs of ABS/Graphene composites prepared with 0.3, 0.6, and 0.9 wt% of graphene are represented in Figure 2. The degradation of ABS/graphene composites is observed in two steps. The degradation of the composite starts slowly in the first step at a temperature of 190 ℃. The loss of mass from 100% to 95% takes place over a temperature range from 190 ℃ to 390 ℃ due to degradation. During the second step of degradation, there is an abrupt drop in tweight lossat a temperature of 390 ℃ for all three ABS/graphene composites [28]. This degradation is related to the evolution of the volatile products derived from polybutadiene. It is observed that the thermal stability of ABS material is increased due to the addition of graphene filler. The ash content in ABS/graphene is larger than thatof pure ABS, and it may be one of the reasons to improve thermal stability.

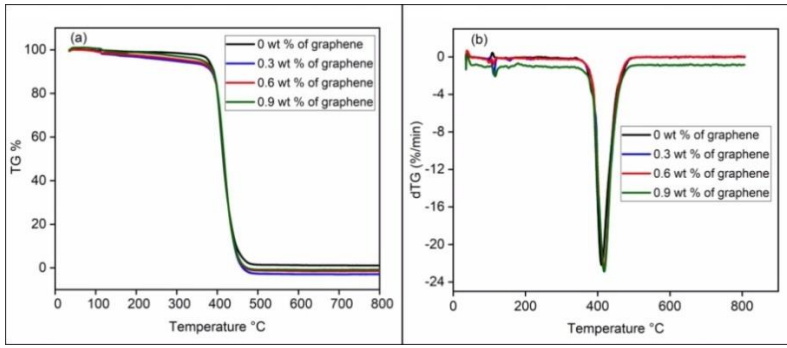

Figure 2: TGA Thermograms (a) temperature vs. TG% (b) temperature vs DTG

Dynamic Mechanical Analysis (DMA)

The DMA technique is used to understand the viscoelastic characteristics of ABS/graphene composites. The material properties may vary based on temperature, time, frequency, and stress. So, to understand these effects on the materials DMA test is important. In the DMA test, the storage modulus refers to the amount of energy stored in the polymer. The loss modulus is an indicator of the amount of energy the polymer dissipates. How the viscoelastic material absorbs and releases,the Tan Delta quantifies energy. The peak value of Tan Delta indicates the glass transition temperature.

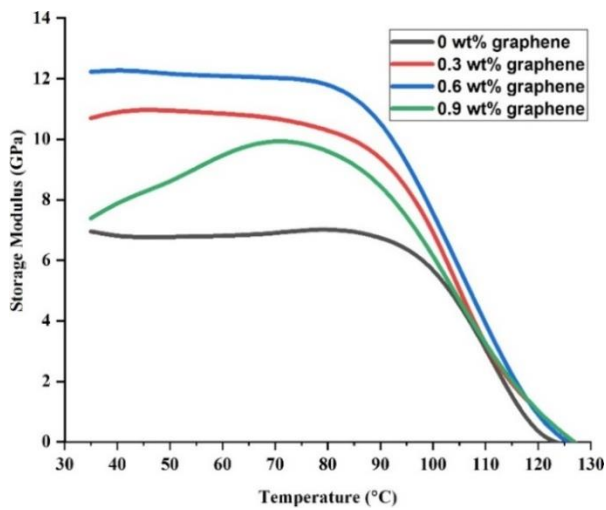

Figure 3: Effect of graphene content in storage modulus in ABS/graphene composite

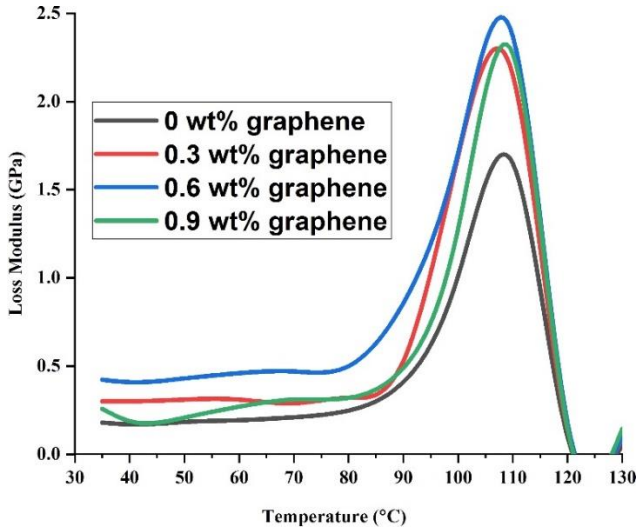

Figure 4: Effect of graphene content in loss modulus of ABS/graphene composite

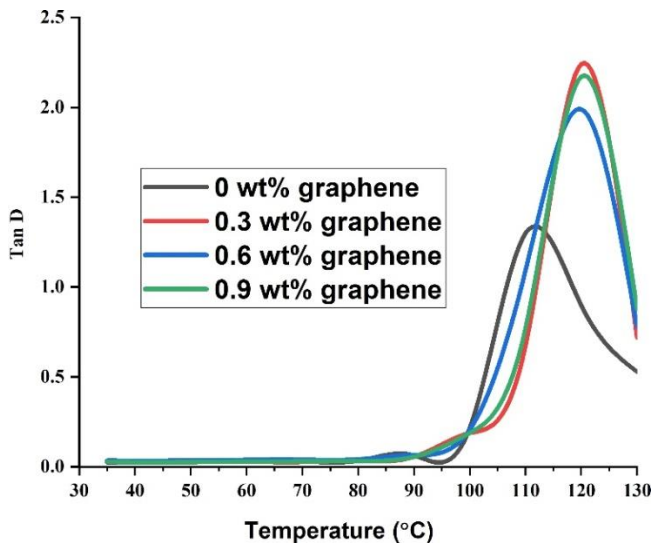

Figure 5: Effect of graphene content in Tan D of ABS/graphite composite

The mechanical properties correspond to changes in temperature examined by thermomechanical characterization. The storage modulus, loss modulus, and Tan Delta curves as a function of temperature are shown in

Figure 3, Figure 4, and Figure 5. From the DMA curves of the prepared composites, it was observed that the gradual increase of graphene filler in the ABS matrix has a substantial impact on improving the storage modulus at all temperature ranges, and similar results are reported by researchers [21]-[22], [25]-[27]. One of the main reasons for to increase in the storage modulus and glass transition temperature (T_g) may be the large difference in mechanical properties of the matrix and filler [27].

Table 1: Storage Modulus corresponds to different temperatures

Temperature in ℃	Storage modulus of Neat ABS in GPa	Storage modulus of ABS with 0.3 wt% of graphene in GPa	Storage modulus ABS with 0.6 wt% of graphene in GPa	Storage modulus ABS with 0.9 wt% of graphene in GPa
40	6.87	11	12.3	7.63
70	6.89	10.7	11.8	10.2
100	4.66	7.22	8.23	6.75

Table 1 shows that at all the temperatures, the storage modulus maximum corresponds to 0.6 wt% of graphene in the ABS matrix compared to the other composites. The storage modulus of 0.6 wt% graphenes in ABS at a temperature of 40 ℃ is 79% higher than that of pure ABS. Its modulus is much higher than the other composites, even at higher temperatures. The addition of graphene increases the storage modulus compared to neat ABS, but the optimum value corresponds to 0.6 wt% of graphene.

As the storage modulus decreases beyond 0.6 wt% of graphene, the probable reason may be the deterioration of chemical bonding between the ABS matrix and the graphene filler. The weak bonding is due to agglomeration of filler content beyond 0.6 wt% of graphene,which is evident from the SEM images (Figure 9) of composites. It is noticed that the storage modulus becomes very negligible beyond the glass transition temperature, and the curve is a rubbery plateau [25]-[26]. The increased stiffness is due to the homogeneous dispersion of graphene in the ABS material, which restricts the movement of a polymer chain, which is difficult to move.

From the storage modulus vs. temperature, it was observed that the storage modulus of the composites slowly decreases from 35 to 80 ℃ and its value falls abruptly from 80 ℃ to 120 ℃. At a temperature of 84 ℃, the storage modulus of 0.3, 0.6, and 0.9 wt% graphenes with ABS composites are 10.4 GPa, 11.2 GPa, and 9.6 GPa, respectively.

Tan Delta is the representation of the damping of the composite materials, and it also represents the glass transition temperature of polymer materials. From the Tan Delta vs. temperature curves, it is noticed that the

glass transition temperature of 0.3, 0.6, and 0.9 wt% graphene composites are 120 ℃, 116 ℃, and 115 ℃, respectively.It was found that the addition of bentonite and alumina fillers in ABS improves the thermal stability and increases the glass transition temperature (T_g) of the ABS matrix [2], [5]. Compared to bentonite and alumina, the improvement in the glass transition temperature of ABS was found slightly more in graphene filler.

Mechanical characteristics

The mechanical properties of the composites are presented in Figure 6, Figure 7, and Figure 8. The shore hardness with the varying wt% of graphene is shown in Figure 6a, and with the addition of 0.6 wt% of graphene in the ABS, the matrix increases the shore hardness up to 93 and reduces when 0.9 wt% of graphene was incorporated in ABS [2], [6], [25], [28]. The impact strength vs. the wt% of graphene is represented in Figure 6b. It shows that the impact strength of ABS material continuously decreases with the increases in wt% of graphene content. It has been reduced from 187 J/m to 109 J/m, a reduction of 41.71% compared to the pure ABS material [2].

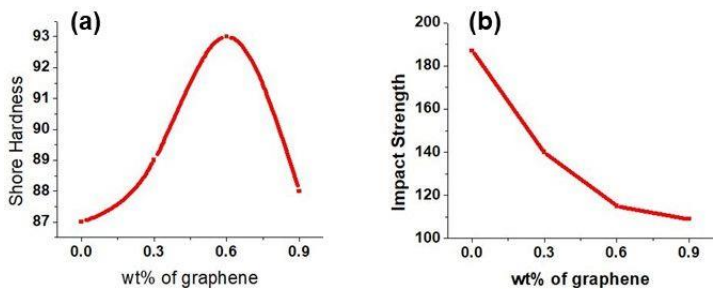

Figure 6: Effect of wt% of graphene in ABS matrix; (a) shore hardness, and (b) impact strength

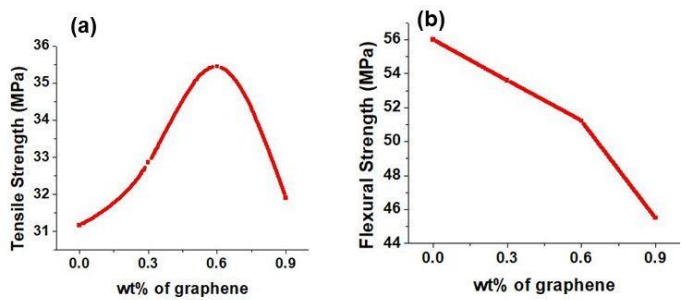

Figure 7: Effect of wt% of graphene in ABS matrix; (a) Tensile strength, and (b) flexural strength

The tensile and flexural strengths of the composites with the different wt% of graphene are shown in Figures 6a and 6b, respectively. The tensile strength increased with the increase of graphene content up to 0.6 wt% and was then found to decrease, but the flexural strength of the composites continuously decreased with an increase in the filler content.We can attribute this strength weakening to the result of poor dispersion of graphite content (0.9 wt% of graphene) in the ABS. With a smaller amount of graphene powder, the bonding between the matrix and filler was strong, and the tensile strength increased [5]. But at a higher graphene concentration, graphene dispersion was difficult, and agglomeration and voids reduced the tensile strength. The tensile strength is increased from 31.17 MPa of neat ABS to 35.45 MPa, corresponding to 0.6 wt% in the matrix [29]-[30], which has an increment of 13.73%, and the flexural strength is reduced from 56 MPa to 45.5 MPa (reduction of 18.75% compared to neat ABS). It was reported that the mechanical properties increased by 1.8 times with the inclusion of reduced graphene oxide in ABS [25]. It was also reported that the hardness and modulus improved by 49% and 61%, respectively, by adding MWCNT in ABS [6].

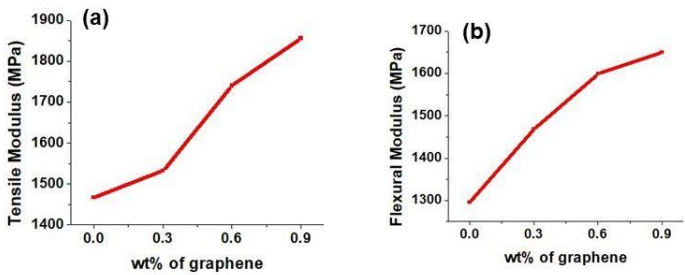

Figure 8: Effect of graphene content in ABS matrix (a) tensile modulus (b) flexural modulus

Figures 8a and 8b represent the tensile modulus and the flexural modulus of neat ABS and the ABS/graphene composites with varying graphene content ratios. The tensile and flexural modulus of the composites increased with the increase in the wt% of graphene in the matrix. The tensile modulus shows an improvement of 4.43, 18.6, and 26.51% with the addition of 0.3, 0.6, and 0.9 wt% of graphene in the thermoplastic ABS material. Similar results were reported by adding ZnO and nano zirconia in ABS [1]-[2]. The flexural modulus increases gradually from 1296 MPa to 1650 MPa, an increase of 27.31% compared to the neat ABS material [10]-[16]. The addition of graphene content in ABS improves the tensile and flexural modulus, which may be attributed to an increase in stiffness due to the

uniform dispersion of graphene filler, which restricts the chain mobility, making it difficult for the polymer chains to move.

SEM analysis

Figure 9 represents the SEM images of ABS/graphene composites varying wt% of graphene (0.3, 0.6, and 0.9). The dispersion of graphene filler in the ABS matrix is visible in the SEM images. The dispersion of graphene corresponding to 0.6 wt% is much better compared to 0.3 and 0.9 wt% of graphene in ABS. The homogeneity in mixing reflected in the dynamic mechanical and the mechanical properties, as it was represented the 0.6wt% of graphene gave better properties than the composites prepared with 0.3 and 0.9 wt% of graphene. The size of the voids in the ABS with 0.9 wt% graphenes is much larger than the other composites.The chemical bonding between the ABS matrix and the graphene filler was strong when a smaller amount of graphene was added to ABS. So, the properties were gradually increasedup to 0.6 wt% of graphene in ABS. But when a higher amount of graphene was added in ABS, the graphene powder hadhigh surface energy, and it was easy to agglomerate and also created voids. It made the composite weaker, and the mechanical properties started decreasing. It is mainly attributed to the weak interface interaction and weak chemical bonding between the matrix and filler.

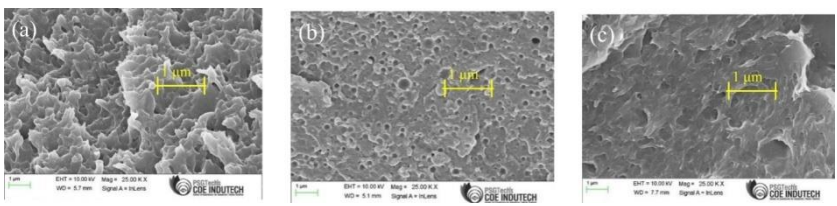

Figure 9: SEM Images; (a) ABS and 0.3 wt% graphene, (b) ABS and 0.6wt% graphene, and (c) ABS and 0.9 wt% graphene

Conclusions

The compounding of ABS and graphene was carried out by extrusion, and the specimen was prepared by injection molding. TGA, DMA, and UTM characterized the thermal, dynamic mechanical, and mechanical properties. As per the results obtained from the various characterization, ABS/graphene composites are promising candidates and potential future materials for automotive and 3-D printing applications. The DMA studies confirmed that the storage modulus of the pure ABS matrix improved with the addition of graphene content over a wide range of temperatures. The storage modulus is

enhanced by 70% over a wide range of temperatures. The tensile strength, flexural strength, and shore hardness of the ABS/graphene composite increased up to 0.6 wt% of graphene, and beyond 0.6 wt% of graphene in ABS, the properties decreased. The tensile and flexural modulus of the composites gradually increased with the increase in the graphene particulates. Still, the flexural strength of the pure ABS decreased with an increase in filler content. The stiffness of ABS/graphene composite corresponds to the 0.9wt% of graphene content in the ABS matrix, increased by 27% compared to the neat ABS. The TGA results revealed that the thermal stability of the pure ABS material improved due to the inclusion of graphene. The better dispersion of filler and the adhesion between the filler and matrix enhanced the viscoelastic, mechanical, and thermal properties of pure ABS material.

Contributions of Authors

All the authors have the equal contribution in each part of this work. All authors reviewed and approved the final version of this work.

Funding

This work received no specific grant from any funding agency.

Conflict of Interests

All authors declare that they have no conflicts of interest.

References:

[1] J.Sudeepan, K.Kumar, T. K. Barman and P. Sahoo, "Study of mechanical and tribological properties of ABS/ZnO polymer composites," *Advanced Materials Manufacturing and Characterization*, vol. no. 5, 2015.

[2] Amrishraj.D and Senthilvelan.T, "Acrylonitrile Butadiene Styrene composites Reinforced with nano zirconia & PTFE: Mechanical and Thermal Behaviour," *Polymer Composites*, vol. 39, no. 3, pp. 1520-1530, 2017.

[3] B.BenDifallah, M.Kharrat, M.Dammak and G.Monteil, "Mechanical and tribological response of ABS polymer matrix filled with graphite powder," *Materials and Design*, vol. 34, pp. 782-787, 2012.

[4] Sithiprumnea Dul, Luca Fambri, and Alessandro Pegoretti, "Filaments Production and Fused Deposition Modelling of ABS/Carbon Nanotubes composites," *Nanomaterials*, vol. 8, no. 1, pp. 49, 2018.

[5] Vivek Kumar, J.Ramkumar, S.Aravindan, and S.K Malhotra, "Fabrication and characterization of ABS nanocomposite reinforced by nanosized alumina particulates," *International Journal of Plastics Technology*, vol. 13, no. 2, pp.133-149, 2009.

[6] P.Jindal, J. Jyothi and N. Kumar, "Mechanical characterization of ABS/MWCNT composites under static and dynamic loading," *Journal of Mechanical Engineering and Sciences*," vol. 10, no. 3, pp. 2288-2299, 2016.

[7] Vinay Kumar, Rupinder Singh, and IPS Ahuja, "On the correlation of rheological, thermal, mechanical and morphological properties of tertiary recycling for 3D printing applications," *Advances in Materials and Processing Technologies*, vol. 8, no. 3, 2021.

[8] B.Neher, N.Nova, R. Hossain, M. Gafurand F. Ahmed, "Fabrication and Characterization on Physico-Mechanical and Structural Properties of Sawdust Reinforced Acrylonitrile Butadiene Styrene (ABS) Composites," *Materials Sciences and Applications*, vol. 11, pp. 644-658, 2020.

[9] Fatin Najwa Joyal Abidin, Hamidah Abdul Hamid, Abbas F.M. Alkarhi, Salem S. Abu Amr, N.A.Khalil, Amzan Hassan and Md. Sohrab Hossain, "The effect of graphene oxide and SEBS-g-MAH compatibilizer on Mechanical and Thermal Properties of Acrylonitrile-Butadiene - Styrene/Talc Composite," *Polymers*, vol. 13, pp. 3180, 2021.

[10] N. Song, J. Yang, P. Ding, S. Tang, and L. Shi, "Effect of polymer modifier chain length on the thermal conductive property of polyamide 6/graphene nanocomposites," *Composites Part A Applied Science and Manufacturing*, vol. 73, pp. 232–24, 2015.

[11] W. Hou, B. Tang, L. Lu, Jun Sun, J. Wang, C.Oin and Lixing Dai, "Preparation and physicomechanical properties of amine-functionalized graphene/polyamide6 nanocomposite fiber as a high-performance material," *RSC Advances*, vol. 4, no. 10, pp. 4848–4855, 2014.

[12] Jeevan Jyoti andAbhishek. Arya, "EMI shielding and dynamic mechanical analysis of grapheme oxide-carbon nanotube-acrylonitrile butadiene styrene hybrid composites," *Polymer Testing*, vol. 91, 2020.

[13] Mar Lopez-Gonzalez, Araceli Flores, Fabrizio Marra, Garry Ellis, M.Gomez-Fatou and H.J Salavagione, "Graphene and Polyethylene: A strong combination towards multifunctional nanocomposites," *Polymers*, vol. 12, no. 9, 2020.

[14] Na Song, Donglei Cao, Xian Luo, Qi Wang, Peng Ding, and Liyi Shi, "Highly thermally conductive Polypropylene/graphene composites for thermal management," *Composites Part – A: Applied Science and Manufacturing*, vol. 135, 2020.

[15] Lucheng Qi, Yandi Li, Jiangfeng Weng, Boping Liu and Xuelian He, "The mechanical properties of polyethylene/graphene nanocomposites by in-situ synthesis," *Material Research Express*, vol. 6, no. 6, 2019.

[16] Jacek Andrzejewski, Amar K.Mohanty and Manjusri Mishra, "Development of hybrid composites reinforced with biocarbon/carbon fiber system.The comparative study for PC,ABS & PC/ABS based materials," *Composites Part B: Engineering,* vol. 200, 2020.

[17] Mohammed Abdul Kadhim and Ehssan AI-Bermany, "New fabricated PMMA-PVA/graphene oxide nanocomposites; Structure, optical properties, and application," *Journal of Composite Materials,* vol.55, no. 20, pp. 2793-2806, 2021.

[18] M. Bastiurea, M.S Rodeanu, D.Dima, M.Murarescu and G.Andrei, "Thermal and Mechanical properties of polyester composites with graphene and graphite," *Digest Journal of Nanomaterials and Biostructures*, vol. 10, no. 2, pp. 521-53, 2015.

[19] Lei Gong, Lan-Peng Li, and Ming-bo Yang, "Nylon-6/Graphene composites modified through polymeric modification of graphene," *Composites Part B: Engineering*, vol. 73, pp. 49 – 56, 2014.

[20] Jelena Vasiljevic, Andrej desar, Mirjam Leskovsek, Barbara Simoncic, N.C Korosin, Ivan Jerman, M, Sobek, Gregor Zitko, N. V de Velde, and Marija Colovic, "Characterization of polyamide 6/multilayer Graphene Nanoplatelet Composite Textile filaments obtained via In Situ polymerization and melt spinning," *Polymers*, vol. 12, no. 8, 2020.

[21] Johnney N.Martins, Tobias G.Klohn, Otavia Bianchi, Rudinei Fiorio and Estevao Freire, "Dynamic Mechanical,Thermal and morphological study of ABS/textile fiber composites," *Polymer Bulletin*, vol. 64, no. 5, pp. 497-510, 2010.

[22] Wu-Jian Long, Jing-Jie Wei, Hongyan Ma, and Feng Xing, "Dynamic Mechanical properties and microstructure of graphene oxide nanosheetsreinforced composites," *Nanomaterials*, vol. 7, no. 12, 2017.

[23] Nitin K.Gupta, Pankaj Pandey, Samarth Mehta, and Shilpi Swati, "Characterization of ABS material in Hybrid composites; A Review," Advances in Engineering Design, pp.619-630, 2019.

[24] Barun Das, K.Eswar Prasad, U.Ramamurty and CNR Rao, "Nano-indention studies on polymer matrix composites reinforced by few-layer graphene," *Nanotechnology*, vol. 20, no. 12, 2009.

[25] Vinay Panwar and Kaushik Pal, "An optimal reduction technique for rGO/ABS Composites having high-end dynamic properties based on Cole – Cole Plot, degree of entanglement and C-factor," *Composites Part B: Engineering*, vol. 114, pp.46–57, 2017.

[26] Hesham Moustafa, Ahmed M.Youssef, Sophie Duquesne, and Nabila.A.Darwish, " Characterization of bio–filler derived from sea-

wastes and its effect on the mechanical, thermal and flame retardant properties of ABS composites," *Polymer Composites,* vol. 38, pp. 2788 – 2797, 2017.

[27] Johny.Martins,Tobias.Kohan et.al, "Dynamic mechanical, thermal and morphological study of ABS/textile fiber composites," *Polymer Bull*, vol. 64, pp. 497 – 510, 2010.

[28] Vignesh Sekar, Mazin Zarrouq and Satesh Narayana Nama Sivayam, "Development and Characterization of Oil Palm Empty Fruit Bunch Fiber Reinforcements for Fused Deposition Modelling," *Journal of Mechanical Engineering*, vol. 18, no. 1, pp. 89 – 107, 2021.

[29] Izdhar Tharazi, Abu Bakar Sulong, Farrahshaida Mohd Salleh, Abdul Hakim Abdullah, and Nur Farahi Ismail, "Application of Response Surface Methodology for parameters optimization in Hot Pressing Kenaf Reinforced Biocomposites," *Journal of Mechanical Engineering*, vol. 17, no. 3, pp. 131 – 144, 2020.

[30] Ahmed Fuad Ab Ghani and Jamaluddin Mahmud, "Hardness, Tensile and Microstructure Assessment of Carbon/Glass Hybrid Composite Laminate," *Journal of Mechanical Engineering*, vol. 15, no. 2, pp. 91 – 105, 2018.

Computational Numerical Analysis of a Magnetic Flux Permanent Magnet with Different Shape for The Development of a Hybrid Generator

M.Saiful Bahari[*]*, M. Firdaus*
School Of Mechanical Engineering, College of Engineering,
Universiti Teknologi MARA,40450 Shah Alam, Selangor, MALAYSIA
[*]*saifulbahari@uitm.edu.my*

Zulkifli Mohamed, M. Hanif M.Ramli
Sports Engineering & Artificial Intelligence Center - SEA IC,
Universiti Teknologi MARA,40450 Shah Alam, Selangor, MALAYSIA

ABSTRACT

A hybrid generator is one of the attempts to reduce carbon emissions in electricity generation, as it could replace the combustion system currently used in generator sets to generate electricity while increasing carbon emissions. In the hybrid generator system, Lenz's rule of electromagnetic induction is applied in reverse by using a relay to change the polarity of the solenoid coil's electric current. The permanent magnet in the solenoid coil generates mechanical energy (motion) and thereby moves the generator engine, since the permanent magnet is connected to the generator engine via the crankshaft. The objective of this study is to determine and compare the behaviour of N55, N52, N42, N42SH, and samarium-cobalt permanent magnets for the magnet system. The objective of this study is also to find a suitable permanent magnet for use in the magnet system to increase the power generation efficiency. A simple model is simulated to achieve the desired result, including magnetic flux density inside and around the magnets, magnetic field strength calculation, and applied force. The simulations and analysis are performed using ANSYS R19 software and finally all the data are recorded and compared to select the best magnet and develop a prototype. The permanent magnet inside the solenoid plays an important role in the hybrid generator and it is crucial to choose the suitable permanent magnet to increase the efficiency of power generation. From the data, Alliance N-55 permanent magnet has the highest

ISSN 1823-5514, eISSN 2550-164X

https://doi.org/10.24191/jmeche.v20i1.21087

Received for review: 2022-07-24
Accepted for publication: 2022-12-20
Published: 2023-01-15

magnetic force of 131.57 N for 1 mm because it has significantly higher magnetic flux density, magnetic flux intensity and magnetic force.

Keywords: *Hybrid Generator; Permanent Magnet; Magnetism*

Introduction

In today's world, fossil fuels are one of the primary sources of energy currently used, whether to generate electricity or for transportation. Even though renewable energy sources have been discovered for years, they are not as efficient or stable as fossil fuel sources [1].

Most renewable energy sources came from the environment such as solar energy. Solar energy is renewable energy that requires sunlight to generate electricity, and this technology can only be used during the day since the solar source is a photovoltaic cell panel, this system necessitates a large amount of space for the panel. Nowadays, the study of renewable energy focuses on magnets as the main source still in the preliminary, and difficult to find a focus journal on it as a reference.

A hybrid generator gets its inspiration from electromagnet energy to move the mechanical system in the generator. This system differed from existing generators in that the diesel or gasoline generator used a combustion system to move the mechanical system in the generator. This generator project defines how to produce electricity from green energy or renewable energy by using magnetic mechanisms as the sources to produce linear mechanical energy and rotate the brushless motor and generate electricity. Essentially, the concept was like a generator that generates electricity using oil and diesel. In the combustion chamber, the air is oxidized by the combustion generator, which uses a heat engine and fossil fuel as a source [2]. Internal combustion produces high pressure and high temperature, which generate force and moves mechanical energy.

The hybrid generator innovation is part of sustainable development to provide renewable energy to future generations. Furthermore, electromagnet energy was green energy that had no side effects or pollution to the environment or habitat [3]. With this generator innovation, it will be possible to electrify the entire world, especially in rural and island areas where electricity supply is difficult to obtain. In addition, the low input current to high output current generator innovation is one of the most stable energy outputs in renewable energy than other renewable energy. For the economic sector, it can reduce the cost of living for people who are affected by the rising price of fossil fuels. This generator's innovation has the probability to become one of the primary sources of electricity generation around the world.

Permanent magnet

Many engineering applications and devices have chosen magnetic material to replace some traditional engineering applications to achieve optimal performance and efficiency [4]. The use of permanent or temporary magnets can also be beneficial to the environment. Mechanisms that use magnetic elements, for example, can significantly reduce heat generation and thus increase machine efficiency. Magnets such as Neodymium type magnets are an excellent choice for producing efficient output due to their capabilities and low operating temperature, particularly in applications requiring electrical motors [5]. Since Neodymium is a type of permanent magnet containing rare earth material, its supply is limited over time. Nowadays, the most promising permanent magnet without the use of rare-earth materials with high magnetic energy and low cost is the Iron Nitride magnet. Based on their findings, they believe that the Iron Nitride Magnet permanent magnet will be a viable replacement for the Neodymium permanent magnet [6].

Faraday's law

The law of electromagnetic induction was discovered by Michael Faraday. The discovery of electromagnetic induction led to the development of generators and transformers. Faraday experimented to demonstrate the ability of magnetic fields to induce currents. As Michael Faraday demonstrated, a changing magnetic field can induce an electromagnetic field in a circuit. The induction of a magnetic field can be demonstrated by conducting a closed-circuit wire loop with an ammeter (A) and a bar magnet placed above the wire loop's center axis. When the magnet is held stationary inside the loop, there is no current in the loop. Based on his observations, Faraday concluded that the induced current is related to the changing magnetic field [7].

$$\varepsilon = N\frac{\Delta \Phi B}{\Delta t} \tag{1}$$

According to the equation, is the magnetic flux and B is the electromotive force (EMF), also known as the induced voltage. The number of coils can be increased to generate more flux changes, which will increase the EMF's overall strength. Consequently, where N is the number of coils turns.

Lenz's Law

Lenz's law is an electromagnetism law that is primarily related to electromagnetic induction. The focus of Lenz's law is the direction of the current induced in a circuit by the effect of a magnetic field. According to Lenz's law, the current generated in the coil counteracts the flux change caused by the moving magnet [7]. The mechanical linkage produces linear movement in the solenoid by reversing the Lenz Law. The magnetism concept reverses the concept by manipulating the direction of the current to change the polarity

of the electromagnetic field of the solenoid. By manipulating the current, the permanent magnet will produce a linear movement inside the solenoid since the electromagnetic field inside the solenoid is changing shown in Figure 1.

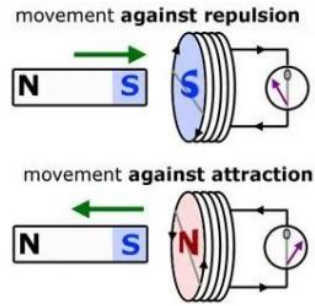

Figure 1: Lenz's law concept [7]

Electromagnetic induction and Lenz's law are both closely related to electromagnetism laws. Lenz's law focuses on the direction of the current that is induced into a circuit as a result of changes in the magnetic field. It is stated in Lenz's law that the flux change caused by the moving magnet is offset by the current produced in the coil [7].

$$\varepsilon = -N\frac{\Delta\Phi B}{\Delta t} \tag{2}$$

As a result, the equation has a negative sign. In opposition to the moving magnet, which applies a mechanical force, the magnetic field from the coil will act. A repulsive force can be felt when a magnet bar is introduced into a coil because the magnet and coil both have the same pole and magnets with similar magnetic poles repel one another. Another example is when a magnetic ball is dropped through an aluminium or copper pipe, this phenomenon is visible. The magnet moves noticeably more slowly through the pipe than if it were dropped into thin air.

Magnetic flux

Magnets of various forms are commonly utilized in a vast array of electromagnetic devices today. Transformer cores are the most prominent example of a device that utilizes magnetic flux. In order to induce EMF across secondary coils from the same core more effectively and with better flux distribution, it is necessary to assess the magnetic flux in the air gap between the core windings of the transformer [8].

According to the idea, magnetic flux is the motion of a magnetic field through a surface. Magnetic flux is the number of magnetic field lines that

traverse a body [9]. A surface with a vector area is subjected to a magnetic flux represented by:

$$\Phi_B = BA \cos \theta \quad (3)$$

where:

ΦB = Magnetic Flux (Wb)
B = magnetic field magnitude (T)
A = surface area (m2)
θ = angle between magnetic field lines and normal to the surface area

Halbach array arrangement

Dr. K. Halbach of the Lawrence Berkeley National Laboratory in the United States proposed the Halbach array, which is a permanent magnet structure. The Halbach array can produce extremely high and consistent flux densities without the use of electricity or cooling. Figure 2 shows a strong magnetic field can be created on one side by arranging several permanent magnets in a linear form and magnetizing each magnet in a different direction according to a specific order of arrangement; however, a weaker magnetic field will also be created on the opposite side of the permanent magnet [10].

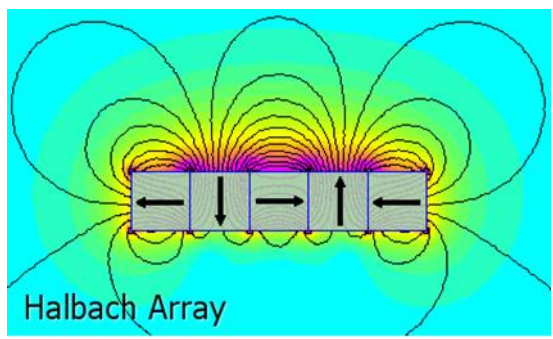

Figure 2: Halbach array arrangement [10]

Hybrid generator

The hybrid generator gets its inspiration from electromagnet energy to move the mechanical system in the generator. This system differed from existing generators in that the diesel or gasoline generator used a combustion system to move the mechanical system in the generator. This generator project defines how to produce electricity from green energy or renewable energy by using magnetic mechanisms as the sources to produce linear mechanical energy and rotate the brushless motor and generate electricity [11].

Essentially, the concept is like that of a generator that generates electricity using oil and diesel. In the combustion chamber, the air is oxidized by the combustion generator, which uses a heat engine and fossil fuel as a source. Internal combustion produces high pressure and high temperature, which generate force and moves mechanical energy. But for the concept of an electric generator, this device will innovate the internal combustion system to the electromagnet system energy to move the linear mechanical energy. For the prototype shown in Figure 3, the linear mechanical energy is produced by generating an electromagnet field at the solenoid to move the cylinder's permanent magnet inside the solenoid core [12]. By manipulating the current, the cylinder's permanent magnet will produce a linear movement inside the solenoid since the electromagnetic field of the solenoid is changing. The concept of the system was inspired by combining and reversing Lenz's Law with a permanent magnet.

The permanent magnet inside the solenoid plays the important role in the hybrid generator and it is crucial to decide the suitable permanent magnet so that it can increase its efficiency to generate electricity. For this project, the goal is to choose a suitable type of permanent magnet in terms of its grade, shape, and arrangement of the permanent magnets since it can affect the strength of the permanent magnet and its movement inside the solenoid.

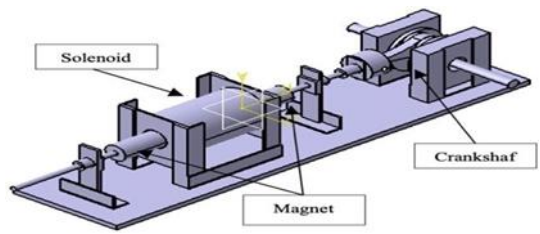

Figure 3: Prototype of hybrid generator

Methodology

The methodology for all the simulations and analysis is conducted by using Magnetostatic Analyse System in ANSYS Software R19 Version and all the data of the analysis are obtained from the Magnetostatic solver.

Data input

The data input section mainly focused on applying the magnetic properties of the materials that have been collected from the Alliance LLC website into the ANSYS software shown in Table 1. Alliance LLC is a nationally recognized supplier of magnetic materials for the automotive, industrial, defence,

alternative energy, and communication industries in the United States and the company provides various data about the mechanical and magnetic properties of all the permanent magnets 2 types of magnetic properties of the permanent magnets that were required for the analysis which is the Magnetic Remanence (Br) and the Magnetic Coercive Force (Hc). Magnetic Remanence is the amount of ability of a material to acquire and keep its magnetic properties.

For the Magnetic Coercive Force, it is the amount of magnetic field required to demagnetize the material. So, the Magnetic Remanence will increase linearly with the Magnetic Coercive Force. The larger the Magnetic Remanence, the larger the Magnetic Coercive Force will be. Below were the Magnetic Remanence and the Magnetic Coercive Force for each of the 5 permanent magnets that were used in the analysis.

Table 1: Magnetic properties of permanent magnets

Permanent Magnets	Magnetic Remanence, B_r (T)	Magnetic Coercive Force, H_c (A/m)
Alliance S-28H Samarium Cobalt Magnetic Material	1.10	835558.50
Alliance N-42 Neodymium Iron Boron Magnetic Material	1.30	994712.50
Alliance N-42SH Neodymium Iron Boron Magnetic Material	1.30	1114078.00
Alliance N-52 Sintered Neodymium Iron Boron Magnetic Material	1.48	1114078.00
Alliance N-55 Sintered Neodymium Iron Boron Magnetic Material	1.52	1153866.50

Designing

There were 2 types of software that have been used in designing which are ANSYS SpaceClaim and ANSYS DesignModeler. Each of software has its advantages and disadvantages to design the geometry for the simulation. ANSYS SpaceClaim is design software that is friendly to the user while ANSYS DesignModeler is design software that gives freedom and flexibility to the user in designing certain geometry for the analysis. The design software that has been used is ANSYS SpaceClaim and the design consists of a cuboid shape permanent magnet (25 x 10 x 50 mm) and cylinder shape permanent magnet (249.99 x 2 x 50 mm) shown in Figure 4.

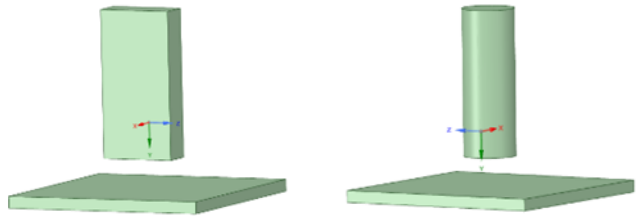

Figure 4: Cuboid and cylinder shape permanent magnet

For the solenoid, the dimension was 120 mm in length and with an inlet radius of 30 mm. The solenoid consists of 500 turns shown in Figure 5. The design must be in a hollow semi-cylinder to apply the current input and voltage input at the interior surface of the solenoid so that it can be analysed in magnetostatic analysis.

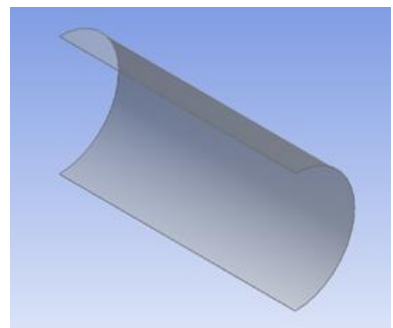

Figure 5: Solenoid design in semi-cylinder

Meshing

The meshing section is the one that will decide the accuracy of the results and it will depend on the sizing of the meshing because every intersection point between the mesh elements is the node. The smaller the sizing of the meshing, the more the number of nodes and the more the accuracy of the result. However, it will take a long time to get the results, and it will depend on the capability of certain ANSYS software. The mesh sizing for this project was 5 mm which is the default amount of the meshing for this software shown in Figure 6 and the detailed meshing for this simulation is shown in Figure 7.

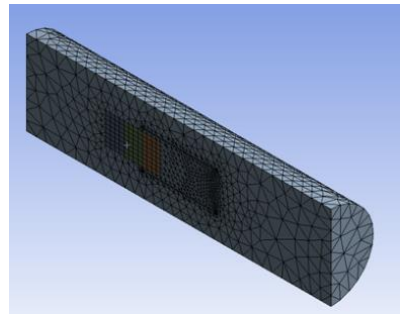

Figure 6: Meshing sample

Details of "Mesh"	
Display	
Display Style	Use Geometry Setting
Defaults	
Physics Preference	Electromagnetics
Element Order	Quadratic
Element Size	Default
Sizing	
Quality	
Inflation	
Advanced	
Statistics	

Figure 7: Meshing parameter

Analysis

The magnetostatic analysis can give the results of the magnitude of flux density, the magnitude of flux intensity, and the magnetic force of the permanent magnet. However, the magnetostatic analysis is dependent on the enclosure of the analysis illustrated in Figures 8 and 9. The enclosure represents the surrounding since the type of surrounding and temperature can affect the magnetic field such as air and vacuum condition. For the project, the environment temperature is 22 ˚C type the enclosure was air and applied on the cuboid shape.

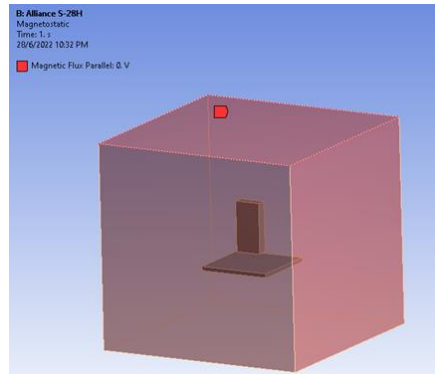

Figure 8: Magnetostatic analysis for cuboid shape

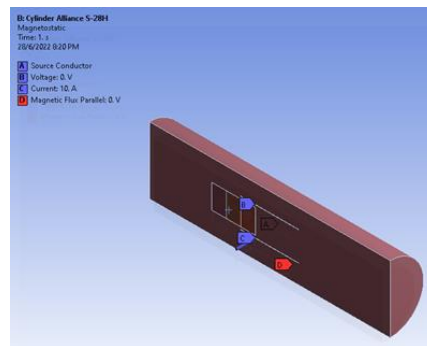

Figure 9: Magnetostatic analysis for cylinder shape

Results and Discussion

For the analysis, the cuboid shape permanent magnet had been placed 10 mm above the plate and the magnetostatic analysis analysed the behaviour of the magnetic field and the magnetic force from that location.

Due to the cuboid shape of the permanent magnet, the greatest magnetic flux density is located between 20 mm and 30 mm from the permanent magnet, as shown in Figure 10. Figure 11 shows that the largest magnetic flux density was located at the ends of the cuboid-shaped permanent magnets, and the ability to magnetise other ferromagnetic materials is greater at the ends than in the middle. Figure 12 shows that as the distance between the permanent magnets and the cast iron plate increased, the force summation of the permanent magnets to the cast iron plate decreased.

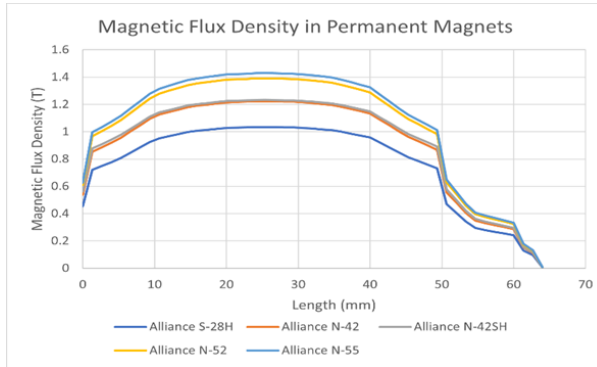

Figure 10: Magnetic flux density across the body

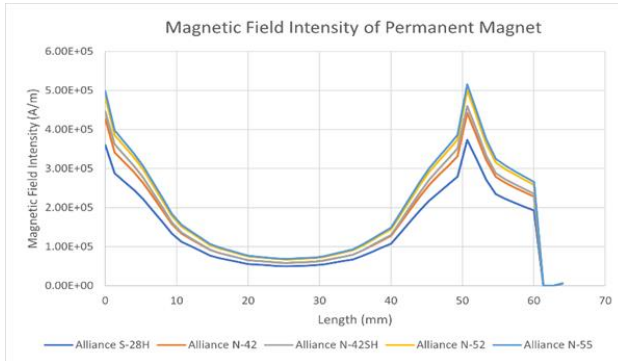

Figure 11: Magnetic flux intensity across the body

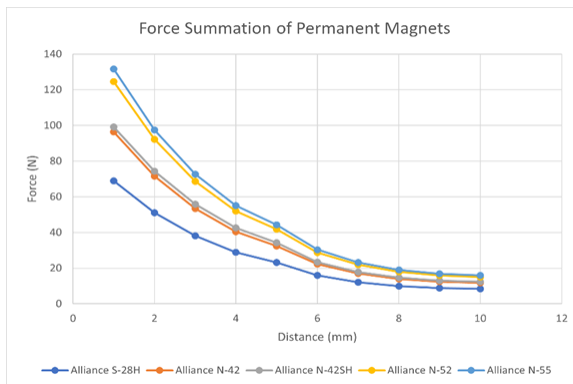

Figure 12: Force summation of permanent magnets

Figure 13 shows the results of comparing two different shapes of Alliance N-55 permanent magnets, a cube shape and a cylinder shape. The plots show the magnetic flux density, the magnetic flux strength, and the sum of the forces between the two shapes. With 2 mm and 1 mm between the permanent magnet and the cast iron plate, the sum of forces for the cube-shaped Alliance N-55 is slightly higher than for the cylindrical-shaped Alliance N-55, 25.71%. For the same height, contact area and volume, the cuboid-shaped permanent magnet is slightly stronger than the cylindrical permanent magnet, as shown in Table 2.

Table 2: Force summation between cylinder shape and cuboid shape permanent magnet

Distance (mm)	Force Summation (N)	
	Cylinder Shape Permanent Magnet	Cuboid Shape Permanent Magnet
1	104.66	131.57
2	89.36	97.45
3	70.49	72.64
4	56.89	55.10
5	43.94	44.23
6	31.92	30.33
7	24.58	23.16
8	20.42	19.02
9	17.49	16.905
10	15.31	15.96

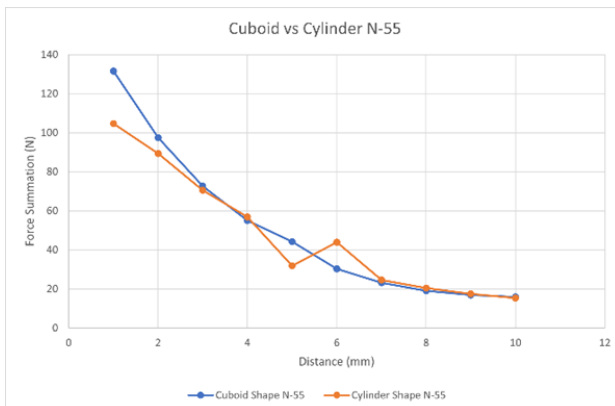

Figure 13: Force summation of cuboid and cylinder shape N-55

The direction of the magnetic field for the 2-semicylindrical permanent magnet was outward from the aluminium half-cylinder (middle half-cylinder), hence the north pole is at the end of both cylinder shapes. For the cuboid shape, each end of the design represented the strongest side of the magnetic field data. Figures 14 and 15 show the magnetic field behaviour for the two shapes within the magnetic core. Since the purpose of the analysis was to study the behaviour and magnetic strength of the permanent magnet of the magnetic core, only one type of current flow, 1.0 amps, was used. The magnetic coil generates an electromagnetic field with the north pole on the right side and the south pole on the left side, with a magnetic flux density of 0.045 T and a magnetic flux strength of 36151 A/m at the centre of the core.

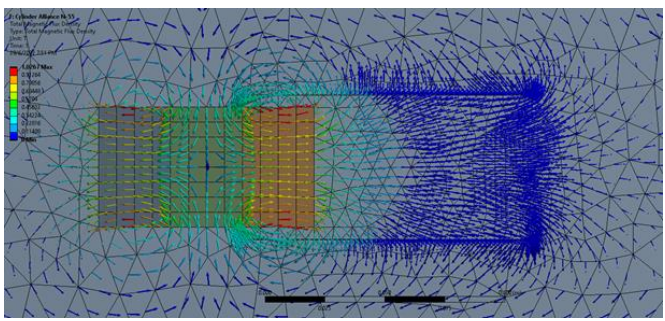

Figure 14: Design 1 inside solenoid core

The magnetic field in the core of the Design 1 solenoid was in one direction only, indicating that the north pole (right side) of Design 1 was facing the north pole of the solenoid. Therefore, they repelled each other, and since the north pole (left side) of Design 1 was facing the south pole of the solenoid, they attracted each other and caused a linear motion to the left.

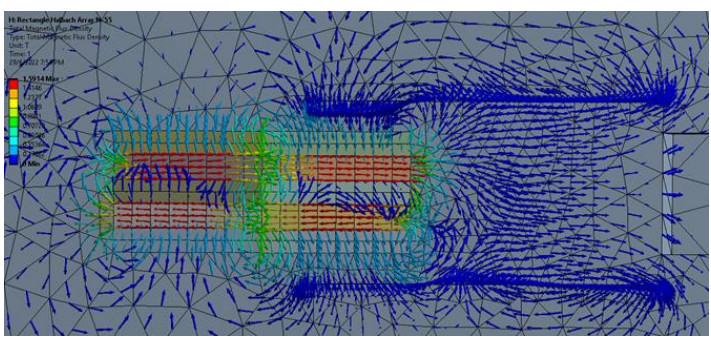

Figure 15: Design 2 inside solenoid core

Thus, the presence of the south pole on the strong side (both ends) of Design 2 slightly attracts the permanent magnet toward the north pole of the solenoid, causing the opposite movement of the permanent magnet for the hybrid generator system. This result is tally that already discuss in Energy Management through Electromagnetic Conversion the resulting output power depends crucially on the design, the covered area among the magnet and coils, the lineal or angular velocity induced, the relative permeability of the implemented materials, and the time-varying magnetic field generated, as well as the magnetic flux density and magnetic field strength of the magnets [4].

Conclusion

Based on the results, the Alliance N-55 permanent magnet had the strongest magnetic force because the permanent magnet had the highest magnetic flux density, the highest magnetic flux intensity, and the highest magnetic force among the other permanent magnets. However, the availability of the N-55 permanent magnet is limited because the N-55 grade is still new to the market. In addition, the difference in the shape of the permanent magnet also affects the magnetic force of the permanent magnet, and the result shows that the cuboid permanent magnet performs better than the cylindrical permanent magnet. So, the most suitable permanent magnet for this hybrid generator is the cuboid N-55 permanent magnet.

The results show that the force sum for the cuboid Alliance N-55 is 25.71% higher than that of the cylindrical Alliance N-55 at 2 mm and 1 mm between the permanent magnet and the cast iron plate. With comparable height, contact area and volume, it can be concluded that the cuboid permanent magnet is slightly stronger than the cylindrical permanent magnet. This study also can conclude that electromagnetic conversion provides a modern background between renewable energy systems, exergy analysis and electromagnetic engineering concepts to ensure long life, instant power generation, efficiency, performance and optimization of energy.

Contributions of Authors

The authors confirm the equal contribution in each part of this work. All authors reviewed and approved the final version of this work.

Funding

This work was supported by the “LESTARI SDG” [600-RMC/LESTARI SDG-T 5/3 (135/2019)].

Conflict of Interests

All authors declare that they have no conflicts of interest.

Acknowledgment

We are thankful to and fortunate enough to get constant encouragement, support and guidance from all Teaching staffs and final year project student at school of mechanical engineering which helped us in successfully completing our project work. Also, we would like to extend our sincere esteems to all staff in laboratory for their timely support.

References

[1] Kinsler, P., "Physics Faraday's Law and Magnetic Induction: cause and effect, experiment and theory" *Physics*, vol. 2, no. 2, pp. 150-163, 2020.

[2] Prosperi, D., Bevan, A. I., Ugalde, G., Tudor, C. O., Furlan, G., Dove, S., Lucia, P., and Zakotnik M., "Performance comparison of motors fitted with magnet-to magnet recycled or conventionally manufactured sintered NdFeB," *Journal of Magnetism and Magnetic Materials*, vol. 460, pp. 448–453, 2018.

[3] Jiang, Y., Deng, Y., Zhu, P., Yang, M., and Zhou, F., "Optimization on Size of Halbach Array Permanent Magnets for Magnetic Levitation System for Permanent Magnet Maglev Train," *IEEE Access*, vol. 9, pp. 44989–45000, 2021.

[4] J. Wang, Y. Jiang, M. A. Mehedi, J. Liu, Y. Wu and B. Ma, "Fe16N2: from a 40-year mystery of magnetic materials to one of the promises for rare-earth-free magnets.," *IEEE International Magnetics Conference* (INTERMAG), pp. 1-1, 2018.

[5] P. Bernstein and J. Noudem, "Superconducting magnetic levitation: Principle, materials, physics and models," *Superconductor Science and Technology*, vol. 33, no. 3, pp. 033001, 2020.

[6] A. M. Patel, B. N. Prajapati, H. R. Rathod, P. R. Yagnik and S.P Sinha, "Electromagnetic Induction in Traction System," In Proc. *1st National Conference on Emerging Trends, Challenges and Opportunities in Power Sector*, pp. 108–109, 2017.

[7] L. Li, X. Du, J. Pan, A. Keating, D. Matthews, H. Huang and J. Zheng, "Distributed magnetic flux density on the cross-section of a transformer core," *Electronics*, vol. 8, no. 3, pp. 1–12, 2019.

[8] R. Siva Srinivas, R. Tiwari, and C. Kannababu, "Application of active magnetic bearings in flexible rotordynamic systems – A state-of-the-art

review," *Mechanical System and Signal Processing*, vol. 106, pp. 537–572, 2018.
[9] K. D. Bachovchin, J. F. Hoburg, and R. F. Post, "Magnetic fields and forces in permanent magnet levitated bearings," *IEEE Transaction on. Magnetics*, vol. 48, no. 7, pp. 2112–2120, 2012.
[10] P. Peng, H. Xiong, J. Zhang, W. Li, F. Leonardi, C. Rong and L. Zhu, "Effects of External Field Orientation on Permanent Magnet Demagnetization," *IEEE Energy Conversion Congress and Exposition*, vol. 53, no. 4, pp. 3438–3446, 2017.
[11] N. Yogal, C. Lehrmann, M. Henke, and X. Liu, "How to measure the demagnetization of permanent magnet synchronous machines used in explosive environments," *In 2017, IEEE International Electric Machines and Drives Conference (IEMDC)*, pp. 1– 8, 2017.
[12] B. K. Bose, "Global warming: energy, environmental pollution, and the impact of power electronics," *IEEE Industrial Electronics Magazine*, vol. 4, no. 1, pp. 6–17, 2010.
[13] Panwar, N.L., Kaushik, S.C., Kothari, S, "Role of renewable energy sources in environmental protection: a review," *Renewable Sustainable Energy Reviews*, vol. 15, no. 3, pp. 1513–1524, 2011.
[14] L. T. Wood, R. M. Rottmann, and R. Barrera, "Faraday's law, Lenz's law, and conservation of energy," *American Journal of Physics*, vol. 72, no. 3, pp. 376–380, 2004.
[15] A. Elliot, "Solving Energy Challenges in Remote Communities," *Third Way*, February 2018, pp. 1–7, 2018.
[16] U. Shahzad, "The need for renewable energy sources," *Energy*, vol. 2, pp. 16–18, 2012.
[17] R. G. Newell, D. Raimi, and G. Aldana, "Global Energy Outlook 2019: The Next Generation of Energy," *Resources for the Future*, vol.1, pp. 8-19, 2019.
[18] E. Kabir, P. Kumar, S. Kumar, A. A. Adelodun, and K. H. Kim, "Solar energy: Potential and future prospects," *Renewable and Sustainable Energy Reviews*, vol. 82, pp. 894–900, 2018.
[19] E. I. Konstantinidis and P. N. Botsaris, "Wind turbines: current status, obstacles, trends and technologies," In *2016 IOP Conference Series: Material Science Engineering*, vol. 161, pp. 1-8, 2016.
[20] Ari Kahan, "EIA projects nearly 50% increase in world energy usage by 2050, led by growth in Asia," *International Energy Outlook*, pp. 2019–2021, 2019.

Experimental and Finite Element Method (FEM) of Dowelled Mortise and Tenon Joint for Kapur Species

Amira Ruzailin Dzulkifli,
School of Civil Engineering, College of Engineering,
Universiti Teknologi MARA (UiTM), 40450 Shah Alam, MALAYSIA

Rohana Hassan[*]*, Sakhiah Abdul Kudus*
School of Civil Engineering, College of Engineering,
Universiti Teknologi MARA (UiTM), 40450 Shah Alam, MALAYSIA
Institute for Infrastructure Engineering and Sustainable Management (IIESM), Universiti Teknologi MARA, 40450 Shah Alam, MALAYSIA
[*]*rohan742@uitm.edu.my*

Mohd Nizam Shakimon
Faculty of Engineering &Technology Infrastructure,
Infrastructure University Kuala Lumpur (IUKL), Unipark Suria,
Jalan Ikram-Uniten, 43000 Kajang, Selangor, MALAYSIA

Arkitek Azman Zainal
No 17A Jalan Tengku Ampuan Zabedah J9/J, Seksyen 9, 40100 Shah Alam, Selangor, MALAYSIA

Buan Anshari
Department of Civil Engineering, University of Mataram, Kota Mataram, Nuasa Tenggara Barat, 83115, INDONESIA

ABSTRACT

Kapur (Dryobalanops spp.) is one of the Malaysian common species used for structural construction material. It is capable of serving as a beam and column. This study focused on the experimental mortise and tenon connection fastened with wood; glass fibre reinforced polymer (GFRP), and steel dowel. The finite element method (FEM) was used to model the behaviour of mortise and tenon joint for wood dowel subjected to pull-out loads using ABAQUS software. The experimental results were used to validate a three dimensional finite element model of mortise and tenon joint. The full structural scale of

ISSN 1823-5514, eISSN 2550-164X
Received for review: 2022-08-01
Accepted for publication: 2022-12-20
Published: 2023-01-15

https://doi.org/10.24191/jmeche.v20i1.21091

mortise and tenon was fastened with a 21 mm diameter dowel. The investigation was carried out by applying tensile loads to the top of the tenon. This study adopted a linear elastic orthotropic material to represent the Kapur wood behaviour using the FEM. In this study, the results reveal the load carrying capacity of the mortise and tenon in a sequence of highest to the lowest is when the joint dowelled with GFRP, steel and wood. The stiffness value obtained from the FEM for wood dowel is found higher than the experimental value. Thus, the findings from finite element method (FEM) and the experimental results both had slightly dissimilar load–displacement curve shape. However, this study contributes to a better knowledge of mortise and tenon performance when secured with a wood dowel.

Keywords: *Tropical Timber; Finite Element Analysis; Wood Connection*

Introduction

The most prevalent type of traditional timber joint used in timber structures is the mortise and tenon. This type of joint has been used for hundreds of years and is known to be capable of supporting structural members. A good joint with ductile behaviour is to reinforce with rod or dowel because dowel connections are one of the most common types of joints in timber construction. The strength of the joint connection determines how long a timber construction will last. Any failure of a timber structure's joint will have an impact on the structure's overall performance [1].

Research publications especially in the mortise and tenon for structural timber connections were found to be very limited. There have been studies on using timber frames prior to the publications of a dissertation in Stanford University by Brungraber [2]. Brungraber [2] was the first person who highlighted some concerns on the performance of mortise and tenon in a timber structural framing system. He studied the mortise and tenon using a wood dowel as an individual joint, together with full-scale frame testing, finite element analysis of joint behaviour and a computer model that incorporated connection behaviour. Brungraber [2] found that the dowels and mortises failed before the tenons and also concluded that increasing the dowel diameter is the most effective way to increase the mortise and tenon connection's strength and stiffness. His study has directed the traditional timber frame research in the modern years.

Throughout the years, the compilation of research for mortise and tenon was evolved accordingly; such as the study of design considerations for mortise and tenon connections [3]-[4]; experimental performance of mortise and tenon connections in green Oak [5]-[6]; shear and bending of mortise and tenon performance for Kempas [7]-[9] and mechanical performance of mortise and tenon joints pre-reinforced with slot-in bamboo scrimber plates [10].

Mechanical fasteners are now widely accepted as an important component of modern timber construction [11]. There are few types of fasteners such as nails, staples, bolts, dowels and screws that can be used to create mechanical connections that transmit lateral and withdrawal loads. Bearing stresses develop between the fastener and the connection members are used to transmit lateral loads. For structural or furniture joint applications, wood dowels often known as pegs are commonly used to connect traditional timber joints such as mortise and tenon. Hence, dowels are a low cost and easy to manufacture type of joint.

In this research, the Kapur species has been studied on its structural performances and behavior of failure. The FEM is used to further analyse the mortise and tenon joint fastened with the wood dowel.

Finite Element Method (FEM)

The finite element method (FEM) is now one of the most powerful and commonly utilised methods available in the engineering field. According to Amaruddin [1], many studies employ FEM to simulate the stress–strain state of a complex model under certain conditions.

Several research reported on the FEM to evaluate the mortise and tenon joint strength such as Shank [5] and Amaruddin [1], Jin and Wu [12] and Hu et al. [13] and Zhang and Hu [14], with the goal of finding a more general method to examine the mortise and tenon joint. According to Hu et al. [15], the suggested finite element model was capable of estimating the bending moment capacity of mortise and tenon joints when compared to previous experimental data. They conducted research by using the combination of finite element method (FEM) and response surface method to study the bending moment capacity and bending stiffness of the mortise and tenon joint in order to optimize the mortise and tenon joint's tenon size.

Based on the research done by Zhang and Hu [14], the response surface method was used to investigate the relationship between withdrawal load capacity and tenon length and width. The effect of tenon length and tenon breadth on withdrawal load capacity of the mortise and tenon (M-T) joint was explored using the finite element method (FEM). As a result, the findings demonstrated that the tenon width and length had a notable influence on the sample's M-T joint T-shaped withdrawal load capability. Thus, it stated that the expenses of materials and experiment time can be cut by using FEM to gain a better visual understanding of the M-T joint.

Other than that, Hu and Guan [16] created a new numerical model of a mortise and tenon joint using the finite element method (FEM) to evaluate the semi-rigid timber connection which takes into account the glue line and friction coefficient. To begin, experimental methods were used to evaluate the friction coefficient, glue distributions, and mortise and tenon joint strengths. Second, these parameters were entered into a T-shaped mortise and tenon joint model in order to create a finite element model of the joint. Finally,

experimental and numerical approaches were used to study the pull-out and bending load capacity of T-shaped specimens. The findings revealed that the testing methods used to determine the coefficient, distributions and the glued mortise and tenon joint strengths were all efficacious in determining the mechanical properties of the timber mortise and tenon joint and that the finite element model of joint can be used to analyse the semi-rigid mortise and tenon joint with consistency exceeding 85%.

Meanwhile, Ming and Jianhua [17] have validated that finite element analysis (FEA) may be used to analyse plastic and elastic deformation of materials and point out areas that are vulnerable to damage and failure. In addition, finite element analysis (FEA) has also been used in the modelling and simulation of furniture structure analysis and studies on the evaluation of timber products using FEA has been established.

Methodology

Experimental works

The density of Kapur species is 770 kg/m^3 which can vary by 20% or more at 12% moisture content**.** Five (5) actual structural size mortise and tenon joint manufactured from Kapur for each type of wood, GFRP and steel dowels were tested. The column consists of the mortise section while the beam is the tenon section, accordingly. Each mortise and tenon joint is inserted with a single 21 mm dowel. Pre-drilling of the timber elements, with 3mm oversize to the dowel diameter was adopted in all specimens. The actual structural size of column and beam with mortise and tenon connection specimens were prepared and constructed as shown in Figure 1 and Figure 2, accordingly.

Figure 1 and Figure 2 indicate a nomenclature that is used in the description of a typical mortise and tenon joint subjected to tensile load. It shows the outline of the position of the mortise and tenon joint. Five (5) numbers of LVDTs denoted as 1, 2, 3, 4 and 5 were mounted on the column and beam to measure the respective displacements. The mortise-and-tenon joints were pulled out at the u-shape steel plate that fixed to the tenoned member using a servo-hydraulic IPC 1000 tons test machine. The rate of loading was applied at 1.7 mm/min. for all tests. Limiting rotation was defined by the maximum stroke of the hydraulic jack that is at 25 mm. All joints were tested until total failure i.e. when the tenon member was fully separated from the mortise member.

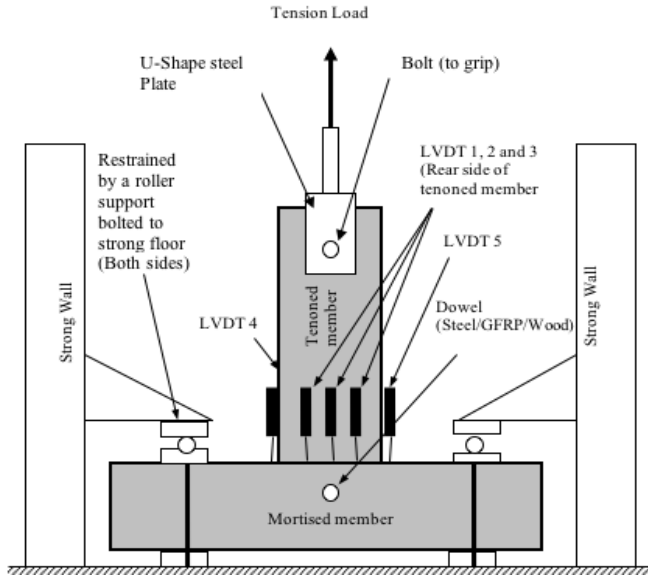

Figure 1: Experimental tensile test set up

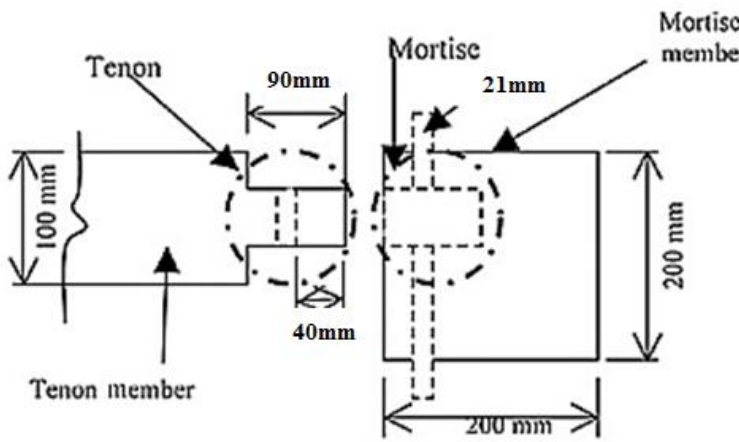

Figure 2: Mortise and tenon joint

Table 1 shows the mechanical properties of Kapur wood used in the finite element model taken from Hassan et al. [18].

Table 1: Material properties of Kapur wood

Mechanical properties of Kapur wood	
Modulus of Elasticity, E (N/mm^2)	13700
Poisson's Ratio, υ	0.69
Shear Modulus, G (N/mm^2)	2812
Tensile Strength, σu (N/mm^2)	116.7

Finite element model using ABAQUS

Abaqus FEA or formerly ABAQUS is one of the application software suites for finite element analysis and computer-aided engineering that was originally released in 1978. The FEM is used to generate accurate and approximate solutions for all linear and non-linear stress, dynamics and thermal problems. The ABAQUS 6.14-1 (academic version) was used in this study. As this version is for academic use, limitation on number of nodes and some functions applied. Therefore, this study is bound to those limitations.

To describe the joint in tension, the connection could only be represented in the elastic range, since the linear elastic orthotropic material was employed [4]. However, the behaviour of elastoplastic materials may be similar to timber's behaviour because timber has some ductility before failure. In this study, solid orthotropic material properties were defined for all members as guided by Amaruddin et al. [1]. For solid orthotropic material, nine mechanical properties must be identified in finite element modelling as indicated in Table 2. The size of this FEM element is similar to the experimental work explained earlier.

The rod of wood dowel may necessitate higher order meshing components, necessitating the addition of more nodes. As the number of nodes grows, so does the amount of time it takes to analyse them. In this project, a fit dowel was assumed. Therefore, there are 64,136 nodes and 42,083 quadratic tetrahedral elements of type C3D10 applied in the finite element model as shown in Figure 3.

All members were given solid orthotropic material properties. MS544 provided the mechanical properties of Kapur species. For solid orthotropic materials, nine mechanical properties must be established in finite element modelling. Since there are no orthotropic material properties for Malaysian timber in MS544, the Poisson's ratio of Kapur was assumed to be similar to the Poisson's ratio of Red Oak, which has an approximate specific gravity as described in the Wood handbook. In addition, Kapur and Red Oak are medium hardwoods where the densities for both species are comparable, 770 kg/m^3 and 740 kg/m^3 respectively. Nevertheless, the strength group of Kapur which is S3 (unseasoned) and SD4 (seasoned) is slightly higher than Red Oak with the strength group of S6 (unseasoned) and SD6 (seasoned). The young modulus ratios in the three orthotropic axes, E_x:E_y:E_z, were considered as

1:6:14 as stated in the Wood Handbook for red oak wood, while the shear modulus, G_{xy}, was obtained as a 1:12 proportion to the young modulus in the longitudinal direction, E_x.

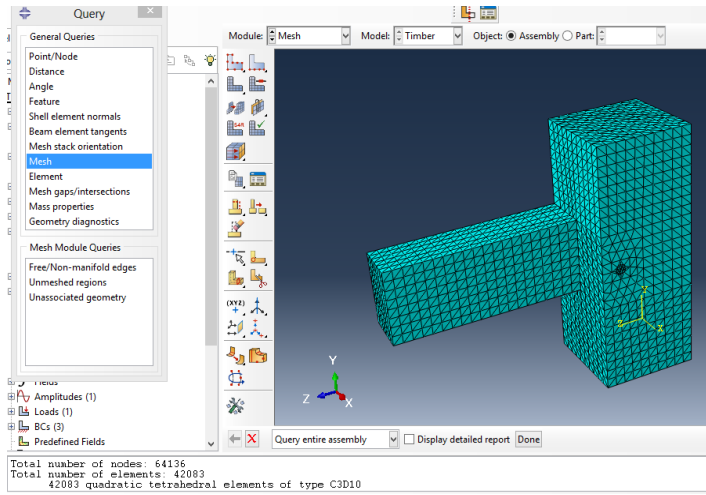

Figure 3: Number of nodes and number of elements applied in the finite element model

Table 2: Orthotropic material properties for Kapur in finite element model

Property	Kapur	Value
E_L (N/mm^2)	E_X	13700
E_R (N/mm^2)	E_Y	2109
E_T (N/mm^2)	E_Z	1123
G_{LR} (N/mm^2)	G_{XY}	1219
G_{LT} (N/mm^2)	G_{XZ}	1109
G_{RT} (N/mm^2)	G_{YZ}	122
μ_{LR}	μ_{XY}	0.35
μ_{LT}	μ_{XZ}	0.448
μ_{RT}	μ_{YZ}	0.56
Mass density		770

As a result, E_y equals 0.154 E_x, resulting in E_y of 2109 N/mm^2. The E_x comes from MS 544 Part 2 with a value of 13700 N/mm^2. E_z has a value of 1123 N/mm^2 when its value is equivalent to 0.082 E_x. While the value of shear modulus (G) was calculated using the supplied ratio of G_{xy} equals to 0.089 E_x, obtaining G_{xy} equals to 1219 N/mm^2. The shear moduli in the xz and yz

planes were determined using the Sangree and Schafer relation. G_{xy}:G_{xz}:G_{yz} in the ratio of 10:9.4:1 was used to describe the relationship between the shear modulus in the three planes. Similar to the experimental laboratory test, the pull-out loading was applied to the tenon top surface. The loading was applied as an incremental concentrated load with a total load of 8 kN. By introducing load factors, non-linear analyses were undertaken to see how the stress state behaved. The loading was then increased to 30 kN to observe the wood dowel behaviour under higher loading. The mortise and tenon joint was modelled in three dimensions in finite element modelling to closely resemble the actual mortise and tenon joint in the laboratory.

Results and Discussion

The failure mode behavior of the mortise and tenon has been observed accordingly. Figures 4 and 5 are showing the mortise and tenon physical failure mode after total fracture under tensile loads, respectively. The result of an experimental test of tensile and stiffness capacity of mortise and tenon joints manufactured from Kapur species is shown in Table 3.

(a) (b)

Figure 4: Mortise and tenon failure; (a) side of the mortised-member failed in major failure – heavy splitting or shearing-out of the mortise, and (b) tenon-end failed in major failure – heavy splitting or shearing-out of the tenon end

For the mortise and tenon dowelled using steel dowel, only 3 out of 5 joint failed in mode I_m and others failed in mode I_s. This means that after the tests, steel dowel remains in its straight form. Though all joints did not fail in the dowel, the mortise failed in different modes (M_{II} and M_{III}). Tenoned-end was found with splits and shearing out and experienced a major mortised-side failure. Due to the lower density of Kapur, it shows that pulling-out the tenoned member from the mortise will affect the mortise side member. The lesser density and weaker strength in Kapur has made the tenoned-member

disperse the energy to the mortised-member and subsequently major cracks or split occurred in the mortise-side member. The weaker and less densifications of Kapur affected the tensile strength of the joints.

Figure 5: Half of hole can be seen and associated with decreasing load

The behaviour of mortise and tenon joint fastened with wood dowel under pulling-out loads was demonstrated by the load-displacement graph (Figure 6) and bar (Figure 7). The load-displacement behaviour of mortise and tenon in tensile passes through four phases as the load increases.

The dowel's distorted shape was in mode IV of the European Yield Model (EYM) mode of failure which was identical to the failure behaviour of wood dowels in the laboratory. There were two plastic hinges with concomitant wood crushing formed as the loads rose during the investigation. Consequently, the plastic hinge was found to be under greater stress.

As a conclusion, tensile strength capacity of different dowel material connections is affected by the dowel materials. Different dowel material was dominant to the different species. The connection shows the highest strength when dowelled with GFRP followed by steel and wood dowelled. The failure modes of mortise and tenon dowelled with steel or GFRP correspond to mode I_m or I_s failure based on National Design Specification (NDS), 2005 [19] classifications. Whilst all joints dowelled with wood failed in mode IV. Steel or GFRP dowel occurred without the yielding of the dowel due to the stiffness of the materials. This also indicates that the mortise and tenon joint dowelled with steel or GFRP performed in a similar manner and they are better than those dowelled with wood.

Table 3: Tensile load and stiffness capacity of mortise and tenon joints

Type of Dowel	Descript.	Stiffness at 5% Offset Load	Proport. Load	5% offset Load	Ultimate Load
		N	N	N	N
Steel	Mean	85,154.84	13,928	16,032.01	19,929.99
	Std.dev.	3,553.25	314.90	668.07	491.67
	CoV(%).	18.87	9.86	18.87	10.77
GFRP	Mean	84,387.26	16,292.01	16,955.19	19095.99
	Std.dev.	2,871.93	353.93	664.13	780.67
	CoV(%).	15.27	9.88	17.07	17.96
Wood	Mean	26,010.97	5,369.98	5,695.01	12,042.49
	Std.dev.	707.49	242.95	279.95	431.76
	CoV(%).	11.68	19.76	21.56	16.16

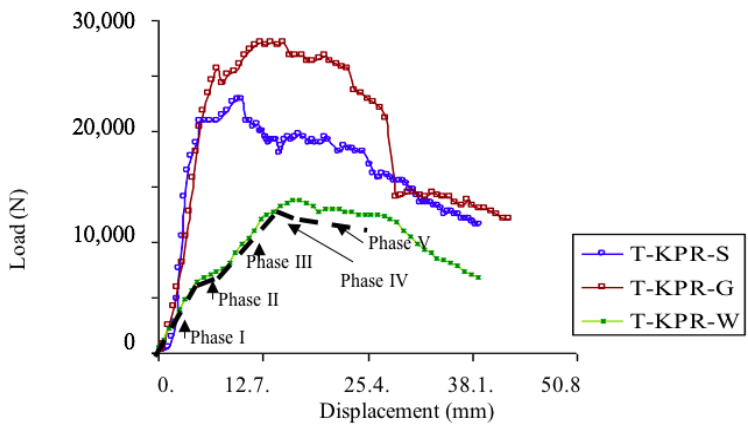

Figure 6: The Load versus displacement of mortise and tenon dowelled with steel, GFRP and wood

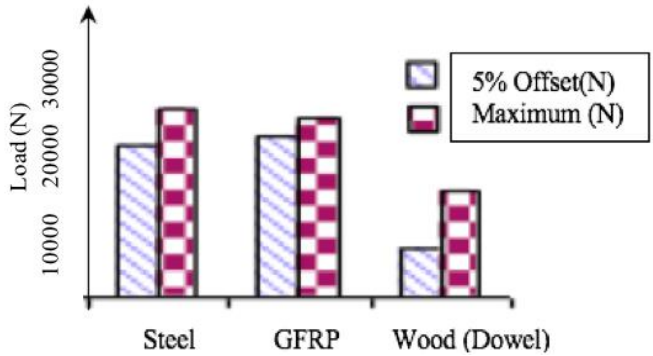

Figure 7: The bar of load carrying capacity differences between the mortise and tenon dowelled with steel, GFRP and wood for 5% offset (N) and maximum (N)

Stress state along the wood dowel under tensile loads

The behaviour of mortise and tenon joint fastened with wood dowel using Kapur species under pulling-out loads was demonstrated by the deformed mesh. As seen in Figure 8, the finite element outputs of stress results were shown in a colour contour. The colour contour can be compared to the key plot to determine the stress state of the dowel at any position. The red colour denotes an area with a higher level of stress where the data has been tabulated in Table 4 according to the tensile load applied.

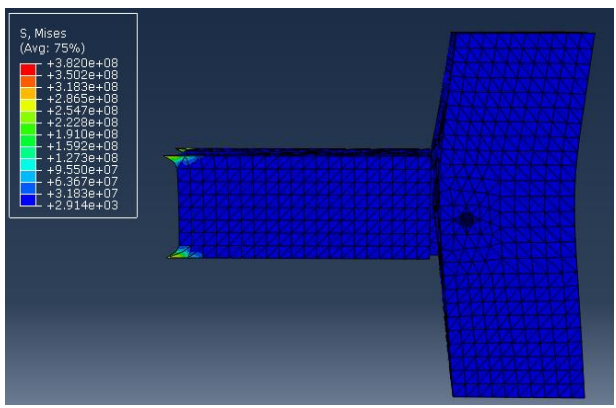

Figure 8: The stress state along the wood dowel subjected to 30kN tensile load

Table 4: Stress of wood dowel obtained from ABAQUS

Load (N)	Stress (N/mm^2)
8000	333.5
16000	335.7
24000	338.1
30000	382.0

From the modelling result, it was observed that the higher stress concentration was focused in the bearing area. Referring to the result from Table 4, the 8 kN load has the least stress value equivalent to 333.5 N/mm² while the highest tensile load of 30kN has the maximum stress value which is 382.0 N/mm². The result shows that the stress state along the wood dowel increases as the tensile load increases. The dowel began to bend as the tensile load rose, forming two plastic hinges at the edge between the tenon and mortise surfaces. Thus, these locations were under a heavy strain zone.

The behaviour of mortise and tenon joint fastened with wood dowel using Kapur species under pulling-out loads was demonstrated by the deformed mesh. The load-displacement behaviour of mortise and tenon in tensile goes through four phases as the load increases. These four phases are easily distinguishable and noticeable by observing Figure 9.

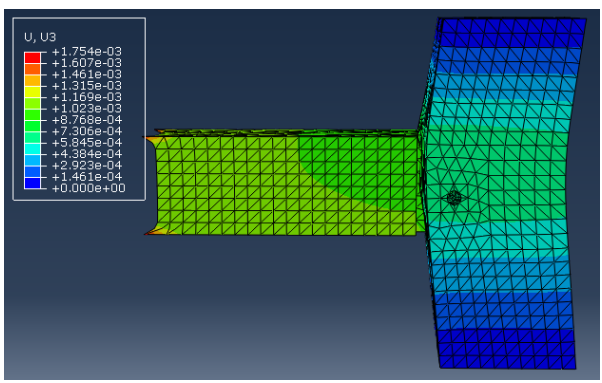

Figure 9: The displacement of mortise and tenon joint fastened with wood dowel subjected to 30 kN tensile load

By referring to Figure 10, it is clear that the results from FEM for the wood dowelled mortise and tenon have linear and well consistent curve shape with those of the experiment in pulling out loads. This is due to the assumption that the finite element model would react linearly elastically which may not be the scenario in a laboratory test. The curve shape was slightly incomparable to the laboratory data in which the stiffness was

considered as yield at a highest value. The graph, on the other hand, reveals that the stiffness of the joint is over-estimated using FEM.

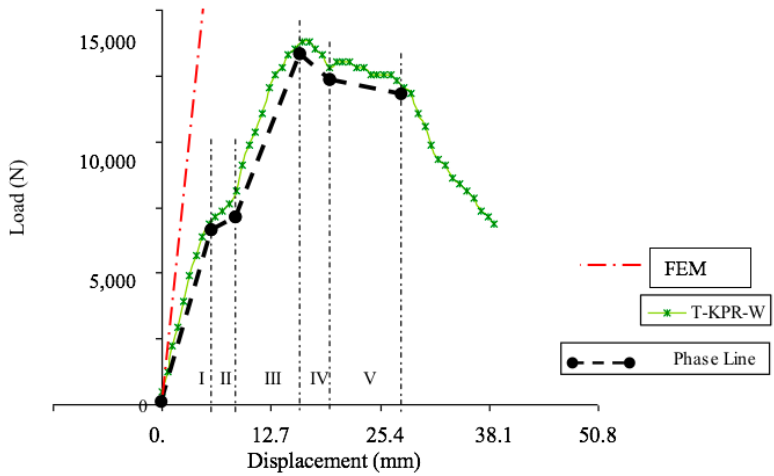

Figure 10: Comparisons of load-displacement curve between laboratory test and finite element method for wood dowel

The value of stiffness at 15 kN obtained from the FEM is 3.94 kN/mm which is high compared to the value of 1.18 kN/mm from laboratory tests. At the yield tensile load of 8 kN, the FEM simulated the displacement at 2.82 mm whilst the laboratory test displaced at 6.35 mm. The displacements obtained from FEM fails to exactly replicated the experimental by 44% differences. In comparison to Hu and Guan [16], they reported their achievement between FEM simulation and laboratory work at 85% similarity where this study found a lower percentage capacity. As stated in the methodology sections, this study is bound to the limitations on the number of nodes and some functions available in the applied FEM. Therefore, the exact simulations of nonlinear performances were not achieved. However, this result supports the finding reported by Amaruddin et al. [1]. Their FEM simulations was achieved only up to linear behaviour for the Kempas species with the similar experimental T-shaped mortise and tenon joint. The simulation was made using LUSAS software and has limited nodes similar to this study.

Conclusion

The findings of this study contribute to a better knowledge of mortise and tenon performance when secured with a different type of dowel. The

experimental work successfully showed a sequence of strength in an order dowelled with GFRP, steel and wood material when mortise and tenon were loaded under tensile load. In this study, the FEM findings and the experimental results both had slightly dissimilar load–displacement curve shape. The linear FEM on the other hand, overestimates the stiffness of the connection for the wood dowel strengthening as well as the incomparable displacement value with experimental tests since the actual behaviour were in non-linear performances.

Contributions of Authors

The authors confirm the equal contribution in each part of this work. All authors reviewed and approved the final version of this work.

Funding

This work was supported by the Fundamental Research Grant Scheme (FRGS) FRGS/1/2018/TK01/UITM/02/21

Conflict of Interests

All authors declare that they have no conflicts of interest.

Acknowledgement

The authors would like to thank the Ministry of Science, Technology and Environment, Malaysia for funding the project through Fundamental Research Grant Scheme (FRGS) FRGS/1/2018/TK01/UITM/02/21.

References

[1] H. I. Amaruddin, R. Hassan, N. A Hamid and N. J. Abd Malek, “Finite Element Model of Mortise and Tenon Joint Fastened with Wood Dowel Using Kempas Species”, *Proceedings of the International Civil and Infrastructure Engineering Conference*. DOI: 10.1007/978-981-4585-02-6_1, Sarawak, Malaysia, September 2014.

[2] R. Brungraber “Traditional Timber Joinery: A Modern Approach”, PhD Thesis, University of Stamford, 1985.

[3] R.J. Schmidt and E. D. Daniels, "Design Considerations for Mortise and Tenon Connections", Report for Timber Framers Guild. Becket. MA., 1999.
[4] R.J. Schmidt, "Timber Wood dowels Consideration for Mortise and Tenon Joint Design", *Wood Design Focus*, vol. 14, no.3; pp. 44-47, 2006.
[5] J.D. Shanks, "Developing Rational Design Guidelines for Traditional Joints in Oak Frame Construction", PhD Thesis, University of Bath, 2005.
[6] J.D. Shanks and P. Walker, "Experimental performance of mortise and tenon connections in green oak", *Structural Engineer*, vol. 83, no. 17, pp. 40-45, 2005.
[7] R. Hassan, A. Ibrahim, and Z. Ahmad, "Shear and Bending Performance of Mortise And Tenon Connection Fastened With Dowel", *Journal of Tropical Forest Science*, vol. 22, no.4, pp. 425–432, 2010.
[8] R. Hassan, "Structural Performance of GFRP Dowelled Mortise and Tenon Connections Made of Selected Tropical Species", PhD. Thesis, Faculty of Civil Engineering, Universiti Teknologi MARA (UiTM), Shah Alam, Selangor, Malaysia, 2011.
[9] R. Hassan, A. Ibrahim and Z. Ahmad, "Shear Capacity of Dowelled Mortise and Tenon in Tropical Timber", *IOP conference series: Material science and engineering*, vol. 17, no.1, pp. 012012, 2011.
[10] G. Wu, M. Gong and Y. Gong, "Mechanical performance of mortise and tenon joints pre-reinforced with slot-in bamboo scrimber plates", *Journal of Wood Science,* vol. 65**,** no. 1, 2019.
[11] W.M.C. McKenzie and B. Zhang, Design of Structural Timber. To Eurocode 5. Macmillan International Higher Education, 2007.
[12] H. Jin and H. Wu, "Finite element modelling of fracture in dowel-type timber connections", 2014. Retrieved from http://lnu.diva potal.org/smash/get/diva2:722437/FULLTEXT02.pdf.
[13] W. Hu, H.Y. Guan and J. Zhang, "Finite element analysis of tensile load resistance of mortise-and-tenon joints considering tenon fit effects", *Wood and Fiber Science,* vol. 50, no.2, pp. 121-131. 2018.
[14] T. Zhang and W. Hu, "Numerical Study on Effects of Tenon Sizes On Withdrawal Load Capacity of Mortise And Tenon Joint", *Wood Research*, vol. 66. no. 2. pp 321-330. 2021.
[15] W. Hu and N. Liu, "Comparisons of finite element models used to predict bending strength of mortise and tenon joints", *BioResources,* vol. 15, no. 3, pp. 5801-5811, 2020.
[16] W. Hu and H.Y. Guan, "A finite element model of semi-rigid mortise-and-tenon joint considering glue line and friction coefficient", *Journal of Wood Science*, vol. 65, no.1, pp. 1-9, 2019.
[17] M. Chen and J. Lyu, "Properties of double dowel joints constructed of Medium Density Fiberboard", *Maderas. Ciencia y tecnología*, vol. 20, no. 3, pp. 369-380, 2018.

[18] R. Hassan, S.S.A. Syed Mubarat and A. Alisibramulisi, "Young Modulus and Poisson's Ratio of Merpauh, Kapur and Sesenduk Species", *Jurnal Teknologi*, vol. 78, no. 5-2, pp. 29-33, 2016.
[19] NDS, "National Design Specification" for Wood Construction American Forest and Paper Association (AFPA) Washington D.C, 2005.
[20] A. Iqbal and P. Sejkot, "Finite element modelling of ductile wood connections", *CSCE Annual Conference*, Growing with youth – Croître avec les jeunes, 2019.
[21] B.H. Xu, M. Taazount, A. Bouchair and P. Racher, "Numerical 3D finite element modelling and experimental tests for dowel-type timber joints", *Construction and Building Materials*, vol. 23, no. 9, pp. 3043-3052, 2009.
[22] Mesut Uysal and Eva Haviarova, "Evaluating Design of Mortise and Tenon Furniture Joints Bending Loads by Lower Tolerance Limits", *Wood and Fiber Science Journal*, vol 53, no. 2, 2021.
[23] W. Hu and H.Y. Guan, "Research on Withdrawal Strength of Mortise and Tenon Joint by Numerical and Analytic Methods", *Wood Research*, vol 62, no. 4, pp. 575-586, 2017.
[24] Wenming Liu and Jiajun Leng, "The Application Research of Mortise and Tenon Structure in Cultural and Creative Products", *IOP Conf. Ser.: Mater. Sci. Eng.*, vol. 573, no. 1, pp. 012006, 2019.
[25] Wood Handbook, "*Wood as an Engineering Material"*, United States Department of Agriculture, 1999.

A Comparative Study on the Physical and Rheological Properties of 60/70 and 80/100 Penetration Grade Bitumen in Malaysia

Rickey Santhanasamy[*], Muslich Hartadi Sutanto
Department of Civil and Environmental Engineering,
Universiti Teknologi PETRONAS (UTP), 32610 Bandar Seri Iskandar,
Perak, MALAYSIA
[*]rickey_20002051@utp.edu.my

ABSTRACT

The engineering properties of a bitumen plays vital role in determining the suitability of the bitumen usage for a pavement structure. Presently, bituminous pavements in Malaysia are constantly subjected to high-speed loading of vehicles as well as increased pavement temperature due to extreme solar heat which causes rutting and fatigue failure issues. In this research, the 60/70 and 80/100 penetration grade bitumen were subjected to both physical and rheological testing. Physical testing was used to determine the softening point, ductility, penetration and penetration index value whereas rheological testing chiefly determined the engineering properties of the bitumen such as complex modulus and phase angle which interprets the stiffness and viscoelastic behavior. Physical testing results indicate that the 60/70 penetration grade bitumen possesses lower penetration value, higher softening point, adequate ductility and higher penetration index value compared to the 80/100 penetration grade bitumen. Besides, rheological results show that the complex modulus and rutting factor of 60/70 bitumen indicates good stiffness towards temperature rise compared to the 80/100 penetration grade bitumen, thus, posing better resistance towards permanent deformation. Additionally, the 60/70 penetration grade bitumen generally possesses better elasticity compared to the 80/100 penetration grade bitumen which is observed through the phase angle determination.

ISSN 1823-5514, eISSN 2550-164X
Received for review: 2022-08-23
Accepted for publication: 2022-12-08
Published: 2023-01-15

https://doi.org/10.24191/jmeche.v20i1.21092

Keywords: *60/70 Penetration Grade Bitumen; 80/100 Penetration Grade Bitumen; Physical Testing; Rheological Testing*

Introduction

Currently, the rapid development parallel to high population demands a good mode of transportation. Among the current mode of transportations, roadways play the vital role as the widely available and commonly used travel mode. Bitumen is the key material of pavement structures in which it is used as bituminous binder. Although bitumen makes up only 4% to 6% by weight of the asphaltic mixture, it is nevertheless pivotal in defining the pavement performance. Bitumen is often described as a material consisting complex chemical composition which exhibits characteristics that are time and temperature dependent [1].

In Malaysia, common pavement distresses faced are the rutting and fatigue failures. Rutting is the deterioration of road surfaces faced in high temperature regions whereas the fatigue cracking is much prominent in the low temperature regions. This can be credited to bitumen's unique trait, viscoelasticity, in reference to the partly elastic solid-like behaviour exhibiting recoverable deformation in cold environment and partly viscous fluid-like properties influencing permanent deformation after loading at high temperature whereas both merged as viscoelastic behaviour at mid-temperatures [2].

The commonly adopted bitumen specifications for road surfacing are based on the results of physical testing of bitumen such as softening point test, penetration test, ductility test and viscosity. However, these physical tests are insufficient to describe the viscoelastic properties of bitumen required, to adequately relate the bitumen to in-service asphaltic mixture performance as it only measures the properties within a constant temperature. Besides, these tests are also arguable as they do not account for the time-dependent response of bitumen binder [3].

Presently, a modern equipment called dynamic shear rheometer (DSR) is used to determine the rheological properties of bitumen which produces more accurate results over a range of time and temperature. The viscoelastic properties of bitumen can be described through the rheological parameters of complex shear modulus (G*) and phase angle (δ). The complex shear modulus is the measure of total deformation resistance of bitumen when subjected to repeated shear loading [2], [4]-[7]. It has two different components as shown in Figure 1. The elastic modulus (G') is as depicted on the horizontal axis and the viscous modulus (G") as indicated on the vertical axis. The phase or loss angle (δ) is the time lag between the applied shear stress and the shear strain response during rheological testing [5] or in other words indicates the amount of temporary and permanent deformation [8]. As seen in Figure 1, the phase

angle is the angle between the complex modulus and horizontal axis. A large phase angle value indicates that the material possesses more viscous behavior whereas lower phase angle value depicts an elastic behavior [9]. Hence, the determination of G* and δ can illustrate the viscoelastic property of bitumen with regards to rate of loading (time) and temperature [8].

In this study, the commonly used bitumen in Malaysia which are of the penetration grades 60/70 and 80/100 are subjected to rheological testing to evaluate its viscoelastic properties. Besides, these bitumen are also subjected to physical testing to determine its physical properties.

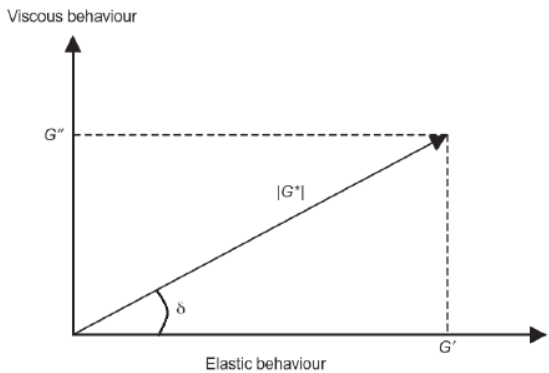

Figure 1: Correlation of |G*|, G', G" and δ [10]

Methodology

Materials

The bitumen used in this study is of penetration grade 60/70 and 80/100. The bitumen samples were supplied by PETRONAS Refinery Malacca, Malaysia. Both samples of bitumen were subjected to testing to obtain its physical properties and rheological properties.

Preparation of bitumen

All bitumen samples used in this study were unmodified. The 60/70 and 80/100 bitumen were melted by heating them to a temperature between 75 °C to 100 °C. Upon reaching the desired temperature, the bitumen becomes sufficiently fluid to be used for further testing.

Physical properties evaluation

Penetration test

The penetration test was conducted using the Semi-Automatic Penetrometer in accordance with the ASTM D5 standards as in Figure 2. The sufficiently fluid

bitumen was first poured into penetration test container and left to cool at room temperature for about 1.5 hours. The cooled sample is then conditioned in a water bath with a temperature maintained at 25 °C for another 1.5 hours before subjecting to testing. This test was conducted at a temperature of 25 °C with a known load of 100 g and a period of 5 seconds. The penetration value is obtained by observing penetration depth produced by the needle in units of 0.1mm on the tested sample. This test was used to determine the consistency of the bitumen as well as the mode of classifying the bitumen according to its penetration grade.

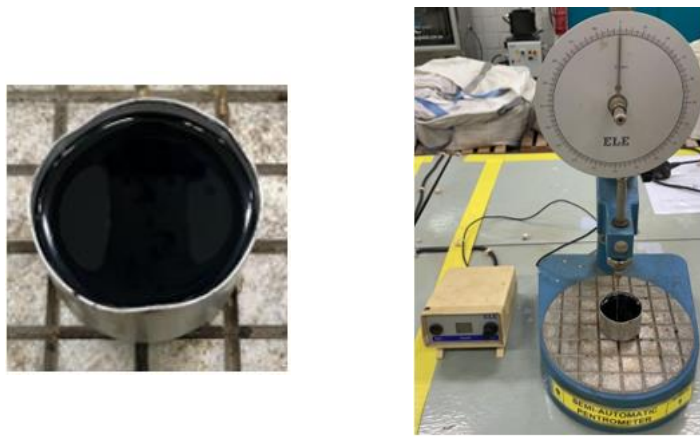

(a) (b)

Figure 2: (a) Prepared bitumen sample, and (b) apparatus setup for penetration test

Softening point test

The softening point test or ring and ball test (ASTM D36) was conducted to determine and characterize the temperature at which the bitumen softens. The heated bitumen with sufficient viscosity was poured into the ring and cooled down to room temperature. Then the excess bitumen in the ring was trimmed level with a warm knife. The assembled ring and ball apparatus with bitumen sample, the ball centralization guide, steel balls of weight 3.5 g were all immersed in a water bath maintained at 5 °C for 15 minutes. Then the ball was placed in the center of the ball guide and the set-up was heated to a temperature of 5 °C/min. The softening point temperature was recorded when the bitumen sample softens and can no longer support the steel ball. The apparatus setup is illustrated in Figure 3.

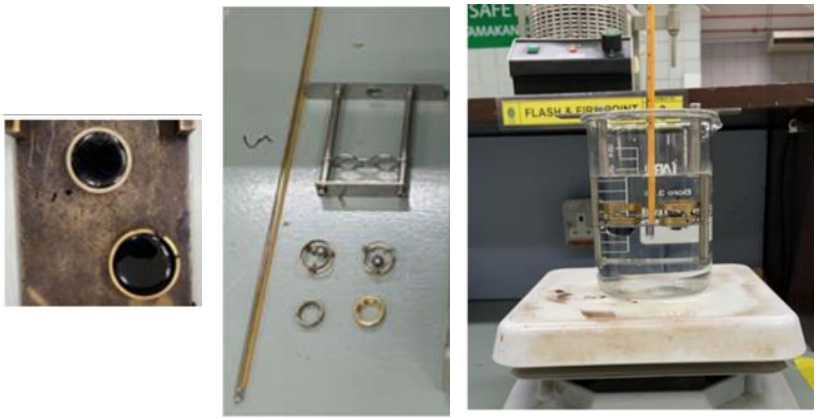

(a) (b) (c)

Figure 3: (a) Bitumen sample preparation, (b) apparatus of softening point test, and (c) apparatus setup for softening point test

Ductility test

The ductility test was conducted in accordance with ASTM D113 standards as pictured in Figure 4. The prepared molten bitumen was poured into the mould assembly known as briquette and cooled down to room temperature for about 40 minutes. It was then conditioned inside a water bath maintained at a temperature of 27 °C for 30 minutes. The mould assembly containing the sample was removed and the excess bitumen was trimmed before it was again subjected to conditioning in water bath at 27 °C for 90 minutes. After that, the sides of the mould assembly are removed, and the briquette was hooked on the machine whereby the machine pulls the specimen apart at a rate of 50 mm/min. The point at which the bitumen specimen thread breaks is described as the ductility value of the sample in cm.

(a) (b)

Figure 4: (a) Bitumen filled briquettes conditioned in 27 °C water bath, and (b) Briquettes removed from mould and hooked into place

Penetration Index (PI)

The penetration index (PI) was evaluated to determine the temperature susceptibility of the 60/70 and 80/100 penetration grade bitumen. The PI value is computed by using the formula below as described by the Shell Bitumen Handbook [1], [11]-[12].

$$PI = \frac{1952 - 500\log(Pen_{25}) - 20SP}{50\log(Pen_{25}) - SP - 120} \quad (1)$$

The Pen_{25} in Equation (1) represents the penetration value of the bitumen tested at 25 ℃ whereas SP stands for the softening point value of the sample. Table 1 shows the standard test specification for penetration test, softening point test and ductility test according to the ASTM standards.

Table 1: Standard specification of penetration test, softening point and ductility test [13]

	Range		Standard
	Bitumen 60/70	Bitumen 80/100	ASTM
Penetration @ 25 ºC	60-70	80-100	D5
Softening point (ºC)	49-56	45-52	D36
Ductility @ 25 ºC	> 100cm	>100cm	D113

Rheological properties evaluation

All the rheological tests to evaluate the viscoelastic properties of the bitumen were conducted using the Dynamic Shear Rheometer (DSR) machine of Kinexus Pro+ model as shown in Figure 5a. Generally, the test is operated by placing the bitumen between two parallel plates as shown in Figure 5b where the bottom plate is fixed, and the top plate creates an oscillatory motion producing shear stress on the bitumen. The test yields rheological parameters such as complex shear modulus, phase angle, elastic modulus and loss modulus at different temperatures which was automatically recorded by the DSR software. The outputs are principally calculated using the Equation (2), Equation (3) and Equation (4).

$$\sigma = \frac{2T}{\pi r^3} \quad (2)$$

$$\gamma = \frac{\theta r}{h} \quad (3)$$

$$G^* = \frac{\sigma_{max}}{\gamma_{max}} \quad (4)$$

Amplitude sweep test

All the rheological tests were carried out under strain-controlled mode and at a constant frequency of 10 rad/s. Both types of bitumen were tested at temperatures 10 to 40 ºC by using the 8 mm diameter plates with 2 mm gap and at 40 to 80 ºC by using the 25 mm diameter plates with 1mm gap [8]-[14]. Preliminary amplitude sweep test were performed on all samples to determine its linear viscoelastic limit with the strain amplitude varied from 0.01% to 100%.

Temperature sweep test

Similar to amplitude sweep test, temperature sweep test was carried out under strain-controlled mode and at a constant frequency of 10 rad/s. The temperatures of test range from 10 to 80 ºC with an increment of 2 ºC per minute and the strain limit was kept low as determined from the amplitude sweep test so that the test is performed within the linear viscoelastic region.

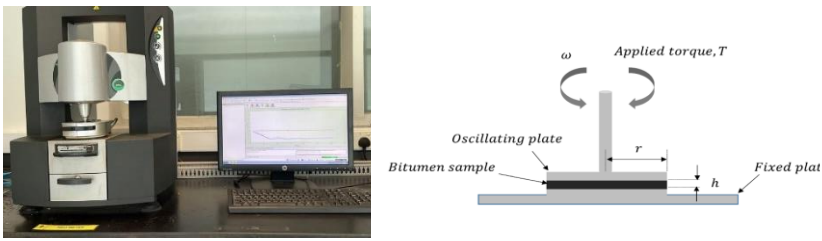

(a) (b)

Figure 5: (a) KINEXUS pro+ dynamic shear rheometer, and (b) DSR testing configuration

Results and Discussion

Physical properties

Penetration test results

Penetration test chiefly determines the hardness of bitumen [15]. Based on Table 2, it can be inferred from the test, penetration values of bitumen grades 60/70 and 80/100 are 65.44 and 88.22, respectively. Comparing the experimental results to the standard penetration range of bitumen from Table 1, the test proves that the bitumen samples belong to 60/70 and 80/100 penetration grade where it falls in the standard penetration range. The penetration value of bitumen grade 60/70 is lower compared to the latter which indicates that this bitumen is harder. This depicts that the resistance against temperature defects is higher when bitumen grade 60/70 is used.

Softening point test results

As Table 2 indicates, the softening point temperatures for the 60/70 and 80/100 bitumen are 51.65 ºC and 46.6 ºC respectively. The experimental values are within the standard specification range specified thus, accrediting the results obtained. As bitumen is a semi-solid and possesses viscoelastic properties naturally, it has the tendency to transition from a solid to molten liquid phase under certain degree of temperature. The viscoelastic property causes the bitumen to soften at a certain temperature and based on this softening point test, it can be seen that the 60/70 penetration grade bitumen requires a higher temperature range to soften when compared to the 80/100 penetration grade bitumen. Thus, 60/70 grade bitumen is more suitable to be used at places with higher pavement temperature.

Table 2: Data Sheet for 60/70 and 80/100 bitumen physical properties

Bitumen	Penetration value	Softening point (°C)	Ductility value (cm)	Penetration index (PI) value
60/70	65.44	51.65	128.88	-0.15
80/100	88.22	46.60	132.93	-0.68

Ductility test results

Ductility test conducted on the bitumen samples specifies that the ductility values of the 60/70 and 80/100 grade bitumen are 128.88 cm and 132.93 cm respectively. The ductility values of both 60/70 and 80/100 grade bitumen meet the standard requirement of minimum 100cm. Theoretically, bitumen with high ductility possess high adhesive property [16]. This shows that each bitumen possesses a good ductility rate, which is an important parameter in preventing cracks of the bituminous pavement.

Penetration Index (PI)

The PI values calculated from penetration value and softening point indicate the temperature susceptibility of bitumen. It can be observed that the PI value of 60/70 grade bitumen is -0.15 whereas -0.68 for 80/100 grade bitumen which are within the acceptable range of -2 to +2 [17]-[18]. The penetration index provides an insight on the temperature susceptibility of the bituminous binder. A higher penetration index indicates a lower temperature susceptibility which means the bitumen has a higher temperature resistance whereas lower penetration index indicates higher temperature susceptibility thus causing the bitumen to be lesser resistance towards temperature rise. Thus, the 60/70 penetration grade bitumen which possesses a higher PI value indicates a greater resistance to temperature susceptibility and concurrently, a higher temperature resistance compared to the 80/100 grade bitumen.

Rheological properties

Amplitude sweeps test results

Amplitude sweep test is used to establish the linear viscoelastic limit of the bitumen. The linear viscoelastic limit is defined as the strain percentage (%) when the complex shear modulus reduces to 95% of its starting value [19]. Preliminary observation on the amplitude sweep test indicates that the strain limit increases with an increase in temperature [20]. Therefore, a low testing temperature was taken at each testing geometry. Table 3 lists the linear viscoelastic limits determined from each type of bitumen sample. The strain limit values obtained from testing at 8 mm spindle was lower compared to 25 mm. As such, the strain limit from 8 mm spindle testing was taken as the limit of linear viscoelastic range and further analysis were done at this strain limit to ensure all tests are performed within the linear viscoelastic range.

Table 3: Linear viscoelastic strain limits

Bitumen	60/70	80/100
8 mm (2 mm gap) at 10 ºC	1.0%	1.1%
25 mm (1 mm gap) at 40 ºC	2.4%	3.5%

From Table 3, it is seen that the linear viscoelastic limit of 60/70 grade bitumen is 1.0% whereas for 80/100 grade bitumen is 1.1%. The strain limit of 80/100 is higher compared to the 60/70 grade bitumen.

Temperature sweep test results

Figure 6 shows the isochronal plot of the 60/70 and 80/100 bitumen. The plot clearly distinguishes the changes of complex modulus with an increase in the temperature. 80/100 bitumen possess higher G* modulus value at temperatures below 40 °C indicating a stiffer bitumen compared to the 60/70 grade. Nevertheless, extremely high stiffness can be detrimental in a cold environment as it would compromise the fatigue resistance of the pavement. It is because during increased traffic and reduced temperature condition, the accumulation of stresses cause the bitumen to deform that would increase the susceptibility to fatigue cracking of the pavement.

On the contrary, as the temperature increases over 35 ºC the 60/70 bitumen seems to show a consistent superiority of resistance to deformation as compared to 80/100 sample indicating the former to be a stiffer bitumen within this temperature range. This points that the 60/70 bitumen is beneficial in terms of rutting resistance in hot climatic countries like Malaysia because higher stiffness can resist the deformation caused by combined action of increased temperature with repeated wheel loading of vehicle.

On the other hand, Figure 7 illustrates the plots of phase angle versus temperature for the 60/70 and 80/100 bitumen. From Figure 7, it can be inferred that the 60/70 bitumen possess lower phase angle compared to the

80/100 bitumen. This trend proves that the 60/70 bitumen comparatively holds a better deformation recovery due to better elasticity property. It was also found that the phase angle of both bitumen increased with a rise in temperature which is observed until it eventually reaches a plateau region at a high temperature above 70 ºC.

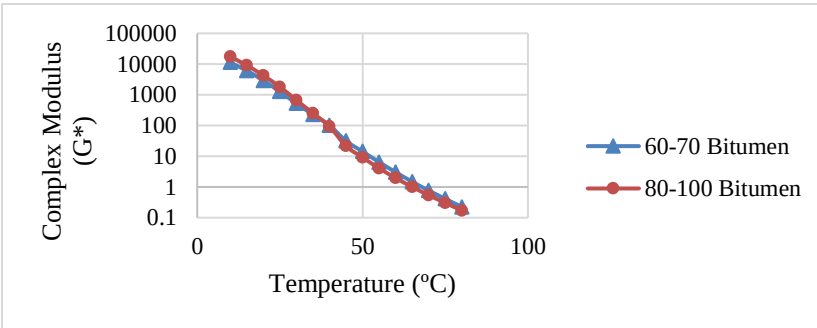

Figure 6: Effect of temperature on the complex modulus of 60/70 and 80/100 bitumen

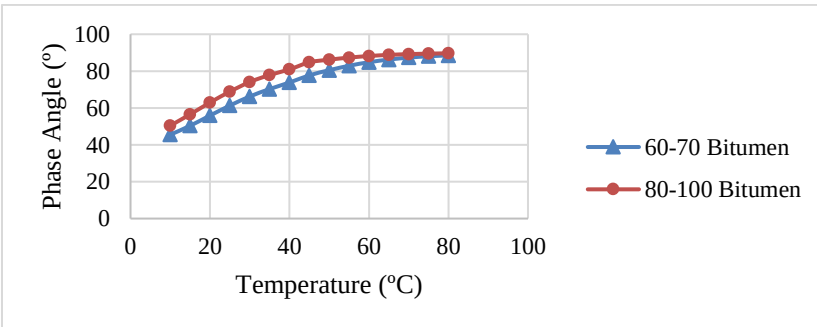

Figure 7: Effect of temperature on the phase angle of 60-70 and 80-100 bitumen

Rutting factors for unaged binders

The rutting factor, G*/sin δ indicates resistance to permanent deformation of the bitumen, which is subjected to severe environmental and traffic conditions. The Superpave specifies the minimum rutting resistance, G*/sin δ to be valued at 1.0 kPa for unaged bitumen [21]-[23]. This ensures that the unaged bitumen possess adequate resistance towards rutting before being used. Based on Figure 8, it is noticed that the rutting failure temperature for the 60/70 and 80/100 bitumen are 67.48 ºC and 64.89 ºC, respectively. When the rutting failure

temperature is high, it indicates lower permanent deformation upon implication of high temperature. The 60/70 bitumen clearly has a higher rutting resistance ability than the 80/100 bitumen. Thus, the 60/70 bitumen at 1.0 kPa limit performs better in terms of its resistance against rutting problems than the 80/100 bitumen in hot climatic country such as Malaysia.

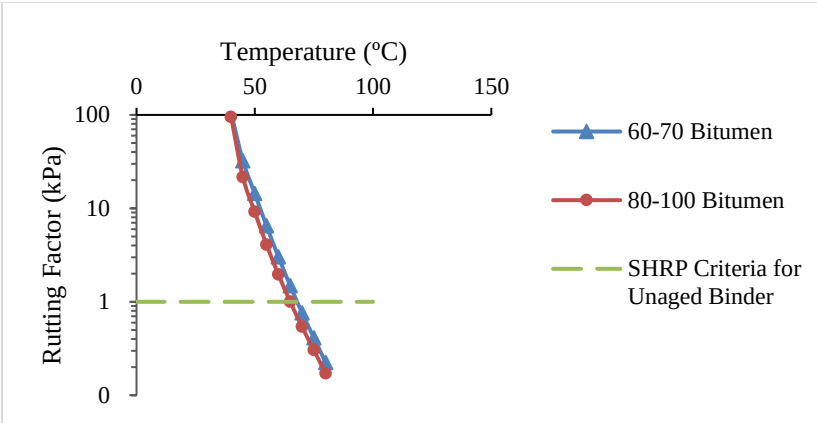

Figure 8: Rutting factors for unaged 60-70 and 80-100 bitumen

Conclusion

Based on the preliminary physical testing, the results indicate that the 60/70 penetration grade bitumen holds a better resistance to temperature influence as well as adequate hardness than the 80/100 penetration grade bitumen. Besides, the penetration index or temperature susceptibility evaluation indicates that the 60/70 grade bitumen possess less susceptibility to temperature due to a slightly higher PI value. Nevertheless, both bitumen grades are well within the acceptable requirements.

Moving forward, rheological testing proves that the 60/70 bitumen exhibits better stiffness above 35 ºC as compared to the 80/100 bitumen which depicts that the former possesses more resistance to deformation in high temperature regions like Malaysia where the pavement temperature can reach up to 55 ºC [24]. Nevertheless, at lower temperatures, the 80/100 bitumen is deemed to hold higher stiffness with lower elasticity, but 60/70 bitumen exhibits more elasticity as well as moderate stiffness thus posing a better resistance to fatigue cracking.

Besides, the rutting factor which is determined according to the SHRP specification indicates that the 60/70 bitumen has higher rutting failure temperature compared to the 80/100 bitumen. Overall, it can be concluded that

the 60/70 grade bitumen exhibits decent engineering properties in terms of both fatigue and rutting resistance. Thus, this finding confirms with the Ministry of Public Works Department directive of encouraging the wide usage of 60/70 grade bitumen in Malaysian roads [25].

Contributions of Authors

The authors confirm the equal contribution in each part of this work. All authors reviewed and approved the final version of this work.

Funding

This work was supported and funded by Yayasan Universiti Teknologi PETRONAS (YUTP) under a grant (cost center: 015LC0-200).

Conflict of Interests

All authors declare that they have no conflicts of interest.

Acknowledgement

The authors would like to express utmost gratitude and acknowledge the funding from Yayasan Universiti Teknologi PETRONAS (YUTP) and to all those who have directly or indirectly contributed to this study.

References

[1] N. Bala, I. Kamaruddin, M. Napiah and N. Danlami, "Rheological and rutting evaluation of composite nanosilica/polyethylene modified bitumen," in *7th International Conference on Key Engineering Materials*, 2017. https://doi.org/10.1088/1757-899X/201/1/012012

[2] S. S. Galooyak, B. Dabir, A. E. Nazarbeygi and A. Moeini, "Rheological properties and storage stability of bitumen/SBS/montmorillonite composites," *Construction and Builiding Materials*, vol. 24, no. 3, pp. 300-307, 2010. https://doi.org/10.1016/j.conbuildmat.2009.08.032

[3] N. I. Md. Yusoff, M. T. Shaw and G. D. Airey, "Modelling the linear viscoelastic rheological properties of bituminous binders," *Construction*

and Building Materials, vol. 25, no. 5, pp. 2171-2189, 2011. https://doi.org/10.1016/j.conbuildmat.2010.11.086

[4] I. Hafeez, J. Hussain, K. Riaz, A. Khitab, S. Hussain, B. Zaidi, U. Farooqi, A. Hayat, I. Ahmed and A. Asif, "Influence of Time and Temperature on Asphalt Binders Rheological Properties," *Life Science Journal*, vol. 10, no. 12s, pp. 894-898, 2013. http://www.dx.doi.org/10.7537/marslsj1012s13.146

[5] G. D. Airey and B. Rahimzadeh, "Combined bituminous binder and mixture linear rheological properties," *Construction and Building Materials*, vol. 18, no. 7, pp. 535-548, 2004. https://doi.org/10.1016/j.conbuildmat.2004.04.008

[6] A. A. Mohamed, S. Y. Wong, L. T. Leong, M. A. Farooqi, R. P. Jaya, Z. H. Al - Saffar and H. Yaacob, "Durability Phenomena of Bitumen and Bituminous Pavement Materials," *The Open Civil Engineering Journal*, vol. 15, no. 1, pp. 279-289, 2021. http://dx.doi.org/10.2174/1874149502115010279

[7] F. Giustozzi, K. Mansour, F. Patti, M. Pannirselvam and F. Fiori, "Shear rheology and microstructure of mining material-bitumen composites as filler replacement in asphalt mastics," *Construction and Building Materials*, vol. 171, pp. 726-735, 2018. https://doi.org/10.1016/j.conbuildmat.2018.03.190

[8] M. Javid and A. Rahim, "Characterization of Visco-Elastic Properties of Locally Available Asphalts in Pakistan," *Pakistan Journal of Engineering and Applied Science*, vol. 9, pp. 17 - 23, 2011. http://dx.doi.org/10.1201/b12754-80

[9] N. Mashaan, A. Chegenizadeh and H. Nikraz, "A Comparison on Physical and Rheological Properties of Three Different Waste Plastic-Modified Bitumen," *Recycling*, vol. 7, no. 2, p. 18, 2022. https://doi.org/10.3390/recycling7020018

[10] G. D. Airey and E. Hunter, "Dynamic mechanical testing of bitumen: sample preparation methods," in *Proceedings of the Institution of Civil Engineers - Transport*, 2003. https://doi.org/10.1680/tran.2003.156.2.85

[11] J. Read and D. Whiteoak, Shell bitumen handbook, 5th Edition, London: Thomas Telford Publishing, 2003.

[12] B. V. Kok, B. Irhan, M. Yilmaz and E. Yalcin, "Research on the rheological properties of bitumen modified with waste photopolymer," *Construction and Building Materials*, vol. 346, pp. 128446, 2022. https://doi.org/10.1016/j.conbuildmat.2022.128446

[13] M. R. Rahman, S. Chowdhury, Md Abdullah, A. Sarkar, R. S. Sayeed and M. M. Islam Real, "A Comparative Study on Properties of Different Grade Bitumen Used in The Transportation Projects in and Around

Dhaka City," *Trends in Civil Engineering and its Architecture*, vol. 3, no. 2, pp. 1-7, 2019. http://dx.doi.org/10.32474/TCEIA.2019.03.000159

[14] D. A. Anderson, D. W. Christensen, H. W. Bahia, R. Dongre, M. G. Sharma, C. E. Antle and J. Button, "Binder Characterization and Evaluation Volume 3: Physical Characterization," Strategic Highway Research Program, Washington DC, 1994.

[15] R. A. Yousif, S. A. Tayh, I. F. Al-Saadi and A. F. Jasim, "Physical and Rheological Properties of Asphalt Binder Modified with Recycled Fibers," *Advances in Civil Engineering*, vol. 2022, pp. 1-12, 2022. https://doi.org/10.1155/2022/1223467

[16] J. G. Speight, "Chapter 4 - Test Methods for Asphalt Binders," in *Asphalt materials science and technology*, Boston, Butterworth-Heinemann, pp. 137-203, 2016. https://doi.org/10.1016/B978-0-12-800273-5.00004-0

[17] L. Hruskova, B. Kiselova and P. Daucik, "Criteria for evaluation of unmodified and modified bitumens," *Petroleum & Coal*, vol. 57, no. 6, pp. 650-660, 2015.

[18] Y. H. Abed and A. H. A. Al-Haddad, "Temperature susceptibility of modified asphalt binders," *IOP Conference Series: Materials Science and Engineering*, vol. 671, pp. 1-12, 2020. https://doi.org/10.1088/1757-899X/671/1/012121

[19] M. Rochlani, S. Leischner, D. Wareham, S. Caro, G. C. Falla and F. Wellner, "Investigating the performance-related properties of crumb rubber modified bitumen using rheology-based tests," *International Journal of Pavement Engineering*, vol. 23, no. 3, pp. 877-887, 2022. https://doi.org/10.1080/10298436.2020.1776868

[20] N. I. Md. Yusoff, D. Monieur and G. Airey, "The 2S2P1D: An Excellent Linear Viscoelastic Model," *Journal of Civil Engineering, Science and Technology*, vol. 1, no. 2, pp. 1-7, 2010. https://doi.org/10.33736/jcest.76.2010

[21] H. Zhang, H. Luo, H. Duan and J. Cao, "Influence of zinc oxide/expanded vermiculite composite on the rheological and anti-aging properties of bitumen," *Fuel*, vol. 315, pp. 1-9, 2022. https://doi.org/10.1016/j.fuel.2022.123165

[22] X. Han, S. Mao, S. Xu, Z. Cao, S. Zeng and J. Yu, "Development of novel composite rejuvenators for efficient recycling of aged SBS modified bitumen," *Fuel*, vol. 318, pp. 1-11, 2022. https://doi.org/10.1016/j.fuel.2022.123715

[23] M. Sutanto, N. Bala, K. A. Zaro and S. Sunarjono, "Properties of Crumb Rubber and Latex Modified Asphalt Binders using Superpave Tests," in *International Conference on Civil, Offshore & Environmental Engineering, 2018*. https://doi.org/10.1051/matecconf/201820305007

[24] N. S. Mashaan, A. H. Ali, S. Koting and M. R. Karim, "Performance Evaluation of Crumb Rubber Modified Stone Mastic Asphalt Pavement in Malaysia," *Advances in Materials Science and Engineering*, vol. 2013, pp. 1-8, 2013. https://doi.org/10.1155/2013/304676

[25] S. Habibu, "Better grade bitumen mixture to be used from May 1," Feb 16, 2017. [Online]. Available: https://www.thestar.com.my/news/nation/2017/02/16/better-grade-bitumen-mixture-to-be-used-from-may-1/ (Accessed Aug 8, 2022).

Single Droplet Size and Volume Measurement – Comparison Between Experiment and Theory

Suhaimi Illias[*], *Suhaila Hussain, Mohamad Shaiful Ashrul Ishak, Md. Tasyrif Abdul Rahman, Syamsul Syahrun Awang @ Hashim*
Fakulty of Mechanical Engineering and Technology,
Universiti Malaysia Perlis (UniMAP), Main Campus Pauh Putra,
02600 Arau, Perlis, MALAYSIA
**suhaimi@unimap.edu.my*

Salsuwanda Selamat
Faculty of Civil Engineering and Technology,
Universiti Malaysia Perlis (UniMAP), Main Campus Pauh Putra,
02600 Arau, Perlis, MALAYSIA

Mohd Hanafi Ani
Department of Manufacturing and Materials,
Kulliyyah of Engineering, International Islamic University Malaysia,
PO Box, 50728 Kuala Lumpur, MALAYSIA

ABSTRACT

The main objective of this paper is to conduct a manual drop test experiment to investigate the actual size and volume of a single droplet. Both experimental result and theoretical value were calculated for comparison. In this study methanol was chosen as the test liquid. The drop test was repeated numerous times with the droplet size measurement being calculated for every 50, 100 and 150 drops. A digital weight measurement was used to precisely measure the droplet weight in the drop test. Meanwhile for theoretical calculation, measurement was made based on chemical properties of the liquid itself. Based on the comparison, it was found that the experimental measurement of droplet size and volume is comparable with the theoretical calculation.

Keywords: *Single Droplet; Size; Volume; Methanol Liquid*

ISSN 1823-5514, eISSN 2550-164X

https://doi.org/10.24191/jmeche.v20i1.21093

Received for review: 2022-08-23
Accepted for publication: 2022-12-08
Published: 2023-01-15

Introduction

Drop test experiment is very important in heat and mass transfer study. For decades, it has been used to enhance the understanding regarding the nucleate boiling [1]-[2], transition boiling [3]-[5] and film boiling [6]-[8] process. This technique was used to study the boiling process and evaporation characteristic of droplet during impact on solid surfaces whether when being heated or in room temperature. This basic experimental work normally is equipped and supported with the usage of high-speed camera. The high-speed video camera is used to analyze the sequential images of every drop during the impact process. The drop test experiment and its results is important in thermal engineering application such as power plant [9]-[10], material manufacturing process [11], thermal energy and cooling studies [12]-[14], quenching and spray cooling studies [15]-[17] and many others. Drop impact researcher such as Moita and Moreira [18], Illias et al. [19]-[26], Mitsutake et al. [27]-[28], Inada et al. [29]-[30] and many other uses a single drop test in their experimental work. Drop test experiment can be used to study the behavior of impacting droplets, evaporation characteristic, vapor film generation, heat flux analysis and many others. Therefore, a precise droplet size and volume is needed to ensure the accuracy of the result.

Moita and Moreira [18] conducted an experimental work to study the deformation of spherical liquid droplets impacting onto flat and dry surfaces using a charged-coupled device (CCD) camera. During the experiments, each measurement was systematically repeated five times to confirm the reproducibility of the phenomena and to obtain the average values. The results show that an accurate characterization of the physical processes occurring during deformation and splash must take into account the forces involved (surface tension, shear forces and inertial), as well as the liquid properties and the nature of the impact surface. Illias et al. [19] conducted an experimental work to study the transient transition boiling phenomena that occur when a single ethanol droplet comes in contact with a hot surface (nickel). An extremely fast response chromel-nickel thermocouple was fixed at approximately 3 μm beneath the surface. This sensor has a very short response time of 80 μs. Therefore, it is capable enough to measure the transient boiling heat transfer. The outcomes of the studies confirm that droplet impact velocity, degrees of liquid subcooling, and the initial temperature of the solid may give an effect on the generation time of stable vapor film.

In this experimental work, the size and volume of single droplet were measured using scientific measurement and theoretical calculation. Methanol which has a low boiling point of 64.7 °C was chosen as a test liquid. A digital weight measurement was used in the experimental work to measure the liquid weight. A manual droplet dispenser which has a nozzle size of approximately 3.0 mm diameter was used in the drop test. Based on the findings, it was found that the experimental measurement of droplet size and volume is comparable

with the theoretical calculation. Therefore, it can be concluded that the technique outline in this paper may be used to maintain constant droplet size for other droplet studies which would increase the credibility of the findings of the studies.

Experimental Set-Up

This study primarily consists of drop test with schematic diagram of the experimental setup shown in Figure 1. The experimental apparatus consists of a droplet dispenser, retort stand, beaker and digital weight measurement. Methanol liquid was used in the experimental work. The drop test was performed for every 50, 100 and 150 times in order to measure the average of the single droplet weight. A digital weight measurement (MH-100 pocket scale) has been used to precisely measure the single droplet weight. As shown in Figure 2a, this digital weight measurement can give reading up to two digits (0.00 g). Therefore, it can produce an accurate and consistent reading. A manual droplet dispenser was used to release the droplet. The inner nozzle of manual droplet dispenser is 3.0 mm in diameter. Image of the manual droplet dispenser and its nozzle are shown in Figure 2b and 2c for easy reference. Meanwhile, Equations (1) and (2) [22] are used experimentally and theoretically to predict the radius and diameter of the falling droplet. In Equation (2), σ, g and ρ_{liq} represents the surface tension, gravity and density of the methanol liquid. The experimental conditions are tabulated in Table 1 for easy references and understanding.

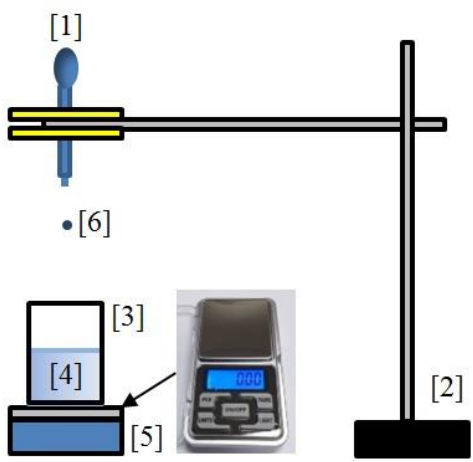

[1] Manual droplet dispenser
[2] Retort stand
[3] Beaker
[4] Methanol liquid
[5] Digital weight measurement
[6] Methanol droplet

Test 1: 50 drops
Test 2: 100 drops
Test 3: 150 drops

Figure 1: Schematic diagram of experimental apparatus

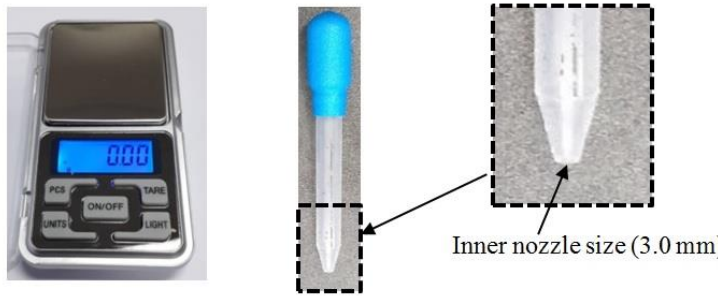

Figure 2: (a) Digital weight measurement, (b) manual droplet dispenser, and (c) inner nozzle size (3.0 mm)

$$V = (4/3)\pi r^3 \quad (1)$$

$$d = (6\sigma d_{needle}/\rho_{liq} g)^{1/3} \quad (2)$$

$$Percentage\ error\ (\%) = |\ (E_d - T_d) / (T_d)\ |\ x\ 100\% \quad (3)$$

Table 1: Experimental conditions and related information

Density of methanol ρ_{liq} (kg/m^3)	792
Surface tension of methanol, σ (N/m)	0.0219
Gravity, g (m/s^2)	9.81
Boiling point of methanol (°C)	64.7
Inner nozzle size diameter (mm)	3.0

Results and Discussion

The overall results from the methanol drop test measurement are shown in Table 2. A total number of 450 drops has been conducted during the experimental work. In Table 2, number of drops, mass of drops in gram, average mass per drop and estimation diameter of droplet has been listed systematically for easy understanding. From the overall results, it was observed that the average data for 50, 100 and 150 drops were approximately 1.083 g, 2.286 g and 3.260 g, respectively. Meanwhile, the average mass per drop for 50, 100 and 150 drops were 0.02166 g, 0.02286 g and 0.02173 g, respectively. Therefore, the cumulative average for single droplet was 0.022083 g. By using Equation (1), the estimation diameter of droplet measured is 3.4804 mm in cumulative average. The results from these two

different equations are shown in Table 3 for comparison. As evident in Table 3, the estimated diameter of methanol droplet calculated from the Equation (1) gives 3.4804 mm and Equation (2), 3.702 mm for experimental and theoretical value, respectively. In Table 3, we also provide a percentage differences between experimental data and theoretical calculation for references. The percentage of differences is based on Equation (3). The experimental and theoretical values were represented by E_d and T_d, respectively. Figure 3 shows an experimental result for three different number of drop test conducted. Each test numbered by 1, 2 and 3 were represented by the black, red and blue square dots, respectively in the plots. It was observed in Figure 3a that the average mass for 50 drops is 1.083 g as shown by the green dashed line. On top of that, average mass for 100 and 150 drops are 2.286 g and 3.260 g, respectively. From Figure 3, it can be concluded that the overall result is good agreement among each other. Figure 4 shows the experimental result of droplet diameter that was calculated based on Equation (1). The calculated diameter for single droplet based on the equation is 3.4580 mm for 50 drops, 3.5211 mm (100 drops) and 3.4621 mm (150 drops). Therefore, the average droplet diameter from the overall experimental work is 3.4804 mm. From Figure 4, the average result was represented by orange dashed line for easy understanding.

Based on the theoretical calculation, the estimated diameter of single methanol droplet is 3.702 mm. The calculation was based on the Equation (2) which uses methanol properties such as density and surface tension in the calculation. From Table 2 and Table 3, it can be concluded that the experimental result agrees closely with the theoretical calculation. The obtained results are similar to that already reported in our previous paper [22] which also employed the same technique of measurement.

Table 2: Overall result from drop test

No. of drops	Mass of drops (g)			Average mass (g)	Average mass per drop (g)	Estimation diameter of droplet from Equation (1) (mm)
	Test 1	Test 2	Test 3			
50	1.10	1.06	1.09	1.083	0.02166	3.4580
100	2.28	2.25	2.33	2.286	0.02286	3.5211
150	3.21	3.25	3.34	3.260	0.02173	3.4621
Cumulative average					**0.022083**	**3.4804**

Table 3: Comparison result between Equation (1) and Equation (2)

Formula	Equation (1) (mm)	Equation (2) (mm)	Percentage error based on Equation (3) (%)
Estimated diameter of methanol droplet	3.4804	3.702	6%

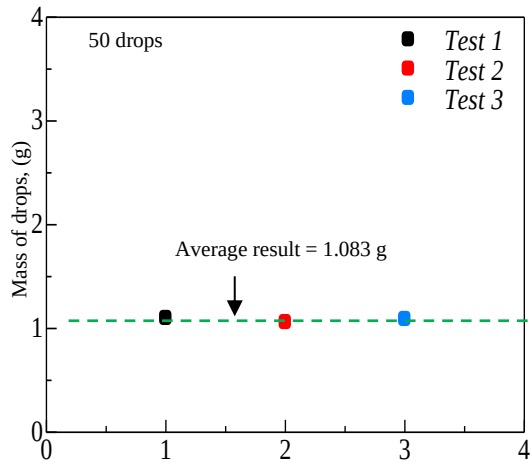

(a)

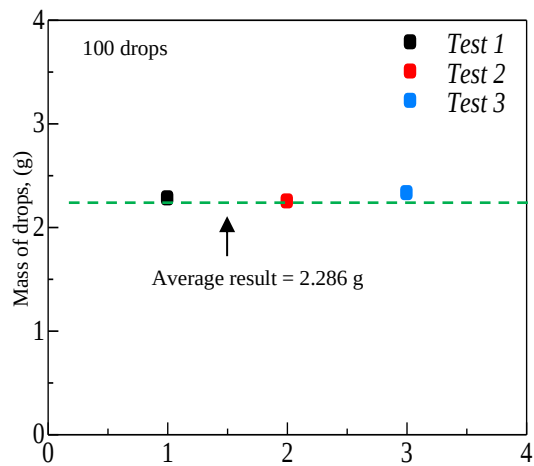

(b)

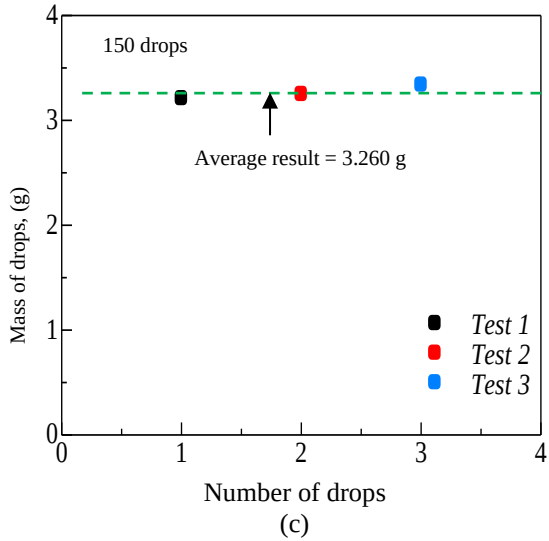

Figure 3: Experimental result for; (a) 50 drops, (b) 100 drops, and (c) 150 drops

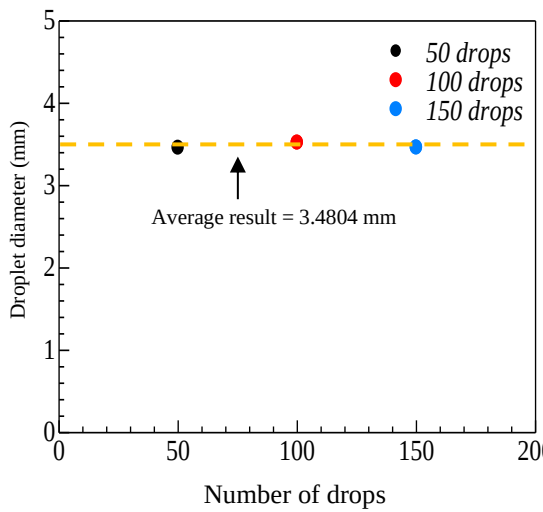

Figure 4: Relationship between number of drops and droplet diameter from Equation (1)

Conclusion

The experimental work has been conducted to investigate the size and volume of single droplet using simple drop test. A digital weight measurement was used to precisely measure the droplet weight in the drop test. For theoretical calculation, measurement was made based on chemical properties of the liquid itself. Based on the comparison, it can be concluded that the experimental measurement of droplet size and volume is comparable with the theoretical calculation. Therefore, it can be concluded that the technique outline in this paper may be used to maintain constant droplet size for other droplet studies which would increase the credibility of the findings of the studies.

Acknowledgement

The author would like to thank the Ministry of Education Malaysia, Universiti Malaysia Perlis (UniMAP) and the Research Management Centre (RMC) of Universiti Malaysia Perlis (UniMAP) for awarding a research grant to undertake this project.

Contributions of Authors

The authors confirm the equal contribution in each part of this work. All authors reviewed and approved the final version of this work.

Funding

This work was supported by the Fundamental Research Grand Scheme [FRGS/1/2018/TK03/UNIMAP/02/11].

Conflict of Interest

The authors declare that they have no competing interests.

References

[1] L. Gui, X. D. Wang, W. M. Yan,“Nucleate boiling inside small evaporating droplets: An experimental and numerical study”,

International Journal of Heat and Mass Transfer, vol.108, pp. 2253-2261, 2017. https://doi.org/10.1016/j.ijheatmasstransfer.2017.01.081

[2] M. N. Hasan, Ashik Hasan, S. Illias, Y. Mitsutake, M. Monde, "Characteristics of Homogeneous Nucleation Boiling in Ethanol during Rapid Linear Boundary Heating", *Procedia Engineering,* vol. 90, pp. 624-630, 2014. https://doi.org/10.1016/j.proeng.2014.11.782

[3] B. V. Balakin, M. I. Delov, A. Kosinska, K. V. Kutsenko, and A. A. Lavrukhin, "Heat transfer during transition to nucleate boiling", *International Journal of Heat and Mass Transfer*, vol. 91, pp. 1101-1105, 2015. https://doi.org/10.1016/j.ijheatmasstransfer.2015.08.026

[4] A. B. Ahmed and M. S. Hamed, "Modeling of transition boiling under an impinging water jet", *International Journal of Heat and Mass Transfer*, vol. 91, pp. 1273-1282, 2015. https://doi.org/10.1016/j.ijheatmasstransfer.2015.07.130

[5] L. J. Qi, J. Y. Zhang, L. W. Mou, Y. H. Zhang, L. W. Fan, "Enhanced transition heat flux by wicking during transition boiling on microporous hydrophilic and superhydrophilic surfaces", *International Journal of Heat and Mass Transfer*, vol 141, pp. 835-844, 2019. https://doi.org/10.1016/j.ijheatmasstransfer.2019.07.020

[6] V.V. Yagov, M. A. Leksin, A. R. Zabirov, M. A. Denisov, "Film boiling of subcooled liquids. Part II: Steady regimes of subcooled liquids film boiling", *International Journal of Heat and Mass Transfer,* vol. 100, pp. 918-926, 2016. https://doi.org/10.1016/j.ijheatmasstransfer.2016.04.069.

[7] C. F. Gomez, C. W. M. van der Geld, J. G. M. Kuerten, M. Bsibsi, B. P. M. van Esch, "Film boiling in quench cooling with high-temperature jets", *International Journal of Heat and Mass Transfer,* vol. 164, pp. 120578, 2021. https://doi.org/10.1016/j.ijheatmasstransfer.2020.120578

[8] Q. Liu, and X. Sun, "Wall heat transfer in the inverted annular film boiling regime", *Nuclear Engineering and Design,* vol. 363, pp. 110660, 2020. https://doi.org/10.1016/j.nucengdes.2020.110660

[9] S. D. Park, J. H. Kim, I. C. Bang, "Experimental study on a novel liquid metal fin concept preventing boiling critical heat flux for advanced nuclear power reactors", *Applied Thermal Engineering,* vol. 98, pp. 743-755, 2016. https://doi.org/10.1016/j.applthermaleng.2015.12.123

[10] L. Santini, A. Cioncolini, M. T. Butel, M. E. Ricotti, "Flow boiling heat transfer in a helically coiled steam generator for nuclear power applications", *International Journal of Heat and Mass Transfer,* vol. 92, pp. 91-99, 2026. https://doi.org/10.1016/j.ijheatmasstransfer.2015.08.012

[11] L. E. Murr, and W. L. Johnson, "3D metal droplet printing development and advanced materials additive manufacturing", *Journal of Materials Research and Technology*, vol. 6, no. 1, pp. 77-89, 2017. https://doi.org/10.1016/j.jmrt.2016.11.002

[12] H. Lv, Q. Bi, Z. Zhang, G. Zhu, K. Li, and H. Liu, "Hydraulic resistance of in-tube cooling supercritical water accompanying out-tube pool

boiling", *Applied Thermal Engineering*, vol. 141, pp. 394-405, 2018. https://doi.org/10.1016/j.applthermaleng.2018.04.136

[13] J. D. Engerer, J. H. Doty, T. S. Fisher, "Transient thermal analysis of flash-boiling cooling in the presence of high-heat-flux loads", *International Journal of Heat and Mass Transfer*, vol. 123, pp. 678-692, 2018. https://doi.org/10.1016/j.ijheatmasstransfer.2018.02.109

[14] A.K. Sadaghiani, N. S. Saadi, S. S Parapari, T. Karabacak, M. Keskinoz, and A. Koşar, "Boiling heat transfer performance enhancement using micro and nano structured surfaces for high heat flux electronics cooling systems", *Applied Thermal Engineering*, vol. 127, pp. 484-498, 2017. https://doi.org/10.1016/j.applthermaleng.2017.08.018

[15] X. Liu, J. Liu, R. Xue, L. Chen, Y. Hou, "Heat transfer optimization of R134a phase change spray cooling in a closed loop system", *Experimental Thermal and Fluid Science*, vol. 92, pp. 248-258, 2018. https://doi.org/10.1016/j.expthermflusci.2017.11.010

[16] O. Lamini, R. Wu, C. Y. Zhao, and Z. G. Xu, "Enhanced heat spray cooling with a moving nozzle", *Applied Thermal Engineering*, vol. 141, pp. 921-927, 2018. https://doi.org/10.1016/j.applthermaleng.2018.06.025

[17] C. Wang, R. Xu, Y. Song, P. Jiang, "Study on water droplet flash evaporation in vacuum spray cooling", *International Journal of Heat and Mass Transfer*, vol. 112, pp. 279-288, 2017. https://doi.org/10.1016/j.ijheatmasstransfer.2017.04.111

[18] A.S Moita, A. L. N. Moreira, "The deformation of single droplets impacting onto a flat surface", *SAE Transactions*, pp. 1477-1489, 2002.

[19] S. Illias, M. N. Hasan, Y. Mitsutake, M. Monde, "High speed observation and measurement of surface temperature and surface heat flux during impact of a droplet on hot surface", In *International Heat Transfer Conference Digital Library*. Begel House Inc., (IHTC-15) 2014.

[20] S. Illias, S. Hussain, M. S. A. Ishak, M. Z. M. Zain, and M. A. Idris, "Visual study of droplet bouncing phenomena upon impact on hot horizontal surface", *International Journal of Applied Engineering Research*, vol. 12, no. 7, pp. 1305-1310, 2017.

[21] S. Illias, S. Hussain, N. A. Rosman, N. S. Abdullah, M. S. A. Ishak, M. N. B. Omar, H. Ani, "Receding height of water droplet in the film boiling regime", *In IOP Conference Series: Materials Science and Engineering*, vol. 670, no. 1, pp. 012038, 2019. 10.1088/1757-899X/670/1/012038

[22] S. Illias, N. A. Rosman, N. S. Abdullah, S. Hussain, M. E. Baharudin, M. A. Idris, K. A. Ismail, "Critical heat flux and Leidenfrost temperature on hemispherical stainless steel surface", *Case Studies in Thermal Engineering*, vol. 14, pp. 100501, 2019. https://doi.org/10.1016/j.csite.2019.100501

[23] S. Illias, M. N. Hasan, Y. Mitsutake, M. Monde, "Generation time of stable vapor film during impact of a droplet on hot surface", *Thermal Science and Engineering*, vol. 22, no. 2, pp. 21-31, 2014.

[24] S. Illias, M. S. A. Ishak, S. Hussain, K. A. Ismail, "High speed visualization and analysis of maximum spreading of water droplet during impact on hot horizontal surface", *International Journal of Applied Engineering Research*, vol. 11, no. 22, pp. 10832-10837, 2016.

[25] S. Illias, S. Hussain, N. A. Rosman, N. S. Abdullah, M. S. A. Ishak, M. N. B. Omar, K. A. Ismail, H. Ani, "Evaporation lifetime and boiling curve on hemispherical stainless steel (304) surface", In *IOP Conference Series: Materials Science and Engineering*, vol. 670, no. 1, pp. 012013. IOP Publishing, 2019. 10.1088/1757-899X/670/1/012013

[26] S. Illias, M. A. Idris, and M. Z. M. Zain, "Experimental Studies of Film Boiling Phenomena on Carbon Heated Surface", *International Review of Mechanical Engineering* vol. 5.5, pp. 812-817, 2011.

[27] Y. Mitsutake, S. Illias, K. Tsubaki, M. N. Hasan, M. Monde, "Measurement and Observation of Elementary Transition Boiling Process after Sudden Contact of Liquid with Hot Surface", *Procedia Engineering*, vol. 105, pp. 5-21, 2015. https://doi.org/10.1016/j.proeng.2015.05.002

[28] Y. Mitsutake, S. Illias, A. K. Mozumder, M. Monde, "Measurement of surface temperature and surface heat flux during impact of a droplet on a hot surface", *In 49th National Heat Transfer Symposium*, 2011.

[29] S. Inada, K. Shinagawa, S. Illias, H. Sumiya, H. A. Jalaludin, "Micro-bubble emission boiling with the cavitation bubble blow pit", *Scientific reports* 6, no. 1, pp. 1-7, 2016. https://doi.org/10.1038/srep33454

[30] S. Inada, H. Sumiya, K. Shinagawa, S. Illias, "Mechanism Elucidation for the miniaturization-boiling phenomena in droplet collision boiling system", In *International Heat Transfer Conference Digital Library*. Begel House Inc., (IHTC-13) 2006.